Elucidating the Mechanisms Behind Pre-Breakdown Phenomena in Transformer Oil Systems

by

Jae-Won George Hwang

B.A.Sc., University of Toronto (2004)

M.A.Sc., University of Toronto (2007)

Submitted to the Department of Electrical Engineering and Computer Science
in partial fulfillment of the requirements for the degree of

Doctor of Philosophy

at the

Massachusetts Institute of Technology

June 2010

Author _____
Department of Electrical Engineering and Computer Science
May 21, 2010

Certified by _____
Markus Zahn
Thomas and Gerd Perkins Professor of Electrical Engineering and Director, VI-A Internship Program
Thesis Supervisor

Accepted by _____
Terry P. Orlando
Chairman, Department Committee on Graduate Students

Elucidating the Mechanisms Behind Pre-Breakdown Phenomena in Transformer Oil Systems

by

Jae-Won George Hwang

Submitted to the Department of Electrical Engineering and Computer Science
on May 21, 2010, in partial fulfillment of the
requirements for the degree of
Doctor of Philosophy

Abstract

THE WIDESPREAD use of dielectric liquids for high voltage insulation and power apparatus cooling is due to their greater electrical breakdown strength and thermal conductivity than gaseous insulators. In addition, their ability to conform to complex geometries and self-heal means that they are often of more practical use than solid insulators. Unfortunately, as with all insulation, the failure of the liquid insulation can cause catastrophic damage. This has led researchers to study the insulating properties of dielectric liquids in an attempt to understand the underlying mechanisms that precede electrical breakdown in order to prevent them.

This thesis develops a set of mathematical models which contain the physics to elucidate the pre-breakdown phenomena in transformer oil and other oil-based systems. The models are solved numerically using the finite element software package COMSOL Multiphysics. For transformer oil, the results show that transformer oil stressed by a positively charged needle electrode results in the ionization of oil molecules into positive ions and electrons. The highly mobile electrons are swept back towards the positive electrode leaving a net positive space charge region that propagates towards the negative electrode causing the maximum electric field to move further into the oil bulk. It is the moving electric field and space charge waves that allow ionization to occur further into the oil. This leads to thermal dissipation and creates a low density streamer channel.

In comparing the numerical results to experimental data found in the literature, the results indicate that positive streamer propagation velocity regimes or modes are dictated by the onset of different ionization mechanisms (i.e., field ionization, impact ionization, photo-ionization) that are dependent on the liquid molecular structure and the applied voltage stress. In particular, the field ionization of different families of molecules plays a major role in development of slow and fast mode streamers, especially in liquids that are comprised of many different types of molecules such as transformer oil. The key characteristics of the molecules that affect streamer propagation are their molecular structure (i.e., packing, density, and separation distance) and ionization potential. A direct outcome of this work has been the ability to show that by adding low ionization potential additives to pure dielectric liquids, the voltage at which streamers transition from slow to fast mode can be significantly increased, a result counter-intuitive to conventional wisdom and common practice.

For transformer oil with nanoparticle suspensions (nanofluids), the effects of nanoparticle charging on streamer development have been thoroughly investigated. The charging dynamics of a nanoparticle in transformer oil show that electron trapping by conductive nanoparticles is the cause of a decrease in positive streamer velocity resulting in higher electrical breakdown strength for transformer oil-based nanofluids. Further generalized analysis of the charging of a perfectly conducting sphere from a single charge carrier or two charge carriers of opposite polarity, with different values of volume charge density and mobility and including an ohmic lossy dielectric region surrounding a perfectly conducting sphere or cylinder are also examined.

Streamer development in liquid-solid insulation systems, such as oil-pressboard systems, is also investigated. Great effort has been undertaken to model the solid insulation region and a method has been developed to model the oil-solid interface to account for surface charge build up, which is important for streamer dynamics. Various ohmic and migration conduction laws are used for oil and solid insulation to solve for the time and space development of surface charge distributions in closed form for one-dimensional parallel plane and numerically for two-dimensional geometries. The work on streamers in oil-pressboard systems has shown that streamers are attracted to the oil-pressboard interface, due to the larger permittivity of the pressboard. Moreover, the models have shown that the determination of how streamers propagate in the presence of solid insulation is strongly dependent on the extent to which the solid insulation alters the streamer shape and the electric field created by the streamer's space charge. These results obtained from the modeling of streamers in oil-pressboard systems are supported by and help to explain the experimental data in the literature.

Thesis Supervisor: Markus Zahn
Title: Thomas and Gerd Perkins Professor of Electrical Engineering and Director, VI-A Internship Program

Acknowledgements

I want to thank Prof. Markus Zahn, my thesis advisor, for his guidance, support and friendship during the course of this journey. He is an outstanding teacher and person.

A special thanks to my thesis committee: Prof. Jeffrey Lang and Prof. Paulo Lozano for their support, advice and direction.

Thanks to the sponsors of my work: ABB and National Sciences and Engineering Council of Canada (NSERC). From ABB, I would like to thank Dr. Leif Pettersson and Dr. Olof Hjortstam who have helped me tremendously throughout the course of this thesis.

I want to acknowledge the contributions and all things learned from members, both past and present, of my research group, all excellent individuals and good friends: Alex Trubitsyn, Benjamin Cannon, Fergus Hurley, Francis O'Sullivan, Jiankang Wang, Justin Burkhart, Samuel Chang, Shahriar Khushrushahi, Uzoma Orji, Warit Wichakool, and Wei Li.

I'm also grateful for all the help provided by my colleagues and staff from LEES: Dimonika Bizi, Makikio Wada, and the late Vivian Mizuno.

This work is also dedicated to my friends that have supported me during my graduate studies: In Boston: to my friends Anthony Sagneri, Cody Gilleland, Courtney Schmitt, Doris Lin, Grace Cheung, Jackie Hu, Jason Chang, Marcus Yip, and Melinda Tang. Elsewhere: Andy Song, Antonio Coccia, Bob Won, Daniel Ku, Jonathon Edward, Mina Choi, and Yoonjin Lee. You all have played a great role in my life and I could not ask for better friends.

I owe my deepest gratitude to my parents Ho-Yun and Yang-Sook, my siblings Eun-Soo and Steve, Sang-Won and Priscilla, and Jee-Soo and Chris, and to the nieces and nephew, Mia, Ella and Owen, who only know me as DumDum. Without their love and support I would not be where I am today.

Contents

1 Introduction **29**

1.1 Liquid Insulation and Pre-breakdown Phenomena 30

1.2 Lumped Circuit Analogy of Streamers and Electrical Insulation 32

1.3 Modeling of Streamers in Dielectric Liquids 34

1.4 Thesis Organization 36

2 Streamers in Dielectric Liquid-Based Insulation Systems **39**

2.1 Mineral Oil 39

2.1.1 Positive Streamer Propagation Modes in Transformer Oil 40

2.2 Streamers in Other Dielectric Liquids 44

2.2.1 Ester Liquids 44

2.2.2 Other Dielectric Liquids 47

2.3 The Effects of Additives on Hydrocarbon Oils 47

2.3.1 Exxon Marcol 70 Naphthenic Oil with Low Ionization Potential Additives 49

2.3.2 Pure Cyclohexane and Cyclohexane with Pyrene Additive 49

2.4 Transformer Oil-Based Nanofluids 52

2.5 Transformer Oil-Solid Insulation Systems 54

2.5.1 Liquid-Solid Interface Oriented Parallel to the Main Electric Field Component 55

2.5.2 Liquid-Solid Interface Oriented Perpendicular to the Main Electric Field Component 58

2.5.3 The Effects of Permittivity Differences Between Transformer Oil and Solid Insulation on Streamer Propagation 61

3 General Electrohydrodynamic Model for Dielectric Liquids **63**

3.1 Governing Equations 63
3.2 Needle-Sphere Geometry 65
3.3 Boundary Equations 68
3.4 Charge Carrier Mobility 69
3.5 Recombination 70
3.6 Electron Attachment 70
3.7 Charge Generation Mechanisms in the Liquid State 71
3.7.1 Field Ionization 72
3.7.2 Impact Ionization 74
3.7.3 Photo-ionization 75
3.8 Conceptual Understanding of Field Ionization 77

4 On the Development of Positive Streamers and Their Distinct Propagation Modes in Transformer Oil 81

4.1 Comparing 2^{nd} and 3^{rd} Mode Streamers 81
4.2 Slow 2^{nd} Mode Streamers: Field Ionization of Aromatic Molecules 84
4.2.1 $V_{app} = 130\,\text{kV}$ – Figures 4.1 and 4.2 84
4.2.2 $V_{app} = 200\,\text{kV}$ – Figures 4.3 and 4.4 86
4.2.3 $V_{app} = 300\,\text{kV}$ – Figures 4.5 and 4.6 86
4.3 Fast 3^{rd} Mode Streamers: Field Ionization of Naphthenic /Paraffinic Molecules 94
4.3.1 $V_{app} = 130\,\text{kV}$ – Figures 4.7 and 4.8 94
4.3.2 $V_{app} = 200\,\text{kV}$ – Figures 4.9 and 4.10 94
4.3.3 $V_{app} = 300\,\text{kV}$ – Figures 4.11 and 4.12 95
4.4 Verifying Biller's Model for Streamer Propagation Modes 103
4.5 Preliminary Model of Streamer Protrusions 104
4.6 The Space Charge Shielding Effect: Increasing the Acceleration Voltage . . 107
4.6.1 Streamers in Heterogeneous Dielectric Liquids 108
4.6.2 Case 1 – Figures 4.15 and 4.16 111
4.6.3 Case 2 – Figures 4.17 and 4.18 114
4.6.4 Discussion 117
4.6.4.1 The Effect of Additive Ionization Potential 117

4.6.4.2 The Effect of Additive Concentration and Liquid Purity . . 119
4.6.4.3 Engineering Dielectric Liquids with Increased Acceleration Voltage 120
4.7 Fast Event 4^{th} Mode Streamers: A Transition to New Charge Generation Mechanisms 120
4.7.1 Field Ionization Revisited 121
4.7.2 Impact and Photo-Ionizations: The Transition from Solid-State Physics to Gas-State Physics 124
4.7.3 Results and Discussion 127
4.8 Summary and Key Results 129

5 The Charging of Nanoparticle Suspensions in Dielectric Liquids and the Effect on Streamer Development 133
5.1 Charge Relaxation Time 134
5.2 Unipolar Charging Dynamics of a Spherical Nanoparticle 135
5.2.1 Perfectly Conducting Nanoparticle 136
5.2.2 Finitely Conducting Nanoparticle 140
5.2.3 Solution for the Electric Field Lines 142
5.2.3.1 Perfectly Conducting Nanoparticle 143
5.2.3.2 Finitely Conducting Nanoparticle 144
5.2.4 Evaluating Nanoparticle Charging 145
5.3 Bipolar Charging Dynamics of a Spherical Nanoparticle 149
5.3.1 Solution for the Electric Field Lines 150
5.3.2 Critical Points 151
5.3.3 Total Current that Charges the Sphere 152
5.3.4 Method to Check the Sphere Charging Current 153
5.3.5 Unipolar Charging of the Sphere 154
5.3.5.1 Positive Charging 154
5.3.5.2 Negative Charging 155
5.3.6 Bipolar Charging of the Sphere 156
5.4 Model of Streamer Propagation in Transformer Oil-Based Nanofluids . . . 157

5.4.1 Governing Equations and Model Parameters 158
5.4.2 Modeling Nanoparticle Charging 160
5.5 Results and Discussion of Streamer Propagation in Transformer Oil-Based Nanofluids 161
5.5.1 Electric Field Dynamics 161
5.5.2 Charge Density Dynamics 163
5.5.3 Electric Potential 165
5.6 Summary and Key Results 166

6 General Electrodynamic Models for Multi-Dielectric Systems 167
6.1 Modeling Solid Insulators 167
6.1.1 Migration Model 168
6.1.2 Ohmic Model 170
6.1.3 Insulator Model 172
6.2 Preliminary Studies of Simplified Multi-Dielectric Insulation Systems . . . 174
6.2.1 Steady-State Study of Migration-Migration Model 175
6.2.1.1 Analytical Model 175
6.2.1.2 Numerical Model 177
6.2.1.3 Results and Discussion 179
6.2.2 Steady-State Study of Migration-Ohmic Model 183
6.2.2.1 Analytical Model 183
6.2.2.2 Numerical Model 184
6.2.2.3 Results and Discussion 185
6.2.3 Step Current Transient Study of Migration-Ohmic Model 186
6.2.3.1 Analytical Model 186
6.2.3.2 Numerical Model 190
6.2.3.3 Results and Discussion 192
6.3 Complete Models for Liquid-Solid Insulation Systems 192
6.3.1 Governing Equations for the Migration Model of the Liquid Dielectric 193
6.3.2 Governing Equations for the Ohmic Model of the Solid Dielectric . 194
6.3.3 Governing Equations for the Insulator Model of the Solid Dielectric 195

6.3.4 Artificial Diffusion 196

7 The Influence of Solid Insulation on Streamer Development in Dielectric Liquids 199

7.1 Streamers in Oil with Solid Insulation Oriented Parallel and Perpendicular to the Primary Electric Field Direction 199

7.1.1 Governing Equations of the Oil-Solid Insulation System 200

7.1.1.1 Oil Governing Equations 200

7.1.1.2 Solid Insulation Governing Equation 201

7.1.1.3 Oil-Solid Interface Governing Equation 201

7.1.2 Parallel Oriented Interface – PTFE Cylindrical Tube 202

7.1.3 Perpendicular Oriented Interface – Pressboard Barrier 202

7.2 Oil-PTFE Tube System with the Interface Oriented Parallel to the Primary Electric Field Direction 204

7.2.1 $V_{app} = 130\,\text{kV}$ – Figures 7.4(a), 7.4(b) and 7.5 205

7.2.2 $V_{app} = 200\,\text{kV}$ – Figures 7.4(c), 7.4(d) and 7.6 207

7.2.3 $V_{app} = 300\,\text{kV}$ – Figures 7.4(e), 7.4(f) and 7.7 209

7.2.4 Summary 215

7.3 Oil-Pressboard Barrier System with the Interface Oriented Perpendicular to the Primary Electric Field Direction 215

7.3.1 Results – Figures 7.9 and 7.10 216

7.3.1.1 Streamer Prior to Contacting Interface – Figs. 7.10(a) and 7.10(b) 217

7.3.1.2 Streamer Immediately After Contacting Interface – Fig. 7.10(c) 217

7.3.1.3 Streamer Traveling along Perpendicular Interface - Figs. 7.9 and 7.10(d)-7.10(f) 219

7.3.2 Summary 221

7.4 The Effects of Permittivity Differences of Oil and Solid Insulation on Streamer Propagation 221

7.4.1 Permittivity and Polarization 222

7.4.2 Analytical Study of the Electric Fields in a Simplified Two Dielectric System with Unique Permittivities 223

7.4.3 Parallel Oriented Interface – Cylindrical Tube 225
7.4.3.1 $\epsilon = 4.4\epsilon_0$ – Figures 7.13(a), 7.13(b) and 7.14 226
7.4.3.2 $\epsilon = 3.3\epsilon_0$ – Figures 7.13(c), 7.13(d) and 7.15 227
7.4.3.3 $\epsilon = 1.0\epsilon_0$ – Figures 7.13(e), 7.13(f) and 7.16 229
7.4.4 Perpendicular Oriented Interface – Solid Barrier 235
7.4.4.1 $\epsilon = 3.3\epsilon_0$ – Figures 7.17(a), 7.17(b) and 7.18 235
7.4.4.2 $\epsilon = 2.2\epsilon_0$ – Figures 7.17(c), 7.17(d) and 7.19 236
7.4.4.3 $\epsilon = 1.0\epsilon_0$ – Figures 7.17(e), 7.17(f) and 7.20 237
7.4.5 Summary 244
7.5 Summary and Key Results 245

8 Conclusion **247**
8.1 Thesis Summary and Contributions 247
8.1.1 Transformer Oil 248
8.1.2 Dielectric Liquids with Conductive Nanoparticle Suspensions 249
8.1.3 Liquid-Solid Insulation Systems 250
8.2 Future Work 253
8.2.1 Expanding the Streamer Model 253
8.2.2 Experimental Work 254

A Numerical Current Calculation Methods in COMSOL Multiphysics **257**
A.1 Generalized Power Method via Poynting's Theorem 258
A.1.1 Implementation of Terminal Current Calculation in COMSOL Multiphysics 259
A.1.2 Results 261
A.2 Boundary Area Integration of Total Current Density 263
A.2.1 Implementation of Terminal Current Calculation in COMSOL Multiphysics 263
A.2.2 Results 265
A.3 Summary 265

B Implementation of Internal Boundary Conditions at the Liquid-Solid Interface 267

C A Low Ionization Potential Additive Method to Increase the Electric Breakdown Strength of Insulation Materials 271

D COMSOL Multiphysics Settings for Transformer Oil Model 289

E COMSOL Multiphysics Settings for Composite Transformer Oil-Solid Cylindrical Tube Model 305

Bibliography 321

List of Figures

1.1 Propagation of fast positive streamer in transformer oil in a point-plane electrode geometry under 0.5 μs rise time and 85 μs fall time impulse voltage. Gap length 27.5 mm. Tip radius 30 μm; Crest voltage 178 kV. Schlieren photograph (frame exposure time 8 ns) [1,2] 31

1.2 Lumped circuit model of transformer oil. 33

2.1 Experimental data from ABB Corporate Research regarding positive streamer propagation modes for the needle-sphere geometry detailed in IEC Standard 68097 [3] and used in the modeling work of this thesis. Courtesy of R. Liu and L. A. A. Pettersson at ABB Corporate Research in Västerås, Sweden. . 43

2.2 Experimental data from Duy *et al.* regarding positive streamer propagation in rape-seed oil comprised of natural esters [4–6]. Summary of measurements carried out on positive streamers with $d=2$ cm gap distance (V_b: 50% probability breakdown voltage, V_a: acceleration voltage). (a) streamer stopping length, (b) streamer average velocity (c) streamer charge. (Figure 3, [6]) . . 45

2.3 Experimental data from ABB Corporate Research regarding positive streamer propagation in natural and synthetic esters for the needle-sphere geometry detailed in IEC Standard 68097 [3]. Courtesy of R. Liu and L. A. A. Pettersson at ABB Corporate Research in Västerås, Sweden. 46

2.4 Experimental data from ABB Corporate Research comparing the average positive streamer velocity versus applied voltage in ester liquids and transformer oils for the needle-sphere geometry detailed in IEC Standard 68097 [3]. Courtesy of R. Liu and L. A. A. Pettersson at ABB Corporate Research in Västerås, Sweden. 47

2.5 Experimental data from the Lesaint group regarding positive streamer velocity as a function of applied voltage for several different dielectric liquids [7–10]. 48

2.6 Gap and voltage dependence of positive streamer velocities in Marcol 70 at various DMA concentrations. Hap: (open points) 1.27 cm, (solid points) 2.54 cm, ($\times$) 0.64 cm. Concentration of DMA: ($\circ$) 7×10^{-3} M, ($\square$) 2.2×10^{-2} M, ($\triangle$) 6.7×10^{-2} M, ($\triangledown$) 1.27×10^{-1} M, ($\times$) 1.58×10^{-1} M, ($\Diamond$) 2.1×10^{-1} M. Dashed line for transformer oil. (Figure 33, [11]) 50

2.7 Experimental data from Lesaint and Jung regarding positive streamer propagation in cyclohexane with pyrene additive [12]. 51

2.8 Experimental data from Lesaint and Jung showing typical photographs of streamers, taken 0.8 μs after the voltage rise at $V = 30$ kV, for various pyrene concentrations: (a) $c = 0$M; (b) $c = 0.1$M; (c) $c = 0.7$M; and (d) $c = 1$M (Figure 8, [12]). 52

2.9 Qualitative examples of the two transformer oil-pressboard orientations discussed in the literature. 55

2.10 Experimental results of Massala and Lesaint [13] for streamers in point-plane systems with and without pressboard. In an oil-pressboard system, the streamer travels along a pressboard surface parallel to the point-plane axis (*i.e.*, surface is parallel to dominant field direction) with gap length $d = 10$ cm. Their results suggest that in such systems the breakdown probability/voltage is unchanged by the pressboard (see Fig. 2.10(a)), however the acceleration voltage is dramatically reduced (see Fig. 2.10(b)). 56

2.11 Experimental results of Massala and Lesaint [13] for streamers whose propagation is restricted within cylindrical tubes of polytetrafluoroethylene or polypropylene with length $d = 10$ cm and varying diameters. The setup is such that main electric field component within the inner tube is parallel to the oil-tube interface. Their results suggest that in such systems the streamer propagation is aided by the presence of the tube, which restricts the radial growth of the streamer and alters the streamer shape from that of the case where no tube is present. 57

2.12 Hypothesis from Lundgaard *et al.* [14] regarding the acceleration of positive streamers at over-voltage along solid surfaces where the surface is parallel to the direction of the main electric field component. Upper: The positive streamer model. Lower: Actual tracks observed on pressboard surface. Lundgaard *et al.* hypothesize that the solid insulation hinders the branching of streamers, which regulates the electric field enhancement at the head of the streamer. Consequently, due to the lack geometrical symmetry of the streamer shape the field enhancement at the streamer head is higher at lower voltages and drives faster charge generation resulting in the acceleration of streamers. (Figure 18, [14]) 58

2.13 Experimental results of Massala and Lesaint [13] for streamers whose propagation is along a pressboard surface that is perpendicular to the symmetry axis. Photograph of a 2^{nd} mode streamer traveling along the pressboard surface (dashed line). The intensifier gate was closed 10 μs before breakdown, gap distance $d = 10$ cm, plane-to-pressboard distance of 2 cm, $V_{app} = 208$ kV. The setup is such that main electric field component is perpendicular with the pressboard interface. Their results show that as the streamer comes in contact with the pressboard surface its propagation direction is altered and it begins to grow radially along the pressboard surface thereby increasing the time to breakdown. (Figure 2, [13]) 59

2.14 Experimental results of Liu *et al.* [15, 16] for streamers whose propagation is restricted along oil impregnated laminated papers that cover the ground electrode. The setup is such that the main electric field component is perpendicular to the paper interface. Their results suggest that the introduction of a solid pressboard into the oil system can increase breakdown voltage and decrease streamer propagation velocity. As the streamer comes in contact with the perpendicular paper surface it cannot propagate axially towards the ground electrode. Therefore, it travels radially along the surface increasing the time to breakdown and decreasing the average streamer velocity. 60

3.1 Needle-sphere electrode geometry system for which experimental tests at ABB and computer simulations at MIT are conducted to study pre-breakdown conditions for transformer oil in this thesis. 66

3.2 Needle-sphere electrode geometry system in COMSOL Multiphysics. The needle-sphere z-axis about which the geometry is symmetric has been clearly indicated with a red dashed line. Throughout this work, line plots for various quantities, such as electric field magnitude, space charge density, and oil temperature, will be taken along the needle-sphere z-axis where $r=0$. . . . 67

3.3 (a) Laplacian electric field magnitude [V/m] distribution (*i.e.*, $\nabla\cdot(\epsilon\vec{E}) = 0$) at $t=0^+$ for 300 kV applied voltage near the 40 μm radius needle electrode apex at the origin. The sphere electrode (not shown) is at $r=0$, $z=25$ mm. (b) The field enhancement is largest near the sharp needle tip quickly decreasing as z increases. 68

4.1 Temporal dynamics along the needle-sphere electrode axis at 25 ns intervals from $t=25-100$ ns given by the solution to the streamer model of (4.4)-(4.8) for an applied voltage of $V_{app}=130$ kV and the field ionization mechanism of (4.1). The oil is comprised of low number density, low ionization potential aromatic hydrocarbon molecules only with parameter values summarized in Table 4.1. Note, at time $t=0^+$ the electric field represents the Laplacian electric field and the oil temperature is 300 K. 88

4.2 Electric field magnitude [V/m] spatial distributions (as a function of r and z in the electrode geometry) from $t=25-325$ ns given by the solution to the streamer model of (4.4)-(4.8) for an applied voltage of $V_{app}=130$ kV and the field ionization mechanism of (4.1). The oil is comprised of low number density, low ionization potential aromatic hydrocarbon molecules only with parameter values summarized in Table 4.1. 89

4.3 Temporal dynamics along the needle-sphere electrode axis at 25 ns intervals from $t = 25 - 100$ ns given by the solution to the streamer model of (4.4)-(4.8) for an applied voltage of $V_{app} = 200$ kV and the field ionization mechanism of (4.1). The oil is comprised of low number density, low ionization potential aromatic hydrocarbon molecules only with parameter values summarized in Table 4.1. Note, at time $t = 0^+$ the electric field represents the Laplacian electric field and the oil temperature is 300 K. 90

4.4 Electric field magnitude [V/m] spatial distributions (as a function of r and z in the electrode geometry) from $t = 25 - 100$ ns given by the solution to the streamer model of (4.4)-(4.8) for an applied voltage of $V_{app} = 200$ kV and the field ionization mechanism of (4.1). The oil is comprised of low number density, low ionization potential aromatic hydrocarbon molecules only with parameter values summarized in Table 4.1. 91

4.5 Temporal dynamics along the needle-sphere electrode axis at 25 ns intervals from $t = 25 - 100$ ns given by the solution to the streamer model of (4.4)-(4.8) for an applied voltage of $V_{app} = 300$ kV and the field ionization mechanism of (4.1). The oil is comprised of low number density, low ionization potential aromatic hydrocarbon molecules only with parameter values summarized in Table 4.1. Note, at time $t = 0^+$ the electric field represents the Laplacian electric field and the oil temperature is 300 K. 92

4.6 Electric field magnitude [V/m] spatial distributions (as a function of r and z in the electrode geometry) from $t = 25 - 100$ ns given by the solution to the streamer model of (4.4)-(4.8) for an applied voltage of $V_{app} = 300$ kV and the field ionization mechanism of (4.1). The oil is comprised of low number density, low ionization potential aromatic hydrocarbon molecules only with parameter values summarized in Table 4.1. 93

4.7 Temporal dynamics along the needle-sphere electrode axis at 25 ns intervals from $t = 25 - 100$ ns given by the solution to the streamer model of (4.4)-(4.8) for an applied voltage of $V_{app} = 130$ kV and the field ionization mechanism of (4.1). The oil is comprised of high number density, high ionization potential naphthenic/paraffinic hydrocarbon molecules only with parameter values summarized in Table 4.2. Note, at time $t = 0^+$ the electric field represents the Laplacian electric field and the oil temperature is 300 K. 97

4.8 Electric field magnitude [V/m] spatial distributions (as a function of r and z in the electrode geometry) from $t = 25 - 100$ ns given by the solution to the streamer model of (4.4)-(4.8) for an applied voltage of $V_{app} = 130$ kV and the field ionization mechanism of (4.1). The oil is comprised of high number density, high ionization potential naphthenic/paraffinic hydrocarbon molecules only with parameter values summarized in Table 4.2. Note there is no streamer formation. 98

4.9 Temporal dynamics along the needle-sphere electrode axis at 25 ns intervals from $t = 25 - 100$ ns given by the solution to the streamer model of (4.4)-(4.8) for an applied voltage of $V_{app} = 200$ kV and the field ionization mechanism of (4.1). The oil is comprised of high number density, high ionization potential naphthenic/paraffinic hydrocarbon molecules only with parameter values summarized in Table 4.2. Note, at time $t = 0^+$ the electric field represents the Laplacian electric field and the oil temperature is 300 K. 99

4.10 Electric field magnitude [V/m] spatial distributions (as a function of r and z in the electrode geometry) from $t = 25 - 100$ ns given by the solution to the streamer model of (4.4)-(4.8) for an applied voltage of $V_{app} = 200$ kV and the field ionization mechanism of (4.1). The oil is comprised of high number density, high ionization potential naphthenic/paraffinic hydrocarbon molecules only with parameter values summarized in Table 4.2. Note there is no streamer formation. 100

4.11 Temporal dynamics along the needle-sphere electrode axis at 25 ns intervals from $t = 25 - 100$ ns given by the solution to the streamer model of (4.4)-(4.8) for an applied voltage of $V_{app} = 300$ kV and the field ionization mechanism of (4.1). The oil is comprised of high number density, high ionization potential naphthenic/paraffinic hydrocarbon molecules only with parameter values summarized in Table 4.2. Note, at time $t = 0^+$ the electric field represents the Laplacian electric field and the oil temperature is 300 K. 101

4.12 Electric field magnitude [V/m] spatial distributions (as a function of r and z in the electrode geometry) from $t = 25 - 100$ ns given by the solution to the streamer model of (4.4)-(4.8) for an applied voltage of $V_{app} = 300$ kV and the field ionization mechanism of (4.1). The oil is comprised of high number density, high ionization potential naphthenic/paraffinic hydrocarbon molecules only with parameter values summarized in Table 4.2. 102

4.13 Electric field magnitude [V/m] spatial distribution (as a function of r and z in the electrode geometry) at $t = 100$ ns given by the solution to the streamer model of (4.4)-(4.8) for an applied voltage of $V_{app} = 300$ kV and the field ionization mechanism of (4.1). The oil is comprised of high number density, high ionization potential naphthenic/paraffinic hydrocarbon molecules only with parameter values summarized in Table 4.2. 105

4.14 Frequency (solid curves) and growth rates (dashed curves) normalized to $\omega_j = (\gamma\rho R^3)^{1/2}$ for circular jet with uniform charge density as a function of normalized wavenumber kR. Curves accentuate space charge effects by setting $\epsilon = \epsilon_0$. (a) $m = 0$; (b) $m = 1$; (c) $m = 2$; (d) $m = 3$ (Figure 6, [17]). . . 106

4.15 Temporal dynamics along the needle-sphere electrode axis at 25 ns intervals from $t = 25 - 100$ ns given by the solution to the streamer model of (4.15)-(4.19) for an applied voltage of $V_{app} = 300$ kV and the field ionization mechanisms of (4.20) and (4.21). The oil is composed of two molecular species from Case 1 with parameter values summarized in Table 4.3. Note, at time $t = 0^+$ the electric field represents the Laplacian electric field and the oil temperature is 300 K. 112

4.16 Electric field magnitude [V/m] spatial distributions (as a function of r and z in the electrode geometry) from $t = 25 - 100$ ns given by the solution to the streamer model of (4.15)-(4.19) for an applied voltage of $V_{app} = 300$ kV and the field ionization mechanisms of (4.20) and (4.21). The oil is composed of two molecular species from Case 1 with parameter values summarized in Table 4.3. 113

4.17 Temporal dynamics along the needle-sphere electrode axis at 25 ns intervals from $t = 25 - 100$ ns given by the solution to the streamer model of (4.15)-(4.19) for an applied voltage of $V_{app} = 300$ kV and the field ionization mechanisms of (4.20) and (4.21). The oil is composed of two molecular species from Case 2 with parameter values summarized in Table 4.4. Note, at time $t = 0^+$ the electric field represents the Laplacian electric field and the oil temperature is 300 K. 115

4.18 Electric field magnitude [V/m] spatial distributions (as a function of r and z in the electrode geometry) from $t = 25 - 100$ ns given by the solution to the streamer model of (4.15)-(4.19) for an applied voltage of $V_{app} = 300$ kV and the field ionization mechanisms of (4.20) and (4.21). The oil is composed of two molecular species from Case 2 with parameter values summarized in Table 4.4. 116

4.19 Electric field dynamics along the needle-sphere electrode axis at 10ns intervals from $t = 10 - 50$ ns given by the solution to the streamer model of (4.4)-(4.8) for an applied voltage of $V_{app} = 350$ kV and the field ionization mechanism with parameter values summarized in Table 4.5. Note, at time $t = 0^+$ the electric field represents the Laplacian electric field. 122

4.20 Electric field magnitude [V/m] spatial distributions (as a function of r and z in the electrode geometry) from $t = 10 - 50$ ns given by the solution to the streamer model of (4.4)-(4.8) for an applied voltage of $V_{app} = 350$ kV and the field ionization mechanism with parameter values summarized in Table 4.5. 123

4.21 Temporal dynamics along the needle-sphere electrode axis at 0.2 ns intervals from $t = 0 - 1$ ns given by the solution to the streamer model of (4.25)-(4.28) for an applied voltage of $V_{app} = 350$ kV and the impact and photo-ionization mechanisms with parameter values summarized in Table 4.6. Note, at time $t = 0^+$ the electric field represents the Laplacian electric field. 127

4.22 Electric field magnitude [V/m] spatial distributions (as a function of r and z in the electrode geometry) from $t = 1 - 5$ ns given by the solution to the streamer model of (4.25)-(4.28) for an applied voltage of $V_{app} = 350$kV and the impact and photo-ionization mechanisms with parameter values summarized in Table 4.6. 128

5.1 Electric field lines for various times after a uniform z-directed electric field is turned on at $t = 0$ around a perfectly conducting spherical nanoparticle of radius R surrounded by transformer oil with permittivity ϵ_1, conductivity σ_1, and free electrons with uniform charge density ρ_e and mobility μ_e. The thick electric field lines terminate on the particle at $r = R$ and $\theta = \theta_c$ where $E_r(r = R) = 0$ and separate field lines that terminate on the nanoparticle from field lines that go around the particle. The cylindrical radius $R_a(t)$ of Eq. (5.27) of the separation field line at $z \to +\infty$ defines the charging current $I(t)$ in Eq. (5.29). The cylindrical radius $R_b(t)$ of Eq. (5.28) defines the separation field line at $z \to -\infty$. The dominant charge carrier in charging the nanoparticles are electrons because of their much higher mobilities than positive and negative ions. The conductivity of transformer oil, $\sigma_1 \approx 1 \times 10^{-12}$ S/m, is much less than the effective conductivity of the electrons, $\sigma_e \approx -\rho_e \mu_e \approx 1 \times 10^{-1}$ S/m. The electrons charge each nanoparticle to saturation, $Q_s = -12\pi\epsilon_1 E_0 R^2$ as given in Eq. (5.8) with time constant $\tau_{pc} = 4\epsilon_1/(|\rho_e|\mu_e)$ given in Eq. (5.12). The electric field lines in this figure were plotted using Mathematica StreamPlot [18]. 137

5.2 Charging dynamics, $|Q(t)|$, of a perfectly conducting nanoparticle versus time in transformer oil as given by (5.13) with $Q_s = -1.836 \times 10^{-18}$ C (approximately equals 11 electrons) and $\tau_{pc} = 7.79 \times 10^{-10}$ s. 140

5.3 Screen-shot of the the closed form solution for $Q(t)$ in Eq. (5.20) generated by *Mathematica* when numerical values are given to each variable (*e.g.*, $\epsilon_1 = 2.2\epsilon_0$, $\sigma_1 = 10^{-12}$ S/m, $\rho_e = -10^3$ C/m^3, $\mu_e = 10^{-4}$ m^{2}V^{-1}s^{-1}, $\epsilon_2 = \epsilon_0$, $\sigma_2 = 0.01$ S/m, $\tau_r = 4.78 \times 10^{-9}$ s, $\Upsilon_c = -0.222$, $\Sigma_c = 1$, $\tau_{pc} = 7.79 \times 10^{-10}$ s). 146

5.4 Charging dynamics, $|Q(t)|$, of a nanoparticle with constant conductivity σ_2 and varying permittivity $\epsilon_2 = 1\epsilon_0$ (○), $10\epsilon_0$ (▽), and $100\epsilon_0$ (×) in transformer oil ($\sigma_1 = 1 \times 10^{-12}$ S/m, $\epsilon_1 = 2.2\epsilon_0$). The other charging parameter values used, such as E_0, ρ_e, μ_e, R, ϵ_1, and σ_1, are the same as given in Section 5.2.1 (*i.e.*, $E_0 = 1 \times 10^8$ V/m, $\rho_e = -1000$ C/m^3, $\mu_e = 1 \times 10^{-4}$ m^{2}V^{-1}s^{-1}, $R = 5 \times 10^{-9}$ m, $\epsilon_1 = 2.2\epsilon_0$, and $\sigma_1 = 1 \times 10^{-12}$ S/m). 147

5.5 Initial 70 ns of the charging dynamics, $|Q(t)|$, for particles with conductivity $\sigma_2 = 0.01$ S/m and varying permittivity ϵ_2. 148

5.6 Unipolar charging of a perfectly conducting sphere versus time for (a) positive mobile charge ($\rho_- \mu_- = 0$ for various values τ_s/τ_+) and for (b) negative mobile charge ($\rho_+ \mu_+ = 0$ for various values of τ_s/τ_-). Note that the (a) positive charge plot has $Q(t) > 0$ for all time with time constant $\tau = \tau_+ = 4\epsilon/(\rho_+ \mu_+)$ while the (b) negative charge half plot has $Q(t) < 0$ for all time with time constant $\tau = \tau_- = -4\epsilon/(\rho_- \mu_-) = 4\epsilon/(|\rho_-|\mu_-)$. 156

5.7 Perfectly conducting sphere in a perfectly insulating dielectric ($\tau_s \to \infty$) for bipolar charging versus time for various values of (a) $\rho_+\mu_+ > -\rho_-\mu_-$ for positive charging and (b) $-\rho_-\mu_- > \rho_+\mu_+$ for negative charging. Note that (a) the upper positive charge plot has $\rho_+\mu_+ > -\rho_-\mu_-$ so that $Q(t) > 0$ for all time with time constant $\tau = \tau_+ = 4\epsilon/(\rho_+\mu_+)$ while (b) the negative charge plot has $-\rho_-\mu_- > \rho_+\mu_+$ so that $Q(t) < 0$ for all time with time constant $\tau = \tau_- = -4\epsilon/(\rho_-\mu_-) = 4\epsilon/(|\rho_-|\mu_-)$. 157

5.8 Electric field distribution along the needle-sphere z-axis at $t = 1$ μs given by the solutions to the streamer model of Eqs. (5.70)-(5.75) for the three nanofluid (NF) case studies with different nanoparticle attachment time constants τ_{np} and the pure transformer oil. 162

5.9 Charge density distributions along the needle-sphere z-axis at time $t = 0.1$ μs given by the solution to the streamer model for transformer oil and transformer oil-based nanofluid with $\rho_{np,sat} = -500$ C/m^3 and varying τ_{np}. 163

5.10 Electric potential distribution along the needle-sphere z-axis at $t = 1$ μs given by the solution of the nanofluid field ionization case studies and the equivalent solution in pure oil. The needle tip is at $z = 0$ and the streamer tail is to the left of the knee, where the slope changes dramatically, in each electric potential plot. The location of the streamer tip is at the knee in each electric potential plot. 165

6.1 Two series dielectric parallel plane geometry to represent a simplified liquid-solid insulation system. 174

6.2 Two series dielectric parallel plane model where Regions 1 and 2 are defined by unique permittivities (ϵ_1, ϵ_2) and carrier mobilities (μ_1, μ_2). 176

6.3 Analytical and numerical results for migration-migration model of two series dielectric parallel plane system (Fig. 6.2) where the surface charge density at the interface is set to $\rho_s = 0$. 180

6.4 Analytical and numerical results for migration-migration model of two series dielectric parallel plane system (Fig. 6.2) where the surface charge density at the interface is set to $\rho_s = 2$ C/m^2. 181

6.5 Analytical and numerical results for migration-migration model of two series dielectric parallel plane system (Fig. 6.2) where the surface charge density at the interface is set to $\rho_s = 3.52$ C/m^2. 182

6.6 Two series dielectric parallel plane model where Region 1 is defined by a permittivity ϵ_1 and carrier mobility μ_1 and Region 2 is defined by a different permittivity ϵ_2 and conductivity σ_2. 183

6.7 Analytical and numerical results for migration-migration model of two series dielectric parallel plane system (Fig. 6.6). 186

6.8 Two series dielectric parallel plane model where Region 1 is defined by a permittivity ϵ_1 and charge carrier mobility μ_1 and Region 2 is defined by a different permittivity ϵ_2 and ohmic conductivity σ_2. 187

6.9 Characteristic trajectories in the x-t space under space charge limited conditions for the charging transient to a step current. 189

6.10 Analytical and numerical results for step current excited migration-ohmic model of two series dielectric parallel plane geometry (Fig. 6.8). 192

7.1 2D-axisymmetrical oil-solid tube system, where the main z-directed electric field component is parallel to the inner tube surface, within the needle-sphere electrode geometry outlined in Section 3.2. 203

7.2 2D-axisymmetrical oil-solid barrier system, where the main z-directed electric field component is perpendicular to the interface, within the needle-sphere electrode geometry outlined in Section 3.2. 204

7.3 Portion of the inner oil-tube interface along which the electric field magnitude and surface charge density line distributions are measured from the top of the line to the bottom (*e.g.*, see Fig. 7.4). 205

7.4 Temporal dynamics along the liquid-solid interface shown in Fig 7.3 at 25 ns intervals from $t = 25 - 100$ ns given by the solution to the oil-solid insulation model of (7.1)-(7.9) for the field ionization mechanism of (7.5) and varying applied voltage (*e.g.*, 130 kV, 200 kV, and 300 kV). The oil is comprised of low number density, low ionization potential aromatic hydrocarbon molecules only with parameter values summarized in Table 4.1. The solid insulator's permittivity is $2.2\epsilon_0$ 211

7.5 Electric field magnitude [V/m] spatial distributions (as a function of r and z in the electrode geometry) from $t = 5 - 100$ ns given by the solution to the oil-solid insulation model (7.1)-(7.9) for an applied voltage of $V_{app} = 130$ kV and the field ionization mechanism of (7.5). The oil is composed of low number density, low ionization potential aromatic hydrocarbon molecules only with parameter values summarized in Table 4.1. The solid insulator's permittivity is $2.2\epsilon_0$ 212

7.6 Electric field magnitude [V/m] spatial distributions (as a function of r and z in the electrode geometry) from $t = 5 - 100$ ns given by the solution to the oil-solid insulation model (7.1)-(7.9) for an applied voltage of $V_{app} = 200$ kV and the field ionization mechanism of (7.5). The oil is composed of low number density, low ionization potential aromatic hydrocarbon molecules only with parameter values summarized in Table 4.1. The solid insulator's permittivity is $2.2\epsilon_0$ 213

7.7 Electric field magnitude [V/m] spatial distributions (as a function of r and z in the electrode geometry) from $t = 5 - 100$ ns given by the solution to the oil-solid insulation model (7.1)-(7.9) for an applied voltage of $V_{app} = 300$ kV and the field ionization mechanism of (7.5). The oil is composed of low number density, low ionization potential aromatic hydrocarbon molecules only with parameter values summarized in Table 4.1. The solid insulator's permittivity is $2.2\epsilon_0$ 214

7.8 Portion of the oil-solid barrier interface along which the electric field magnitude and surface charge density line distributions are measured from the z-axis radially outwards (*e.g.*, see Fig. 7.9). 216

7.9 Temporal dynamics along the liquid-solid interface in Fig 7.8 at several time instances after the streamer makes contact with the perpendicular surface. Results given by the solution to the oil-solid insulation model of (7.1)-(7.9) for an applied voltage of $V_{app} = 130$ kV and the field ionization mechanism of (7.5). The oil is composed of low number density, low ionization potential aromatic hydrocarbon molecules only with parameter values summarized in Table 4.1. The solid insulator's permittivity is $4.4\epsilon_0$. 218

7.10 Electric field magnitude [V/m] spatial distributions (as a function of r and z in the electrode geometry) at several time instances before (a)-(b) and after (c)-(f) the streamer makes contact with the perpendicular surface. Results given by the solution to the oil-solid insulation model of (7.1)-(7.9) for an applied voltage of $V_{app} = 130$ kV and the field ionization mechanism of (7.5). The oil is composed of low number density, low ionization potential aromatic hydrocarbon molecules only with parameter values summarized in Table 4.1. The solid insulator's permittivity is $4.4\epsilon_0$ 220

7.11 (a) The net charge enclosed within a differential-sized volume of dipoles has contributions only from dipoles that are cut by the surfaces. All totally enclosed dipoles contribute no net charge. (b) Only those dipoles within a distance $\vec{d} \cdot \vec{n}$ of the surface are cut by the volume. (Figure 3-4, [19]) 223

7.12 Two dielectric parallel plane geometry to represent a simplified liquid-solid insulation system. 224

7.13 Temporal dynamics along the liquid-solid interface in Fig 7.3 at 25ns intervals from $t = 25 - 100$ ns given by the solution to the oil-solid insulation model of (7.1)-(7.9) for the field ionization mechanism of (7.5) and an applied voltage of $V_{app} = 130$ kV. The oil is comprised of low number density, low ionization potential aromatic hydrocarbon molecules only with parameter values summarized in Table 4.1. Three case studies are examined where the solid insulator's permittivity is $4.4\epsilon_0$, $3.3\epsilon_0$ and $1.0\epsilon_0$. 231

7.14 Electric field magnitude [V/m] spatial distributions (as a function of r and z in the electrode geometry) from $t = 5 - 100$ ns given by the solution to the oil-solid insulation model (7.1)-(7.9) for an applied voltage of $V_{app} = 130$ kV and the field ionization mechanism of (7.5). The oil is composed of low number density, low ionization potential aromatic hydrocarbon molecules only with parameter values summarized in Table 4.1. The solid insulator's permittivity is $4.4\epsilon_0$ 232

7.15 Electric field magnitude [V/m] spatial distributions (as a function of r and z in the electrode geometry) from $t = 5 - 100$ ns given by the solution to the oil-solid insulation model (7.1)-(7.9) for an applied voltage of $V_{app} = 130$ kV and the field ionization mechanism of (7.5). The oil is composed of low number density, low ionization potential aromatic hydrocarbon molecules only with parameter values summarized in Table 4.1. The solid insulator's permittivity is $3.3\epsilon_0$ 233

7.16 Electric field magnitude [V/m] spatial distributions (as a function of r and z in the electrode geometry) from $t = 5 - 100$ ns given by the solution to the oil-solid insulation model (7.1)-(7.9) for an applied voltage of $V_{app} = 130$ kV and the field ionization mechanism of (7.5). The oil is composed of low number density, low ionization potential aromatic hydrocarbon molecules only with parameter values summarized in Table 4.1. The solid insulator's permittivity is $1.0\epsilon_0$ 234

7.17 Temporal dynamics along the liquid-solid interface in Fig 7.8 at several time instances after the streamer makes contact with the perpendicular surface. Results given by the solution to the oil-solid insulation model of (7.1)-(7.9) for an applied voltage of $V_{app} = 130$ kV and the field ionization mechanism of (7.5). The oil is composed of low number density, low ionization potential aromatic hydrocarbon molecules only with parameter values summarized in Table 4.1. The solid insulator's permittivity is $3.3\epsilon_0$, $2.2\epsilon_0$ and $1.0\epsilon_0$. 240

7.18 Electric field magnitude [V/m] spatial distributions (as a function of r and z in the electrode geometry) at several time instances before (a)-(b) and after (c)-(f) the streamer makes contact with the perpendicular surface. Results given by the solution to the oil-solid insulation model of (7.1)-(7.9) for an applied voltage of $V_{app} = 130$ kV and the field ionization mechanism of (7.5). The oil is composed of low number density, low ionization potential aromatic hydrocarbon molecules only with parameter values summarized in Table 4.1. The solid insulator's permittivity is $3.3\epsilon_0$ 241

7.19 Electric field magnitude [V/m] spatial distributions (as a function of r and z in the electrode geometry) at several time instances before (a)-(b) and after (c)-(f) the streamer makes contact with the perpendicular surface. Results given by the solution to the oil-solid insulation model of (7.1)-(7.9) for an applied voltage of $V_{app} = 130\,\text{kV}$ and the field ionization mechanism of (7.5). The oil is composed of low number density, low ionization potential aromatic hydrocarbon molecules only with parameter values summarized in Table 4.1. The solid insulator's permittivity is $\underline{2.2\epsilon_0}$ 242

7.20 Electric field magnitude [V/m] spatial distributions (as a function of r and z in the electrode geometry) at several time instances before (a)-(b) and after (c)-(f) the streamer makes contact with the perpendicular surface. Results given by the solution to the oil-solid insulation model of (7.1)-(7.9) for an applied voltage of $V_{app} = 130\,\text{kV}$ and the field ionization mechanism of (7.5). The oil is composed of low number density, low ionization potential aromatic hydrocarbon molecules only with parameter values summarized in Table 4.1. The solid insulator's permittivity is $\underline{1.0\epsilon_0}$ 243

A.1 Formulation of the integrands for stored energy density W of (A.11) and power dissipation P_d density of (A.12) in COMSOL Multiphysics 2D-axisymmetrical mode within the subdomain integration coupling variables. 261

A.2 Simple co-axial cylindrical parallel plane geometry test case with positive space charge injection at top electrode using a linear space charge injection law $\rho = A|\vec{E}|$ [20]. The carrier mobility is $\mu = 1\ \text{m}^2\text{V}^{-1}\text{s}^{-1}$ and dielectric permittivity is $\epsilon = 1\ \text{F/m}$. Other values are $V(t) = V_0 u(t)$ with $V_0 = 1\ \text{V}$, $d = 1\ \text{m}$ and $a = 20\ \text{mm}$. The closed boundary areas 1 and 2 are used to calculate the current using the boundary area integration of the total current density, as discussed in Section A.2. 262

A.3 Terminal current derived from generalized power method via Poynting's theorem. Results are shown for the two cases when the $2\pi r$ contribution in the integrands of Fig.A.2 are included, as in (A.16), and not included. 262

A.4 Formulation of the integrands for the determination of the displacement current i_{disp} of (A.25) and conduction current i_{cond} of (A.26) in COMSOL Multiphysics 2D-axisymmetrical mode within the boundary integration coupling variables. 264

A.5 Terminal current derived from the integration of current density across two different closed boundaries and the generalized power method via Poynting's theorem (same as the correct formulation (A.16) plotted in black in Fig. A.3). All three currents are nearly identical showing that the total current density integration method gives correct results and that it may be more powerful to use in multi-port systems and systems with awkward geometries. 266

B.1 Pictorial example of how COMSOL Multiphysics enforces a zero diffusive boundary condition at the oil-pressboard interface by creating and subsequently injecting numerical "ghost" numerical electrons from the pressboard into the transformer oil. These ghost charge carriers give incorrect results. By applying the new conditional interface boundary conditions of (B.2)-(B.5), this error in COMSOL Multiphysics is resolved. 269

List of Tables

2.1 Characterization of Positive Streamer Propagation Modes [14, 21, 22] 42

2.2 ABB experimental data of breakdown and acceleration voltages for needle-sphere geometry from Fig. 2.1 42

2.3 Results of impulse voltage withstand testing in 25.4 mm electrode gap system [23] 53

3.1 Parameter Values for the Streamer Model in Transformer Oil 65

4.1 Parameter Values for Low Number Density, Low Ionization Potential Aromatic Molecules 84

4.2 Parameter Values for High Number Density, High Ionization Potential Naphthenic/Paraffinic Molecules 84

4.3 Two Molecular Species Liquid: Case 1 Field Ionization Parameter Values . 110

4.4 Two Molecular Species Liquid: Case 2 Field Ionization Parameter Values . 110

4.5 Field Ionization Parameter Values for 4^{th} Mode Streamer Investigation . . . 121

4.6 Parameter Values for Impact Ionization and Background Ionization 125

5.1 Electrical and thermal properties of representative insulating and conducting nanoparticle materials 136

6.1 Parameter Values for Simplified Two Series Dielectric Parallel Plane Model 175

6.2 Mobility Values for the Simplified Migration-Migration Model 178

6.3 Mobility and Conductivity Values for the Simplified Migration-Ohmic Model 185

Chapter 1

Introduction

ELECTRICAL insulation is a vital component of all electrical systems, whether it be the electrical system of a computer, automobile, or the electric power grid. In the world of VLSI design, taking the MOSFET for example, the electrical insulation of the gate from the semiconductor channel via an oxide layer is critical for proper operation. Without this insulation, ones and zeros in the digital world cannot be processed correctly and common household electronics like the personal computer would not exist today.

An electrical system without insulation is as useful as an automobile without tires. It has all the potential to perform a useful service, however, it is missing a critical component. Therefore, any electrical system must have adequate electrical insulation to perform under normal operating conditions, and also provide insulation at the extremes when the system is over-stressed.

The consideration of electrical insulation is often secondary, or an after thought. For instance, when most people think of the electric power grid, their thoughts focus on the conductors within power lines, generators, and transformers. However, the electrical insulation systems that are so vital to the proper and fault-free operation of these components are often forgotten. This is puzzling as it is often the electrical insulation that is the first component to fail. Furthermore, power systems ratings are limited by the insulation strength of power lines, transformer and generator insulation. In fact, insulation strength is the determining factor for machine and component sizing such that it is the insulation that is the bottleneck for transferring energy more efficiently (*i.e.*, at higher voltages and lower currents).

With our growing need for more energy to power our homes, schools, and businesses, the growing stress on the deteriorated and aged electric power network in the United States is reaching a critical point. Additionally, with the growing energy and environmental concerns, there is a strong push to add vast amounts of renewable energy and to become more energy efficient. Trying to add capacity and renewable energy sources to the current electric power network is pushing the limits of existing power generation, transmission and distribution technologies and the materials that insulate them. New high voltage equipment will need better electrical insulation if they are to be more reliable and efficient. Therefore, un-

derstanding the mechanisms that lead to electrical breakdown in solid, gaseous, and liquid insulators such as cross-linked polyethylene (XLPE), SF_6, and transformer oil is critical in engineering better components and to have a more reliable and efficient electric power grid.

1.1 Liquid Insulation and Pre-breakdown Phenomena

Dielectric liquids, in which transformer oil is categorized, is defined as a liquid in which self dissociation is extremely small and its resistivity is greater than $1 \times 10^9\ \Omega\,\mathrm{cm}$ [24]. The widespread use of dielectric liquids for high voltage insulation and power apparatus cooling is due to their greater electrical breakdown strength and thermal conductivity than gaseous insulators, while their ability to conform to complex geometries and self-heal means that they are often of more practical use than solid insulators [24]. Unfortunately, as with all insulation, the failure of the liquid insulation can cause catastrophic damage to not only the power equipment, but also the surrounding environment. In some cases, the insulation failure can lead to injury and death. Furthermore, failure often leads to major operational disruption, financial loss, and possible environmental legal action for the failed equipment's owner [25]. Furthermore, liquid insulated high voltage equipment, such as power transformers, play a major role in electrical transmission and distribution systems and have extremely high costs associated. Therefore, electric utilities and power systems operators continually monitor the state of such high voltage equipment to ensure safe operation.

Due to the disastrous consequences of insulation failure, researchers have studied the insulating properties of dielectric liquids in an attempt to understand the underlying mechanisms that lead to electrical breakdown in order to prevent them [1, 25]. Electrical breakdown in a dielectric liquid occurs when the liquid is bridged from the high voltage electrode to a grounded electrode by highly conductive and luminous channels called arcs. At this point, excessive currents will propagate through the arcs, which would otherwise be insulating in normal operation, causing severe damage to the insulation and the high voltage equipment. Therefore, avoiding arc formation is of the utmost importance to ensure safe, reliable operation.

Arc formation is the last step in a series of events, albeit very short time events on the nanosecond to microsecond timescale, before breakdown. Pre-breakdown phenomena called streamers precede arc formation and play a critical role in leading to breakdown. Streamers are low density conductive structures that form in regions of oil that are over-stressed by electric fields on the order of $1{\times}10^8\,\mathrm{V/m}$ or greater [26]. The high field levels ionize molecules to create free charge, such as ions and electrons, in the dielectric liquid [25]. The movement

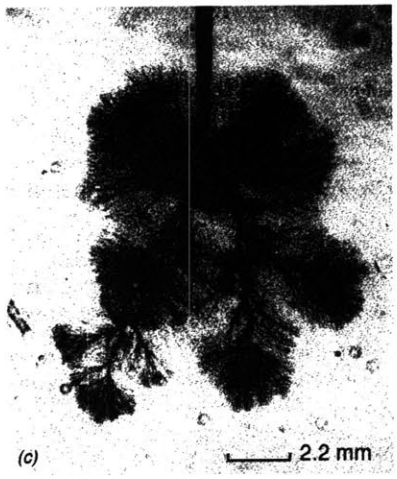

Figure 1.1: Propagation of fast positive streamer in transformer oil in a point-plane electrode geometry under 0.5μs rise time and 85μs fall time impulse voltage. Gap length 27.5mm. Tip radius 30 μm; Crest voltage 178 kV. Schlieren photograph (frame exposure time 8 ns) [1, 2]

of these free charges in the presence of the high field results in a phase change of the liquid due to significant Joule heating. Figure 1.1 shows a positive streamer in transformer oil. Note that the streamer forms at the needle electrode near the top and propagates toward the grounded electrode at the bottom (not shown). Furthermore, the phase change in the streamer body/tail is evident by the differing refractive index compared to the surrounding transformer oil.

Once a streamer initiates in the high field region it tends to elongate, growing from the point of initiation towards a grounding point. Streamers are often characterized by shapes that are qualitatively referred to as bushy, branched, tree-like and filamentary. Figure 1.1 is exemplary of a tree-like, bushy streamer. The extent of a streamer's development depends upon many factors including both the nature of the dielectric liquid (*i.e.*, chemical composition) and the applied electrical excitation (*i.e.*, magnitude, duration, rise time, polarity, etc.). Sustained over-excitation can result in a streamer short circuiting the oil gap between electrodes. When this happens an arc will form and electrical breakdown will occur [25].

Over the past half century, there has been significant scientific investigation devoted to characterizing and understanding streamers, which has led to the formation of a large body of literature on the subject [1, 2, 11–14, 21, 22, 26–39]. Much of the work has been empirical in nature and there has been little effort devoted to uncovering the underlying mechanisms in a theoretical and systematic method such as numerical modeling. This is in part due to the computational limits of those who studied streamers in the past. But it is also due to the variability in the experimental data and the difficulty of characterizing many dielectric liquids, especially at high field levels like those in electrical breakdown studies. Unlike the

gaseous and solid states, the molecular structure and behavior of liquids is more complex and even in the purest liquids there exists trace amounts of impurities that make it difficult to isolate the mechanisms behind electrical breakdown [11,30]. As a result of the complexity of the liquid state and the varying experimental tests, there does not exist a universally accepted breakdown theory.

1.2 Lumped Circuit Analogy of Streamers and Electrical Insulation

In general, nature seeks balance, order, predictability and non-extreme environment/states. Simple yet powerful examples of this are homeostasis, weather/rain cycle, and food chain. When things such as illnesses, natural disasters, and viruses disrupt this normal balance the environment is put into shock, which can lead to damaging and unpredictable behavior. The same holds true for insulating materials, where under normal conditions these materials electrically insulate (block the flow of conduction current through them) within a normal rated range of operating voltages. Furthermore, under normal operation dielectric liquids are used to thermally conduct excess heat away from the source, which is often the high voltage conductors, and to electrically insulate the many conductors from each other and the external environment. Therefore, under normal operation the dielectric liquid is to be a good thermal conductor and electrical insulator.

The presence of streamers in dielectric liquids is a non-normal state, often occurring when voltages and field levels exceed that for which the insulation has been rated for, and are out of the range for the normal operation of the electrical equipment. As stated earlier, if the conductive steamers are allowed to persist and propagate, due to the application of high fields for an extended period of time, they will bridge the insulation from the high voltage electrode to the ground electrode. Once this occurs the streamer will create a short circuit between the two electrodes and cause electrical breakdown of the dielectric liquid.

To facilitate the understanding of dielectric liquids, streamers, and operating ranges we examine a lumped circuit analogy [40]. For a detailed background on lumped circuit modeling and components please refer to [40]. From an electrical insulation standpoint, all materials fall between the spectrum of insulator and conductor. Since there are no perfect insulators and no perfect conductors (neglecting superconductors) all materials can be modeled as a lossy insulator or a poor conductor. The amount of lossy-ness is dependent on whether the material exhibits dominant properties of an insulator or conductor.

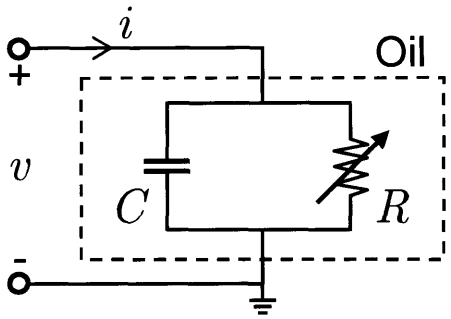

Figure 1.2: Lumped circuit model of transformer oil.

For dielectric liquids, such as transformer oil, that insulates high voltage transformers and other high voltage equipment, there are two generalized regimes of operation, called normal and over-voltage for simplicity. The dielectric liquid changes from a slightly lossy insulator in the normal regime to a poor conductor in the over-voltage regime. The normal operating regime is where the voltages applied to the liquid are below the rated specifications. The over-voltage operating regime is where the applied voltage exceeds the rated values for the liquid and pre-breakdown phenomena, such as streamers, develop.

To gain a conceptual understanding of the key differences of the two regimes the dielectric liquid is modeled as a parallel potentiometer-capacitor combination as shown in Fig. 1.2. In its normal operation, the liquid modeled lumped circuit acts almost entirely as a capacitor, where the resistance R of the potentiometer is very large such that the resistor looks like an open circuit, and the majority of the current i that passes through the element model is in the form of displacement current. Moreover, the resistance of the potentiometer does not change considerably with increased applied voltage in the normal regime and within rated specifications, such that the $v-i$ relationship of the circuit element can be considered linear. Therefore, the Joule heating is minimal as the conduction current is negligible and their is minimal current through the potentiometer.

As the voltage is increased and passes normal limits of operation into over-voltage the resistance of the potentiometer sharply decreases and more conduction current is drawn through the lumped element. The decrease in resistance is effectively due to the formation of conductive streamers in the dielectric liquid. Streamers are a result of the generation of free charge carriers in the dielectric liquid that contribute to the conductivity σ and conduction current density $\vec{J_c}$ by

$$\sigma = \rho_+\mu_+ - \rho_-\mu_-, \tag{1.1}$$

$$\vec{J_c} = \sigma\vec{E} = (\rho_+\mu_+ - \rho_-\mu_-)\vec{E}, \tag{1.2}$$

where ρ_+ and ρ_- are generalized positive and negative charge carriers, respectively, and μ_+ and μ_- are their respective mobilities. The movement of free charge carriers in the presence of an electric field leads to significant Joule heating and losses, which is equivalent to the power $P = i^2R$ dissipated in the resistor shown in Fig. 1.2.

In the over-voltage operation regime, the resistance of the potentiometer is a strongly inverse proportional to the applied voltage magnitude and duration, such that the resistance quickly decreases with increased voltage magnitude and duration. If the over-voltage excitation and duration is significant and prolonged the resistance of the potentiometer will tend to zero, which will result in short-circuiting of the element. This will cause significant levels of conduction current to flow leading to breakdown of the oil element.

The resistance of the potentiometer decreases due to the development and propagation of streamers. In lumped circuit terms, this thesis investigates why the resistance of the potentiometer varies in over-voltage (*i.e.*, what makes it vary?) and how to create a better resistor such that it does not vary.

1.3 Modeling of Streamers in Dielectric Liquids

Published research on the subject of electrical pre-breakdown and breakdown processes in dielectric liquids, such as transformer oil, has had a strong empirical focus. With the advancement of measurement technologies over the past several decades the quantity and quality of these results has increased significantly. The material in the literature generally reports on the qualitative physical characteristics of streamers (*i.e.*, shape, velocity, light emission, etc.) under various experimental conditions, along with detailing their voltage and current dynamics. For example, researchers have experimentally observed that streamers have different propagation characteristics that are strongly dependent on the voltage excitation (*i.e.*, magnitude, polarity, wave shape, duration, rise time, fall time, etc.) to the liquid [1, 2, 14, 21, 22, 26, 29].

The liquid dielectric medium of interest in this study is transformer oil, however the models introduced in this work can be generalized to other dielectric liquids. The analysis focuses on positive streamers that lead to breakdown, which are excited by a stepped voltage. In the case of transformer oil, experimental evidence has shown that positive streamers tend to initiate at lower applied voltage magnitude and propagate faster and further than their negative counterparts [1, 29]. As a result, positive streamers constitute a greater risk to oil insulated high voltage electrical equipment than do negative streamers.

The plethora of experimental data on streamers provides very useful insight into pre-breakdown processes in transformer oil and allows researchers to develop better models to fully understand streamers and the mechanisms that drive them. Surprisingly though, there is a lack of modeling work on the topic. While there have been many hypotheses on the mechanisms and conditions that play an important role in streamer development, where references [11,14,21,41,42] are a select few, little work has been undertaken to prove or disprove them. Now with advanced numerical methods, multiphysics solvers, and more computing power the modeling of this phenomena is possible.

There have been research groups who have attempted to model streamer development [43–50], however much of their focus has been modeling the physical characteristics of streamers (*i.e.*, shape, fractal geometry, stochastic branching) with little emphasis on the underlying physics driving streamer development [48]. To the author's best knowledge O'Sullivan *et al.* were the first to examine pre-breakdown phenomena and streamers in transformer oil from a deterministic and mechanics perspective [25,51–53]. They focused on the electrodynamic mechanisms that drove slowly propagating streamers in transformer oil by using a hydrodynamic continuum model for three charge carriers (*i.e.*, positive ions, negative ions, and electrons) that are coupled through Gauss' Law. The results showed that streamer development from a positive electrode is strongly dependent on electric field molecular ionization of the oil molecules [25, 53]. The work also investigated other charge generation mechanisms like Fowler-Nordheim electron injection from a negative electrode and electric field dependent ionic dissociation [25,51]. The aim of this thesis is to develop a set of mathematical models and parameter values which contain the physics to elucidate pre-breakdown phenomena in transformer oil and other oil-based systems.

The successful modeling of streamer dynamics is a very complex task because of its multi-disciplinary nature involving electrodynamics, fluid mechanics and thermodynamics. The modeling work that is being carried out as a part of this thesis has a strong focus on the electrodynamic mechanisms for positive streamers that occur in transformer oil during periods of high electrical stress near a positive electrode since these mechanisms drive positive streamer growth. By having this focus on electrodynamics it is possible to develop a model that accurately predicts the electric field levels, free charge densities and the wide range of propagation velocities associated with positive streamers in transformer oil. The finite element package COMSOL Multiphysics [54] is used extensively for solving the models. The accuracy and validity of the models are assessed by comparing numerical results to the experimental results regarding streamers from the literature.

The results will provide insight into pre-breakdown and breakdown processes in transformer oil and hopefully lead to the engineering of next generation dielectric liquids with improved electrical insulation characteristics. Furthermore, by having a clearer understanding of

the mechanisms that cause liquid dielectrics to fail, engineers will have the know-how to develop more reliable electrical systems and the ability to engineer improvements to existing insulating liquids like transformer oil.

1.4 Thesis Organization

A main objective of this research is to gain a thorough understanding of pre-breakdown phenomena in transformer oil and oil-based systems. There are three different systems in which streamers and charging phenomena are investigated and as such the thesis is partitioned along these different systems. The oil systems and their respective chapters are:

1. Transformer oil (Chapters 3 and 4)
2. Systems with spherical nanoparticles suspended within a dielectric liquid such as transformer oil(Chapter 5)
3. Liquid-solid systems such as transformer oil-pressboard systems (Chapters 6 and 7)

The failure of the insulation systems, such as those listed above, in high voltage equipment for power systems can have disastrous impact on numerous aspects of society including the environment, industry, financial markets, national safety, and human comfort. Therefore, the understanding of the mechanisms leading to electrical breakdown in insulation systems is of the utmost importance. This thesis investigates, through modeling and comparison to experimental data, the electrodynamic mechanisms responsible for the development of streamers that precede and lead to electrical breakdown.

The outcome of this work, that is a better understanding of the underlying physics of streamer formation in dielectric liquid-based systems, will impact the development of new high voltage equipment, such as power transformers, that have improved electrical insulation performance making them more safe, reliable, and efficient. Furthermore, from the systematic study of streamers, a deeper appreciation and comprehension of the connection between electric field and space charge will result. Empowered with this understanding, this thesis investigates new methods to engineer better insulation technology through techniques such as space charge shielding, charging dynamics of nanoparticles, and regulation of the streamer's electric field enhancement via geometrical symmetry and radial growth.

The thesis is organized in the following sections. Chapter 2 is an overview on the experimental data on streamer development and characterization in transformer oil-based insulation

systems and other dielectric liquids. Also, the important physical properties of transformer oil and hypotheses from the literature regarding the streamer formation in liquids and along liquid-solid interfaces will be discussed.

In Chapter 3, all components of the dielectric liquid model will be discussed including system geometry, governing equations, model parameters, and charge generation mechanisms. In Chapter 4, the model results for streamer development in transformer oil are given. A thorough discussion on the key mechanisms affecting streamer propagation in transformer oil will be revealed.

In Chapter 5, analysis of unipolar and bipolar charging of spherical nanoparticles in a dielectric liquid is investigated. This nanoparticle charging model is used within a comprehensive electrodynamic analysis to study the impact of nanoparticle charging on streamer development in transformer oil-based nanofluids.

Chapter 6 investigates modeling method of multi-dielectric insulation systems. It begins with the modeling and comparison of three different methods to model a solid insulator. Special attention is given to the correct interfacial boundary condition for each modeling method within a liquid-solid insulation system. Each case is analytically and numerically compared using a simplified two-series dielectric parallel-plane geometry. These models are utilized in Chapter 7 to create a complete electrodynamic oil-solid model to study the effects of insulator permittivity mismatch. Furthermore, the role of the oil-solid interface orientation on streamer development is investigated. A detailed discussion on the results and driving mechanisms is given.

A summary of the conclusions and key points of this work can be found in Chapter 8. The chapter concludes with suggested future work to extend the theoretical work found in this thesis, including several suggested experiments that would help deepen the understanding of breakdown in dielectric liquids and validate several of the conclusions from this body of work.

Chapter 2

Streamers in Dielectric Liquid-Based Insulation Systems

LIQUID insulation is a key component to the reliable transmission and distribution of electric power. From power transformers to cables to switch gear, liquid insulation ensures the safe operation of these equipment by effectively removing excess thermal energy and electrically insulating the conductors that transmit power. This chapter discusses several dielectric liquids that are used to insulate electrical equipment, with an emphasis on transformer oil, and their over-voltage or streamer characteristics. Special attention will also be given to the effects of additives, such as low ionization potential molecules and conductive nanoparticles, on the breakdown characteristics of transformer oil. Also, the effect of solid insulation on streamer formation in dielectric liquids is explored.

2.1 Mineral Oil

Since the early 1900s, oils have been used to electrically insulate a variety of electrical equipment including circuit breakers, cables and transformers. The majority of high voltage components, such as paper insulated oil impregnated cables and high voltage power transformers in use today rely on mineral oil, also called transformer oil, as a vital piece of their electrical insulation system [1, 55]. The widespread use of transformer oil for high voltage insulation and power apparatus cooling is due to their greater electrical breakdown strength and thermal conductivity than gas insulators, while their ability to conform to complex geometries and self-heal means that they are often of more practical use than solid insulators. As such, the electrical insulation strength and characteristics of transformer oil has become the de facto standard for high voltage liquid insulation. Key physical properties of transformer oil that make it an excellent electrical insulator and cooling medium are high density, high dielectric strength, high specific heat and thermal conductivity along with low viscosity and pour point to provide effective heat transfer. Other general characteristics of most commercially available transformer oils are: relative permittivity $\epsilon_r = 2.2$, resistivity of $1 \times 10^9\ \Omega\,\mathrm{cm}$ or greater, and a dissipative power factor of approximately 0.001 at 60 Hz. The physical and chemical properties of transformer oil are subject to specifications issued

by national standards boards and vary from region to region (*e.g.*, Standard C-50 by the Canadian Standards Association, ASTM D3487 in the United States, and IEC 2961982 internationally) [24].

Transformer oil, which is derived from petroleum, is comprised of a variety of complex hydrocarbons with specific composition and concentration variations dependent on manufacturer and petroleum source. In general, transformer oil is a mixture of many different paraffinic (alkanes), naphthenic (cycloalkanes), and aromatic molecules with complex molecular structures and a distribution of molecular sizes and weights. In particular, transformer oil can be comprised of straight and branched chain paraffins, cyclic saturated and unsaturated (aromatic) hydrocarbons, and combinations of cyclic with branched and linear chain hydrocarbons (naphthenes) [24]. The aromatic base is characterized by the chemical formula C_nH_n, the naphthenes by $C_{2n}H_{2n}$, and the paraffins by $C_{2n}H_{2n+2}$ [56].

The three types of hydrocarbon molecules greatly affect the chemical behavior of the complete oil. For example, aromatic molecules tend to be more chemically reactive than saturated hydrocarbons and as such they dominate the chemical behavior of the transformer oil. On the other hand, paraffinics and naphthenics generally constitute a larger amount of the oil such that the physical characteristics reflect these hydrocarbons. [24].

Traditionally, transformer oils have been refined from petroleum with a large portion of naphthenes and low in aromatics and paraffins. Aromatics are generally kept to low levels (*e.g.*, less than 5% for weakly aromatic [36]) to reduce their chemical reaction with other hydrocarbon molecules [24] and due to the low ionization potentials of many polyaromatics [11]. The low paraffin content allows for an oil with low pour point and satisfactory performance at low temperatures because paraffins tend to be more viscous. Also, due to the lower viscosity of naphthenic-based oils they allow for better oil impregnation of cellulose material, which is commonly used as a solid insulator in high voltage equipment along with transformer oil. Thorough oil impregnation of cellulose material is critical to eliminate voids and gas pockets that otherwise would compromise the electrical insulating strength of the oil-pressboard insulation system of transformers [24]. Therefore, most commerical transformer oils are comprised by a majority of naphthenic hydrocarbon molecules [24,36].

2.1.1 Positive Streamer Propagation Modes in Transformer Oil

The literature contains a plethora of empirical data regarding streamer development in transformer oil [2, 11, 13, 14, 21, 22, 31, 55, 57, 58]. Unfortunately, even with all this data there still does not exist a complete theory on the mechanisms behind electrical breakdown in dielectric liquids like transformer oil. However, much of the data in the literature gives

deep insight into potential mechanisms behind streamer formation and ultimately electrical breakdown in dielectric liquids. This section details important streamer characteristics in transformer oil, such as qualitative physical characteristics (*i.e.*, shape, velocity, light emission, etc.), along with applied voltage ranges.

Researchers have experimentally observed that streamers have different propagation characteristics that are strongly dependent on the voltage excitation (*i.e.*, magnitude, polarity, wave shape, duration, rise time, fall time, etc.) to the liquid and the chemical composition of the dielectric liquid [1,2,14,21,22,26,29]. In transformer oil, experimental evidence has shown that streamers that initiate from a positive voltage electrode, also called positive streamers, generally have a more filamentary structure and tend to initiate at lower applied voltages than streamers that initiate from negative voltage electrodes, or negative streamers, for the same electrode geometry [1,29,59]. Furthermore, for the same voltage magnitude, positive streamers propagate faster and further than their negative counterparts [1,29]. As a result, positive streamers constitute a greater risk to oil insulated systems than do negative streamers and are the focus of this work.

For positive streamers, minimum field levels for streamer initiation are on the order of 1×10^{8}V/m [1,11]. Depending on the applied voltage (or electric field) above these minimum levels, the resulting streamer can have very different characteristics. A key observation related to positive streamer propagation in transformer oil is the existence of four distinct positive streamer propagation modes, called the 1st, 2nd, 3rd, and 4th modes, for lightning impulse (1.2 μs rise time, 50 μs fall time) voltage excitations in transformer oil. The onset of the four modes are dependent on the magnitude of the excitation with the 1st mode initiating at the lowest voltage magnitude and the 4th mode at the highest. The 2nd mode initiates at the breakdown voltage V_b which denotes 50% probability of breakdown, while the 3rd mode initiates at the acceleration voltage V_a where the streamer propagation velocity rises dramatically [21]. Therefore, with increased applied voltage the streamer velocity and shape changes dramatically.

In pre-breakdown studies, the 1st mode is often disregarded as the probability of breakdown occurring is low [60]. The 1st mode streamers initiate near the minimum field levels discussed above and travel at relatively low velocities on the order of 100 m/s. They often result in a partial discharge as the streamer extinguishes in mid-gap because of the lack of input energy to overcome the potential drop along the streamer channel as it elongates towards the counter-electrode. In such a case, the streamer channel's potential drop diminishes the electric field magnitude at the streamer tip to a level where significant charge generation is stifled and the streamer propagation stops.

Table 2.1: Characterization of Positive Streamer Propagation Modes [14, 21, 22]

Mode	Applied Voltage	Velocity Range	Streamer Shape
1^{st}	$V < V_b$	~ 100 m/s	Few trunks surrounded by a less luminous zone
2^{nd}	$V_b \leq V < V_a$	$1 - 5$ km/s	Branched filamentary structure
3^{rd}	$V \approx V_a$	$10 - 30$ km/s	Extremely branched structure
4^{th}	$V > V_a$	> 100 km/s	Highly filamentary with 1 or 2 main branches

Table 2.2: ABB experimental data of breakdown and acceleration voltages for needle-sphere geometry from Fig. 2.1

	Positive Streamer		**Negative Streamer**
	Breakdown voltage, V_b	Acceleration voltage, V_a	Breakdown voltage, $\lvert V_b \rvert$
Mineral Oil A	105 kV	312 kV	251 kV
Mineral Oil B	126 kV	412 kV	166 kV

Above a certain field level, which is generally associated with the 50% probability breakdown voltage V_b, the streamers have much more energy to bridge the oil gap and travel with significant velocities. These streamers, the 2^{nd}, 3^{rd}, and 4^{th} modes, propagate at velocities on the order of 1 km/s, 10 km/s, and 100 km/s, respectively [2, 14, 21, 22, 29]. The attributes of the four modes are summarized in Table 2.1 and are categorized by their respective propagation velocities [2, 14, 21, 22, 28, 29]. In the literature, the 2^{nd}, 3^{rd}, and 4^{th} modes are often called slow streamer, fast streamer, and fast event, respectively [14, 21, 22].

The applied voltage range for the 3^{rd} mode region, between where the streamer transitions from the slow 2^{nd} mode to the highly energetic 4^{th} mode, is relatively small compared to the large applied voltage range for which the 2^{nd} mode streamer dominates. Therefore, the transition to 3^{rd} mode streamers is extremely dangerous because of their fast propagation velocities that allow these streamers to quickly traverse the oil gap to the cathode causing electrical breakdown before the applied voltage impulse can be extinguished. Figure 2.1 is experimental data from ABB Corporate Research which clearly shows the dependence of the time to breakdown and streamer propagation velocity on the applied voltage. Table 2.2 summarizes the breakdown voltage V_b and acceleration voltage V_a of the ABB experimental data shown in Fig. 2.1.

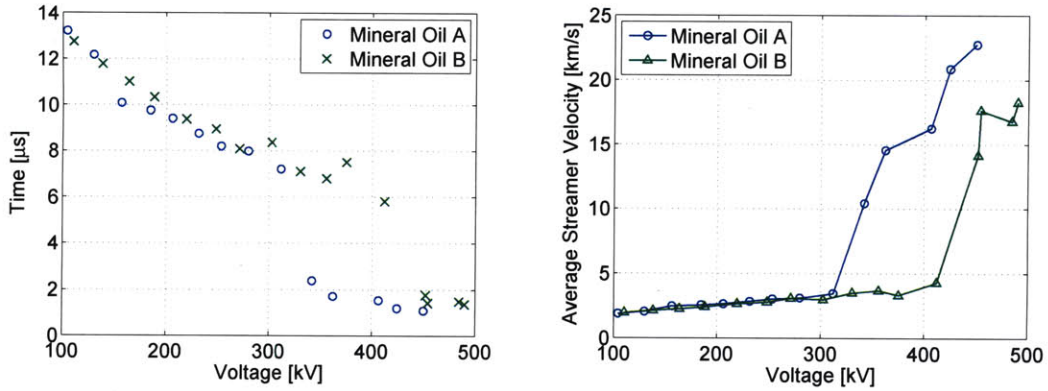

(a) Time to breakdown versus applied voltage (b) Average streamer velocity versus applied voltage

Figure 2.1: Experimental data from ABB Corporate Research regarding positive streamer propagation modes for the needle-sphere geometry detailed in IEC Standard 68097 [3] and used in the modeling work of this thesis. Courtesy of R. Liu and L. A. A. Pettersson at ABB Corporate Research in Västerås, Sweden.

The majority of streamer data in the literature prior to 1990 is concerned with 1st and 2nd modes due to instrumentation constraints. However, over the past 20 years, the amount and quality of experimental results for the fast traveling 3rd mode, and to a lesser extent the 4th mode, has also increased significantly. This increase in empirical results has allowed researchers to better understand and hypothesize the underlying mechanisms that lead to streamer development and the different modes. For example, Biller [42] hypothesized that for heterogeneous dielectric liquids, like transformer oil, the equivalent of slow 2nd mode streamers were linked to the ionization of "easily ionizable" molecules, while the faster modes result from the ionization of main "ordinary" molecules. In the context of transformer oil, the easily ionizable species are equivalent to aromatic molecules which have lower ionization energies [61, 62] and lower number density [63, 64] than the naphthenic and paraffinic molecules. The "ordinary" molecules are precisely the main naphthenic and paraffinic hydrocarbons that comprise the majority of transformer oil.

In the literature, there are a number of postulated mechanisms that result in streamer propagation. While the underlying physics differ between each mechanism, they all share the central concept that the generation of space charge, either by injection from the electrode or ionization of the oil itself, is critical to streamer propagation. In this thesis the mechanisms that lead to 2nd, 3rd, and 4th mode positive streamers will be investigated. It will be seen that the three charge generation mechanisms of field, impact, and photo-ionizations, play a vital role in streamer development and the different propagation modes. Another key component to the propagation of positive streamer modes that will be discussed extensively

is the chemical composition of transformer oil and the ionization parameters of different molecular types.

2.2 Streamers in Other Dielectric Liquids

Transformer oil is by no means the only dielectric liquid to be used as an electrical insulator and thermal conductor in high voltage electrical equipment. This section deals with the pre-breakdown characteristics for several other dielectric liquids used in electrical transmission components. Of particular interest is ester liquids, which are vegetable-based oils and therefore biodegradable.

2.2.1 Ester Liquids

Within the past decade there has been considerable interest in finding a green, environmentally friendly replacement for transformer oil. In particular, much of the work has focused on vegetable-based oils composed of natural or synthetic esters [4–6,59,65] that are biodegradable. Unfortunately, ester liquids have shown to have electrical insulation characteristics that are greatly inferior to transformer oil at extremely high voltages [4–6,59].

Ester liquids, whether natural or synthetic, have pre-breakdown characteristics that are extremely different from transformer oil. This should not come as a surprise as esters have a different chemical composition. The following discussion of streamer propagation in ester liquids will use the same terminology and definition for streamer modes discussed in the last section and summarized in Table 2.1.

As in transformer oil, the onset of the streamer modes in ester liquids are dependent on the magnitude of the voltage excitation. Once again, the 2^{nd} mode initiates at the breakdown voltage V_b which denotes 50% probability of breakdown, while the 3^{rd} mode initiates at the acceleration voltage V_a where the streamer propagation velocity rises dramatically [21]. The 2^{nd}, 3^{rd}, and 4^{th} modes have velocities on the order of 1 km/s, 10 km/s, and 100 km/s, like in transformer oil [4–6,59]. Furthermore, the breakdown voltage V_b of ester liquids and transformer oil, where 2^{nd} mode streamers initiate, has shown to be very close in magnitude for the same experimental setup [4–6,59].

The key difference between ester liquids and transformer oil is the acceleration voltage V_a, where streamers transition to very fast 3^{rd} and 4^{th} mode streamers. For transformer oil, it was shown in Section 2.1.1 that the acceleration voltage is much higher than the

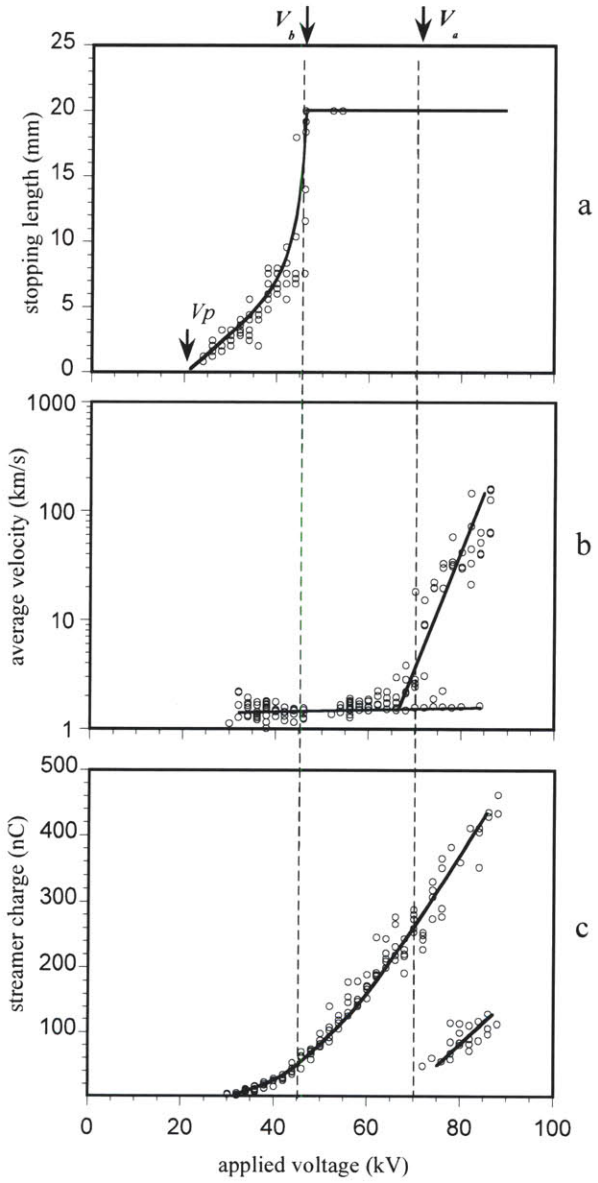

Figure 2.2: Experimental data from Duy *et al.* regarding positive streamer propagation in rape-seed oil comprised of natural esters [4–6]. Summary of measurements carried out on positive streamers with $d = 2$ cm gap distance (V_b: 50% probability breakdown voltage, V_a: acceleration voltage). (a) streamer stopping length, (b) streamer average velocity (c) streamer charge. (Figure 3, [6])

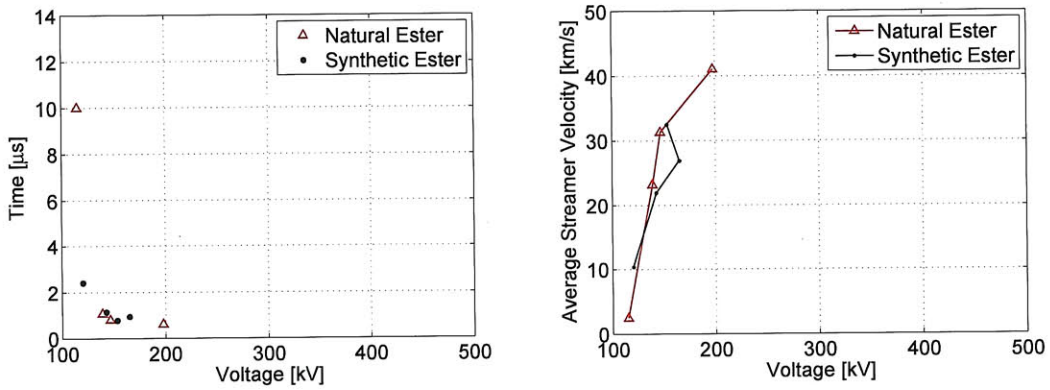

(a) Time to breakdown versus applied voltage (b) Average streamer velocity versus applied voltage

Figure 2.3: Experimental data from ABB Corporate Research regarding positive streamer propagation in natural and synthetic esters for the needle-sphere geometry detailed in IEC Standard 68097 [3]. Courtesy of R. Liu and L. A. A. Pettersson at ABB Corporate Research in Västerås, Sweden.

breakdown voltage. For the ABB experimental data in Fig. 2.1 the acceleration voltage is approximately 3 and 4 times greater than the breakdown voltage for Mineral Oil A and Mineral Oil B, respectively. Therefore, in transformer oil the applied voltage range where the slow 2^{nd} mode streamers dominate is large and the voltage at which the dangerous 3^{rd} and 4^{th} mode streamers propagate is at very high voltages. This ensures a lower probability for propagation of fast streamers that quickly traverse the oil gap to the cathode causing electrical breakdown before the applied voltage impulse can be extinguished.

For ester liquids, the acceleration voltage V_a occurs almost directly above the breakdown voltage as shown by the two different experimental results from Duy *et al.* [4–6] and ABB Corporate Research in Figs. 2.2 and 2.3, respectively. Therefore, when the breakdown voltage is reached the streamers easily transition to fast streamers that propagate at average velocities greater than 10 km/s since $V_b \approx V_a$ for ester liquids. Consequently, ester liquids are not well-suited to insulate high-voltage systems. To easily compare the average velocity of positive streamers in ester liquids and transformer oil, the results of Figs. 2.1 and 2.3 from ABB Corporate Research have been plotted together in Fig. 2.4. To use ester liquids for high-voltage insulation a streamer velocity profile resembling that obtained for transformer oil is required or more plainly, the acceleration voltage needs to be increased considerably such that 3^{rd} and 4^{th} mode streamers initiate at much higher voltage.

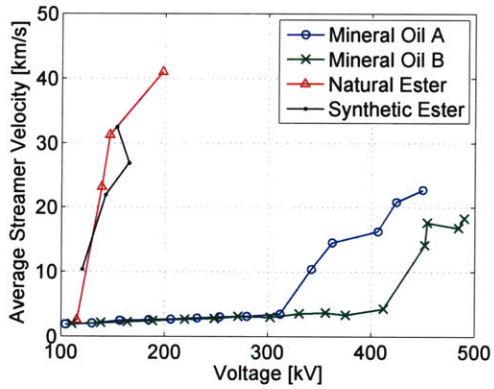

Figure 2.4: Experimental data from ABB Corporate Research comparing the average positive streamer velocity versus applied voltage in ester liquids and transformer oils for the needle-sphere geometry detailed in IEC Standard 68097 [3]. Courtesy of R. Liu and L. A. A. Pettersson at ABB Corporate Research in Västerås, Sweden.

2.2.2 Other Dielectric Liquids

There are other dielectric liquids that have pre-breakdown characteristics that resemble those of ester liquids. In particular, the characteristic where streamers rapidly transition from slow 2^{nd} mode to fast 4^{th} mode streamers over a very narrow applied voltage range, such that the acceleration voltage and breakdown voltage can be considered to be almost equal, can be found in other liquids. The same behavior has been reported in the literature for water [9, 10], two aromatic hydrocarbons (isopropyl-biphenyl and phenyl-xylyl-ethane) [7], a synthetic liquid (benzyl-toluene) [8], and cyclohexane [12], a saturated hydrocarbon. The average streamer velocity versus applied voltage is shown for water and isopropyl-biphenyl in Figs. 2.5(a) and 2.5(b), respectively.

2.3 The Effects of Additives on Hydrocarbon Oils

Due to the complex nature of transformer oil, with its multitude of different molecules including paraffinics, naphthenics and aromatics, the task of isolating streamer mechanisms in such a complex mixture seems daunting. With this in mind researchers have tried to strip away some of the complexity by focusing on pure hydrocarbon liquids such as cyclohexane, n-hexane, and benzene, just to name a few [1, 26, 28, 66–68]. Several researchers took these studies a step further by adding controlled amounts of specific additives to study their affects on pre-breakdown phenomena [11, 12, 32, 34, 35, 55, 69–72]. These researchers realized that to best elucidate streamer mechanisms in transformer oil they would need to engineer

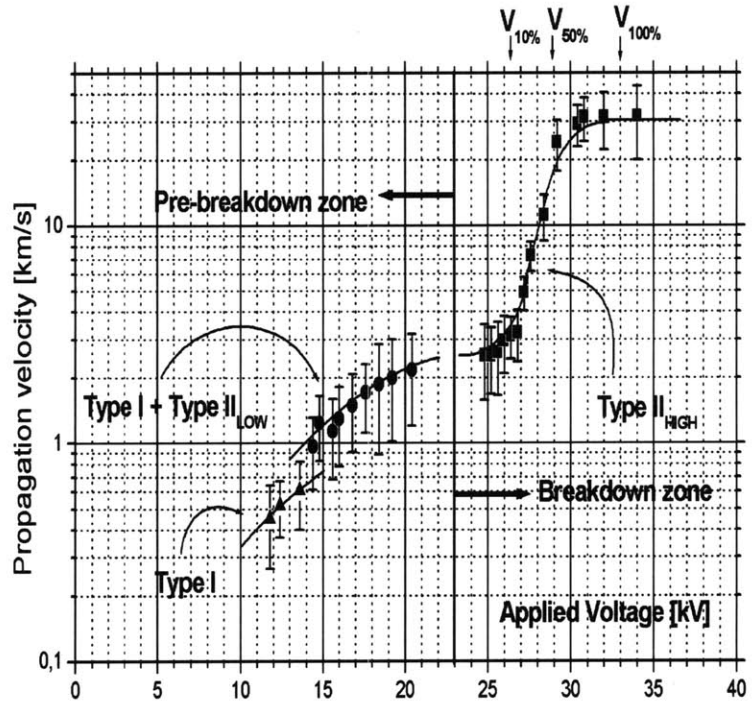

(a) Water (Figure 1, [10])

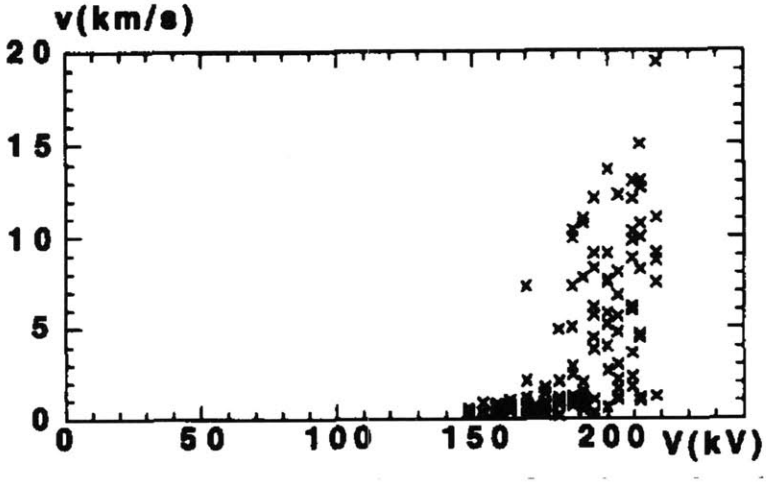

(b) Aromatic hydrocarbons: isopropyl-biphenyl and phenyl-xylyl-ethane (Figure 15, [7])

Figure 2.5: Experimental data from the Lesaint group regarding positive streamer velocity as a function of applied voltage for several different dielectric liquids [7–10].

simple and controlled multi-molecular species liquids, such as a highly naphthenic oil with easily ionizable molecules [11], for breakdown tests. Then they could compare the results of the liquids with additives to the pure sample and transformer oil.

2.3.1 Exxon Marcol 70 Naphthenic Oil with Low Ionization Potential Additives

The ground breaking work by Devins, Rzad and Schwabe [11] investigated the effect of additives in highly refined Exxon Marcol 70 naphthenic oil on streamer propagation for low mode streamers such as 1st and 2nd modes. In particular, Devins *et al.* realized that the main difference between the chemical composition of Marcol 70 and transformer oils was the absence of "easily ionizable" aromatic molecules in Marcol 70 [11]. Therefore, they added the polyaromatic 2-methyl naphthalene and N,N'-dimethylaniline (DMA), which have low ionization potentials of 7.96 eV and 7.14 eV, respectively [11], to Marcol 70. They found that by adding these low ionization potential additives positive streamers were accelerated and the streamer inception voltage was lowered. Furthermore, as the concentration of DMA was increased up to 2%, the streamer propagation velocity of the Marcol 70 mixture closely resembled that of 10C transformer oil (naphthenic base + 20-30% aromatic content) nearing 2nd mode levels of 2 km/s. Figure 2.6 shows the streamer velocity versus applied voltage for Marcol 70 with different concentrations of DMA and 10C transformer oil. The results suggest that the low ionization potential aromatic molecules in transformer oil are responsible for the propagation of slow mode streamers such as the 2nd mode. These results by Devins *et al.* have been confirmed by other researchers [32, 55, 71].

2.3.2 Pure Cyclohexane and Cyclohexane with Pyrene Additive

In [12], Lesaint and Jung studied streamer propagation in cyclohexane with varying concentrations of pyrene added. Compared to cyclohexane, which has an ionization potential of 9.86 eV, pyrene has a low ionization potential of 7.4 eV. The cyclohexane had a purity of 99.5% or greater and the maximum concentration of pyrene added was 19 g to 1 L of cyclohexane. Their obtained experimental results have been duplicated in Fig. 2.7 for convenience.

In Fig. 2.7(a), a comparison of the average velocity for pure cyclohexane and pyrene saturated cyclohexane are given. In the case of pure cyclohexane, the breakdown voltage is $V_b \approx 110$ kV and the acceleration voltage is $V_a \approx 125$ kV such that they are almost equal and streamers readily transition to high velocities, which are associated with fast 3rd and 4th mode streamer propagation, with an incremental voltage increase. In pyrene saturated

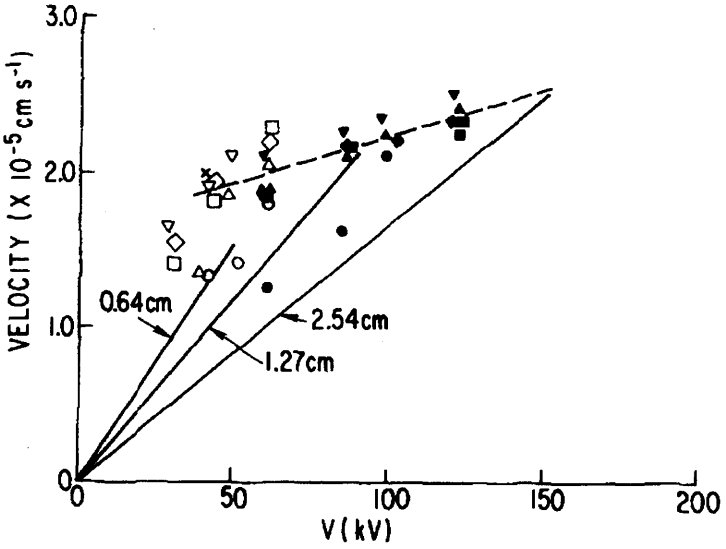

Figure 2.6: Gap and voltage dependence of positive streamer velocities in Marcol 70 at various DMA concentrations. Hap: (open points) 1.27cm, (solid points) 2.54cm, (×) 0.64cm. Concentration of DMA: (○) 7×10^{-3} M, (□) 2.2×10^{-2} M, (△) 6.7×10^{-2} M, (▽) 1.27×10^{-1} M, (×) 1.58×10^{-1} M, (◇) 2.1×10^{-1} M. Dashed line for transformer oil. (Figure 33, [11])

cyclohexane, the breakdown voltage is $V_b \approx 75$kV and the acceleration voltage is $V_a \approx 170$kV, which is a 32% decrease of the breakdown voltage but a 36% increase of the acceleration voltage when compared to the pure cyclohexane case.

Figure 2.7(b) shows the breakdown and acceleration voltage in cyclohexane for varying concentrations of pyrene. The general trend is that with a concentration increase in the low ionization potential additive pyrene the acceleration voltage quickly increases and the breakdown voltage decreases at a slower rate. Lesaint and Jung argued that this phenomena was directly related to the fact that pyrene was easily ionizable and readily created a more branched streamer structure (*i.e.*, a streamer structure with many radial extensions) in cyclohexane, as shown by the streamer photographs in Fig. 2.8. The space charge in the radial branches contributed to the electric field at the streamer tip in such a way to regulate the maximum magnitude of the electric field. By regulating the maximum field at the streamer tip by "geometric field regulation" [14,21], the ionization at the streamer tip, the mechanism which drives streamer propagation [25,26,73], is controlled.

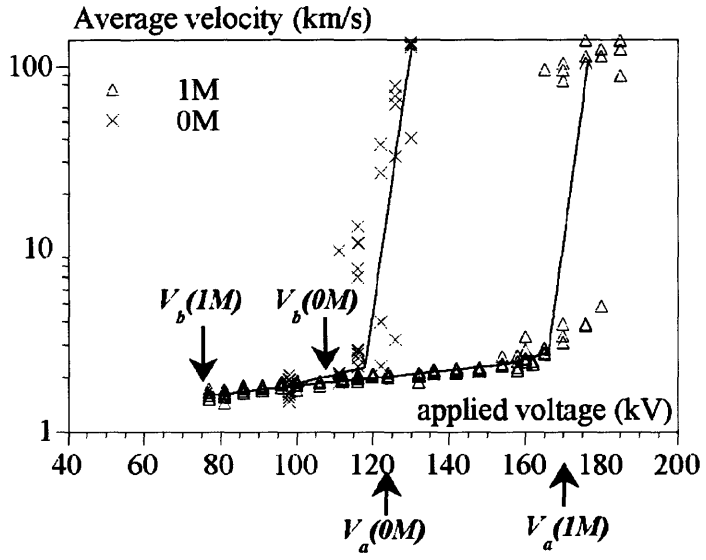

(a) Average propagation velocity versus applied voltage in a $d=5$ cm point-plane gap for pure cyclohexane ($c=0$ M) and pyrene saturated cyclohexane ($c=1$ M). (Figure 10, [12])

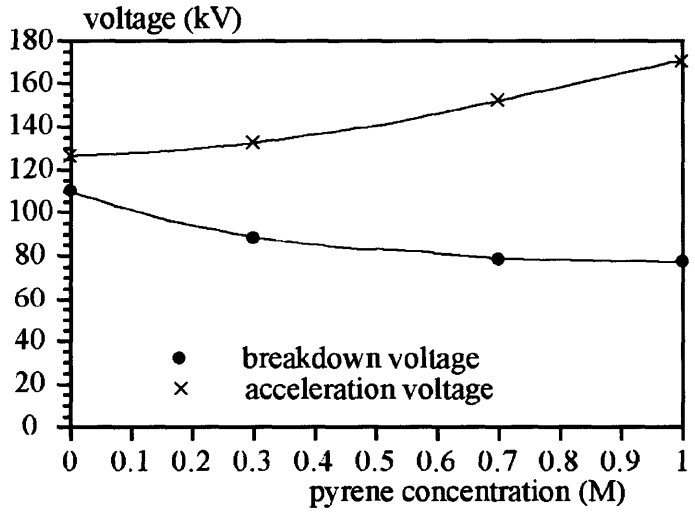

(b) Breakdown and acceleration voltages against pyrene concentration c for $d=5$ cm. (Figure 11, [12])

Figure 2.7: Experimental data from Lesaint and Jung regarding positive streamer propagation in cyclohexane with pyrene additive [12].

2.4 Transformer Oil-Based Nanofluids

Over the past century, transformer oil has become the standard insulation liquid for high voltage insulation and power apparatus cooling. Throughout this time, there has been extensive research focused on enhancing transformer oil's electrical and thermal characteristics. For example, researchers have been investigating the use of nanotechnology in transformer oil to enhance cooling of a transformer's core [23,74–79]. Conducting materials, such as magnetite (Fe_3O_4), have been added to transformer oil as nanoparticle suspensions, with

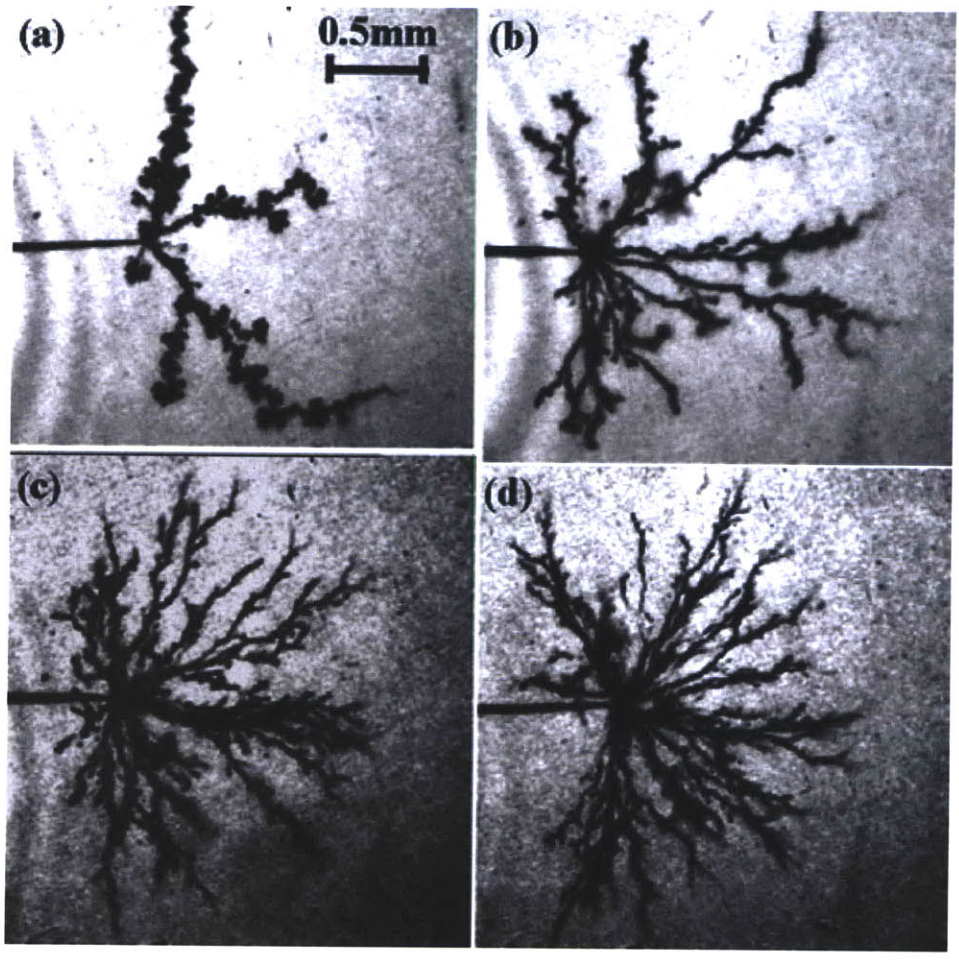

Figure 2.8: Experimental data from Lesaint and Jung showing typical photographs of streamers, taken 0.8μs after the voltage rise at $V=30$kV, for various pyrene concentrations: (a) $c=0$ M; (b) $c=0.1$ M; (c) $c=0.7$ M; and (d) $c=1$ M (Figure 8, [12]).

Table 2.3: Results of impulse voltage withstand testing in 25.4 mm electrode gap system [23]

Fluid	**Breakdown Voltage**		**Time to Breakdown**		**Average Streamer Velocity**	
	Positive	Negative	Positive	Negative	Positive	Negative
Univolt 60 Transformer Oil	86 kV	170 kV	12 μs	27 μs	2.12 km/s	0.94 km/s
Univolt-Colloid Nanofluid	157 kV	154 kV	26 μs	15 μs	0.98 km/s	1.69 km/s
Nytro 10X Transformer Oil	88 kV	177 kV	16 μs	23 μs	1.59 km/s	1.10 km/s
Nytro-Colloid Nanofluid	156 kV	173 kV	25 μs	17 μs	1.02 km/s	1.49 km/s

the aim of enhancing some of the oil's insulating and thermal characteristics [23, 74–79] as is derived in Chapter 5.

Electrical breakdown testing of magnetite nanofluid found that for positive streamers the breakdown voltage of the nanofluids was almost twice that of the base oils during lightning impulse tests [23]. The positive lightning impulse withstand results obtained by Segal *et al.* [23] showed an increase in transformer oil breakdown strength with the addition of conducting nanoparticles for two common transformer oils (*i.e.*, Univolt 60 and Nytro 10X). The results for the base oils and their associated nanofluids are summarized in Table 2.4. Also, the propagation velocity of positive streamers was reduced by the presence of nanoparticles, by as much as 46% for Univolt-Colloid Nanofluid. The results are significant because a slower streamer requires more time to traverse the gap between electrodes to cause breakdown. This allows more time for the applied impulse voltage to be extinguished. These results indicate that the presence of the magnetite nanoparticles in the oil samples inhibits the processes which lead to electrical breakdown. The results found by Segal *et al.* are in direct conflict with conventional wisdom and experience regarding the breakdown of dielectric liquids, where the presence of conducting particulate matter in a dielectric liquid is expected to decrease its breakdown strength.

O'Sullivan [25] presented an electrodynamic model for streamer formation in transformer oil-based nanofluids based upon Gauss' Law and charge transport continuity equations for each charge carrier. A thorough study into the effect of nanoparticles of varying materials and properties on streamer propagation was investigated. It was shown that with increased nanoparticle conductivity, the greater the influence on retarding streamer propagation. The work showed that transformer oil stressed by a positively charged electrode leads to field ionization of oil molecules into slow positive ions and fast electrons [25, 53, 80]. Generally, the fast electrons cause a propagating electric field wave, which is the dominant mechanism in streamer propagation, leading to electrical breakdown. However, the conductive nanoparticles act as electron scavengers in electrically stressed transformer oil-based nanofluids converting fast electrons to slow negatively charged nanoparticles [25,53,80]. Due to the low mobility of these nanoparticles the development of a net space charge zone at

the streamer tip is hindered, suppressing the propagating electric field wave that is needed to drive field ionization and ultimately streamer propagation further into the liquid.

2.5 Transformer Oil-Solid Insulation Systems

High voltage equipment is often composed of several different dielectric materials for improved insulating and thermal characteristics. For example, a large portion of a power transformer's insulation capability is based not only on mineral oil, but also solid insulation materials such as cellulose paper and boards, also known as transformer-board or pressboard [81–83]. Pressboard has high dielectric strength, good mechanical properties, long lifetime, and is compatible with transformer oil making it a good choice for a solid insulation material in transformers. The composite transformer oil and pressboard system generally increases the insulation strength of the transformer against partial discharge, streamers and most importantly electrical breakdown.

Pressboard is nothing more than high-quality, thick insulation cellulose paper. Cellulose materials, of which pressboard is comprised of, is made from slow growing types of woods that have high density, long fibres. These long fibres give long lifetime usage of the cellulose and the high density allows for high dielectric strength [83]. In processing cellulose for use in an oil-filled transformer, it must be dried and oil impregnated. Drying of the cellulose is required to reduce the moisture content, which if not completed can decrease the dielectric strength and accelerate aging [81]. On the other hand, oil impregnating the cellulose, which is done under vacuum at elevated temperatures, ensures that the tiny cavities between the individual fibres are filled with oil. These cavities are small air bubbles that would more easily cause partial discharge if they were not replaced with oil. Therefore, by oil impregnating cellulose, its dielectric strength is increased. For further information regarding cellulose insulation please refer to IEC 60554-3 for cellulose paper and IEC 60641-3 for pressboard and references [81, 82].

It has been reported in the literature that streamer propagation in oil is greatly affected by the presence of pressboard and other solid insulation [13–16, 57, 59, 84–91]. In particular, two critical components or characteristics of oil-solid systems have been shown to have serious impact on streamer propagation. They are the orientation of the oil-solid interface with respect to the dominant electric field direction and the permittivity difference between oil and pressboard. Regarding the oil-solid interface orientation, there are two cases of interest as they are described extensively in the literature and affect streamer propagation differently. These orientations are:

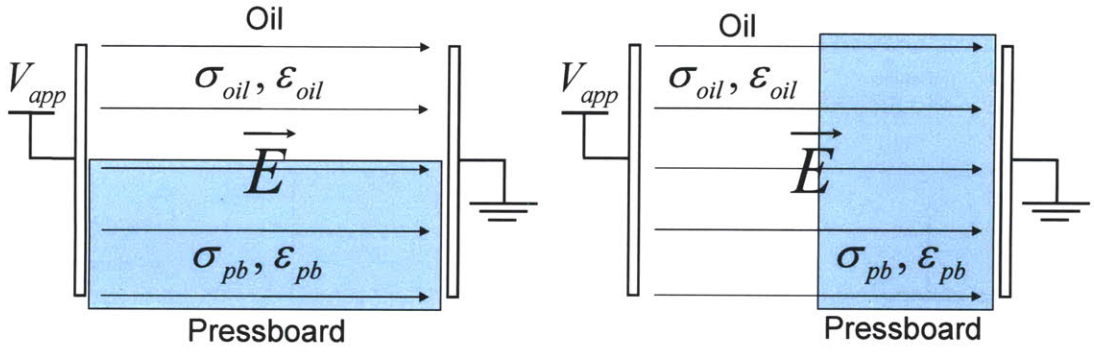

(a) Transformer oil-pressboard system where the interface is oriented parallel to the dominant direction of the electric field.

(b) Transformer oil-pressboard system where the interface is oriented perpendicular to the dominant direction of the electric field.

Figure 2.9: Qualitative examples of the two transformer oil-pressboard orientations discussed in the literature.

- The oil-solid interface is oriented parallel to the dominant direction of the main electric field component, as shown in Fig. 2.9(a) [13, 14, 59].
- The oil-solid interface is oriented perpendicular to the dominant direction of the main electric field component, as shown in Fig. 2.9(b) [16, 57, 85].

The following two sections will discuss in detail these two orientations and their affect on streamer development.

2.5.1 Liquid-Solid Interface Oriented Parallel to the Main Electric Field Component

Experimental evidence has shown that streamer propagation is dramatically altered when the streamer comes in contact with a solid surface. The surface can either assist or impede streamer propagation depending on the direction of the solid surface with respect to the direction of the main electric field component. This section focuses on oil-solid systems where the orientation of the surface is parallel to the main electric field component.

The experimental results from the literature have shown that surfaces that are parallel to the direction of the main electric field component aid streamer development and therefore increase the probability of breakdown [13, 14, 21, 22, 59, 85]. In particular, the results from several groups, including Massala and Lesaint [13, 91], Lundgaard *et al.* [14], and Liu *et al.* [59], have pioneered the study in this field. Their results for point-plane geometries, where the pressboard surface is along the point-plane axis, as shown in the left of Fig. 2.10(a), have

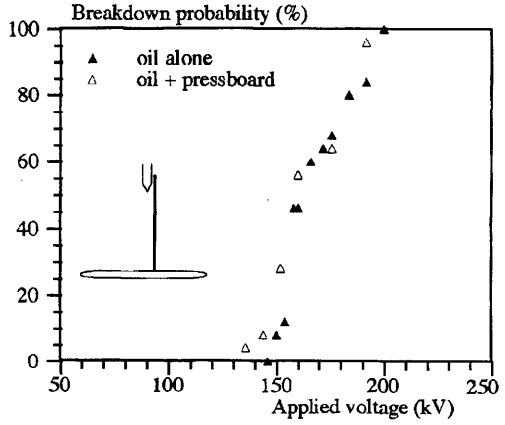

(a) Comparison of breakdown probability with and without pressboard surface. Point-plane gap distance is d=10 cm. (Figure 23, [13])

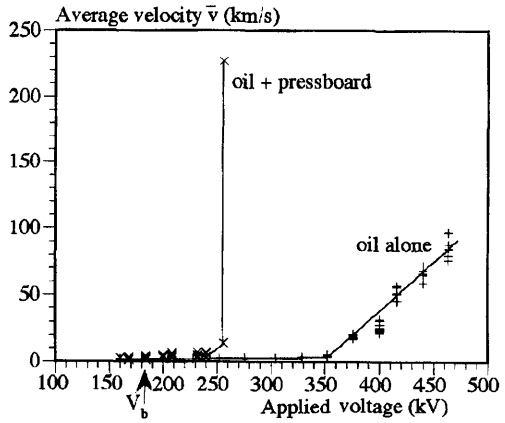

(b) Average breakdown velocity recorded at over-voltages with and without pressboard surface. Point-plane gap distance is d = 10 cm. (Figure 24, [13])

Figure 2.10: Experimental results of Massala and Lesaint [13] for streamers in point-plane systems with and without pressboard. In an oil-pressboard system, the streamer travels along a pressboard surface parallel to the point-plane axis (*i.e.*, surface is parallel to dominant field direction) with gap length d=10cm. Their results suggest that in such systems the breakdown probability/voltage is unchanged by the pressboard (see Fig. 2.10(a)), however the acceleration voltage is dramatically reduced (see Fig. 2.10(b)).

allowed for better understanding of streamer phenomena in these systems at breakdown and over-voltages.

Figure 2.10 are experimental results from Massala and Lesaint [13] that explicitly show the effects of the pressboard at breakdown and over-voltages. They found that the presence of the pressboard had no influence on the breakdown probability (Fig. 2.10(a)) since the breakdown voltage in oil-only and oil-pressboard systems were nearly identical. However, as the voltage was increased above the breakdown voltage V_b, where 2nd mode streamers propagate, the time-to-breakdown and average streamer velocity of the oil-pressboard system greatly differed from an oil-only system. In fact, the transition from slow 2nd mode streamers that propagate on the order of 1 km/s to fast 3rd and 4th mode streamers with velocities greater than 10 km/s occurs at much lower voltages for an oil-pressboard system with interface parallel to the field. Therefore, these systems see a dramatic decrease in the acceleration voltage V_a compared to the oil-only systems (Fig. 2.10(b)) and the insulating strength at over-voltage is compromised.

Massala and Lesaint [13] also observed that by confining the growth of streamers within cylindrical tubes, where the surface was parallel to the main electric field component,

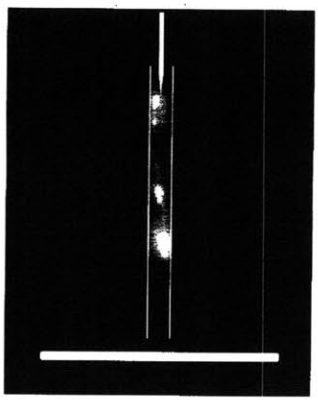

(a) Streamer development within a polytetrafluoroethylene (PTFE) tube in a needle-plane system. Photograph of a s stopped streamer within a PTFE tube, $d = 10$ cm, $V = 13$ kV, 6 mm tube. (Figure 13, [13])

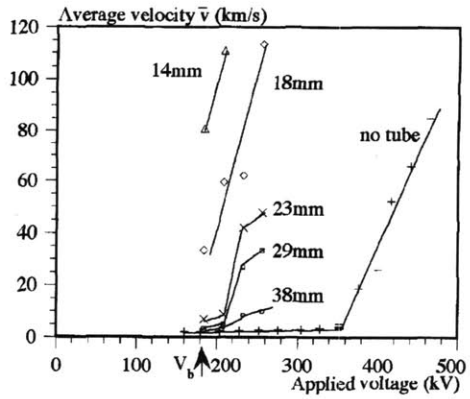

(b) Experimental results of the average streamer velocity versus applied voltage for streamers traveling within polypropylene tubes of length $d = 10$ cm and varying diameters. (Figure 22, [13])

Figure 2.11: Experimental results of Massala and Lesaint [13] for streamers whose propagation is restricted within cylindrical tubes of polytetrafluoroethylene or polypropylene with length $d = 10$ cm and varying diameters. The setup is such that main electric field component within the inner tube is parallel to the oil-tube interface. Their results suggest that in such systems the streamer propagation is aided by the presence of the tube, which restricts the radial growth of the streamer and alters the streamer shape from that of the case where no tube is present.

streamer propagation was greatly increased. The setup and key experimental results from this work are shown in Fig. 2.11. By guiding the streamers within insulating tubes Massala and Lesaint observed that the breakdown voltage was decreased by 15%. Furthermore, they noticed significant changes to the streamer behavior, shape, and velocity. Due to the presence of the tube surface and the restriction of the streamer's radial growth, the streamers propagated at much higher velocities at lower voltages than in the oil-only case. In fact, as the diameter of the tube was decreased, the streamers tended to accelerate at much lower voltages.

These results are consistent with the observations and hypotheses of other researchers. In the literature, it has been noted that when a streamer's radial growth and semi-spherical shape are limited the streamer accelerates at much lower voltages [14,21]. This is known as the geometric field regulation [13], where the electric field associated with the space charge within the streamer branches (those that grow more radial when compared to the main filament that bridges the gap) regulates the electric field magnitude at the streamer tip. Consequently, ionization and charge generation, which drives streamer development at the streamer tip, is controlled. By constricting streamer growth within an insulating tube the

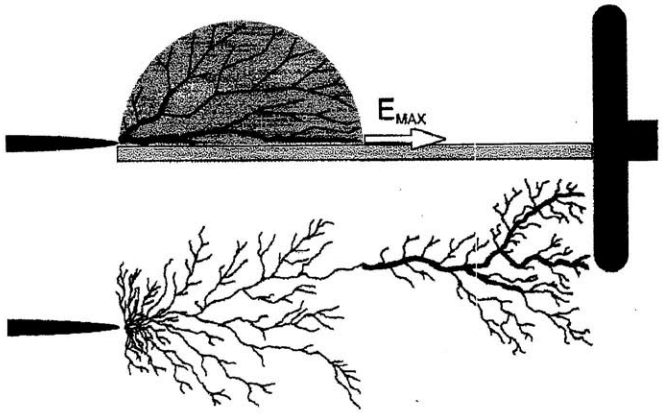

Figure 2.12: Hypothesis from Lundgaard *et al.* [14] regarding the acceleration of positive streamers at over-voltage along solid surfaces where the surface is parallel to the direction of the main electric field component. Upper: The positive streamer model. Lower: Actual tracks observed on pressboard surface. Lundgaard *et al.* hypothesize that the solid insulation hinders the branching of streamers, which regulates the electric field enhancement at the head of the streamer. Consequently, due to the lack geometrical symmetry of the streamer shape the field enhancement at the streamer head is higher at lower voltages and drives faster charge generation resulting in the acceleration of streamers. (Figure 18, [14])

semi-spherical streamer shape is lost. Therefore, the streamer velocities are much higher at lower applied voltages. Figure 2.12 is a graphical representation of how the solid insulator hinders streamer branching leading to high field enhancement at the streamer tip for lower voltages. These results suggest that solid insulation in the parallel configuration aids in the development of fast streamers and increases the probability of breakdown in oil-insulated systems.

2.5.2 Liquid-Solid Interface Oriented Perpendicular to the Main Electric Field Component

Experimental evidence has shown that streamer propagation is dramatically altered when the streamer comes in contact with a solid surface. The surface can either assist or impede streamer propagation depending on the direction of the solid surface with respect to the direction of the main electric field component. This section focuses on oil-solid systems where the orientation of the surface is perpendicular to the main electric field component.

The experimental results have shown that surfaces that are perpendicular to the direction of the main electric field component hinder streamer development, acting as a barrier for streamers and thereby increasing breakdown voltage [15,16,85]. Lesaint and Massala studied

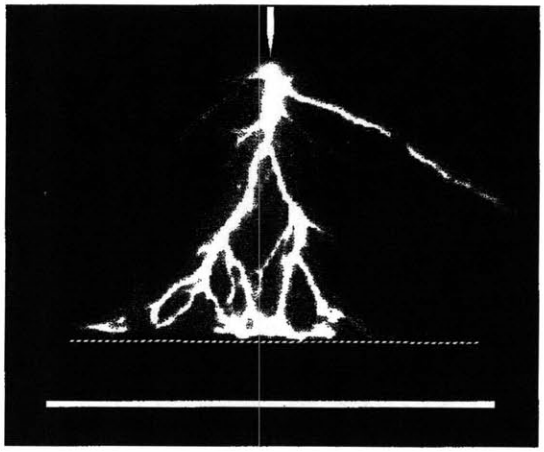

Figure 2.13: Experimental results of Massala and Lesaint [13] for streamers whose propagation is along a pressboard surface that is perpendicular to the symmetry axis. Photograph of a 2nd mode streamer traveling along the pressboard surface (dashed line). The intensifier gate was closed 10 μs before breakdown, gap distance $d = 10$ cm, plane-to-pressboard distance of 2 cm, $V_{app} = 208$ kV. The setup is such that main electric field component is perpendicular with the pressboard interface. Their results show that as the streamer comes in contact with the pressboard surface its propagation direction is altered and it begins to grow radially along the pressboard surface thereby increasing the time to breakdown. (Figure 2, [13])

this type of system, where the pressboard surface is perpendicular to the main field direction in a point-plane geometry, and observed that when the pressboard surface was close to the point electrode the breakdown voltage was significantly increased [91]. As the streamer travels towards the plane electrode it comes in contact with the pressboard surface. The streamer's propagation towards the plane electrode is then impeded as it creeps along the pressboard surface to its sides. The study was restricted to voltages where the pressboard was not punctured. Once it reaches the sides the streamer once again travels towards the plane electrode. The overall propagation velocity, even at over-voltages well above the breakdown voltage, was relatively low in the range of $2-3$ km/s. This was attributed to the increase in streamer channel length as it must travel along the pressboard surface to reach the counter-electrode. Because the streamer path has increased so has the voltage drop within the streamer. Therefore, a greater applied voltage is needed to lead to breakdown. Figure 2.13 shows a photographic snapshot of a streamer creeping along pressboard surface.

Liu *et al.* [15, 16] have observed similar phenomena for streamers that come in contact with a solid insulation surface that is perpendicular to the main electric field component. Figure 2.14 shows the pressboard surface after the experiment, and time-to-breakdown measurements for oil-pressboard systems. They observed streamers that initiated in oil and

(a) Discharge pattern on the surface of a paper covered electrode. (Figure 8, [15])

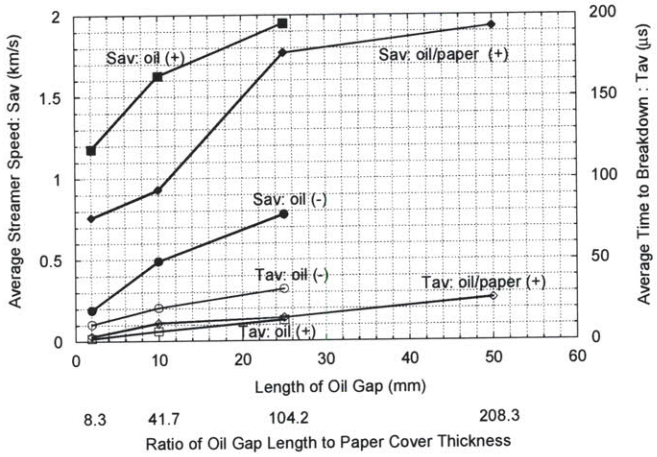

(b) Experimental results of the average streamer velocity and time to breakdown versus the ratio of the oil gap length to the thickness of the ground electrode covering for varying voltage polarities and test conditions. The needle radius is 3 μm and the paper cover thickness is 0.24 mm for the oil-paper test objects. (Figure 7, [15])

Figure 2.14: Experimental results of Liu *et al.* [15, 16] for streamers whose propagation is restricted along oil impregnated laminated papers that cover the ground electrode. The setup is such that the main electric field component is perpendicular to the paper interface. Their results suggest that the introduction of a solid pressboard into the oil system can increase breakdown voltage and decrease streamer propagation velocity. As the streamer comes in contact with the perpendicular paper surface it cannot propagate axially towards the ground electrode. Therefore, it travels radially along the surface increasing the time to breakdown and decreasing the average streamer velocity.

propagated toward the pressboard surface. As the streamer came in contact with pressboard its propagation direction changed and it began to propagate along the surface. As the streamer traveled along the surface it deposited electric charges onto the solid surface which redistributed the electric field in the solid insulation and left noticeable discharge markings (Fig. 2.14(a)). By introducing the pressboard in this perpendicular configuration the breakdown voltage was increased (Fig. 2.14(b)). As the streamer was restricted to traveling along the surface, the time to breakdown is increased considerably thereby decreasing the streamer's average breakdown velocity. These results suggest that pressboard in the perpendicular configuration plays a critical role in hindering the development of streamers and decreases the probability of breakdown in oil-insulated systems.

2.5.3 The Effects of Permittivity Differences Between Transformer Oil and Solid Insulation on Streamer Propagation

It has been reported in the literature that streamer propagation in oil is greatly affected by the presence of pressboard. This should not come as a surprise as pressboard has different material characteristics (*i.e.*, chemical, mechanical, and electrical) than oil. From an electrical perspective, the relative permittivity of pressboard is $\epsilon_r^{pb} = 4.4$ [92], twice that of transformer oil at $\epsilon_r^{oil} = 2.2$ [83], has been shown to dramatically affect streamer propagation, such that streamers in the oil are attracted towards the pressboard surface [57, 84, 93].

In [57], the researchers report that low permittivity insulating solids, such as polyethylene and polypropylene, which have relative permittivities of 2.3 and almost match that of oil, result in high flashover voltages for impulse and 60 Hz excitations. On the other hand, they report that a permittivity mismatch, such as that of oil and pressboard, can assist in discharge propagation and enhance surface irregularities [93].

In other work [84], the researchers observed that the presence of pressboard spacer objects in oil gave way to large field enhancement due to the permittivity mismatch. Therefore, it was postulated that the field enhancement led to the reduction of the breakdown voltage in an oil-pressboard system compared to an oil-only system. They too were able to show that by utilizing solid materials with relative permittivities comparable to transformer oil the reduction in breakdown voltage was not as severe or did not exist in some cases compared to the oil-pressboard system.

The reported impact of permittivity differences between oil and pressboard shows that it is a source of major concern for insulation designers. There have also been several patents that address this issue by innovative techniques to reduce the permittivity of pressboard, such that it is closer to that of transformer oil [94, 95].

Chapter 3

General Electrohydrodynamic Model for Dielectric Liquids

ELECTRICAL breakdown and pre-breakdown in dielectric liquids, including transformer oil, is characterized by observable events such as the formation of streamers and ultimately arcs. These structures form as a result of the electrically dissipative processes, which occur in the liquid when it is electrically over-stressed. Therefore, the modeling of streamer formation in dielectric liquids must primarily focus on the electro-thermal dynamic processes taking place in the liquid. This chapter focuses on the general mathematical model, system geometry, model parameters and their values, and different charge generation mechanisms in dielectric liquids such as transformer oil.

3.1 Governing Equations

The governing equations that contain the physics to model streamer development are based on the drift-dominated charge continuity equations (3.2)-(3.4) for positive ion (ρ_p), negative ion (ρ_n) and electron (ρ_e) charge densities which are coupled through Gauss' Law (3.1). The thermal diffusion equation (3.5) is included to model temperature variations (T) and gas formation in oil. The negative ion and electron charge densities are both negative quantities. The three carrier continuum model is utilized to account for the charge generation and capture mechanisms, which are critical in the study of streamers.

$$\nabla \cdot (\epsilon_r \epsilon_0 \vec{E}) = \rho_p + \rho_n + \rho_e \tag{3.1}$$

$$\frac{\partial \rho_p}{\partial t} + \nabla \cdot (\rho_p \mu_p \vec{E}) = G_p(|\vec{E}|) + \frac{\rho_p \rho_e R_{pe}}{q} + \frac{\rho_p \rho_n R_{pn}}{q} \tag{3.2}$$

$$\frac{\partial \rho_n}{\partial t} - \nabla \cdot (\rho_n \mu_n \vec{E}) = G_n(|\vec{E}|) + \frac{\rho_e}{\tau_a} - \frac{\rho_p \rho_n R_{pn}}{q} \tag{3.3}$$

$$\frac{\partial \rho_e}{\partial t} - \nabla \cdot (\rho_e \mu_e \vec{E}) = G_e(|\vec{E}|) - \frac{\rho_p \rho_e R_{pe}}{q} - \frac{\rho_e}{\tau_a} \tag{3.4}$$

$$\frac{\partial T}{\partial t} + \vec{v} \cdot \nabla T = \frac{1}{\rho_l c_v}(k_T \nabla^2 T + \vec{E} \cdot \vec{J}\,) \tag{3.5}$$

In (3.1)-(3.5), μ_p, μ_n and μ_e are the mobilities of the positive ions ($1{\times}10^{-9}$ $\mathrm{m^2V^{-1}s^{-1}}$) [96], negative ions (1×10^{-9} $\mathrm{m^2V^{-1}s^{-1}}$) [96], and electrons (1×10^{-4} $\mathrm{m^2V^{-1}s^{-1}}$) [97,98], respectively, and all mobilities are taken as positive values. Also, ϵ_r, ϵ_0, k_T, c_v, and ρ_l are the oil's relative permittivity (2.2), permittivity of free space (8.854×10^{-12} F/m), thermal conductivity ($0.13\,\mathrm{Wm^{-1}K^{-1}}$), specific heat ($1.7\times10^3$ $\mathrm{J\,kg^{-1}K^{-1}}$), and mass density (880 $\mathrm{kg/m^3}$) respectively, and these values are representative for transformer oil. In the time scales of interest for streamer formation, that is nanoseconds to microseconds, the oil's velocity is negligible such that no effects of fluid convection are included in (3.1)-(3.5). q is the magnitude of electronic charge (1.602×10^{-19} C) and $\vec{E}$ is the local electric field. Table 3.1 summarizes the parameters and their respective values used for the streamer model in transformer oil.

The terms $G_p(|\vec{E}|)$, $G_n(|\vec{E}|)$, and $G_e(|\vec{E}|)$ model generalized positive ion, negative ion, and electron charge generation sources, respectively. Note a good consistency check of the model is that conservation of charge requires the sum of the right-hand sides of (3.2)-(3.4) must be zero. Therefore, the following equality must always be satisfied:

$$G_p(|\vec{E}|) + G_n(|\vec{E}|) + G_e(|\vec{E}|) = 0. \tag{3.6}$$

It is precisely the physics of these charge generation sources that will determine the mechanisms that occur in the bulk of the insulating liquid that lead to streamer formation. In Section 3.7, three main liquid bulk charge generation sources are discussed and formulated.

The electrodynamics are coupled to the oil's temperature through the $\vec{E} \cdot \vec{J}$ dissipation term in (3.5), where the dissipative conduction current density is

$$\vec{J} = (\rho_p \mu_p - \rho_n \mu_n - \rho_e \mu_e)\vec{E}. \tag{3.7}$$

This $\vec{E} \cdot \vec{J}$ term reflects the electrical power dissipation or Joule heating that takes place in the oil as a result of the motion of free charge carriers under the influence of the local electric field.

Table 3.1: Parameter Values for the Streamer Model in Transformer Oil

Parameter	Symbol	Value	References
Positive ion mobility	μ_p	1×10^{-9} $m^2V^{-1}s^{-1}$	[96]
Negative ion mobility	μ_n	1×10^{-9} $m^2V^{-1}s^{-1}$	[96]
Electron mobility	μ_e	1×10^{-4} $m^2V^{-1}s^{-1}$	[25,97,98]
Permittivity of free space	ϵ_0	8.854×10^{-12} F/m	
Relative permittivity of transformer oil	ϵ_r	2.2	
Thermal conductivity of transformer oil	k_T	$0.13\,Wm^{-1}K^{-1}$	
Specific heat of transformer oil	c_v	1.7×10^{3} $Jkg^{-1}K^{-1}$	
Mass density of transformer oil	ρ_l	$880\,kg/m^3$	
Ion-ion recombination rate	R_{pn}	1.64×10^{-17} m^3/s	[25,99,100]
Ion-electron recombination rate	R_{pe}	1.64×10^{-17} m^3/s	[25,101]
Electron attachment time	τ_a	2×10^{-7} s	[25,101]
Elementary charge	q	1.602×10^{-19} C	
Free electron mass	m_e	9.109×10^{-31} kg	

Due to the high field levels and accompanying large particle velocities, especially the electrons, the convection component of the flux strongly dominates over the diffusion component leading to instability in the numerical solver. Therefore, artificial streamline diffusion is employed in numerical modeling to avoid spurious oscillations in the solutions to the convection and diffusion equations (3.2)-(3.4) and assist in solver stability [102]. This is most important at the space charge fronts where there is a step change to zero ahead of each charge front. While there are other numerical methods to obtain more accurate solutions, such as the finite difference or finite element methods with flux-corrected transport technique [103], the use of artificial diffusion is adequate for transformer oil streamer modeling [104].

3.2 Needle-Sphere Geometry

Many studies of streamers in transformer oil are conducted under a non-uniform geometry such as needle-sphere or needle-plane electrode geometries. The non-uniform geometries generate a highly divergent Laplacian electric field distribution from modest voltages, thereby localizing all high field activity, such as streamer initiation, near the needle elec-

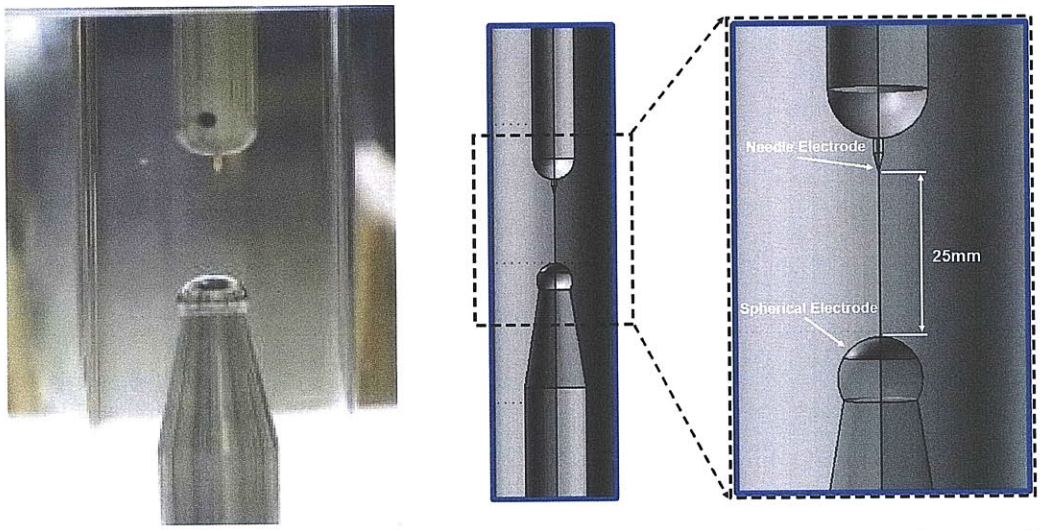

(a) Needle-sphere experimental setup at ABB Corporate Research, Västerås, Sweden. Courtesy of Rongsheng Liu.

(b) Computer-aided design representation of the needle-sphere electrode geometry used for streamer simulation purposes.

Figure 3.1: Needle-sphere electrode geometry system for which experimental tests at ABB and computer simulations at MIT are conducted to study pre-breakdown conditions for transformer oil in this thesis.

trode tip at early times. It is for these reasons that such geometries are used extensively in electrical breakdown and streamer studies, as the sharp needle electrode intensifies the electric field at the needle tip causing ionization that initiates streamers there. In these experiments, the streamer initiates at the high voltage needle electrode, where the electric field is greatest at early times, and propagates to the grounded spherical electrode.

Due to the strong coupling between field and transport equations, the hyperbolic nature of the continuity equations, and the non-uniform geometry, the mathematical model described by the set of equations (3.1)-(3.5) is solved numerically using the finite element software package COMSOL Multiphysics [54]. The setup corresponds to the needle-sphere electrode geometry as shown in Fig. 3.1 and detailed in the IEC 60897 standard [3]. The axial distance between the needle electrode's tip and the grounded spherical electrode is 25 mm. The radius of curvature of the needle electrode and spherical electrode are 40 μm and 6.35 mm, respectively. The applied voltage to the needle electrode is a step voltage. The electrothermal model equations (3.1)-(3.5) are solved in their two-dimensional form with axial symmetry (no ϕ dependence). Figure 3.2 shows the needle-sphere geometry in COMSOL Multiphysics.

Application of the 300 kV step voltage to the needle electrode creates a non-uniform Laplacian electric field distribution at $t=0^+$ with a large field enhancement near the sharp needle

tip as shown in the 2-D electric field magnitude spatial distribution plot of Fig. 3.3. Due to the non-uniform field enhancement near the needle tip, the main activity and dynamics of the electric field dependent charge generation and recombination terms on the right-hand sides of Eqs. (3.2)-(3.4) at times immediately after zero are localized in the needle tip region.

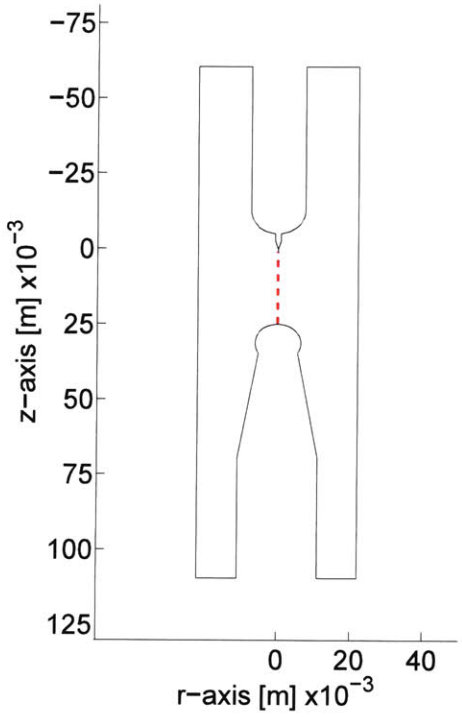

(a) Needle-sphere geometry in COMSOL Multiphyics. To aid in visualization and comparison to Fig. 3.1, the geometry, which is symmetric about the z-axis at $r = 0$, has been shown with its reflected half. The needle-sphere z-axis about which the geometry is symmetric has been indicated with a red dashed line.

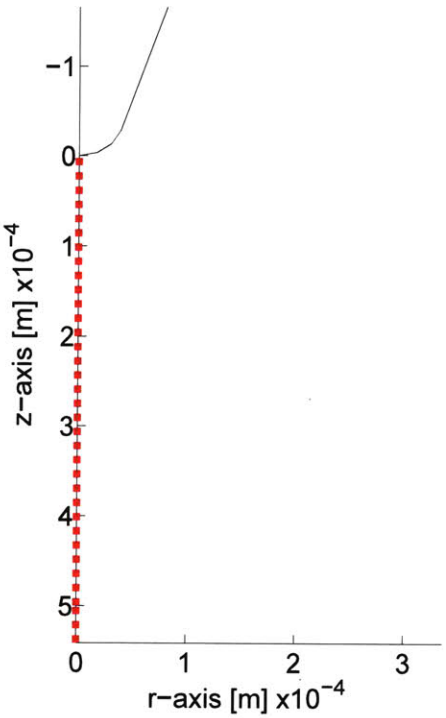

(b) A zoom-in of the high voltage needle electrode tip. Due to the sharp tip a high field enhancement will occur at the needle tip electrode at early times after the application of the high voltage.

Figure 3.2: Needle-sphere electrode geometry system in COMSOL Multiphysics. The needle-sphere z-axis about which the geometry is symmetric has been clearly indicated with a red dashed line. Throughout this work, line plots for various quantities, such as electric field magnitude, space charge density, and oil temperature, will be taken along the needle-sphere z-axis where $r = 0$.

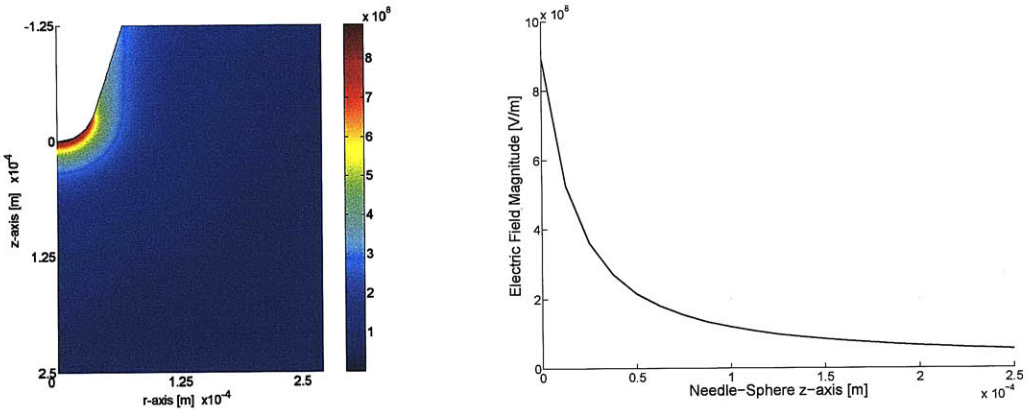

(a) Laplacian electric field magnitude spatial distribution

(b) Laplacian electric field magnitude line distribution along the needle-sphere z-axis.

Figure 3.3: (a) Laplacian electric field magnitude [V/m] distribution (*i.e.*, $\nabla\cdot(\epsilon\vec{E}) = 0$) at $t{=}0^+$ for 300 kV applied voltage near the 40 μm radius needle electrode apex at the origin. The sphere electrode (not shown) is at $r = 0$, $z = 25$ mm. (b) The field enhancement is largest near the sharp needle tip quickly decreasing as z increases.

3.3 Boundary Equations

The boundary conditions applied to the streamer model of Eqs. (3.1)-(3.5) are:

- Gauss' Law Eq. (3.1): The sharp needle electrode is set to a V_0 step voltage at $t{=}0$ with respect to the grounded large sphere. The symmetry z-axis and the top, bottom and side insulating walls have the boundary condition of zero normal electric field components (*i.e.*, $\vec{n}\cdot\vec{E} = 0$).

- Charge Transport Continuity Equations Eqs. (3.2)-(3.4): The boundary condition along the outer boundaries is zero normal flux ($\vec{n}\cdot\vec{J}_p = 0$, $\vec{n}\cdot\vec{J}_n = 0$, $\vec{n}\cdot\vec{J}_e = 0$). In addition, the boundary condition at the electrodes is zero diffusive flux ($\vec{n}\cdot\nabla\rho_p = 0$, $\vec{n}\cdot\nabla\rho_n = 0$, $\vec{n}\cdot\nabla\rho_e{=}0$) where only migration currents are permitted.

- Thermal Equation Eq. (3.5): All boundaries are set to zero normal thermal diffusive flux (*i.e.*, $\vec{n}\cdot\nabla T{=}0$) approximating the system to be adiabatic on the timescales of interest.

3.4 Charge Carrier Mobility

Transformer oil is not a pure liquid hydrocarbon, but is a mixture of many different naphthenic, paraffinic, and aromatic molecules with a complex molecular structure. It is this feature of transformer oil that makes it difficult to characterize many parameters, such as charge carrier mobility. The electron mobility in transformer oil, to the author's best knowledge, has not been well characterized. This is partially due to the reason stated above, as well as the varying sources, types, and distributors of transformer oil. In this work, an educated estimate has been made on the electron mobility in transformer oil based upon the logarithmic average of the electron mobility of common hydrocarbons. Generally, the electron velocity in these liquids are reported to range from 1×10^{-6} $m^2V^{-1}s^{-1}$ to 1×10^{-2} $m^2V^{-1}s^{-1}$ [97, 98]. Therefore, the electron velocity in transformer oil was chosen as 1×10^{-4} $m^2V^{-1}s^{-1}$ in this work.

A method to validate this choice for electron mobility in transformer oil is via the classical electron radius, known as the Lorentz radius [19]. The electron is modeled as a small uniformly charged spherical volume with charge density ρ_0 and radius R_e with total charge $q_e=4\pi R_e^3\rho_0/3$ within a medium with a dielectric permittivity ϵ. The total work needed to assemble the electron sphere is [19]

$$W=\frac{3q_e^2}{20\pi\epsilon R_e}. \tag{3.8}$$

Einstein's theory of relativity tells us that the work necessary to assemble the charge is stored as energy that is related to the mass as $W=m_ec^2$ where $c=1/\sqrt{\epsilon_0\mu_0}\approx3.0\times10^8$ m/s is the speed of light in free space and the dielectric permittivity ϵ_0 and magnetic permeability μ_0 are 8.854×10^{-12} F/m and $4\pi\times10^{-7}$ H/m, respectively. Equating the two expressions results in an expression for the electron radius as

$$R_e=\frac{3q_e^2}{20\pi\epsilon m_ec^2}. \tag{3.9}$$

For the case of an electron ($q_e=-q=-1.6\times10^{-19}$ C, $m_e=9.1\times10^{-31}$ kg) in transformer oil ($\epsilon=2.2\epsilon_0$), the radius is $R_e=7.66\times10^{-16}$ m. Now using Walden's rule [37] for a spherical particle, the electron mobility is

$$\mu_e=\frac{q}{6\pi\eta R_e}=5.5\times10^{-4}\ m^2V^{-1}s^{-1} \tag{3.10}$$

where $\eta=0.02$ Pa/s is a representative value for the viscosity of transformer oil. This result, based on classical methods, is close to the selected electron mobility, thereby confirming that the selection of $\mu_e=1\times10^{-4}$ $m^2V^{-1}s^{-1}$ is reasonable.

Regarding the positive ion and negative ion mobility values in transformer oil, the ion mobility values of $\mu_p = \mu_n = 1 \times 10^{-9}\,\mathrm{m^2V^{-1}s^{-1}}$ has been verified experimentally for transformer oil by Gäfvert *et al.* [96]. It is also in agreement with the analysis of Adamczewski [37].

3.5 Recombination

The Langevin-Debye relationship is used to model ion-ion R_{pn} and ion-electron R_{pe} recombination rates in the transformer oil [96,100]. According to the Langevin-Debye relationship, the recombination rates can be expressed as

$$R_{pn} = \frac{q(\mu_p + \mu_n)}{\epsilon}, \tag{3.11}$$

$$R_{pe} = \frac{q(\mu_p + \mu_e)}{\epsilon}. \tag{3.12}$$

The ion-electron recombination rate of Eq. (3.12) is overestimated because the Langevin-Debye relationship is diffusion limited and valid for situations where the electric field levels are low to moderate and the recombining species are of similar physical scale [100]. It has been shown that this recombination model overestimates the rate of ion-electron recombination in liquids at low to moderate electric field levels [105, 106]. To compensate for the reduction in the recombination cross-section caused by high electric field levels, some authors have used the Langevin-Debye recombination term for ion-ion recombination to model ion-electron recombination [25, 101]. This approach effectively compensates for the reduction in the recombination cross-section by reducing the apparent electron mobility. Using the respective value for each variable (*i.e.*, ion mobilities equal to $1\times10^{-9}\,\mathrm{m^2V^{-1}s^{-1}}$) the recombination rates are $R_{pn} = R_{pe} = 1.64\times10^{-17}\ \mathrm{m^3/s}$ [25].

3.6 Electron Attachment

In addition to recombination, electrons also combine with neutral molecules to form negative ions. This process is modeled as an electron attachment time constant. In very pure hydrocarbon liquids, energetic electrons have attenuation lengths on the order of several centimeters, meaning that an electron can be expected to travel for several centimeters in the liquid from the point where it was formed before it attaches to a neutral molecule to form a negative ion [100]. In commercial dielectric liquids, the attenuation length will be shorter due to higher levels of impurities in the liquid [25].

The attachment time constant is simply the quotient of the electron attenuation length and the electron velocity. A representative set of numbers for such a calculation are an electron attenuation length λ_a of 1 mm, an electron mobility μ_e of $1{\times}10^{-4}\,\mathrm{m^2V^{-1}s^{-1}}$ and an electric field strength $|\vec{E}|$, of 5×10^7 V/m. These numbers give an attachment time τ_a of:

$$\tau_a = \frac{\lambda_a}{\mu_e|\vec{E}|} = 2 \times 10^{-7}\,\mathrm{s} \tag{3.13}$$

which corresponds with values found in the literature [25, 101].

Although attachment undoubtedly takes place during streamer growth in dielectric liquids, its impact on the overall streamer propagation process is reasonably small due to the fact that attachment processes take place on a longer time scale than important dynamics such as the separation of positive ions and electrons in the ionization zone at a streamer's tip [25].

3.7 Charge Generation Mechanisms in the Liquid State

During streamer formation, the generation and movement of free charge carriers such as ions and electrons, in the dielectric liquid results in significant thermal dissipation, which leads to the liquid-to-gas phase change. Therefore, any attempt to understand streamer development in electrically stressed dielectric liquids must focus on uncovering the dominant charge generation mechanisms [25].

The complex nature and structure of liquids has inhibited the development of a comprehensive liquid state theory. Rather, scientists have derived models and understanding of the basic processes in liquids by utilizing theories from both the solid-state [107, 108] or compressed gas-state [26]. In regards to the modeling and understanding of pre-breakdown and breakdown phenomena in liquids, the modeling of the liquid as a compressed gas most often prevails with scientists taking concepts from gas discharge physics [109,110]. This inherently has to do with the development of a low-density gaseous-phase during streamer formation and the ease in which the transition between gas and liquid phases occurs with varying temperature and pressure [26]. However, streamers in liquids show several phenomenological similarities to electrical trees in solids and the comparison of liquids and amorphous solids has found some promising results [111–113]. Therefore, a study of streamer formation based solely upon considering the liquid as a solid or gas would be a narrow minded endeavor. Appropriately, three different mechanisms that find their origins from both solid-state and gas discharge theory and lead to an increase in the free charge carrier concentration in the liquid state when it is electrically over-stressed are discussed in detail. The mechanisms are:

- Electric field dependent molecular ionization (Field ionization)
- Impact ionization
- Photo-ionization

Field emission of electrons at a negatively stressed electrode, also known as Fowler-Nordheim charge injection, is neglected, as this study is restricted to fast positive streamers that propagate above the speed of sound (*i.e.*, ≈ 1.4 km/s in transformer oil). For an in depth study of the contribution of field emission to negative streamer initiation and propagation please refer to O'Sullivan [25]. In that work, O'Sullivan concluded that Fowler-Nordheim electron injection alone is unimportant for streamer development leading to electric breakdown.

Electric field enhanced ionic dissociation or the Onsager effect [114] is another charge generation mechanism hypothesized by researchers to drive streamer development. It is a process that occurs in a dielectric liquid whereupon neutral ion-pairs dissociate to form free positive and negative ions under an applied field. It has been used to describe electrical conduction in non-polar liquids such as transformer oil by several authors [96, 115, 116]. O'Sullivan *et al.* [25,51] showed that electric field enhanced ionic dissociation is also unlikely to be the key catalyst to streamer development in transformer oil because appreciable dissociation of ions and current density occur only in the region close to the high voltage electrode.

3.7.1 Field Ionization

Electric field dependent molecular ionization, also known as field ionization, is a direct ionization mechanism, where an extremely high electric field level results in the elevation of a valence band electron in a neutral molecule to the conduction band, thus generating both a free electron and positive ion. This differs from electric field dependent ionic dissociation where the dissociation of a neutral molecule produces a free negative ion and positive ion, which are both relatively large and immobile compared to electrons. For field ionization, the asymmetry in the generated carriers' mobility values leads to the formation of significant net space charge densities in electrically stressed dielectric liquids within the timescales associated with streamer initiation and growth.

Field ionization as a free charge carrier generation source in dielectric liquids, such as transformer oil, has often been discussed in the literature from a qualitative standpoint [11, 31,41,66,111,117]. In 1969, Halpern and Gomer [118] showed the existence of field ionization as a free charge carrier generation mechanism in cryogenic liquids. Their work spurred other researchers to experimentally validate field ionization in other insulating liquids [68,117,119, 120].

The development of a model that describes the process of field ionization in dielectric liquids, such as transformer oil, is challenging due to the lack of a comprehensive liquid-state theory. Consequently, the literature contains very few publications that propose liquid-phase field ionization models. The models that do exist are based on Zener's theory of electron tunneling in solids [121].

In their ground breaking work, Devins, Rzad, and Schwabe [11] applied the Zener model to dielectric liquids to explain streamer propagation. From their qualitative analysis they extrapolated that the rate of field ionization in a liquid is proportional to the liquid's density and inversely proportional to the ionization potential of the liquid molecule. In this work, the field ionization charge density generation rate source term is

$$G_F(|\vec{E}|) = \frac{q^2 n_0 a |\vec{E}|}{h} \exp\left(-\frac{\pi^2 m^* a \Delta^2}{q h^2 |\vec{E}|}\right), \tag{3.14}$$

which is also based upon the Zener model [121]. In Eq. (3.14), a is the molecular separation distance, h is Planck's constant, m^* is the effective electron mass, n_0 is the number density of ionizable species, and Δ is the ionization potential.

The major difficulty in trying to apply (3.14) to liquids is determining correct parameter values. For well characterized solids, the values of the above parameters are generally known. Conversely, many commonly used dielectric liquids, such as transformer oil, are comprised of numerous individual molecular species, each with unique number density, ionization potential, and mass, that have very complex molecular structures. Also, values for molecular separation, effective electron mass and ionization potential are often not known for molecules in the liquid-phase. Consequently, field ionization parameter values for a molecular species in the solid or gas-state are used or educated assumptions are made based upon known characteristics about the liquid-state and the chemical composition of the particular dielectric liquid of interest.

For example, a typical hydrocarbon liquid has a molecular number density on the order of $1{\times}10^{27}\,\mathrm{m}^{-3}$ to $1{\times}10^{28}\,\mathrm{m}^{-3}$ [26,64], of which only a small percentage is ionized. The molecular separation distance is strictly a solid-state concept and is difficult to find an analogous measure in liquids, however Qian *et al.* [101] state that the molecular separation of water is $3.0{\times}10^{-10}$ m. Also from solid-state physics, the effective electron mass can be assumed from well characterized semiconductor materials, where it generally ranges from $0.01{\times}m_e$ to m_e and $m_e = 9.11{\times}10^{-31}$ kg is the free electron mass. In nonpolar liquids, scientists have found that the effective electron mass can also be less than m_e [122, 123]. Lastly, the ionization potential of hydrocarbon liquids and gases primarily range from $9.6{\times}10^{-19}$ J to $1.92{\times}10^{-18}$ J (6 eV to 12 eV) [11, 61, 62, 97]. In commercial transformer oil there are two main groups of hydrocarbons, the trace aromatic molecules and the main high density naphthenic (or

paraffinic) molecules [63, 124]. Due to their chemical composition and structure, aromatic molecules generally have lower ionization potentials than naphthenic/paraffinic molecules making them easier to ionize [61, 62, 97]. However, due to the high number density of naphthenic/paraffinic molecules in transformer oil, if enough energy were to be supplied to ionize these molecules, and consequently the lower ionization potential aromatic molecules, greater amount of free charge would be produced by the naphthenic/paraffinic molecules.

The charge density generation rate terms in Eqs. (3.2)-(3.4) for a field ionization source are

$$G_p(|\vec{E}|) = -G_e(|\vec{E}|) = G_F(|\vec{E}|) \tag{3.15}$$

$$G_n(|\vec{E}|) = 0. \tag{3.16}$$

3.7.2 Impact Ionization

Impact ionization is a high field process in which inelastic collisions occur between neutral molecules and free electrons accelerated in the high electric field. The collisions energize a valence electron in the neutral molecule promoting it to the conduction band and generating a positive ion and another free electron [26,58,125]. For over a century impact ionization has been empirically shown to be a key mechanism that leads to breakdown in gases [109, 110]. It has also been used to explain breakdown in solids, however to a lesser extent [126].

As with field ionization, the experimental evidence for the occurrence of impact ionization in electrically stressed dielectric liquids is sparse. In the work by Dorenzo *et al.* [127], an electron multiplication via impact ionization was observed in liquid xenon. More recently, there has been work done in characterizing impact ionization in hydrocarbon liquids such as cyclohexane and propane [128]. Even with the sparse experimental evidence, most researchers studying streamers in liquids regard impact ionization as the key charge generation mechanism [34,101] due to the many phenomenological similarities between liquids and gases and the pressure-temperature relationship that often governs the transition between the two states.

Much of the theory about impact ionization and electron multiplication comes from gas-discharge physics. Consequently, the model for impact ionization charge generation in liquids is based upon Townsend's first coefficient α [26, 109] and has the form

$$\alpha = A_t \exp\left(\frac{-B_t}{|\vec{E}|}\right), \tag{3.17}$$

where A_t is the pre-exponential coefficient with units in [m^{-1}] and B_t is the exponential term in [V/m]. For many gases these ionization coefficients are well known but these values cannot be used for dense media like liquids [67] making it difficult to model impact ionization. In [128], experiments were conducted to determine impact ionization coefficients for cyclohexane and the values obtained via extrapolation were $A_t = 2.0 \times 10^8$ m^{-1} and $B_t = 3.0 \times 10^9$ V/m [129]. From (3.17), the impact ionization charge density rate source term is

$$G_T(|\vec{E}|) = A_t|\rho_e|\mu_e|\vec{E}| \exp\left(\frac{-B_t}{|\vec{E}|}\right). \tag{3.18}$$

The charge density generation rate terms in Eqs. (3.2)-(3.4) for an impact ionization source are

$$G_p(|\vec{E}|) = -G_e(|\vec{E}|) = G_T(|\vec{E}|) \tag{3.19}$$

$$G_n(|\vec{E}|) = 0. \tag{3.20}$$

3.7.3 Photo-ionization

The difficulty for many researchers with regards to impact ionization in liquids is determining where the seed electrons that initiate impact ionization and an electron avalanche come from. This is especially troubling when discussing fast traveling positive streamers, where secondary effects such as photo-emission and electron injection from the cathode are negligible or too slow compared to the timescales for streamer development.

Streamer propagation is closely linked to the space charge effects that cause local field enhancement within the liquid and the shielding of the applied electric field. As the local field enhancement continues to ionize the molecules within the liquid, the highly mobile electrons move towards the positive electrode advancing the area of net space charge and consequently the local field enhancement. Therefore, the movement of the ionizing field and streamer tip are dependent on the velocity at which electrons are swept out the region of ionization.

Electron drift velocity is a function of the electric field and at large field levels the velocity saturates. At field levels above 1×10^8 V/m electron velocities in liquid hydrocarbons can reach values found in gases (*i.e.*, 10 to 100 km/s) [26]. If streamer propagation is highly dependent on electron velocity then streamer velocities ranging from 10 to 100 km/s could be plausible. Several researchers have recorded positive streamer velocities exceeding 100 km/s [2, 13, 14, 21, 22, 130].

In gas discharge physics, where streamers of velocities exceeding 1000km/s are observed the dependency of streamer propagation on electron velocity is the same as in liquids. So how do positive streamers propagate at such high velocities in gases without secondary-emission feedback to the cathode? The answer is photo-ionization, where light emitted from the steamer tip ionizes a small amount of molecules ahead of the streamer to create free electrons that are swept into the advancing streamer tip and result in impact ionization [131].

In liquids, there is little or no empirical evidence of the existence of photo-ionization occurring during streamer development, however the propagation of streamers in dielectric liquids have always been linked with light emission [2, 26]. At higher applied field levels, the light emission tends to become brighter and more focalized at the streamer tip [14, 21] suggesting the possible existence of an efficient photo-ionization process occurring ahead of the streamer tip.

Photo-ionization is an extremely difficult phenomenon to model. Unlike field and impact-ionizations, photo-ionization is an irradiative phenomenon that couples all points in space at any time. Consequently, any numerical model of photo-ionization is extremely computationally demanding. Furthermore, for a realistic model to be developed, several parameters, such as absorption coefficient, absorption length, etc., need to be known [132]. Unfortunately, for many pure dielectric liquids, and especially for a heterogeneous mixture such as transformer oil, these parameters are unknown. As such, researchers studying gas-discharge physics via numerical models have used a background ionization method to simulate photo-ionization and this is also done for this work [132–135]. As an initial condition at time $t = 0$, there exists an equal density, N_0, of positive ions and electrons that is much smaller than those involved with streamer formation (*i.e.*, $> 1 \times 10^{19}$ m^{-3}). A number density between 1×10^{10} m^{-3} and 1×10^{14} m^{-3} is often used [132] such that it is several orders of magnitude less than the streamer density especially near the streamer tip. Likhanskii *et al.* [135] describe modeling photo-ionization via initial and background charge densities and perform an analysis on the effect of different density values on modeling plasma formation in air. They show that the density should be much lower (*i.e.*, by orders of magnitude) than that of the plasma density. The initial charge densities used for this work are

$$\rho_p(t = 0) = -\rho_e(t = 0) = qN_0, \tag{3.21}$$

where $N_0 = 1 \times 10^{14}$ m^{-3} is the initial free positive ion-electron density.

3.8 Conceptual Understanding of Field Ionization

The charge generation rate equations for both field and impact ionizations are extremely non-linear. While, the two ionization rate equations have similar forms (see Eq. (3.1) for field ionization and Eq. (3.18) for impact ionization) and the same dependence on the local electric field magnitude $|\vec{E}|$, the impact ionization rate equation has an added degree of complexity by being proportional to the local electron density, ρ_e. From a numerical simulation standpoint, the higher degree of non-linear coupling of impact ionization makes it more computationally demanding and under certain circumstances, more difficult to converge. Also, since the form of field and impact ionizations are similar, as stated above, this section will focus on the simpler field ionization rate term.

Generalizing the form of the field ionization rate term from (3.14) and lumping coefficient and exponential terms, it becomes

$$G_F = A_F(q|\vec{E}|)\exp\left(\frac{-B_F}{|\vec{E}|}\right). \tag{3.22}$$

Note the dependence of the charge generation rate G_F on the electric field magnitude $|\vec{E}|$. In Eq. (3.22), A_F and B_F are

$$A_F = \frac{qn_0a}{h}, \tag{3.23}$$

$$B_F = \frac{\pi^2 m^* a\Delta^2}{qh^2}. \tag{3.24}$$

Therefore, the term G_F has three components (*i.e.*, $q|\vec{E}|$, A_F, and B_F) that under closer examination give insight into the conceptual understanding of field ionization.

The component $q|\vec{E}|$ has the units of Newtons and is the force exerted on a unit charge due to the local electric field. Since field ionization is a direct ionization mechanism that works on neutral molecules in the presence of this local electric field, the $q|\vec{E}|$ term is proportional to the force acted upon each molecule.

The A_F term in G_F has the units of charge density per second per Newton, that is $[\mathrm{Cm^{-3}s^{-1}N^{-1}}]$. This term is a charge density rate per force. Therefore, multiplying $(q|\vec{E}|)$ by A_F is effectively modulating the generation rate of charge density by the electric field force.

Examining the constituents of A_F in (3.23), it depends on the two variables: n_0, the density of ionizable species and a, the molecular separation distance. A_F is proportional to both

n_0 and a, such that by increasing the density or separation distance effectively increases the charge density generation rate. This relation makes intuitive sense for the density of ionizable species n_0, that is increasing the density allows for more molecules to be ionized given a high enough electric field. Hence, a higher charge generation rate results. However, the same intuitive understanding cannot be said for the molecular separation distance a. How can increasing the distance between two molecules increase the charge generation? Furthermore, this is in disagreement with the previous qualitative discussion where the charge generation rate increases by increasing the number density of ionizable species, which would result in increasing the number of molecules per unit volume by decreasing the relative distance between each molecule. To resolve this conflicting nature of a we have to examine how the exponential term B_F affects the charge generation rate G_F.

The exponent $\exp(-B_F/|\vec{E}|)$ of (3.22) takes on values between 0 and 1 depending on the value of the electric field magnitude $|\vec{E}|$ compared to B_F. Put differently, the ratio of B_F to $|\vec{E}|$ is of the utmost importance because small variations in the ratio can have orders of magnitude difference on the overall exponential value. Therefore, the exponent term is like a switch that turns on or off field ionization and it dominates over A_F and $(q|\vec{E}|)$ terms, which only affect G_F linearly. While switches are often controlled manually, this field ionization switch is controlled by the value of B_F, such that the switch turns on (*i.e.*, the exponent has an appreciable value between 0.1 and 1) when the electric field magnitude $|\vec{E}|$ is approximately equal to or greater than B_F (*i.e.*, $|\vec{E}| \gtrsim B_F$); Otherwise the switch is off since the $\exp(-B_F/|\vec{E}|) \ll 1$ for $|\vec{E}| \ll B_F$, which results in a small G_F.

Investigating the variables that comprise B_F in (3.24), they are the molecular separation distance a, the ionization potential Δ, and the effective electron mass m^*. B_F is proportional to all three variables. Considering a constant electric field magnitude $|\vec{E}|$, then by increasing a, Δ, and m^* even slightly (*e.g.*, less than an order of magnitude), the charge generation rate G_F will decrease considerably because of the non-linear nature of $\exp(-B_F/|\vec{E}|)$. Therefore, increasing the molecular separation distance a, otherwise known as decreasing the packing factor of dielectric liquid, truly decreases the ionization rate since the exponent term dominates over the pre-exponential coefficient A_F in G_F.

The two previous observations, where increasing the number density and decreasing the separation distance increases the charge generation rate and ultimately streamer development, have been theorized and observed by Schütte [136]. The observations give general guidelines for engineering and analyzing dielectric liquids, such that they have good electrical insulation characteristics.

Regarding the role of ionization potential in B_F on the charge generation rate G_F, it should not come as a surprise that with increased ionization potential the charge generation rate

would decrease. The higher the ionization potential, the more energy that is required to ionize the liquid and create free charge. Therefore, one criteria for a good electrically insulating dielectric liquid is that it be comprised of molecules with high ionization potential to increase the over-voltage at which considerable volume of molecules ionize and generate free charge that leads to streamer development.

Chapter 4

On the Development of Positive Streamers and Their Distinct Propagation Modes in Transformer Oil

---

DUE TO the complex nature of liquids, a singular universal law that explains streamer formation in dielectric liquids does not exist. But the same is often true for the simplest phenomenon, such that a single law or mechanism that governs any physical event is often an oversimplification. Rather, laws are only obeyed within operating limits and as the conditions pass these limits, then another law dominates. The results presented in this chapter indicate that the same truism holds for streamer development. This chapter investigates the underlying mechanisms that drive streamer propagation in transformer oil and lead to the different streamer propagation modes that are discussed in Section 2.1.1.

4.1 Comparing 2^{nd} and 3^{rd} Mode Streamers

In commercial transformer oil there are two main groups of hydrocarbons, the trace aromatic molecules and the main high density naphthenic (or paraffinic) molecules [63, 124]. Due to their chemical composition and structure, aromatic molecules generally have lower ionization potentials than naphthenic/paraffinic molecules, making them easier to ionize [61,62,97]. However, due to the high number density of naphthenic/paraffinic molecules in transformer oil, if enough energy were to be supplied to ionize these molecules a greater amount of free charge would be produced by the naphthenic/paraffinic molecules. Therefore, it would be of interest to individually model and simulate the following two types of oil molecules:

1. Aromatic molecules with low ionization potential and low number density
2. Naphthenic/paraffinic molecules with high ionization potential and high number density

to study the conditions and effects of charge generation from ionization due to each molecule type.

Previously it was shown that field ionization of low number density and low ionization potential impurity molecules is the key mechanism for 2nd mode positive streamer development in transformer oil [25,53]. By ionizing the low number density and low ionization potential impurity molecules into slow positive ions and fast electrons, an area of net positive space charge quickly develops because the highly mobile electrons are swept back to the positive electrode from the ionization zone leaving behind the low mobility positive ions. The net homocharge modifies the electric field distribution in the oil, such that the electric field at the positive electrode decreases while the electric field ahead of the positive charge in the oil increases. The new field distribution leads to ionization of more impurity molecules occurring further away from the positive electrode, which in turn causes further modification of the electric field distribution. The ultimate result of this electrodynamic process is the development of an ionizing electric field wave, which is a moving dissipative source that raises the temperature to vaporize transformer oil and create a gas phase. This oil vaporization leads to the formation of the low mass density streamer channel in transformer oil.

For convenience, the field ionization source term of Eq. (3.14) is re-written here:

$$G_F(|\vec{E}|) = \frac{q^2 n_0 a |\vec{E}|}{h} \exp\left(-\frac{\pi^2 m^* a \Delta^2}{q h^2 |\vec{E}|}\right), \tag{4.1}$$

where h is Planck's constant, a is the molecular separation distance, m^* is the effective electron mass, n_0 is the number density of ionizable species, and Δ is the liquid-phase ionization potential.

Biller theorized that fast 3rd mode streamers result from ionizing the main high number density liquid molecules, which are naphthenic and paraffinic molecules in transformer oils, generating more space charge [42]. Consequently, the large space charge, produced from ionizing the high number density naphthenic/paraffinic molecules, generates an extremely high electric field which continues the ionization of the same molecules further into the liquid. This results in an efficient streamer propagation due to a higher field ionization rate G_F. Also, researchers have hypothesized that the underlying mechanism that drives 2nd and 3rd mode streamers is comparable due to the similar streamer characteristics between the two modes [21]. Therefore, applying these assumptions to (4.1) would result in the following two constraints

$$n_{0\,\text{aromatic}} \ll n_{0\,\text{naphthenic/paraffinic}}, \tag{4.2}$$

$$\Delta_{\text{aromatic}} < \Delta_{\text{naphthenic/paraffinic}}. \tag{4.3}$$

The major difficulty in trying to apply (4.1) to transformer oil is determining correct parameter values. Transformer oil is comprised of numerous individual molecular species, each with unique number density, ionization potential, and mass, that have very complex molecular structures. Also, values for molecular separation and effective electron mass are not well known for molecules in the liquid-state. In these cases educated assumptions are made based upon known liquid-state characteristics and the chemical composition of transformer oil.

For example, a typical hydrocarbon liquid has a molecular number density on the order of $1{\times}10^{27}\mathrm{m}^{-3}$ to $1{\times}10^{28}\mathrm{m}^{-3}$ [64], of which only a small percentage is ionized [42]. The molecular separation distance is strictly a solid-state concept and is difficult to find an analogous measure in liquids, however Qian *et al.* [101] state that the molecular separation of water is 3.0×10^{-10} m. The effective electron mass in several nonpolar liquids has been found to range from $0.1{\times}m_e$ to m_e, where $m_e{=}9.11{\times}10^{-31}$ kg is the free electron mass [122]. Lastly, the ionization potential of hydrocarbon liquids and gases primarily range from $9.6{\times}10^{-19}$ J to 1.92×10^{-18} J (6 eV to 12 eV) [61, 62].

In this work the field ionization parameters for aromatic and naphthenic /paraffinic molecules used in this study are summarized in Tables 4.1 and 4.2, respectively, where the effective electron mass and molecular separation distance were chosen to be the same for both types.

The governing equations of the three charge carrier continuum model are

$$\nabla\cdot(\epsilon_r\epsilon_0\vec{E}) = \rho_p+\rho_n+\rho_e \tag{4.4}$$

$$\frac{\partial\rho_p}{\partial t}+\nabla\cdot(\rho_p\mu_p\vec{E}) = G_F(|\vec{E}|)+\frac{\rho_p\rho_eR_{pe}}{q}+\frac{\rho_p\rho_nR_{pn}}{q} \tag{4.5}$$

$$\frac{\partial\rho_n}{\partial t}-\nabla\cdot(\rho_n\mu_n\vec{E}) = \frac{\rho_e}{\tau_a}-\frac{\rho_p\rho_nR_{pn}}{q} \tag{4.6}$$

$$\frac{\partial\rho_e}{\partial t}-\nabla\cdot(\rho_e\mu_e\vec{E}) = -G_F(|\vec{E}|)-\frac{\rho_p\rho_eR_{pe}}{q}-\frac{\rho_e}{\tau_a} \tag{4.7}$$

$$\frac{\partial T}{\partial t}+\vec{v}\cdot\nabla T = \frac{1}{\rho_lc_v}(k_T\nabla^2T+\vec{E}\cdot\vec{J}\,). \tag{4.8}$$

A detailed discussion of the model and parameters can be found in Chapter 3.

Table 4.1: Parameter Values for Low Number Density, Low Ionization Potential Aromatic Molecules

Parameter	Symbol	Value	Reference
Number density	n_0	1×10^{23} m^{-3}	[42,63,64,124]
Ionization potential	Δ	9.92×10^{-19} J (6.20 eV)	[61,62]
Molecular separation	a	3.0×10^{-10} m	[25,101]
Effective electron mass	m^*	$0.1\times m_e = 9.11\times10^{-32}$ kg	[122,123]

Table 4.2: Parameter Values for High Number Density, High Ionization Potential Naphthenic/Paraffinic Molecules

Parameter	Symbol	Value	Reference
Number density	n_0	1×10^{25} m^{-3}	[42,63,64,124]
Ionization potential	Δ	1.58×10^{-18} J (9.86 eV)	[61,62]
Molecular separation	a	3.0×10^{-10} m	[25,101]
Effective electron mass	m^*	$0.1\times m_e = 9.11\times10^{-32}$ kg	[122,123]

4.2 Slow 2nd Mode Streamers: Field Ionization of Aromatic Molecules

This section details the results for the field ionization of aromatic hydrocarbon molecules, which have a low number density and low ionization potential as modeled by the parameters in Table 4.1.

4.2.1 $V_{app} = 130$ kV – Figures 4.1 and 4.2

The numerical results to the streamer model of (4.4)-(4.8) for the field ionization mechanism of (4.1) with parameter values corresponding to aromatic hydrocarbon molecules in Table 4.1 are presented in this section. The applied voltage to the needle electrode is $V_{app} = 130$ kV. In Fig. 4.1, the electric field, net space charge density, and temperature profile distributions along the needle-sphere z-axis are shown at several instances in time.

In Fig. 4.2, the rz-plane spatial distribution of the electric field magnitude at the same time instances are shown.

Figures 4.1(a) and 4.1(b) show significant temporal dynamics in the electric field and space charge density distributions with peaks in the profile distributions occurring further out in the oil volume, away from the positive applied voltage at the sharp needle electrode, as time progresses. Field ionization produces positive ions and electrons in the oil that travel in opposite directions, with the positive ions and electrons attracted to the grounded electrode and positively excited needle electrode, respectively. However, due to the relatively high mobility of the electrons ($\mu_e = 1 \times 10^{-4}\ \mathrm{m^2V^{-1}s^{-1}}$) compared to the large positive ions ($\mu_p = 1 \times 10^{-9}\ \mathrm{m^2V^{-1}s^{-1}}$), the newly generated electrons quickly exit the high field ionization zone towards the anode leading to the development of a net positive space charge peak as shown in Fig. 4.1(b) at several different times.

The peaks in space charge density distribution are a source of electric field. It is the superposition of the space charge and the Laplacian electric fields that generate a total electric field with a field enhancement (Fig. 4.1(a)) at the space charge peak (Fig. 4.1(b)) such that field ionization continues further into the oil driving streamer propagation. The maximum of the electric field peak in the oil is approximately $3.5 \times 10^8\ \mathrm{V/m}$. The movement of the free charge generated by field ionization due to the electric field contributes to Joule heating that increases the temperature in the highly stressed oil (Fig. 4.1(c)). The results reveal that field ionization of low number density aromatic hydrocarbon molecules is a key contributor to the development and propagation of positive streamers in transformer oil.

In addition to examining temporal dynamics along the needle-sphere z-axis, the spatial distribution of the electric field magnitude gives insight into streamer physics. From Fig. 4.2(a), at early times the electric field enhancement is localized near the sharp needle electrode due to the applied voltage. As time progresses an extremely large field enhancement occurs further out in the oil (Fig. 4.2(b)). At even later times the electric field distribution shows a cylindrical-like streamer that is adjacent to the z-axis (Figs. 4.2(c), 4.2(d), 4.2(e)). The cylindrical streamer is enveloped by a field enhancement at the cylinder's boundary, with the greatest enhancement occurring at the streamer tip that is furthest away from the needle electrode. This point of greatest field enhancement is exactly the largest electric field peak in Fig. 4.1(a).

By approximating the dimensions of the streamer to be equal to the volume enclosed by the electric field enhancement envelope, the radius of the streamer near the field enhanced streamer tip is $5 - 10\ \mu\mathrm{m}$. The average streamer velocity, as it travels along the z-axis, is $3.0\ \mathrm{km/s}$ after 100 ns.

4.2.2 $V_{app} = 200\,\mathbf{kV}$ – Figures 4.3 and 4.4

The numerical results to the streamer model of (4.4)-(4.8) for the field ionization mechanism of (4.1) with parameter values corresponding to aromatic hydrocarbon molecules in Table 4.1 are presented in this section. The applied voltage to the needle electrode is $V_{app} = 200$ kV. In Fig. 4.3, the electric field, net space charge density, and temperature profile distributions along the needle-sphere z-axis are shown at several instances in time. In Fig. 4.4, the rz-plane spatial distribution of the electric field magnitude at the same time instances are shown.

The application of a $V_{app} = 200$ kV step voltage leads to more ionization of the low number density, low ionization potential molecules, however the ionization region is much more dispersed with considerable growth in the radial r-direction (Fig. 4.4). As such, the peak space charge level along the z-axis (Fig. 4.3(b)) is smaller compared to the $V_{app} = 130$kV case (Fig. 4.1(b)), but due to the sizeable radial growth of the streamer, there is comparable or greater overall space charge. The dispersive streamer structure and its space charge results in lower electric field peak levels that are also more smeared out (Fig. 4.3(a)) compared to the $V_{app} = 130$ kV case. Also, the oil temperature is lower along the z-axis (Fig. 4.3(c)) as a result of lower space charge along the z-axis.

Generally, the higher applied voltage allows for space charge generation further out into the oil in the radial r-direction, such that the charge is not confined only to a region close to the z-axis, and creates a more branched or dispersive streamer structure. Consequently, the streamer geometry is more uniform and less extreme, which produces electric field levels, especially at the streamer tip, that are not as large. This regulates the field-dependent ionization mechanism at the streamer tip and overall streamer growth to the cathode. In contrast, for the $V_{app} = 130$ kV case the majority of charge generation occurs along or close to the z-axis creating a more non-uniform streamer structure. This results in field levels that are slightly higher and streamer growth that is comparable to the $V_{app} = 200$ kV case even though the drive voltage is less.

4.2.3 $V_{app} = 300\,\mathbf{kV}$ – Figures 4.5 and 4.6

The numerical results to the streamer model of (4.4)-(4.8) for the field ionization mechanism of (4.1) with parameter values corresponding to aromatic hydrocarbon molecules in Table 4.1 are presented in this section. The applied voltage to the needle electrode is $V_{app} = 300$ kV. In Fig. 4.5, the electric field, net space charge density, and temperature profile distributions along the needle-sphere z-axis are shown at several instances in time.

In Fig. 4.6, the rz-plane spatial distribution of the electric field magnitude at the same time instances are shown.

Applying $V_{app} = 300$ kV to the low number density, easily ionizable molecules results in streamer growth with similar attributes to the $V_{app} = 200$ kV case. Particularly, the higher applied voltage allows for ionization of a larger volume of oil thereby creating space charge and a streamer that is more dispersed. This diffuse space charge distribution results in a lower field enhancement level at the streamer tip, which regulates streamer growth to have velocities that are characteristic of 2^{nd} mode streamers.

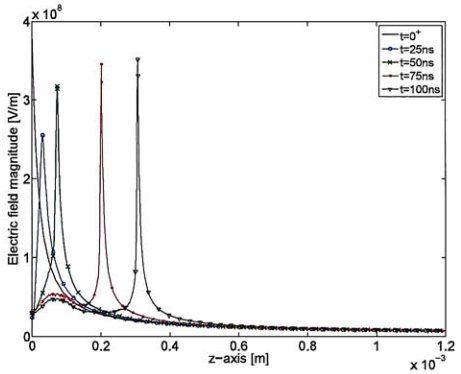

(a) Electric field magnitude distribution

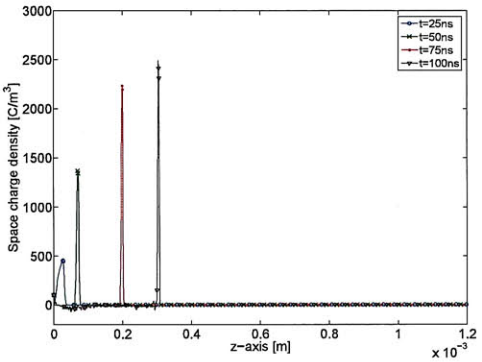

(b) Net space charge density distribution

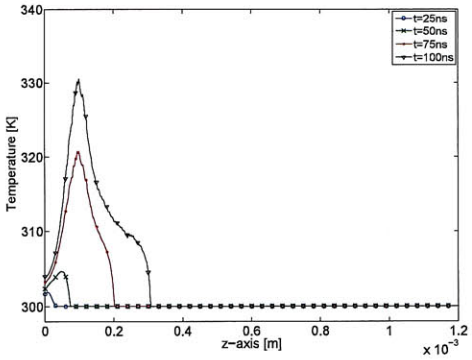

(c) Oil temperature distribution

Figure 4.1: Temporal dynamics along the needle-sphere electrode axis at 25 ns intervals from $t=25-100$ ns given by the solution to the streamer model of (4.4)-(4.8) for an applied voltage of $V_{app}=130$ kV and the field ionization mechanism of (4.1). The oil is comprised of low number density, low ionization potential aromatic hydrocarbon molecules only with parameter values summarized in Table 4.1. Note, at time $t=0^+$ the electric field represents the Laplacian electric field and the oil temperature is 300 K.

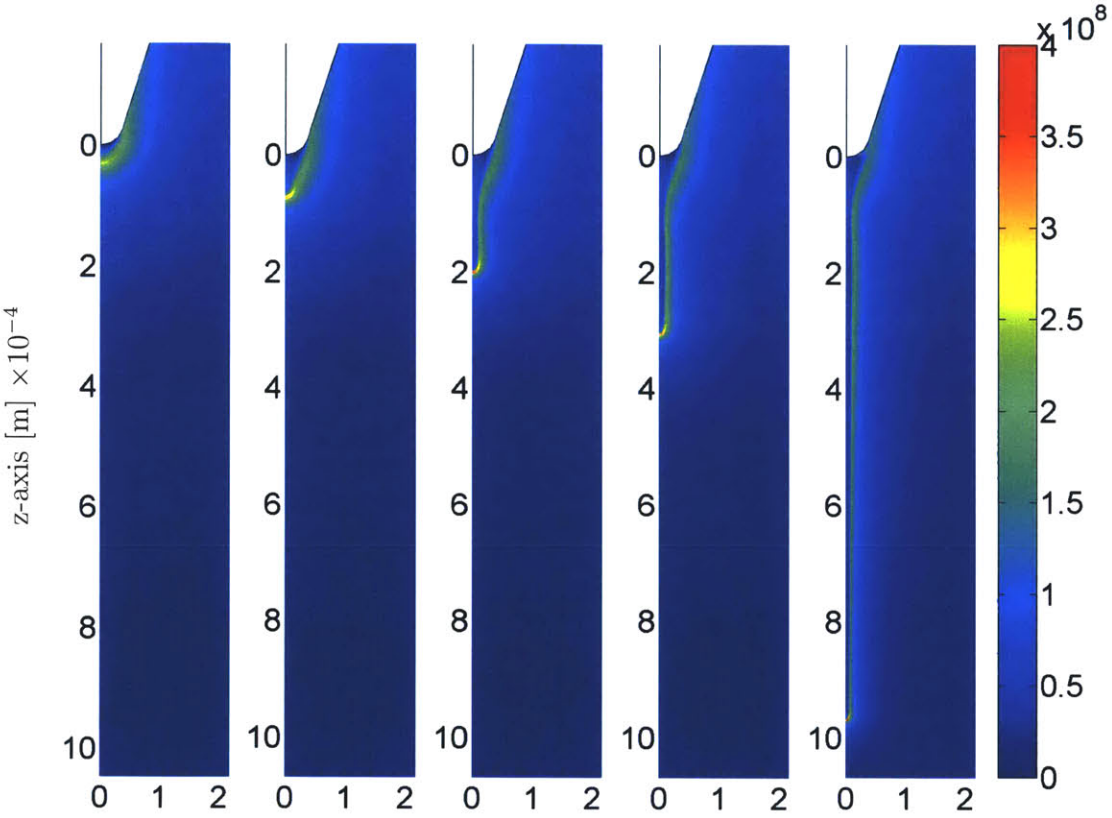

(a) $t = 25$ ns (b) $t = 50$ ns (c) $t = 75$ ns (d) $t = 100$ ns (e) $t = 325$ ns

igure 4.2: Electric field magnitude [V/m] spatial distributions (as a function of r and z in the electrode geometry) from $= 25 - 325$ ns given by the solution to the streamer model of (4.4)-(4.8) for an applied voltage of $V_{app} = 130$ kV and the field onization mechanism of (4.1). The oil is comprised of low number density, low ionization potential aromatic hydrocarbon olecules only with parameter values summarized in Table 4.1.

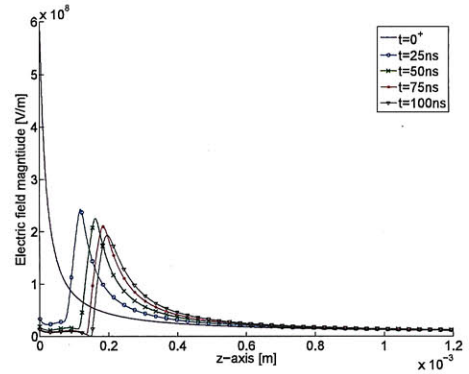

(a) Electric field magnitude distribution

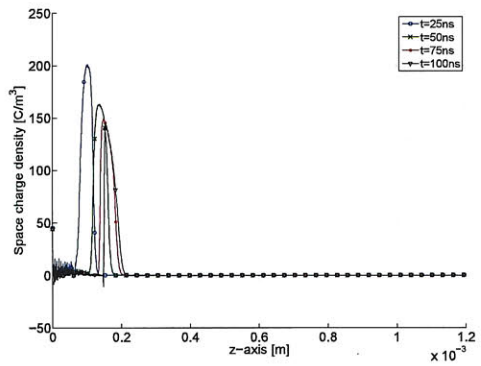

(b) Net space charge density distribution

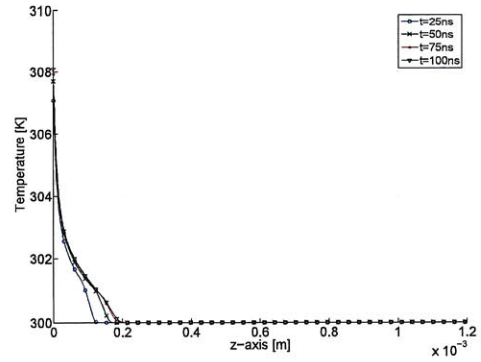

(c) Oil temperature distribution

Figure 4.3: Temporal dynamics along the needle-sphere electrode axis at 25 ns intervals from $t=25-100$ ns given by the solution to the streamer model of (4.4)-(4.8) for an applied voltage of $V_{app}=200$ kV and the field ionization mechanism of (4.1). The oil is comprised of low number density, low ionization potential aromatic hydrocarbon molecules only with parameter values summarized in Table 4.1. Note, at time $t=0^+$ the electric field represents the Laplacian electric field and the oil temperature is 300 K.

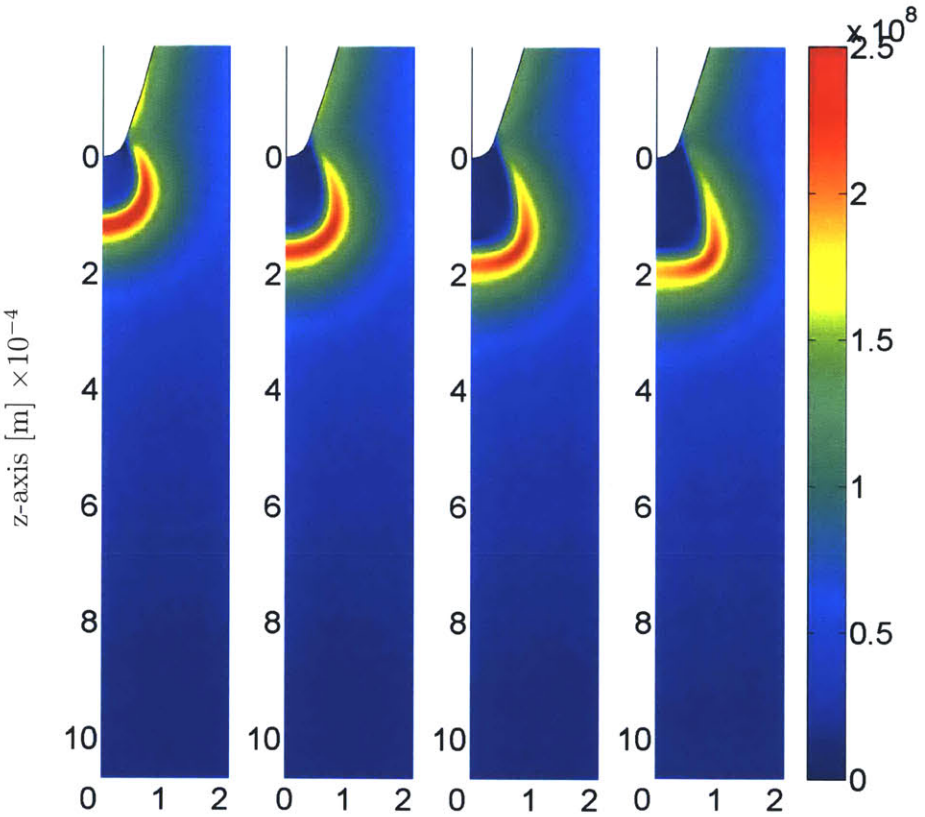

(a) $t = 25$ ns (b) $t = 50$ ns (c) $t = 75$ ns (d) $t = 100$ ns

igure 4.4: Electric field magnitude [V/m] spatial distributions (as a function of r and z in the electrode geometry) from $= 25 - 100$ ns given by the solution to the streamer model of (4.4)-(4.8) for an applied voltage of $V_{app} = 200$ kV and the field ɔnization mechanism of (4.1). The oil is comprised of low number density, low ionization potential aromatic hydrocarbon ıolecules only with parameter values summarized in Table 4.1.

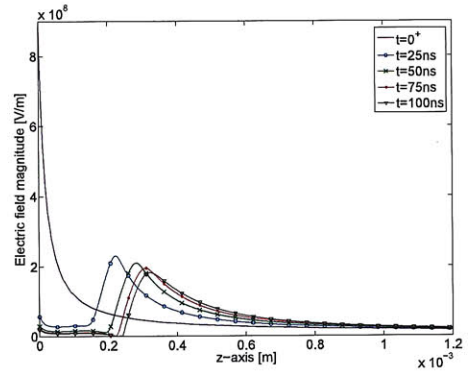

(a) Electric field magnitude distribution

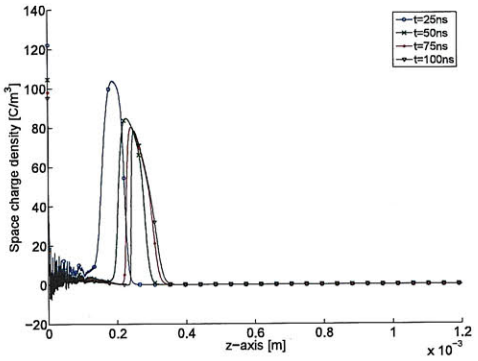

(b) Net space charge density distribution

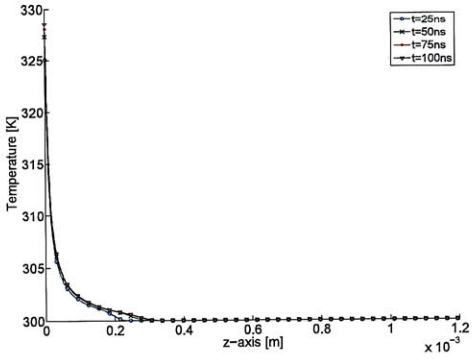

(c) Oil temperature distribution

Figure 4.5: Temporal dynamics along the needle-sphere electrode axis at 25 ns intervals from $t=25-100\,\text{ns}$ given by the solution to the streamer model of (4.4)-(4.8) for an applied voltage of $V_{app}=300\,\text{kV}$ and the field ionization mechanism of (4.1). The oil is comprised of low number density, low ionization potential aromatic hydrocarbon molecules only with parameter values summarized in Table 4.1. Note, at time $t=0^+$ the electric field represents the Laplacian electric field and the oil temperature is 300 K.

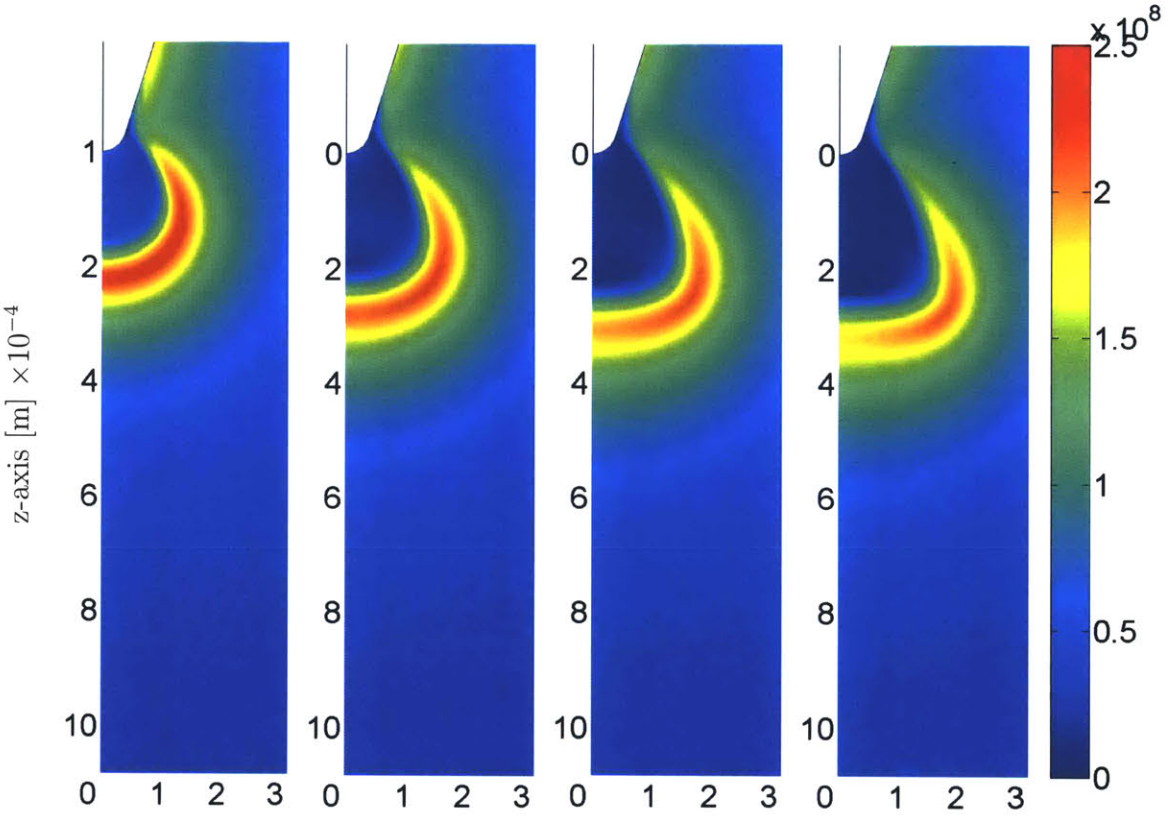

(a) $t = 25$ ns (b) $t = 50$ ns (c) $t = 75$ ns (d) $t = 100$ ns

igure 4.6: Electric field magnitude [V/m] spatial distributions (as a function of r and z in the electrode geometry) from $= 25 - 100$ ns given by the solution to the streamer model of (4.4)-(4.8) for an applied voltage of $V_{app} = 300$ kV and the field nization mechanism of (4.1). The oil is comprised of low number density, low ionization potential aromatic hydrocarbon olecules only with parameter values summarized in Table 4.1.

4.3 Fast 3rd Mode Streamers: Field Ionization of Naphthenic /Paraffinic Molecules

This section details the results to the field ionization of naphthenic/paraffinic hydrocarbon molecules, which have a high number density and high ionization potential as modeled by the parameters in Table 4.2.

4.3.1 $V_{app} = 130\,\mathbf{kV}$ – Figures 4.7 and 4.8

The numerical results to the streamer model of (4.4)-(4.8) for the field ionization mechanism of (4.1) with parameter values corresponding to naphthenic/paraffinic hydrocarbon molecules in Table 4.2 are presented in this section. The applied voltage to the needle electrode is $V_{app}=130$ kV. In Fig. 4.7, the electric field, net space charge density, and temperature profile distributions along the needle-sphere z-axis are shown at several instances in time. In Fig. 4.8, the rz-plane spatial distribution of the electric field magnitude at the same time instances are shown.

Applying a step voltage to the needle electrode of $V_{app} = 130$ kV results in no streamer formation. Figure 4.7(c) shows that there is no or little ionization of high number density, high ionization potential molecules. As a result of the absence of space charge in the oil, the electric field distribution at times $t>0$ is identical to the Laplacian electric field (Figs. 4.7(a) and 4.8). Furthermore, due to the lack of charge motion in the presence of the electric field there is no Joule heating and the oil temperature is not raised above 300 K (Fig. 4.7(e)). Figure 4.8 clearly shows the lack of streamer formation at times after the application of $V_{app} = 130$ kV step voltage. The field enhancement is always at the needle tip, as in the Laplacian case at $t=0^+$.

4.3.2 $V_{app} = 200\,\mathbf{kV}$ – Figures 4.9 and 4.10

The numerical results to the streamer model of (4.4)-(4.8) for the field ionization mechanism of (4.1) with parameter values corresponding to naphthenic/paraffinic hydrocarbon molecules in Table 4.2 are presented in this section. The applied voltage to the needle electrode is $V_{app}=200$ kV. In Fig. 4.9, the electric field, net space charge density, and temperature profile distributions along the needle-sphere z-axis are shown at several instances in time. In Fig. 4.10, the rz-plane spatial distribution of the electric field magnitude at the same time instances are shown.

The application of a $V_{app} = 200$ kV step voltage leads to low level ionization of the high number density, high ionization potential molecules (Fig. 4.9(c)). The lack of significant charge generation, even at late times (*i.e.*, $t = 100$ ns), at this applied voltage level results in electric field distribution that is nearly identical to the Laplacian electric field. However, the field enhancement peak is slightly removed from the needle electrode into the oil bulk (Fig. 4.9(d)). Due to the low drive voltage, as time progresses the creation of space charge begins to decline and subsequently the electric field peak decreases as it travels further out into the oil bulk. The confinement of space charge generation and the electric field peak near to the needle electrode leads to low level heating of the oil in that area (Fig. 4.9(f)). The level of heating is only several degrees, such that boiling or vaporization of the oil to create a low mass density streamer is not possible. Looking at the results from the spatial electric field distribution in Fig. 4.10, there is no streamer formation and the electric field peak occurs at or very near to the needle electrode for all times.

4.3.3 $V_{app} = 300$ kV – Figures 4.11 and 4.12

The numerical results to the streamer model of (4.4)-(4.8) for the field ionization mechanism of (4.1) with parameter values corresponding to naphthenic/paraffinic hydrocarbon molecules in Table 4.2 are presented in this section. The applied voltage to the needle electrode is $V_{app} = 300$ kV. In Fig. 4.11, the electric field, net space charge density, and temperature profile distributions along the needle-sphere z-axis are shown at several instances in time. In Fig. 4.12, the rz-plane spatial distribution of the electric field magnitude at the same time instances are shown.

The macroscopic streamer results for the naphthenic/paraffinic molecules are similar to the aromatic hydrocarbon case in Section 4.2. In particular, the generation of free positive ions and electrons due to field ionization of naphthenic/paraffinic oil molecules leads to significant temporal dynamics in the electric field and space charge (Figs. 4.11(a) and 4.11(b)). Field ionization causes electric field and space charge enhancements to develop in the oil volume further away from the needle electrode as time progresses. The movement of the free charges in the presence of an electric field leads to substantial Joule heating that raises the oil temperature greatly above the nominal 300 K room temperature (Fig. 4.11(c)). As in the case of aromatic hydrocarbon molecules, the results indicate that field ionization of high number density naphthenic/paraffinic hydrocarbon molecules is a key contributor to the development and propagation of positive streamers in transformer oil.

While the qualitative results are similar for aromatic molecules (Section 4.2) and naphthenic/paraffinic molecules, on closer inspection the two cases differ considerably quantitatively (*i.e.*, electric field, space charge density, and temperature values). For example, the

maximum electric field enhancement in the oil is approximately 8×10^8 V/m which is more than double that for the aromatic molecules of Section 4.2. Generally, there is a significant increase in both the space charge density and temperature enhancement for the streamers resulting from the ionization of higher number density naphthenic/paraffinic oil molecules. The higher field level is partially due to the application of a high 300 kV step voltage, however it is also strongly related to the significantly greater space charge levels. The higher applied voltage is required to ionize naphthenic/paraffinic molecules due to their increased ionization potential (6.2 eV) compared to their aromatic (9.86 eV) counterparts (Table 4.2). The increased temperature enhancement is a result of the movement of the greater free charge levels within the electric field.

From the spatial distribution of the electric field (Fig. 4.12) the electric field enhancement is localized near the sharp needle electrode at early times and at later times an extremely large field enhancement occurs further out in the oil. Unlike the aromatic molecules case, the electric field distribution for the ionization of the high density naphthenic/paraffinic hydrocarbon molecules shows a conical-like streamer that is adjacent to the z-axis. The conical streamer is enveloped by a field enhancement at the the cone's boundary, with the greatest enhancement at the streamer tip that is furthest away from the needle electrode. This point of greatest field enhancement is exactly the electric field peak in Fig. 4.11(a).

Approximating the dimensions of the streamer to be equal to the volume enclosed by the electric field enhancement, the radius of the streamer channel near the field enhanced streamer tip is approximately 2.0 μm. Interestingly, the streamer at times after $t=50$ ns has protrusions from the main streamer body that are indicative of streamer branching. The average streamer velocity, as it travels along the z-axis, is 9.5 km/s after 100 ns.

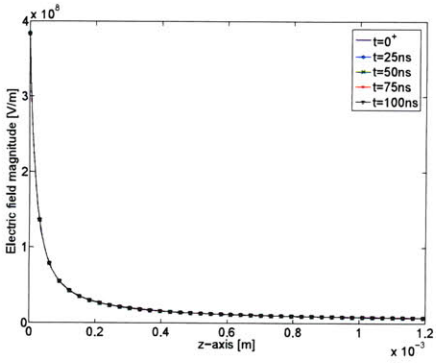

(a) Electric field magnitude distribution

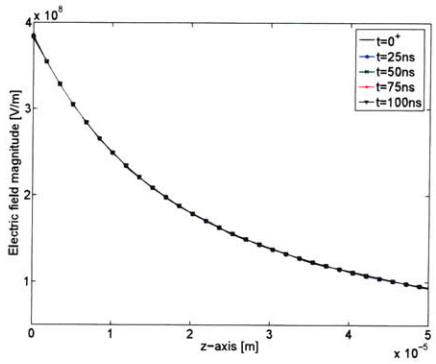

(b) Electric field magnitude distribution near the needle tip

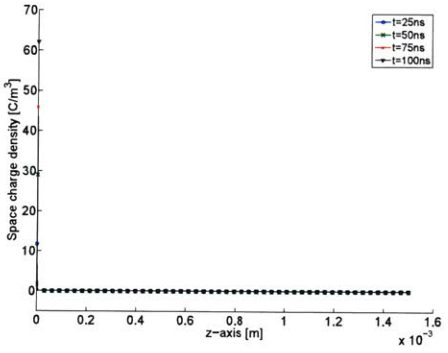

(c) Net space charge density distribution

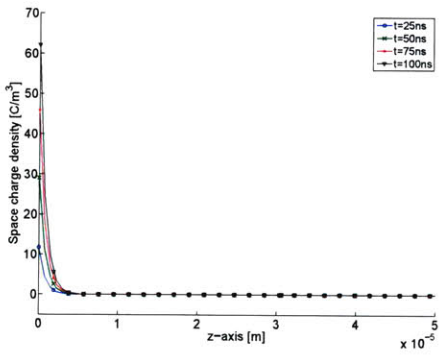

(d) Net space charge density distribution near the needle tip

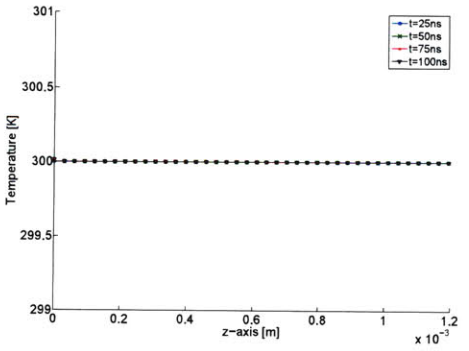

(e) Oil temperature distribution

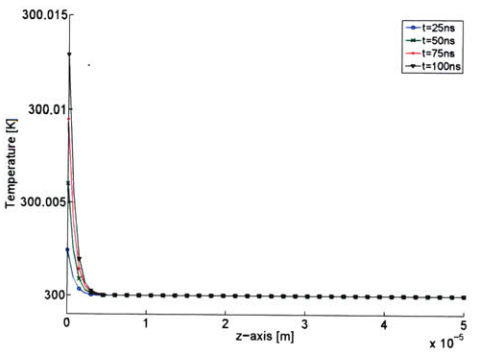

(f) Oil temperature distribution near the needle tip

Figure 4.7: Temporal dynamics along the needle-sphere electrode axis at 25 ns intervals from $t = 25 - 100$ ns given by the solution to the streamer model of (4.4)-(4.8) for an applied voltage of $V_{app} = 130$ kV and the field ionization mechanism of (4.1). The oil is comprised of high number density, high ionization potential naphthenic/paraffinic hydrocarbon molecules only with parameter values summarized in Table 4.2. Note, at time $t = 0^+$ the electric field represents the Laplacian electric field and the oil temperature is 300 K.

(a) $t = 25$ ns (b) $t = 50$ ns (c) $t = 75$ ns (d) $t = 100$ ns

Figure 4.8: Electric field magnitude [V/m] spatial distributions (as a function of r and z in the electrode geometry) from $t = 25 - 100$ ns given by the solution to the streamer model of (4.4)-(4.8) for an applied voltage of $V_{app} = 130$ kV and the field ionization mechanism of (4.1). The oil is comprised of high number density, high ionization potential naphthenic/paraffinic hydrocarbon molecules only with parameter values summarized in Table 4.2. Note there is no streamer formation.

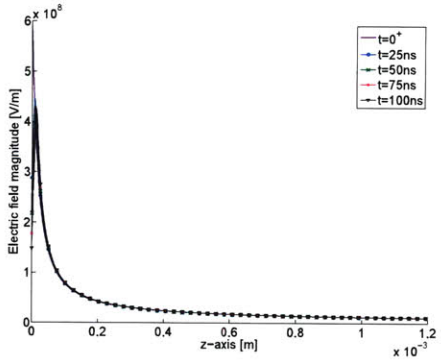

(a) Electric field magnitude distribution

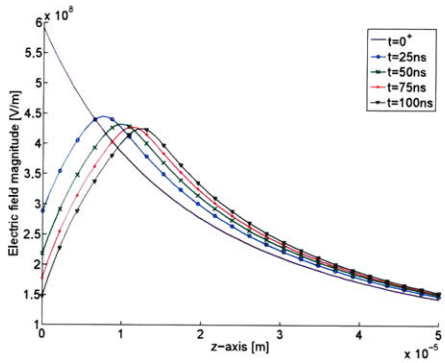

(b) Electric field magnitude distribution near the needle tip

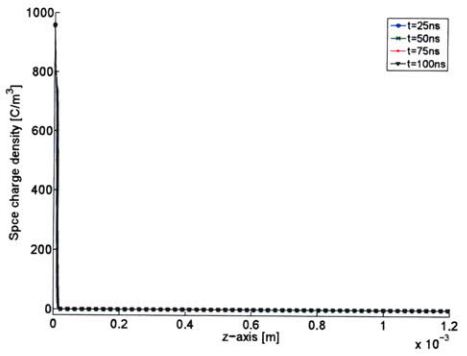

(c) Net space charge density distribution

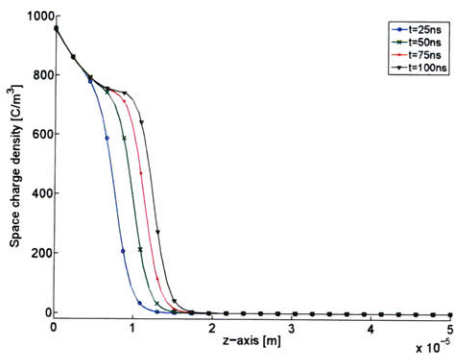

(d) Net space charge density distribution near the needle tip

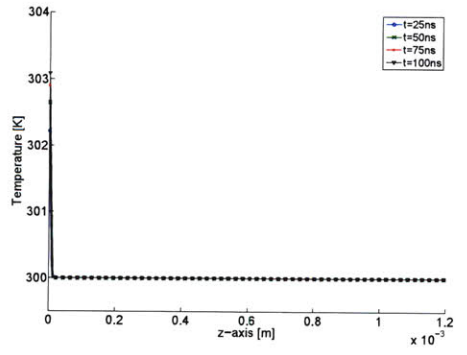

(e) Oil temperature distribution

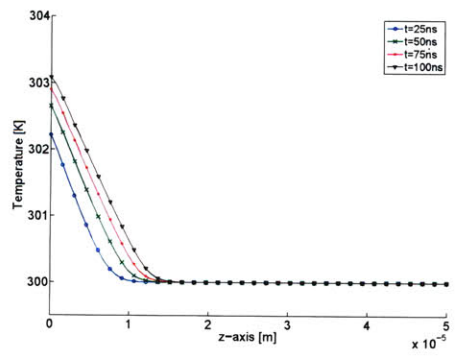

(f) Oil temperature distribution near the needle tip

Figure 4.9: Temporal dynamics along the needle-sphere electrode axis at 25 ns intervals from $t=25-100$ ns given by the solution to the streamer model of (4.4)-(4.8) for an applied voltage of $V_{app}=200$ kV and the field ionization mechanism of (4.1). The oil is comprised of high number density, high ionization potential naphthenic/paraffinic hydrocarbon molecules only with parameter values summarized in Table 4.2. Note, at time $t=0^+$ the electric field represents the Laplacian electric field and the oil temperature is 300 K.

(a) $t = 25$ ns (b) $t = 50$ ns (c) $t = 75$ ns (d) $t = 100$ ns

Figure 4.10: Electric field magnitude [V/m] spatial distributions (as a function of r and z in the electrode geometry) from $t = 25 - 100$ ns given by the solution to the streamer model of (4.4)-(4.8) for an applied voltage of $V_{app} = 200$ kV and the field ionization mechanism of (4.1). The oil is comprised of high number density, high ionization potential naphthenic/paraffinic hydrocarbon molecules only with parameter values summarized in Table 4.2. Note there is no streamer formation.

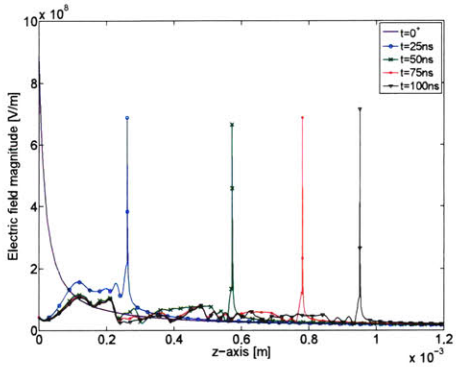

(a) Electric field magnitude distribution

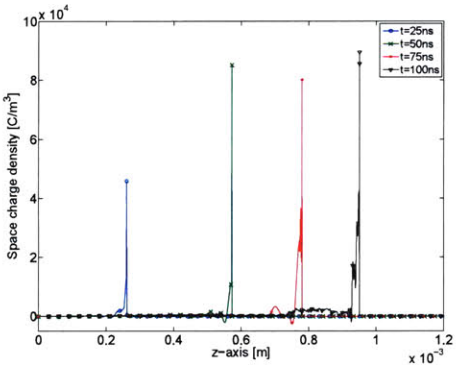

(b) Net space charge density distribution

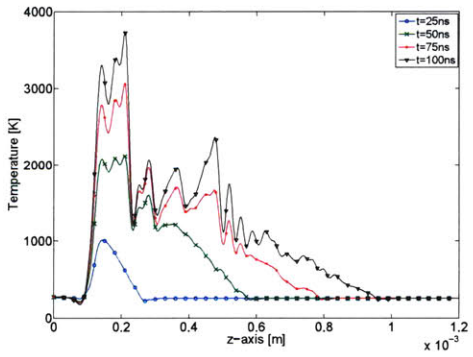

(c) Oil temperature distribution

Figure 4.11: Temporal dynamics along the needle-sphere electrode axis at 25 ns intervals from $t = 25 - 100$ ns given by the solution to the streamer model of (4.4)-(4.8) for an applied voltage of $V_{app} = 300$ kV and the field ionization mechanism of (4.1). The oil is comprised of high number density, high ionization potential naphthenic/paraffinic hydrocarbon molecules only with parameter values summarized in Table 4.2. Note, at time $t = 0^+$ the electric field represents the Laplacian electric field and the oil temperature is 300 K.

(a) $t = 25$ ns (b) $t = 50$ ns (c) $t = 75$ ns (d) $t = 100$ ns

Figure 4.12: Electric field magnitude [V/m] spatial distributions (as a function of r and z in the electrode geometry) from $t = 25 - 100$ ns given by the solution to the streamer model of (4.4)-(4.8) for an applied voltage of $V_{app} = 300$ kV and the field ionization mechanism of (4.1). The oil is comprised of high number density, high ionization potential naphthenic/paraffinic hydrocarbon molecules only with parameter values summarized in Table 4.2.

4.4 Verifying Biller's Model for Streamer Propagation Modes

The results of Sections 4.2 and 4.3 demonstrate that ionization of different families of molecules drives the development and propagation of positive streamers in transformer oil. Figures 4.1 and 4.11 show that both the ionization of low number density, easily ionizable molecules and high number density, high ionization potential molecules create significant temporal dynamics in the electric field distribution occur in the oil volume between the needle tip and spherical electrode. The peak of the electric field does not occur at the needle tip, as it does for the Laplacian field (Fig. 3.3), but rather at a point in the oil gap between the two electrodes. This temporally dynamic electric field distribution represents an ionizing electric field wave that ionizes molecules into slow positive ions and fast electrons.

The key characteristics of the streamers in Section 4.2, which are generated due to the ionization of low number density and easily ionizable molecules, closely resemble slow 2^{nd} mode streamers in transformer oil. In particular, their propagation velocity (3.0 km/s), electric field peak ($\sim 4\times10^8$ V/m), radial dimension (10 μm), and breakdown inception voltage for the 25 mm needle-sphere geometry ($\sim$ 130 kV) match the empirical data from several research groups [2,14,21,22,29,59,111]. Also, Figs. 4.4 and 4.6 showed that with an increased applied voltage, the streamer expanded greatly in the radial direction, however, its axial growth was not significant. This phenomenon is characteristic of 2^{nd} mode streamers in transformer oil that have an increasingly branched structure with greater applied voltage, however their velocity stays relatively constant [21,22].

The streamers in Section 4.3, which are generated due to the ionization of high number density, high ionization potential molecules, resemble fast 3^{rd} mode streamers in transformer oil. Their propagation velocity (9.5 km/s), electric field peak ($\sim 1\times10^9$ V/m), radial dimension (1 μm), and inception voltage for the 25 mm gap needle-sphere geometry ($\sim$ 300 kV) match the empirical data from the same research groups as for slow 2^{nd} mode streamers [2, 14, 21, 22, 29, 59, 111]. The fast 3^{rd} mode streamer inception voltage is equivalent to the acceleration voltage, where the streamer propagation velocity increases an order of magnitude from 2 – 5 km/s for slow 2^{nd} mode streamers to 10 – 20 km/s for fast 3^{rd} mode streamers [21,59]. Consequently, high number density, high ionization potential molecules are not ionized at the lower voltages, as shown in Figs. 4.8 and 4.10 for $V_{app}=130$ kV and $V_{app}=200$ kV, respectively.

The ability to ionize low or high number density molecules is directly related to the amount of space charge created in the ionization region. Ionizing the high number density, high ionization potential molecules creates more space charge (Fig. 4.11(b)) compared to the low number density, easily ionizable molecules (Fig. 4.3(b)). Consequently, a larger electric

field enhancement is produced at the streamer tip producing a more efficient field ionization (*i.e.*, higher $G_F(|\vec{E}|)$). The resulting streamer is of the fast 3rd mode type.

Conversely, the ionization of the lower number density, easily ionizable aromatic molecules in transformer oil generates space charge levels that lead to lower field enhancement. This field enhancement level is too low to ionize high ionization potential naphthenic/paraffinic molecules, such that only slower 2nd mode streamers develop. Note, for the low number density, low ionization potential molecules it takes the streamer 325 ns to reach $z =$ 1 mm (Fig. 4.2(e)) compared to the streamer created by the ionization of the high number density, high ionization potential molecules that travels to $z = 1$ mm in only 100 ns (Fig. 4.12(d)).

For the high number density, high ionization potential molecules, due to the ionization of more molecules, there is a greater number of free charge carriers in the streamer body that contribute to Joule heating. Therefore, the level of dissipation is much higher compared to the 2nd mode streamer case and the oil is heated significantly (Fig. 4.11(c)) such that vaporization occurs quickly creating a low mass density region.

The results presented, which show streamer propagation modes result from the ionization of different families of molecules with unique densities and ionization potentials, corroborates the model presented by Biller [42]. In Biller's hypothesis the specific charge generation mechanism involved in streamer development is not discussed, however researchers have theorized that the same mechanism drives both 2nd and 3rd mode streamers due to their similar streamer characteristics (*i.e.*, shape, light emission,etc.) of the two modes [21, 22]. This work shows that field ionization is the key mechanism that drives both slow 2nd and fast 3rd mode streamers.

4.5 Preliminary Model of Streamer Protrusions

In this section a preliminary model is proposed to explain the streamer protrusions in Fig. 4.12 as being due to an electrohydrodynamic instability of a uniform volume charged filled jet of radius R, surface tension γ, and charge density Q as developed in references [17, 137–139]. For convenience, the $t = 100$ ns spatial electric field solution is replotted in Fig. 4.13.

For simplicity, the space charge effects are emphasized by assuming that the jet and the surrounding oil have the same dielectric permittivity ϵ so that there are no polarization forces on the jet interface. Linear small signal radial perturbations $\xi(\theta, z, t)$ of the cylindrical

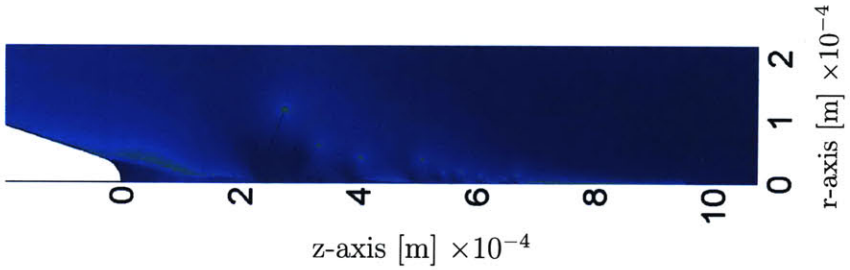

Figure 4.13: Electric field magnitude [V/m] spatial distribution (as a function of r and z in the electrode geometry) at $t=100$ ns given by the solution to the streamer model of (4.4)-(4.8) for an applied voltage of $V_{app}=300$ kV and the field ionization mechanism of (4.1). The oil is comprised of high number density, high ionization potential naphthenic/paraffinic hydrocarbon molecules only with parameter values summarized in Table 4.2.

interface from $r=R$ are of the complex amplitude form

$$\xi(\theta,z,t)=Re\left\{\hat{\xi}\exp\left[j(\omega t-m\theta-kz)\right]\right\}, \tag{4.9}$$

where $j=\sqrt{-1}$. Applying the boundary conditions of continuity of potential, displacement, normal component of electric field, and force balance as given by Eqs. (52)-(54) in Ref. [17] and by Eqs. (34)-(35) in Ref. [139] give the system dispersion relation as

$$\begin{aligned}\left(\frac{\omega}{\omega_j}\right)^2 &= -(kR)^2 I_m'(kR)K_m'(kR)\{(kR)^2+m^2 \\ &\quad -1-Q_j^2[0.5-I_m(kR)K_m(kR)]\},\end{aligned} \tag{4.10}$$

where

$$(\omega_j)^2 = \frac{\gamma}{\rho R^3}, \tag{4.11}$$

$$(Q_j)^2 = \frac{Q^2R^3}{\epsilon\gamma}, \tag{4.12}$$

$$I_m'(kR) = \frac{d[I_m(kR)]}{d[kR]}, \tag{4.13}$$

$$K_m'(kR) = \frac{d[K_m(kR)]}{d[kR]}. \tag{4.14}$$

$I_m(kR)$ and $K_m(kR)$ are respectively the modified Bessel functions of the first and second kind of order m.

The charged jet radius is stable in time if ω is real as then $|\xi(\theta,z,t)/\hat{\xi}|<1$ and is unstable when ω has a negative imaginary part as then $\xi(\theta,z,t)$ in (4.9) will grow exponentially with time. Therefore, it is hypothesized that such unstable growth for small displacements

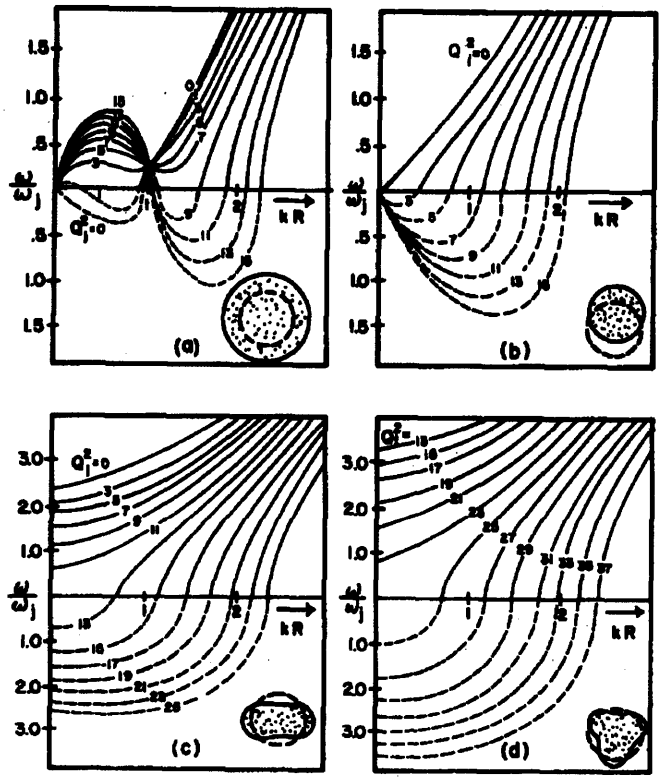

Figure 4.14: Frequency (solid curves) and growth rates (dashed curves) normalized to $\omega_j = (\gamma\rho R^3)^{1/2}$ for circular jet with uniform charge density as a function of normalized wavenumber kR. Curves accentuate space charge effects by setting $\epsilon = \epsilon_0$. (a) $m=0$; (b) $m=1$; (c) $m=2$; (d) $m=3$ (Figure 6, [17]).

of $\xi(\theta, z, t)$ become large signal non-linear growth that result in the protrusions seen in Fig. 4.13.

Figure 6 of Ref. [17], which is reproduced here in Fig. 4.14, non-dimensionally plots ω/ω_j versus kR in Eq. (4.10) considering kR real and allowing $(\omega/\omega_j)^2$ to be positive because with ω real the streamer is stable as represented by the positive part of each plot. With $(\omega/\omega_j)^2$ negative ω is imaginary and the streamer is unstable. For the simulations in Fig. 4.13 it is determined that the representative parameter values are $Q \approx 300\,\mathrm{C/m^3}$, $R \approx 1\,\mu\mathrm{m}$, $\epsilon = 2.2\epsilon_0$, $\rho \approx 880\,\mathrm{kg/m^3}$, $\gamma \approx 0.004\,\mathrm{Nt/m}$ to give $\omega_j \approx 2\times10^6\,\mathrm{rad/s}$ and $Q_j^2 \approx 1.1$.

For this value of Q_j^2 Fig. 4.14 is examined and it is seen that modes $m=2$ and 3 are stable as those modes result in real values of ω. For mode $m=0$, approximate values of $0.2 < kR < 0.9$ are unstable. This range corresponds to a wavelength range of approximately $7 < \lambda/R < 30$. The peak unstable frequency magnitude is about $0.2\omega_j$ corresponding to a growth time

constant of about 2.5 μs. For $m = 1$, the unstable wavenumber range is $0 < kR < 0.35$ corresponding to the wavelength range $\lambda/R > 18$. The peak unstable frequency magnitude is about $0.1\omega_j$ corresponding to a growth time constant of about 5 μs . With $R = 1$ μm we thus expect $m = 1$ protrusions with spacing greater than 18 μm with exponential growth rate of order 5 μs and $m = 0$ protrusions in the range of 7 to 30 μm with exponential growth rate of order 2.5 μs.

In Fig. 4.13 note the protrusion spacings are of order $20 - 100\,\mu$m with a growth rate of order 36ns. Thus this speculative instability analysis is in the right range for protrusion periodicity but predicts a slower growth rate than appears in the calculations of Fig. 4.13. A more refined space charge instability analysis will better fully examine the instability analyses of references [17, 137, 139] which also include polarization forces. It might be expected that the streamer being a low density region might have a dielectric constant closer to that of free space than that of transformer oil. The polarization force might further destabilize the cylindrical interface causing the instability to grow faster.

4.6 The Space Charge Shielding Effect: Increasing the Acceleration Voltage

Some of the most revealing experiments regarding streamer physics have been additive studies, where controlled additives have been added to base hydrocarbon liquids, such as naphthenic oils [11, 69] and cyclohexane [12, 34, 35]. Please refer to Section 2.3 for a summary of some of these experimental studies. By selecting the appropriate additive, with features such as low ionization potential, high electron affinity, etc., a causal relationship between additive feature and streamer characteristics can be drawn. These studies have helped formulate the ideas of the previous sections, whereby it was shown that slow and fast streamers are caused by the ionization of low number density, low ionization potential molecules and high number density, high ionization potential molecules, respectively. However, some additive studies have observed results that have been counter-intuitive and difficult to assess the root cause.

Two different additive studies from Hebner *et al.* [69] and Lesaint and Jung [12] have obtained conclusive results showing the addition of low ionization potential additives (*i.e.*, N,N'-dimethylaniline (DMA) (7.14 eV) in [11, 69] and pyrene (7.4 eV [61, 62]) in [12]) in low concentrations to pure hydrocarbon oils (*i.e.*, naphthenic oil in [11,69] and cyclohexane in [12]) leads to a reduction of the breakdown voltage. This should not come as a surprise, especially in light of results from Section 4.2 with low number density, low ionization potential molecules, because the ionization potential plays a strong role in determining the

minimum field level at which streamers develop (see Section 3.8). Therefore, having a sufficient number density of molecules with a lower ionization potential, such as DMA and pyrene in the additive studies, produces slow streamers at lower voltages than for the case of pure high ionization potential liquids, such as naphthenic oils and cyclohexane, only.

What was unexpected in these these two studies [12, 69], was that the addition of low ionization potential additives seemed to retard the inception of fast mode streamers, such as the 3$^{\text{rd}}$ and 4$^{\text{th}}$ modes, to higher applied voltages. Lesaint and Jung recorded an increase in the acceleration voltage, where the streamer transitions from slow 2$^{\text{nd}}$ mode to fast 3$^{\text{rd}}$ mode, for increased pyrene concentration in cyclohexane (up to 19 g of pyrene in 1 L of cyclohexane). These fascinating results are counter-intuitive to conventional wisdom. How can the addition of a low ionization potential additive increase extreme over-voltage insulation characteristics in the base liquid?

The results of this section show that the increase in acceleration voltage is due to the shielding of the high voltage electrode via the space charge created by the ionization of low number density, low ionization potential additives.

4.6.1 Streamers in Heterogeneous Dielectric Liquids

To model two unique molecular species the governing equations of (4.4)-(4.8) are slightly modified to include charge generation from two sources, $G_{F1}(|\vec{E}|)$ and $G_{F2}(|\vec{E}|)$, which pertain to the two molecular species. The new model is

$$\nabla \cdot (\epsilon_r \epsilon_0 \vec{E}) = \rho_p + \rho_n + \rho_e \tag{4.15}$$

$$\frac{\partial \rho_p}{\partial t} + \nabla \cdot (\rho_p \mu_p \vec{E}) = G_{F1}(|\vec{E}|) + G_{F2}(|\vec{E}|) + \frac{\rho_p \rho_e R_{pe}}{q} + \frac{\rho_p \rho_n R_{pn}}{q} \tag{4.16}$$

$$\frac{\partial \rho_n}{\partial t} - \nabla \cdot (\rho_n \mu_n \vec{E}) = \frac{\rho_e}{\tau_a} - \frac{\rho_p \rho_n R_{pn}}{q} \tag{4.17}$$

$$\frac{\partial \rho_e}{\partial t} - \nabla \cdot (\rho_e \mu_e \vec{E}) = -G_{F1}(|\vec{E}|) - G_{F2}(|\vec{E}|) - \frac{\rho_p \rho_e R_{pe}}{q} - \frac{\rho_e}{\tau_a} \tag{4.18}$$

$$\frac{\partial T}{\partial t} + \vec{v} \cdot \nabla T = \frac{1}{\rho_l c_v}(k_T \nabla^2 T + \vec{E} \cdot \vec{J}\,), \tag{4.19}$$

where the only change comes in (4.16) and (4.18), which include the field ionization sources

$$G_{F1}(|\vec{E}|) = \frac{q^2 n_1 a_1 |\vec{E}|}{h} \exp\left(-\frac{\pi^2 m_1^* a_1 \Delta_1^2}{q h^2 |\vec{E}|}\right) \tag{4.20}$$

$$G_{F2}(|\vec{E}|) = \frac{q^2 n_2 a_2 |\vec{E}|}{h} \exp\left(-\frac{\pi^2 m_2^* a_2 \Delta_2^2}{q h^2 |\vec{E}|}\right) \tag{4.21}$$

on their right-hand sides. A detailed discussion of the model and parameters can be found in Chapter 3.

For the two species model above, there are two cases investigated where the ionization potential of Species 1 (4.20) is varied. The two cases are summarized in Tables 4.3 and 4.4. Species 1 for Case 1 has similar parameter values as those of the low number density aromatic molecules with parameters summarized in Table 4.1, except the ionization potential Δ is greater. On the other hand, Species 1 for Case 2 has identical parameter values as those of the low number density, low ionization potential aromatic molecules with parameters summarized in Table 4.1. Species 1 of Case 2 models low number density additives with ionization potential substantially lower than that of Species 2 that comprises the bulk of the liquid. Therefore, Species 1 is similar to the aromatic molecules in transformer oil discussed in Section 4.2.

Species 2 in both cases are identical and the values match those of high number density, high ionization potential naphthenic/paraffinic molecules with parameters summarized in Table 4.2. These molecules produce fast 3$^{\text{rd}}$ mode streamers under an applied voltage of 300 kV in the needle-sphere geometry. Therefore, Species 2 molecules model the higher number density, high ionization potential molecules that comprise the base of the liquid, such as naphthenic and paraffinic molecules in transformer oil.

In the next section, the aforementioned two cases will be investigated under a 300 kV applied step voltage. Due to the presence of the high number density, high ionization potential Species 2 in both cases and the high 300 kV applied voltage, a fast 3$^{\text{rd}}$ mode streamer is expected to result from the creation of significant space charge and electric field enhancement, as seen in Section 4.3. The ionization of Species 2 molecules are expected to dominate over the low number density molecules of Species 1, such that the presence of Species 1 is expected to be negligible.

Table 4.3: Two Molecular Species Liquid: Case 1 Field Ionization Parameter Values

Parameter	**Symbol**	**Species 1**	**Species 2**	**Reference**
Number density	n_x	1×10^{23} m^{-3}	1×10^{25} m^{-3}	[42, 63, 64, 124]
Ionization potential	Δ_x	1.36×10^{-18} J (8.50 eV)	1.58×10^{-18} J (9.86 eV)	[61, 62]
Molecular separation	a_x	3.0×10^{-10} m	3.0×10^{-10} m	[25, 101]
Effective electron mass	m_x^*	$0.1\times m_e = 9.11\times10^{-32}$ kg	9.11×10^{-32} kg	[122, 123]

Table 4.4: Two Molecular Species Liquid: Case 2 Field Ionization Parameter Values

Parameter	**Symbol**	**Species 1**	**Species 2**	**Reference**
Number density	n_x	1×10^{23} m^{-3}	1×10^{25} m^{-3}	[42, 63, 64, 124]
Ionization potential	Δ_x	9.92×10^{-19} J (6.20 eV)	1.58×10^{-18} J (9.86 eV)	[61, 62]
Molecular separation	a_x	3.0×10^{-10} m	3.0×10^{-10} m	[25, 101]
Effective electron mass	m_x^*	$0.1\times m_e = 9.11\times10^{-32}$ kg	9.11×10^{-32} kg	[122, 123]

4.6.2 Case 1 – Figures 4.15 and 4.16

In this section numerical results are presented for the two species streamer model of (4.15)-(4.19) with field ionization mechanisms of (4.20) and (4.21) and Case 1 parameter values summarized in Table 4.3. The applied voltage to the needle electrode is $V_{app} = 300$ kV. In Fig. 4.15, the electric field, net space charge density, and temperature profile distributions along the needle-sphere symmetry z-axis are shown at several instances in time. In Fig. 4.16, the rz-plane spatial distribution of the electric field magnitude at the same time instances are shown.

The resulting streamer for the Case 1 two species model is similar to the naphthenic/paraffinic hydrocarbon case in Section 4.3.3, where a fast 3rd mode streamer is produced for an applied voltage of $V_{app} = 300$ kV. In particular, the electric field enhancement level, space charge density peak, and thermal enhancement are similar when comparing Fig. 4.15 and Fig. 4.11. Also, the Case 1 streamer's shape and propagation velocity in Fig. 4.16 resembles the highly branched streamer in Fig. 4.12, which is due to the ionization of high number density, high ionization potential molecules that are identical to Species 2 (see Tables 4.3 and 4.2).

In Section 4.3, it was shown that high field and temperature enhancements were directly related to the significant increase in free charge carrier development when a higher number density of ionizable molecules is present, such as the naphthenic/paraffinic oil molecules. Therefore, it is concluded that for the Case 1 streamer presented in this section, which has 3rd mode streamer characteristics, results from the field ionization of the high number density, high ionization potential Species 2 molecules. The low number density Species 1 molecules with slightly lower ionization potential (8.5 eV) do not play a major role in dictating the streamer characteristics at $V_{app} = 300$ kV.

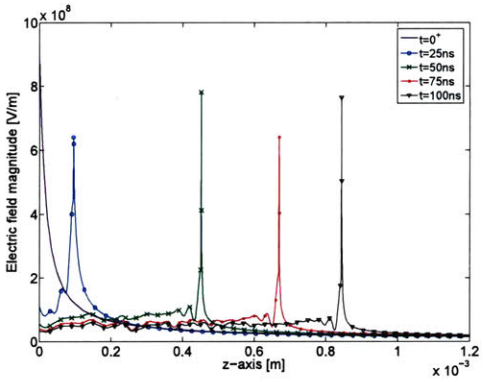

(a) Electric field magnitude distribution

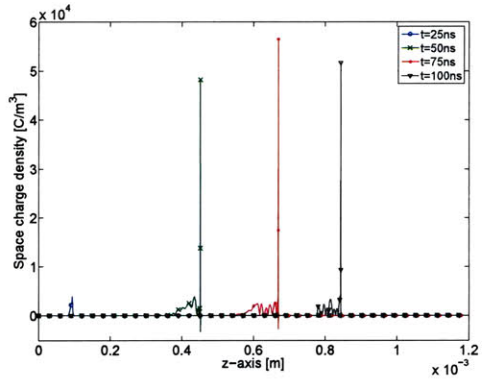

(b) Net space charge density distribution

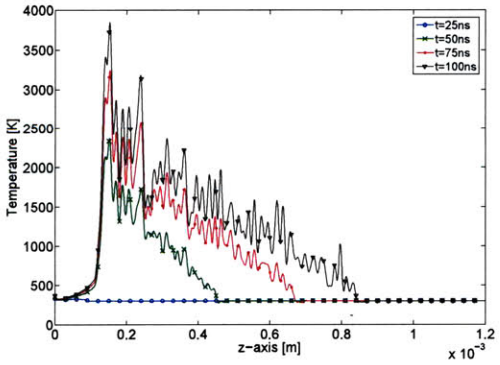

(c) Oil temperature distribution

Figure 4.15: Temporal dynamics along the needle-sphere electrode axis at 25 ns intervals from $t = 25 - 100$ ns given by the solution to the streamer model of (4.15)-(4.19) for an applied voltage of $V_{app} = 300$ kV and the field ionization mechanisms of (4.20) and (4.21). The oil is composed of two molecular species from Case 1 with parameter values summarized in Table 4.3. Note, at time $t = 0^+$ the electric field represents the Laplacian electric field and the oil temperature is 300 K.

(a) $t = 25$ ns (b) $t = 50$ ns (c) $t = 75$ ns (d) $t = 100$ ns

Figure 4.16: Electric field magnitude [V/m] spatial distributions (as a function of r and z in the electrode geometry) from $t = 25 - 100$ ns given by the solution to the streamer model of (4.15)-(4.19) for an applied voltage of $V_{app} = 300$ kV and the field ionization mechanisms of (4.20) and (4.21). The oil is composed of two molecular species from Case 1 with parameter values summarized in Table 4.3.

4.6.3 Case 2 – Figures 4.17 and 4.18

In this section numerical results are presented for the two species streamer model of (4.15)-(4.19) with field ionization mechanisms of (4.20) and (4.21) and Case 2 parameter values summarized in Table 4.4. The applied voltage to the needle electrode is $V_{app} = 300$ kV. In Fig. 4.17, the electric field, net space charge density, and temperature profile distributions along the needle-sphere symmetry z-axis are shown at several instances in time. In Fig. 4.18, the rz-plane spatial distribution of the electric field magnitude at the same time instances are shown.

The resulting streamer for the Case 2 two species model is extremely different from the Case 1 streamer in the last section. For example, the electric field enhancement level, space charge density peak, and thermal enhancement are much lower and the streamer has a much slower propagation velocity. Furthermore, the streamer has extensive growth in the radial direction unlike the Case 1 streamer. Strikingly, the resulting Case 2 streamer has many characteristics that are similar or near identical to the radially branched 2^{nd} mode streamer presented in Section 4.2.3 for $V_{app} = 300$ kV (see Figs. 4.5 and 4.6). It was shown that these 2^{nd} mode streamers result from the ionization of low number density, low ionization potential aromatic hydrocarbon molecules. Therefore, the Case 2 streamer must result from the field ionization of the similar Species 1 only. Note that Species 1 parameter values in Case 2 are identical to those for the aromatic molecules in Section 4.2, as stated earlier.

What then has happened to the high number density, high ionization potential Species 2 molecules? Are they really not being ionized? How can this be when it was shown in Section 4.3.3 that for $V_{app} = 300$ kV application to an oil composed of high number, high ionization potential naphthenic/paraffinic molecules, which are identical to Species 2 molecules, produces a fast 3^{rd} mode streamer? The results and observations of this section are similar to those obtained by Lesaint and Jung [12] and Hebner *et al.* [69], where they noticed that the addition of low ionization potential additives suppressed the development of fast mode streamers pushing their inception to higher voltages. In the next section the results of the Case 2 two species streamer model are further investigated. It is shown that shielding of the high voltage electrode tip occurs by the space charge created from the low number density, low ionization potential additives.

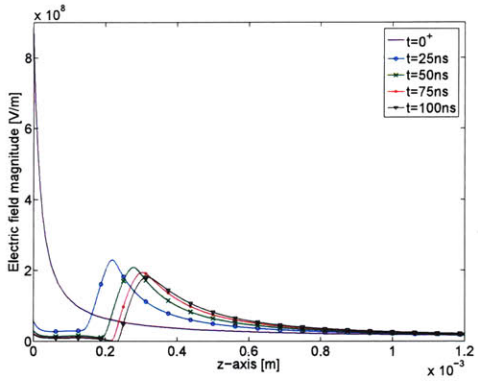

(a) Electric field magnitude distribution

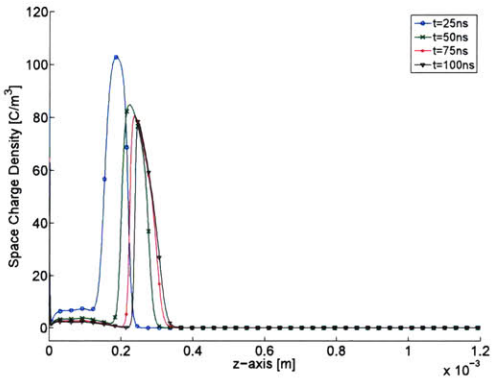

(b) Net space charge density distribution

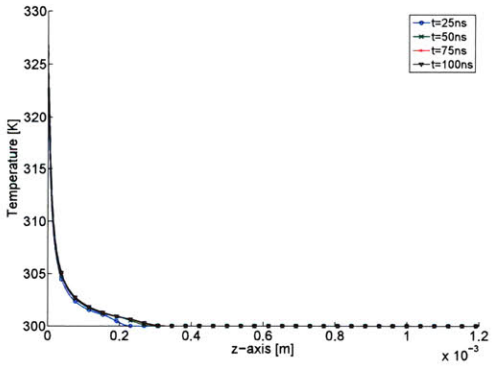

(c) Oil temperature distribution

Figure 4.17: Temporal dynamics along the needle-sphere electrode axis at 25 ns intervals from $t = 25 - 100$ ns given by the solution to the streamer model of (4.15)-(4.19) for an applied voltage of $V_{app} = 300$ kV and the field ionization mechanisms of (4.20) and (4.21). The oil is composed of two molecular species from Case 2 with parameter values summarized in Table 4.4. Note, at time $t = 0^+$ the electric field represents the Laplacian electric field and the oil temperature is 300 K.

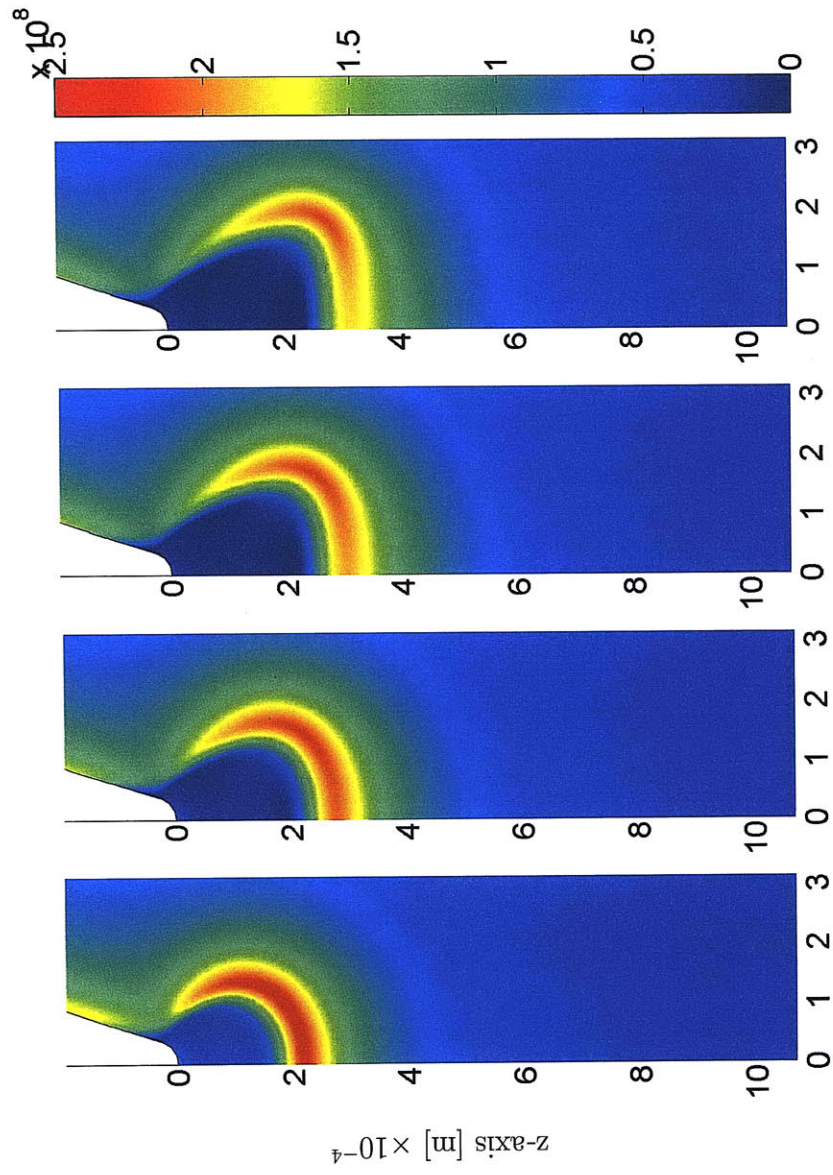

(a) $t = 25$ ns (b) $t = 50$ ns (c) $t = 75$ ns (d) $t = 100$ ns

Figure 4.18: Electric field magnitude [V/m] spatial distributions (as a function of r and z in the electrode geometry) from $t = 25 - 100$ ns given by the solution to the streamer model of (4.15)-(4.19) for an applied voltage of $V_{app} = 300$ kV and the field ionization mechanisms of (4.20) and (4.21). The oil is composed of two molecular species from Case 2 with parameter values summarized in Table 4.4.

4.6.4 Discussion

The results of Case 1 and 2, especially when compared with the earlier results of this chapter, highlight several significant concepts regarding the role of liquid chemistry on streamer development. These concepts deal with

- the effect of the relative ionization potentials of molecular species in a dielectric liquid
- the effect of additive concentrations on the streamer propagation mode
- the role of liquid purity on breakdown and acceleration voltages.

4.6.4.1 The Effect of Additive Ionization Potential

For Case 1 and 2, the only difference in the models is the ionization potentials of Species 1, where 8.50 eV and 6.20 eV are used respectively. The ionization potential of Species 1 in Case 1 is much closer to the ionization potential of the high number density Species 2 of 9.86 eV. However, the decrease in the ionization potential of Species 1 from 8.50 eV in Case 1 to 6.20 eV in Case 2 makes a world of difference on streamer development. While for Case 1 the free charge carrier generation and subsequent electric field enhancement is dominated by the ionization of the high number density, high ionization potential Species 2, thereby producing a fast 3rd mode streamer, the opposite occurs for Case 2.

For Case 1, at early times the level of ionization and resulting space charge generates a field enhancement that drives both the ionization of Species 1 and 2. From there the process continues with the ionization of both Species 1 and 2 and is dominated by the higher concentration Species 2. It is only from the ionization of Species 2 that high levels of free charge carriers and space charges are created which subsequently leads to high field enhancement at the streamer tip and significant temperature rise in the streamer channel. This ultimately leads to an efficient and fast ionization process and fast 3rd mode streamer.

When the ionization potential of Species 1 is substantially lowered, for example to 6.20 eV in Case 2, the resulting streamer is a slow 2nd mode type. This occurs because free charge carrier creation is only from the ionization of the low number density, low ionization Species 1, and not Species 2. At early times, due to the large difference in ionization potentials of Species 1 and 2, where Species 1 is significantly lower than Species 2, the field ionization mechanism $G_{F1}(|\vec{E}|)$ of Species 1 is efficient and fast in the presence of the high 300 kV applied voltage. On the other hand, due to the high ionization potential of Species 2 the field

ionization mechanism $G_{F2}(|\vec{E}|)$ is comparatively inefficient and cannot produce significant space charge levels even though there are many more Species 2 molecules.

At slightly later times the space charge created from Species 1 is small but significant enough to generate a streamer with a low field enhancement level in the oil away from the needle tip. This low field enhancement is high enough to continue ionizing Species 1 molecules, but too low to ionize the high ionization potential Species 2. By this time, the field enhancement has moved away from the streamer tip and moved into the oil, where it is controlled by the ionization of low number density, low ionization potential Species 1, and has not allowed for significant ionization of Species 2 molecules to create a high field enhancement. Therefore, it is the difference in ionization potentials of Species 1 and 2 that allows for the efficient ionization of Species 1 molecules at early times generating low levels of space charge further away from the needle tip. This low level space charge shields the high Laplacian field needle tip, such that field levels within the oil are only high enough to ionize low ionization potential Species 1 molecules and not the high number density, high ionization potential Species 2 that would result in high space charge levels and fast 3$^{\text{rd}}$ mode streamer propagation.

The discussion on the effect of ionization potential closely resembles the more mathematical discussion of the the field ionization mechanism in Section 3.8. Investigating the field ionization model $G_{F1}(|\vec{E}|)$ of (4.20), the ionization potential Δ_1 appears in the numerator of the exponential, which can take on values between 0 and 1 depending on the value of the electric field magnitude $|\vec{E}|$. The ratio of Δ_1 to $|\vec{E}|$ is of the utmost importance because small variations in the ratio can have orders of magnitude difference on the overall exponent value. Therefore, the exponent term is like a switch that turns on or off field ionization and it dominates over the pre-exponential terms, which affect $G_{F1}(|\vec{E}|)$ linearly and include the species concentration n_1. Consequently, even if the species concentration is very high, such as in Species 2, the fact that for Species 1 the ratio $\Delta_1 : |\vec{E}|$ is much smaller than $\Delta_2 : |\vec{E}|$ for Species 2 results in a much more efficient field ionization process for $G_{F1}(|\vec{E}|)$ due to the non-linear nature of the exponential term (*i.e.*, the switch is on and closer to unity).

Case 2 is an example of the space charge shielding effect and can be used to describe the observations of Lesaint and Jung [12] and Hebner *et al.* [69]. They observed that by adding low ionization potential additives (*i.e.*, N,N'-dimethylaniline (DMA) (7.14 eV) in [11, 69] and pyrene (7.4 eV [61, 62]) in [12]) in low concentrations to pure hydrocarbon oils (*i.e.*, naphthenic oil in [11, 69] and cyclohexane in [12]) inhibits the inception of fast mode streamers, such as the 3$^{\text{rd}}$ and 4$^{\text{th}}$ modes, to higher applied voltages. These results, which are counter-intuitive to conventional wisdom, can now be seen as the space charge shielding effect at work, whereby the efficient ionization of low number density, low potential

additives generates low level space charge to shield the higher applied voltage from ionizing the molecules that comprise the main liquid bulk.

4.6.4.2 The Effect of Additive Concentration and Liquid Purity

As discussed in the last section, the ionization potential difference of the two species is very important for effective space charge shielding. However, the concentration of additive species also plays a critical role. For instance, in Cases 1 and 2 the additive specie comprises less than 1% of the total concentration. For Case 1, it is the ionization of the high concentration Species 2 that leads to the development of a fast 3rd mode streamer. Conversely, in Case 2 it is the ionization of the low concentration Species 1, which produces space charge shielding and the development of a slow 2nd mode streamer. Furthermore, investigating Sections 4.2 and 4.3 similar characteristics are recorded, where slow streamers result from ionizing low number density molecules and fast streamers result from ionizing high number density molecules, irrespective of the applied voltage level.

These results show that for effective space charge shielding and over-voltage characteristics, similar to transformer oil, the additive concentration should be relatively low (*i.e.*, less than several percent of the total volume) as to not become the major constituent of the bulk liquid. For transformer oil, above its breakdown voltage V_b the average streamer velocity is low (*i.e.*, $1-5\,\mathrm{km/s}$) over a wide voltage range $V_b < V_{app} < 2V_b$ [14, 21, 22, 59]. Above the acceleration voltage V_a in transformer oil, the streamer accelerates and travels at average velocities greater that 10km/s [21]. Therefore there is a wide voltage range where slow mode streamers dominate and the transition to fast streamer velocities occurs at very high over-voltages. This is significant because a slower streamer requires more time to traverse the liquid gap between electrodes to cause breakdown, which allows more time for the applied impulse voltage to be extinguished.

For many pure dielectric liquids, where the liquid is mainly comprised of one constituent molecule, the space charge shielding effect is absent, such that for voltages slightly above the breakdown voltage the time-to-breakdown is extremely short and the streamer velocity is very high ($\gg 10\,\mathrm{km/s}$). For example, breakdown results in pure cyclohexane show a rapid transition from slow to fast mode streamers above the breakdown voltage [12]. Similar results have been observed for highly purified aromatic hydrocarbon liquids (isopropyl-biphenyl and phenyl-xylyl-ethane) [7], such that the phenomenon is not only restricted to saturated hydrocarbons. In both experiments, the breakdown and acceleration voltage were extremely close to each other, such that once the breakdown voltage was reached only a slight increase in applied voltage leads to the propagation of fast and destructive streamers.

These modeling results also corroborate that both ionization potential and additive concentration play a critical role in dictating streamer inception and propagation velocity.

4.6.4.3 Engineering Dielectric Liquids with Increased Acceleration Voltage

From the understanding gained from these models it is possible to engineer liquids with improved insulation performance. For instance, to engineer dielectric liquids with increased acceleration voltage via the space charge shielding effect, we must start with a minimum of two distinct materials, the base liquid and the additive. Key features of the base liquid are

- High ionization potential (*e.g.*, $>10\,\text{eV}$)
- High purity

Key features of the additive are

- Low ionization potential compared to that of the main dielectric liquid to ensure space charge shielding initiation at lower voltages
- Low number density to create streamer with relatively low velocity at lower voltages

It may be counter-intuitive to add small amounts of low ionization potential additives to create new insulators, but as shown in this section and validated experimentally in the literature [12, 69], this methodology can be used to create new liquids with improved overvoltage characteristics.

4.7 Fast Event 4^{th} Mode Streamers: A Transition to New Charge Generation Mechanisms

The earlier sections of this chapter have focused on investigating streamer propagation with velocities on the order of $1-10\,\text{km/s}$, where the streamers result from field ionization of different molecular species that comprise the liquid. However, the experimental results from several research groups have shown the existence of a fast event, where a positive streamer propagates with an average velocity of approximately 100 km/s or greater. This section details the study to elucidate the mechanisms behind the fast event 4^{th} mode streamers. The study starts with investigating the plausibility that the familiar field ionization is the

driving mechanism behind these streamers. It will quickly be realized that other ionization mechanisms must also be at work, of which impact- and photo-ionizations will play a critical role.

4.7.1 Field Ionization Revisited

Biller proposed that higher streamer propagation modes in non-homogeneous dielectric liquids, like transformer oil, could result from the ionization of a second ionizable species with much higher density and higher ionization potential [42]. Biller never described the actual ionization mechanism at work. Using field ionization as the ionizing mechanism, it was shown in Section 4.3 that a second ionizable species with significantly higher density and higher ionization potential resulted in 3^{rd} mode streamers as the applied voltage was increased.

By the same rationale, it is proposed here that the transition to the 4^{th} mode streamer is related to the ionization of a third type of ionizable species. The parameter values for this species are summarized in Table 4.5 and chosen because:

1. the number density for species would be far greater than that of high number density naphthenic/paraffinic species resulting in 3^{rd} mode streamer development, such that the field ionization charge generation rate in the high field zone would be extremely large resulting in extremely fast streamer propagation,

2. the ionization potential for the third species would be slightly higher than that of the high ionization potential naphthenic/paraffinic species resulting in a transition to the fast event 4^{th} mode at an applied voltage slightly above the acceleration voltage (*i.e.*, $V_{app} = 350\,\text{kV}$).

Table 4.5: Field Ionization Parameter Values for 4^{th} Mode Streamer Investigation

Parameter	**Symbol**	**Value**	**Reference**
Number density	n_0	$1\times10^{27}\,\text{m}^{-3}$	
Ionization potential	Δ	$1.6\times10^{-18}\,\text{J}\,(10\,\text{eV})$	
Molecular separation	a	$3.0\times10^{-10}\,\text{m}$	[25, 101]
Effective electron mass	m^*	$0.1\times m_e = 9.11\times10^{-32}\,\text{kg}$	[122, 123]
Applied voltage amplitude	V_{app}	350 kV	[59]

For comparison the parameter values for the naphthenic/paraffinic species resulting in 3rd mode streamer development are summarized in Table 4.2.

Figures 4.19 and 4.20 show the electric field dynamics at several time instances for the field ionization of the extremely high number density species summarized in Table 4.5. The results illustrate that having a molecular species with substantially higher number density (*i.e.*, $1\times10^{27}\mathrm{m}^{-3}$) only incrementally increases the streamer velocity to approximately 15 km/s. At these density values the model is entering a non-physical approximation of ionizable species in dielectric liquids, while the streamer velocity saturates near 20 km/s. From these results it is apparent that other ionization mechanisms must also be at work to cause the fast event 4th mode.

In the literature it has been experimentally observed that the characteristics of fast event 4th mode positive streamers in oil are radically different from 2nd and 3rd mode positive streamers [13, 14, 21, 22, 130]. Not only do 4th mode streamers propagate at velocities often exceeding 100 km/s, but they exhibit unique qualities such as highly filamentary structure [21], constant light emission at the streamer tip [14] and reduced potential drop along the streamer tail [2]. These observations have led researchers to hypothesize that fast event 4th mode streamers are driven by different charge generation mechanisms than the less energetic 2nd and 3rd modes [14, 21].

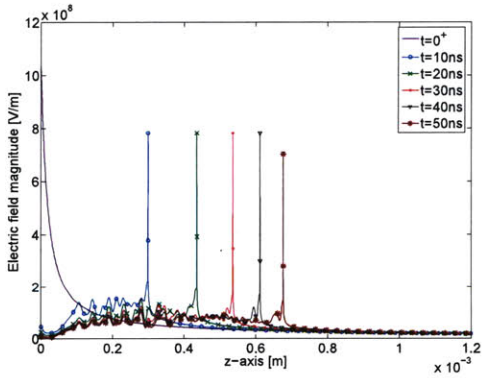

Figure 4.19: Electric field dynamics along the needle-sphere electrode axis at 10 ns intervals from $t = 10 - 50$ ns given by the solution to the streamer model of (4.4)-(4.8) for an applied voltage of $V_{app} = 350$ kV and the field ionization mechanism with parameter values summarized in Table 4.5. Note, at time $t = 0^+$ the electric field represents the Laplacian electric field.

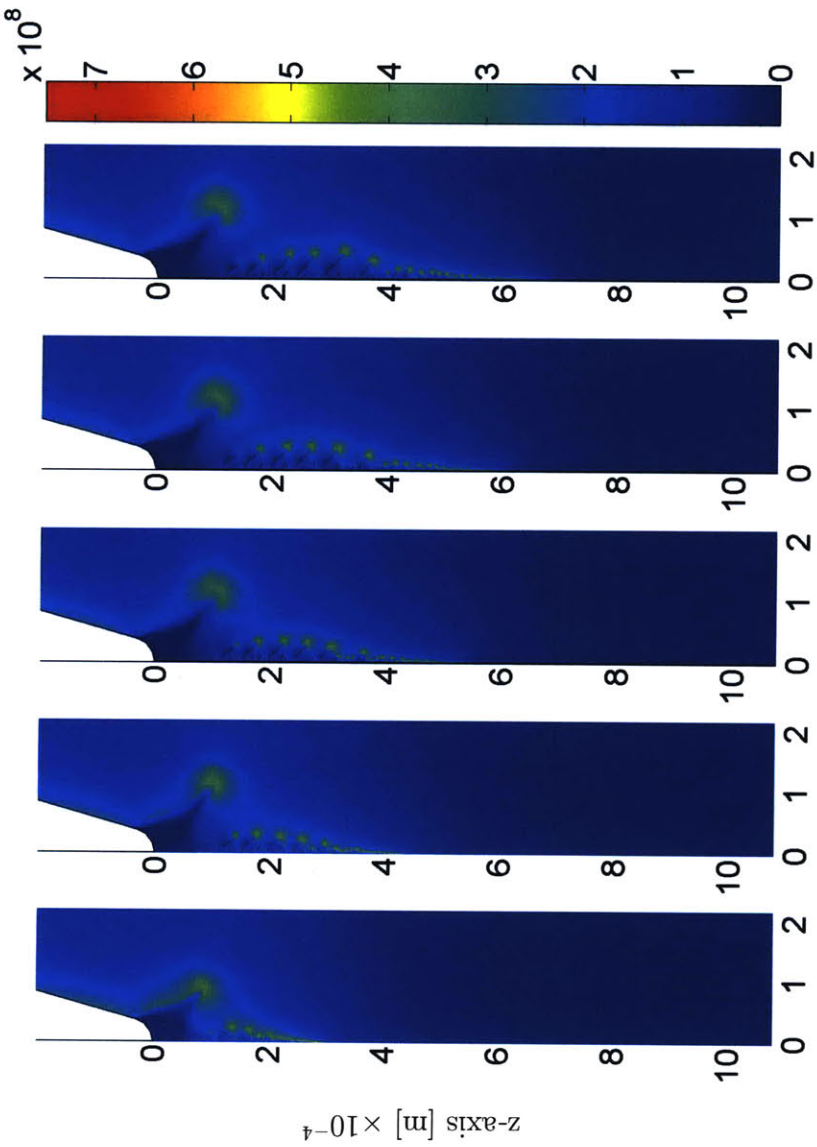

(a) $t = 10$ ns (b) $t = 20$ ns (c) $t = 30$ ns (d) $t = 40$ ns (e) $t = 50$ ns

Figure 4.20: Electric field magnitude [V/m] spatial distributions (as a function of r and z in the electrode geometry) from $t = 10 - 50$ ns given by the solution to the streamer model of (4.4)-(4.8) for an applied voltage of $V_{app} = 350$ kV and the field ionization mechanism with parameter values summarized in Table 4.5.

4.7.2 Impact and Photo-Ionizations: The Transition from Solid-State Physics to Gas-State Physics

Almost all materials can exist in all three phases (*i.e.*, solid, liquid, and gas) depending on the temperature and pressure. At one extreme most materials are solids, while at the other extreme they exist in gaseous state. Therefore, the liquid phase can be considered a transitional phase existing between the two ends of the spectrum. Many of the basic processes surrounding liquids come from viewing a liquid as a solid or a gas [26]. For example, the Zener model for field ionization in crystalline solids has been utilized to describe ionization in liquids.

Up to this point, the focus has been on field ionization as the key source to streamer development, however in light of viewing liquids as a transitional phase it seems most plausible that impact ionization, which was first recorded in vacuum [109], can play an important role in liquid breakdown. Also, the gas phase discharge physics described by impact ionization were successfully included by O'Sullivan [25] via Townsend's first ionization coefficient α [26, 109] for regions where the liquid had boiled. The results showed that impact ionization played a role in increasing the conductivity of the streamer channel making it more conductive, however the mechanism itself played a secondary role to the field ionization in the liquid that drove streamer propagation.

At voltages significantly above the breakdown voltage of transformer oil, it is hypothesized that impact ionization can play a major role in streamer development. Experimental results have shown that the streamer tip emits considerable amounts of light with increased applied voltage above the breakdown voltage [13,14,21,22,26], which suggests the release of photons due to collisions of electrons and molecules in impact ionization. The onset of impact ionization at higher voltages can be explained by the need for the electrons to gain more kinetic energy (*i.e.*, higher velocity) to ionize neutral molecules by collision. Also, the need to determine the gas region is of little importance, as most of the impact ionization occurs at the streamer tip where the streamer is in either liquid phase or high density gas phase. It has been shown by researchers that impact ionization can occur in liquids at high enough field levels [26, 127, 128].

Much of the theory about impact ionization and electron multiplication comes from gas-discharge physics. Consequently, the model for impact ionization charge generation in liquids is based upon Townsend's first coefficient α as discussed in detail in Section 3.7.2. For convenience, Townsend's first ionization coefficient is rewritten here

$$\alpha = A_t \exp\left(\frac{-B_t}{|\vec{E}|}\right), \tag{4.22}$$

where A_t is the pre-exponential coefficient with units in [m^{-1}] and B_t is the exponential term in [V/m]. For many gases these ionization coefficients are characterized, however the same is not often true for dense media like hydrocarbon liquids [67] making it difficult to model impact ionization. In [128], experiments were conducted to observe impact ionization in cyclohexane. From their data, the researchers extrapolated the impact ionization coefficients A_t and B_t values for cyclohexane to be $A_t = 2.0 \times 10^8$ m^{-1} and $B_t = 3.0 \times 10^9$ V/m [129]. In the present work, the values used for the impact ionization coefficients are summarized in Table 4.6, which are close to those obtained by Haidara and Denat [128,129].

Table 4.6: Parameter Values for Impact Ionization and Background Ionization

Parameter	**Symbol**	**Value**	**Reference**
Impact Ionization Pre-exponential coefficient	A_t	1.0×10^8 m^{-1}	[128,129]
Impact Ionization Exponential term	B_t	2.5×10^9 V/m	[128,129]
Background Ionization Density	N_0	1.0×10^{14} m^{-3}	[132]

From (4.22), the impact ionization charge generation rate is

$$\begin{aligned} G_T(|\vec{E}|) &= \alpha|\rho_e||\vec{v}_e| \\ &= A_t|\rho_e|\mu_e|\vec{E}| \exp\left(\frac{-B_t}{|\vec{E}|}\right), \end{aligned} \tag{4.23}$$

where ρ_e is the electron charge density and $\vec{v}_e = \mu_e \vec{E}$ is the local electron velocity.

The difficulty for many researchers with regards to impact ionization in liquids is determining where the seed electrons that initiate impact ionization come from. Looking at the literature there is a plethora of researchers who have observed light emission during streamer propagation in liquids [13,14,21,22,26]. Of greater significance is that Lundgaard *et al.* [14,22] and Lesaint and Massala [21] have both recorded intense, continuous light emission during 4^{th} mode streamer propagation which suggests:

1. Excitation caused by the high electric field strength leads to electron avalanches occurring at the streamer tip and producing light emission.
2. High luminosity allows for a more efficient photo-ionization process to create seed electrons in front of the streamer head.

There have been a handful of researchers who have attempted to model photo-ionization in specific gases such as N_2, SF_6 and air [132–134,140–143]; however it has not been done for liquids. Moreover, these models are very complex requiring gas specific data values

such as secondary ionization coefficient, the excitation coefficient for ionizing radiation, the coefficient of absorption, radiation absorption frequencies, absorption length, etc. To the author's best knowledge, there exists no experimental data on these coefficients for transformer oil.

Several researchers have modeled photo-ionization with a background ionization or pre-ionized positive ion and electron charge densities at the beginning of their simulations [132–134]. Their rationale is that the current models for photo-ionization are not well developed [144] and too complex with their dependence on parameter values that are not often well known. The density of the background ionization is much lower (*i.e.*, 1×10^{10} to 1×10^{14} m^{-3}) than the charge carrier density during streamer development (*i.e.*, $> 1 \times 10^{20}$ m^{-3}). Background ionization simplifies the problem and decreases the computation time by at least half [144]. More importantly, results from the literature have shown that using background ionization to model photo-ionization are similar to those obtained using a real photo-ionization model [132]. Therefore, in the streamer model photo-ionization is modeled by a background ionization number density, N_0, such that the initial positive ion and electron charge densities are

$$\rho_p(t=0) = -\rho_e(t=0) = qN_0, \tag{4.24}$$

where $N_0 = 1 \times 10^{14}$ m^{-3} has been chosen, as shown in Table 4.6.

Utilizing impact ionization of (4.23) as the charge generation mechanism and a background ionization of (4.24) to model photo-ionization, the governing equations of the three charge carrier continuum model are

$$\nabla \cdot (\epsilon_r \epsilon_0 \vec{E}) = \rho_p + \rho_n + \rho_e \tag{4.25}$$

$$\frac{\partial \rho_p}{\partial t} + \nabla \cdot (\rho_p \mu_p \vec{E}) = G_T(|\vec{E}|) + \frac{\rho_p \rho_e R_{pe}}{q} + \frac{\rho_p \rho_n R_{pn}}{q} \tag{4.26}$$

$$\frac{\partial \rho_n}{\partial t} - \nabla \cdot (\rho_n \mu_n \vec{E}) = \frac{\rho_e}{\tau_a} - \frac{\rho_p \rho_n R_{pn}}{q} \tag{4.27}$$

$$\frac{\partial \rho_e}{\partial t} - \nabla \cdot (\rho_e \mu_e \vec{E}) = -G_T(|\vec{E}|) - \frac{\rho_p \rho_e R_{pe}}{q} - \frac{\rho_e}{\tau_a}. \tag{4.28}$$

A detailed discussion of the model and parameters can be found in Chapter 3. Due to the model complexity and high element discretization needed to run these models, the thermal diffusion equation has been removed to reduce the degrees of freedom. Once again, the applied voltage is 350 kV to investigate the onset of the fast event 4^{th} mode streamer at voltages slightly above the acceleration voltage of 300 kV.

4.7.3 Results and Discussion

The numerical results to the streamer model of (4.25)-(4.28) for the impact ionization and photo-ionization mechanisms with parameter values summarized in Table 4.6 are presented in this section. The applied voltage to the needle electrode is $V_{app} = 350\text{kV}$. In Fig. 4.21, the electric field and net space charge density distributions along the needle-sphere symmetry z-axis is shown at several instances in time. In Fig. 4.22, the rz-plane spatial distribution of the electric field magnitude at $t = 25$ ns and 50 ns is shown.

Modeling impact ionization in COMSOL Multiphysics is difficult because the source term (4.23) is non-linear and strongly couples several variables. Just like the field ionization source term, impact ionization is strongly coupled to the local electric field, but it is also dependent on the electron density and velocity. Therefore, when modeling electron avalanches due to impact ionization there must be sufficient discretization along the streamer body, which requires mesh sizes more than an order of magnitude smaller than those used for the field ionization models. Furthermore, with the high A_t and B_t values in Table 4.6 it is difficult to run simulations for an extended amount of time. Consequently, only the first nanosecond of streamer activity has been recorded. However, even in this short amount of time, there are several key results that are unique, especially when compared to the earlier results of this chapter, which used field ionization as the charge generation mechanism.

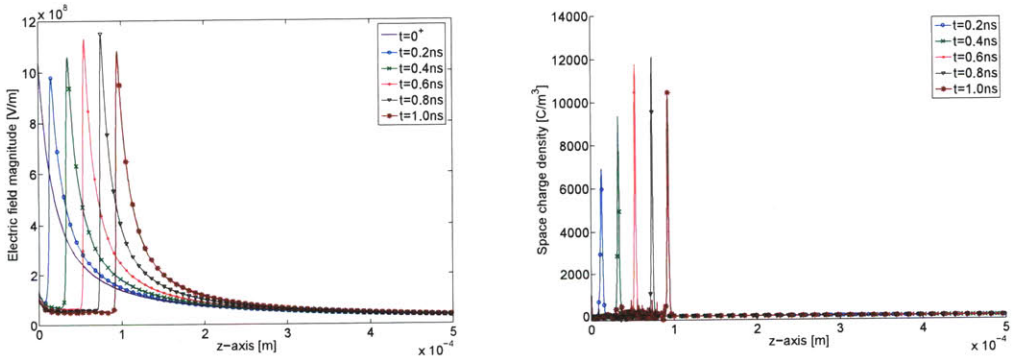

(a) Electric field magnitude distribution

(b) Net space charge density distribution

Figure 4.21: Temporal dynamics along the needle-sphere electrode axis at 0.2 ns intervals from $t = 0 - 1$ ns given by the solution to the streamer model of (4.25)-(4.28) for an applied voltage of $V_{app} = 350$ kV and the impact and photo-ionization mechanisms with parameter values summarized in Table 4.6. Note, at time $t = 0^+$ the electric field represents the Laplacian electric field.

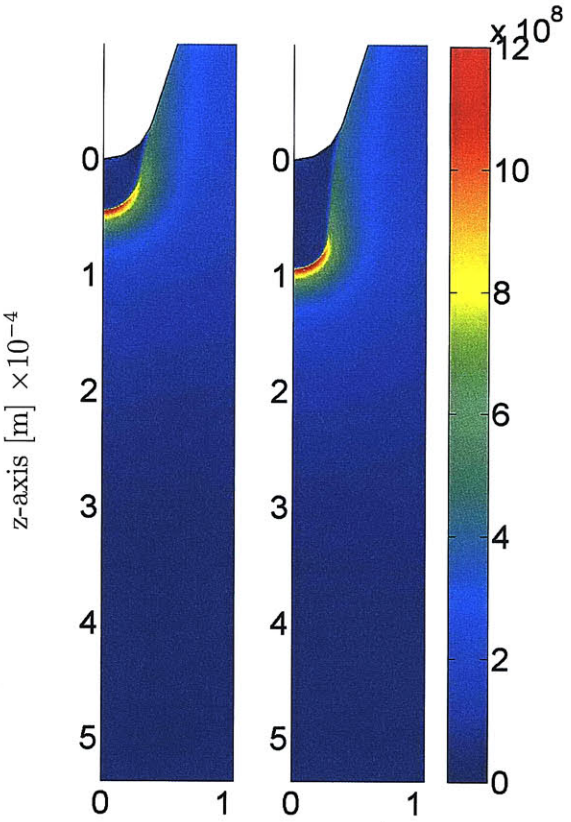

(a) $t = 0.5$ ns (b) $t = 1$ ns

Figure 4.22: Electric field magnitude [V/m] spatial distributions (as a function of r and z in the electrode geometry) from $t = 1 - 5$ ns given by the solution to the streamer model of (4.25)-(4.28) for an applied voltage of $V_{app} = 350$ kV and the impact and photo-ionization mechanisms with parameter values summarized in Table 4.6.

As in the case of field ionization, there is an ionizing electric field wave, which is created by the space charge peaks in the oil volume. In the ionization zone, the field enhancement accelerates free electrons to high velocities, such that they inelastically collide with neutral molecules to create free positive ion-electron pairs. The free or seed electrons that start this process are located ahead of the streamer front created by photo-ionization, which is modeled by the initial background density. Several other simulations have been completed where the initial background density of free charge is significantly decreased or removed. The result is either no streamer development or an extremely long time before streamer development. Therefore, photo-ionization is critical for positive streamer propagation and must occur in liquids for impact ionization to drive fast event 4^{th} mode streamers.

Figures 4.21(a) and 4.21(b) show significant temporal dynamics in the electric field and space charge density distributions with peaks in the profile distributions occurring further out in the oil volume as time progresses and away from the positive applied voltage at the sharp needle electrode. The collision of free electrons produces positive ions and more electrons in the oil forming an electron avalanche. While the positive ions move toward the grounded electrode, the newly liberated electrons are attracted to the positively excited needle electrode. Due to the high electron mobility ($\mu_e = 1 \times 10^{-4}$ m^{2}V^{-1}s^{-1}) compared to the sluggish positive ions ($\mu_p = 1 \times 10^{-9}$ m^{2}V^{-1}s^{-1}), the newly generated electrons quickly exit the ionization zone towards the anode leading to the development of a net positive space charge peak and electric field enhancement. The maximum of the electric field peak in the oil is approximately 1.1×10^9 V/m, which is higher than those observed for the slow 2$^{\text{nd}}$ and fast 3$^{\text{rd}}$ streamers of Sections 4.2 and 4.3, respectively.

From the electric field spatial distribution plots in Fig. 4.22 by approximating the dimensions of the streamer to be equal to the volume enclosed by the electric field enhancement, the radius of the streamer near the field enhanced streamer tip is 30 – 40 μm. Furthermore, the model results in a streamer with average velocity of almost 100 km/s after 1 ns, as it travels along the z-axis, for an applied voltage of $V_{app} = 350$ kV. This is the first time an ultra-fast streamer has been observed with similar characteristics of a fast event 4$^{\text{th}}$ mode streamer. The results demonstrate that impact and photo-ionizations can drive the development and propagation of fast event positive streamers in transformer oil through the creation of ionizing electric field and space charge waves that travel further out into the oil gap away from the needle electrode.

The velocity and electric field enhancement characteristics of these streamers, which are driven by the ionization of neutral molecules via inelastic collisions with free electrons produced by photo-ionization, closely resemble 4$^{\text{th}}$ mode streamers in transformer oil. In particular, their propagation velocity (100 km/s), electric field peak ($\sim 1 \times 10^9$ V/m), and inception voltage for the 25 mm needle-sphere geometry ($\sim$ 350 kV) match the empirical data in the literature [2, 14, 21, 22, 29, 59, 111].

4.8 Summary and Key Results

In this chapter a thorough investigation of the underlying mechanisms that drive streamer propagation in transformer oil has been completed and led to substantial physical insight into how and why streamers develop. It has been shown that positive streamer propagation in transformer oil is greatly affected by the onset of different ionization mechanisms

(*i.e.*, field ionization, impact ionization, photo-ionization) that are dependent on the liquid molecular structure, species and the applied voltage stress.

Through numerical modeling it has been shown that independent of the ionization mechanism, the key ingredient in streamer formation in electrically over-stressed dielectrics is the disparity in inertia of the positive ions and electrons. For example, transformer oil stressed by a positively charged needle electrode leads to ionization of oil molecules to form slow positive ions and fast electrons. Due to the much higher mobility of electrons they are able to exit the ionization zone in a small amount of time leaving behind a net positive space charge region in the oil. It is the space charge that creates a electric field enhancement away from the needle tip that continues the ionization process. Therefore, slow positive ions and fast electrons cause propagating electric field and space charge waves that are the dominant mechanism behind positive streamer propagation leading to electrical breakdown.

For lower applied voltages (*i.e.*, $V_b \leq V_{app} \leq V_a$) streamers in transformer oil are a result of the field ionization of low number density and low ionization potential oil molecules such as the trace aromatic hydrocarbons found in transformer oil. Alternatively, for higher applied voltages (*i.e.*, $V_{app} \approx V_a$) streamer development is from the field ionization of high number density and high ionization potential oil molecules such as naphthenic or paraffinic hydrocarbons, which constitute the bulk of the transformer oil volume. These characteristics of streamers, due to low concentration and high concentration hydrocarbons, are indicative of slow 2^{nd} and fast 3^{rd} mode streamers, respectively. The two streamer modes initiate at different applied voltages due to the unique ionization potentials of each hydrocarbon molecular species. For example, as described in this chapter aromatic molecules generally have lower ionization potentials, such that they ionize at lower applied voltages compared to naphthenic/paraffinic molecules that generally have higher ionization potentials and therefore need a greater applied voltage to ionize. The results confirm the qualitative hypothesis of Biller, who reasoned that streamer propagation modes in heterogeneous dielectric liquids, like transformer oil, resulted from the ionization of different molecular species, such as easily ionizable molecules and ordinary molecules.

For even higher applied voltages (*i.e.*, $V_{app} \geq V_a$) it was hypothesized and validated, via numerical modeling and results, that fast event 4^{th} mode positive streamer propagation is due to the collision of free electrons ahead of the streamer tip with neutral molecules in the ionization zone creating positive ions and more electrons. This high energy process generates intense light emission as discussed in the literature. It is these photons that photo-ionize molecules ahead of the streamer tip to create free electrons to feed and continue impact ionization in the high field ionization zone. Without the free electrons created by photo-ionization this ultra-fast process is stalled and fast event streamer formation does not occur.

A powerful discovery derived from the modeling of this chapter is the space charge shielding effect, whereby adding low ionization potential additives to a pure dielectric liquid can considerably increase its acceleration voltage. This seemingly simple addition to the liquid can dramatically improve its over-voltage performance, such that the transition from slow 2^{nd} mode to fast 3^{rd} mode streamers occurs at higher voltages and allows for more time to extinguish devastating over-voltage situations such as lightning impulses. In space charge shielding the low ionization potential additive ionizes at a lower voltage and initiates a streamer with a net space charge region at the streamer tip. This space charge creates a field enhancement level that supports further ionization of the same low ionization potential additive, while suppressing the ionization of higher potential molecules by shielding the high voltage needle tip. This prevents the inception of fast mode streamers requiring greater applied voltage for their formation. The space charge shielding effect explains the phenomena recorded by Lesaint and Jung [12], where the transition to fast streamers in cyclohexane is inhibited with small concentrations of low ionization potential pyrene.

Chapter 5

The Charging of Nanoparticle Suspensions in Dielectric Liquids and the Effect on Streamer Development

EXTENSIVE research of transformer oil insulated high voltage and power apparatus is aimed at improving the electrical breakdown and thermal characteristics [1]. One approach studied transformer oil-based nanofluids with conductive nanoparticle suspensions that defy conventional wisdom as past measurements have shown that such nanofluids have substantially higher positive voltage breakdown levels with slower positive streamer velocities than that of pure transformer oil [23, 74–79]. This paradoxical superior electric field breakdown performance compared to that of pure oil is due to the electron charging of the nanoparticles that convert high mobility electrons generated by field ionization to slow negatively charged nanoparticles carrying trapped electrons with effective mobility reduction by a factor of about 1×10^5 [25, 53, 73, 145].

This section summarizes and extends the analysis of unipolar negative charging by electrons of infinite and finite conductivity nanoparticles to show that electron trapping is the cause of the decrease in positive streamer velocity resulting in higher positive electrical breakdown strength [25, 53, 73, 145, 146]. Furthermore, the charged nanoparticle model is broadened from only electron unipolar charging of conducting nanoparticle spheres with negligible ohmic conductivity of the surrounding liquid dielectric to bipolar charging of conducting spheres including ohmic loss of the surrounding dielectric liquid. The analysis furthers the analogous Whipple and Chalmers model [147], originally applied to thunderstorm electrification, but in our case there is no flow of dielectric liquid. Similar modeling has also been used to model ion impact charging used in electrostatic precipitators. Analysis is presented for perfectly conducting spheres with possible applications to electrical breakdown research of conducting nanoparticle spheres in dielectric liquid suspensions.

This charged nanoparticle model is used to extend the comprehensive electrodynamic analysis of O'Sullivan [25] for the charge generation, recombination, and transport of positive and negative ions, electrons, and charged nanoparticles between a positive high voltage sharp needle electrode and a large spherical ground electrode. Numerical case studies showed

that in transformer oil without nanoparticles that ionization leads to electric field and space charge waves to travel between electrodes, generating enough heat to vaporize the transformer oil to cause a positive streamer that precedes electrical breakdown. When conductive nanoparticles are added to the oil they effectively trap electrons, which results in a significant reduction in streamer speed offering improved high voltage performance and reliability.

5.1 Charge Relaxation Time

The charge relaxation time of a nanoparticle in a fluid is a measure of the times (and frequencies), where due to the nanoparticles, the electrodynamic processes in the liquid will be affected. If the time constant is short and the timescales of the electrodynamic processes are much longer then the nanoparticles will have a negligible effect on the processes. However, if the converse is true, where the relaxation time constant is much longer than the time scales of the electrodynamic processes, then the presence of nanoparticles will cause significant effect on electrodynamic processes to the point where they are considerably altered.

To calculate a general expression for the relaxation time constant of a nanoparticle of arbitrary material in a fluid consider a spherical nanoparticle of an arbitrary material with radius R, permittivity ϵ_2 and conductivity σ_2, surrounded by a fluid with conductivity σ_1 and permittivity ϵ_1. At time $t = 0^+$ a z-directed electric field $\vec{E} = E_0\vec{i}_z$ is switched on at $r \to \infty$. The presence of the nanoparticle causes the electric field distribution in the fluid near the nanoparticle to deviate from the applied z-directed field. The electric field distribution in the fluid is calculated by using the separation of variables method to solve Laplace's equation (*i.e.*, $\nabla^2 V = 0$, $\vec{E} = -\nabla V$) where a negligible space charge density is assumed. The time dependent radial and polar components of the electric field in the oil outside of the nanoparticle are [19, 25, 148]

$$E_{r0}(r,\theta) = E_0\left[1 + \frac{2R^3}{r^3}\Upsilon_c \exp\left(-\frac{t}{\tau_r}\right) + \frac{2R^3}{r^3}\Sigma_c\left(1 - \exp\left(-\frac{t}{\tau_r}\right)\right)\right]\cos\theta\,, \quad (5.1)$$

$$E_{\theta 0}(r,\theta) = E_0\left[-1 + \frac{R^3}{r^3}\Upsilon_c \exp\left(-\frac{t}{\tau_r}\right) + \frac{R^3}{r^3}\Sigma_c\left(1 - \exp\left(-\frac{t}{\tau_r}\right)\right)\right]\sin\theta \quad (5.2)$$

where the charge relaxation time constant τ_r for the transformer oil/nanoparticle system is

$$\tau_r = \frac{2\epsilon_1 + \epsilon_2}{2\sigma_1 + \sigma_2} \quad (5.3)$$

and

$$\Upsilon_c = \frac{\epsilon_2 - \epsilon_1}{2\epsilon_1 + \epsilon_2}, \tag{5.4}$$

$$\Sigma_c = \frac{\sigma_2 - \sigma_1}{2\sigma_1 + \sigma_2}. \tag{5.5}$$

As discussed in Section 2.4, Segal *et al.* pursued experiments with nanofluids [23, 74–77]. For the experiments of Segal *et al.* [23, 74–79], the nanoparticle and fluid were magnetite (Fe_3O_4) and transformer oil, respectively. Magnetite has conductivity $\sigma_2 = 1 \times 10^4$ S/m at room temperature [149], and permittivity $\epsilon_2 \approx 80\epsilon_0$ [150], where $\epsilon_0 = 8.854 \times 10^{-12}$ F/m is the permittivity of free space. Transformer oil has conductivity $\sigma_1 = 1 \times 10^{-12}$ S/m and permittivity $\epsilon_1 = 2.2\epsilon_0$. Therefore, the relaxation time constant of magnetite in transformer oil is $\tau_{r(Fe_3O_4)} = 7.47 \times 10^{-14}$ s. This time constant is extremely short, especially when compared to the timescales associated with streamer development, in the nanosecond to microsecond times. Consequently, this short relaxation time constant is essentially instantaneous so that the addition of magnetite nanoparticles to the transformer oil will dramatically affect the electrodynamics during streamer development. The relaxation time constant is analogous to the time constant of an RC circuit that describes the charging rate of a capacitor (nanoparticle) when the source (free electrons at $r \to \infty$) is turned on at $t = 0$. Therefore, the small relaxation time constant for magnetite nanoparticles effectively means that the surface charging due to the injected electrons can be considered to be instantaneous [25].

As a comparison to the nanofluid manufactured with magnetite nanoparticles, other common nanoparticles such as ZnO and Al_2O_3 have relaxation time constants of $\tau_{r(ZnO)} = 1.05 \times 10^{-11}$ s and $\tau_{r(Al_2O_3)} = 42.2$ s. Table 5.1 summarizes the properties and relaxation times of several nanoparticle materials. Note that due to Al_2O_3's low conductivity, its relaxation time constant is very long. Therefore, there would be negligible surface charging of Al_2O_3 nanoparticles in the timescales of interest for which streamer development occurs.

5.2 Unipolar Charging Dynamics of a Spherical Nanoparticle

To model the electrodynamics within an electrically stressed nanofluid we must first model and understand the charging of the nanoparticles in the fluid. This model parallels the Whipple-Chalmers model used for the modeling of rain drop charging in thunderstorms taking the flow velocity of oil to be zero [19, 147, 148]. The analysis and results summarize and build upon the work completed by O'Sullivan [25].

Table 5.1: Electrical and thermal properties of representative insulating and conducting nanoparticle materials

	Magnetite Fe_3O_4	Zinc Oxide ZnO	Alumina Al_2O_3	Quartz SiO_2	Silica SiO_2
Density [g/cm^3]	5.17	5.61	3.96	2.65	2.20
Electric conductivity [S/m]	1×10^4 - 1×10^5	10 - 1×10^3	1×10^{-12}	1.3×10^{-18}	1.4×10^{-9}
Relative dielectric constant	80	7.4 - 8.9	9.9	3.8 - 5.4	3.8
Relaxation time [s]	7.47×10^{-14}	1.05×10^{-11}	12.2	36.3	5.12×10^{-2}
Dielectric strength [kV/mm]	–	35	10	–	–
Thermal conductivity [Wm^{-1}K^{-1}]	4-8	23.4	30	11.1	1.4
Thermal expansion coefficient at 20°C [μm m^{-1}K^{-1}]	9.2	2.9	–	8.1	30
Specific heat [J kg^{-1}K^{-1}]	–	494	850	–	670

Consider the situation shown in Fig. 5.1 for a perfectly conducting nanoparticle (*i.e.*, $\sigma_2 \rightarrow \infty$). A uniform z-directed electric field $E_0\vec{i}_z$ is switched on at $t=0$, and a uniform electron charge density ρ_e with electron mobility μ_e is injected into the system from $r \rightarrow \infty$. The injected electrons travel along the electric field lines and approach the nanoparticle where the radial electric field is positive, $0 < \theta < \pi/2$, as shown in Fig. 5.1. The electric field lines will terminate on the bottom side with a negative surface charge and emanate from the top side with a positive surface charge on the particle as shown in Figs. 5.1(a), 5.1(b), and 5.1(c). The electrons in the transformer oil near a nanoparticle will move opposite to the direction of the field lines and become deposited on the nanoparticle where the surface charge is positive. The rate at which a nanoparticle captures electrons is strongly dependent upon its charge relaxation time constant such that nanoparticles with a short relaxation time constant quickly capture free electrons.

The charging dynamics for a perfectly conducting nanoparticle ($\sigma_2 \rightarrow \infty$) is examined first. Afterwards, the analysis is generalized to finitely conducting nanoparticles to model nanoparticles manufactured from real materials.

5.2.1 Perfectly Conducting Nanoparticle

Immediately after the application of the electric field $\vec{E} = E_0\vec{i}_z$ at $r \rightarrow \infty$, that is at $t = 0^+$, a perfectly conducting nanoparticle within the dielectric liquid is perfectly polarized. Consequently, the initial radial electric field on the nanoparticle is positive everywhere on the upper hemisphere defined by $0 \leq \theta \leq \pi/2$ as shown in Fig. 5.1(a) corresponding to positive surface charge density $\sigma_s = \epsilon_1 E_r(r = R, \theta)$. Therefore, the electrons in the vicinity of the

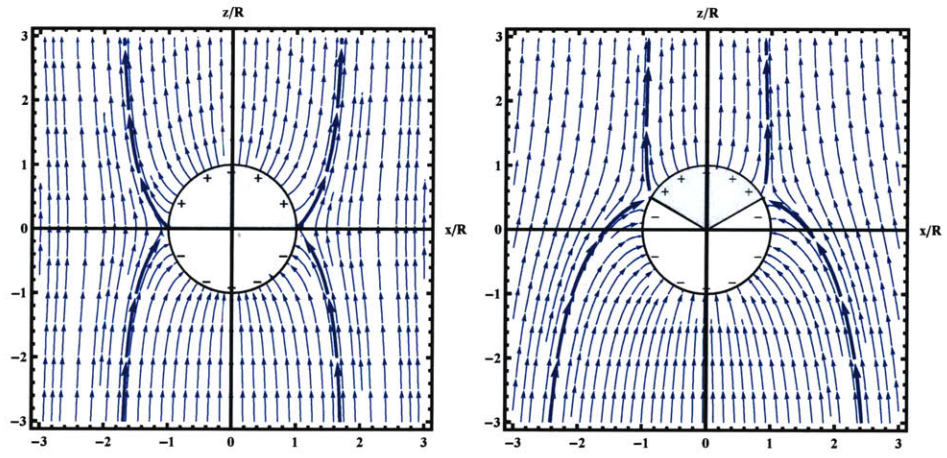

(a) $t = 0^+$, $\theta_c = \frac{\pi}{2}$, $\frac{Q(t)}{Q_s} = 0$, $\frac{R_a(t)}{R} = \frac{R_b(t)}{R} = \sqrt{3}$

(b) $\frac{t}{\tau_{pc}} = 1$, $\theta_c = \frac{\pi}{3}$, $\frac{Q(t)}{Q_s} = \frac{1}{2}$, $\frac{R_a(t)}{R} = \frac{\sqrt{3}}{2}$, $\frac{R_b(t)}{R} = \frac{3\sqrt{3}}{2}$

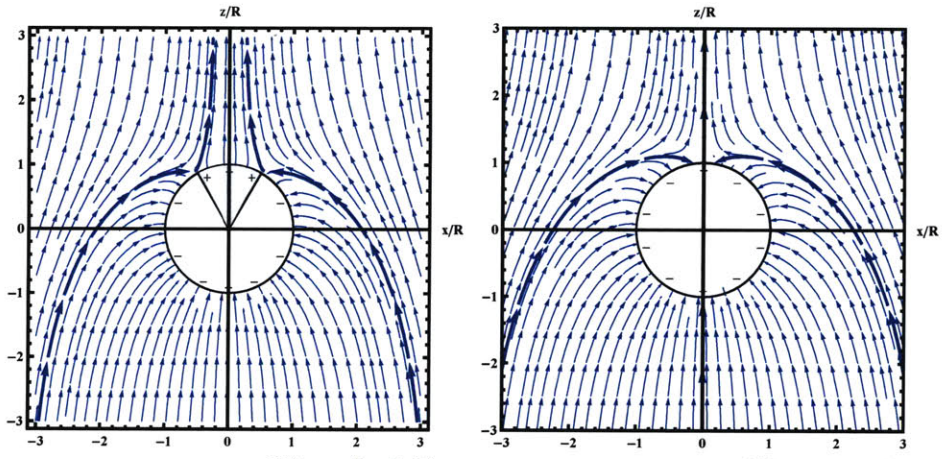

(c) $\frac{t}{\tau_{pc}} \approx 6.464$, $\theta_c = \frac{\pi}{6}$, $\frac{Q(t)}{Q_s} = \frac{\sqrt{3}}{2}$, $\frac{R_a(t)}{R} \approx 0.232$, $\frac{R_b(t)}{R} \approx 3.232$

(d) $\frac{t}{\tau_{pc}} \to \infty$, $\theta_c = 0$, $\frac{Q(t)}{Q_s} = 1$, $\frac{R_a(t)}{R} = 0$, $\frac{R_b(t)}{R} = 2\sqrt{3}$

Figure 5.1: Electric field lines for various times after a uniform z-directed electric field is turned on at $t = 0$ around a perfectly conducting spherical nanoparticle of radius R surrounded by transformer oil with permittivity ϵ_1, conductivity σ_1, and free electrons with uniform charge density ρ_e and mobility μ_e. The thick electric field lines terminate on the particle at $r = R$ and $\theta = \theta_c$ where $E_r(r = R) = 0$ and separate field lines that terminate on the nanoparticle from field lines that go around the particle. The cylindrical radius $R_a(t)$ of Eq. (5.27) of the separation field line at $z \to +\infty$ defines the charging current $I(t)$ in Eq. (5.29). The cylindrical radius $R_b(t)$ of Eq. (5.28) defines the separation field line at $z \to -\infty$. The dominant charge carrier in charging the nanoparticles are electrons because of their much higher mobilities than positive and negative ions. The conductivity of transformer oil, $\sigma_1 \approx 1 \times 10^{-12}$ S/m, is much less than the effective conductivity of the electrons, $\sigma_e \approx -\rho_e \mu_e \approx 1 \times 10^{-1}$ S/m. The electrons charge each nanoparticle to saturation, $Q_s = -12\pi\epsilon_1 E_0 R^2$ as given in Eq. (5.8) with time constant $\tau_{pc} = 4\epsilon_1/(|\rho_e|\mu_e)$ given in Eq. (5.12). The electric field lines in this figure were plotted using Mathematica StreamPlot [18].

nanoparticle are initially deposited on the upper hemispherical surface of the nanoparticle. Directly after deposition onto the surface, the electrons redistribute uniformly over the surface, such that it remains equipotential, and the nanoparticle's total charge becomes more negative over time. As a result of the charging of the nanoparticle the electric field outside the nanoparticle ($r > R$) is modified and the charging window for electrons on the nanoparticle surface continually reduces because the component of the surface that has a positive radial electric field component also decreases with increased charge capturing. This latter result is clearly shown in Figs. 5.1(b) and 5.1(c), and continues until a point where the nanoparticle is charge saturated, such that along the particle's surface there is no area with a positive radial electric field component as shown in Fig. 5.1(d). At such a point, no additional negative charge can flow onto the sphere.

The solution for the electric field outside the perfectly conducting (*i.e.*, $\sigma_2 \to \infty$, $\Sigma_c = 1$, $\tau_r = 0$) spherical nanoparticle is the superposition of the solutions of Eqs. (5.1) and (5.2) plus the radial field component caused by the already deposited electrons with net charge $Q(t)$ where $Q(t) \leq 0$.

$$\vec{E} = \left[E_0 \left(1 + \frac{2R^3}{r^3}\right) \cos\theta + \frac{Q(t)}{4\pi\epsilon_1 r^2}\right] \vec{i}_r - E_0 \left[1 - \frac{R^3}{r^3}\right] \sin\theta \, \vec{i}_\theta \qquad r > R \tag{5.6}$$

The charging of the nanoparticle by electrons can only occur at points where the radial component of the electric field on the nanoparticle surface is positive (*i.e.*, $E_r(r = R) \geq 0$). Therefore, the range of angles for electron charging is determined by

$$\cos\theta \geq -\frac{Q(t)}{12\pi\epsilon_1 E_0 R^2} \, . \tag{5.7}$$

Since the maximum of $\cos\theta$ is one, the nanoparticle's electron saturation charge is

$$Q_s = -12\pi\epsilon_1 R^2 E_0 \, . \tag{5.8}$$

As the nanoparticle charges to Q_s less of the radial electric field at the surface will be positive and the charging will occur over a more narrow area. When the nanoparticle charge reaches Q_s the radial electric field everywhere along the surface will be negative, due to the negative surface charge, and the nanoparticle is electron charge saturated such that no more electrons can be deposited on its surface. The critical angle θ_c, where the radial electric field at $r = R$ is zero (*i.e.*, $E_r(r = R) = 0$), is defined as when Eq. (5.7) is an equality

$$\cos\theta_c = Q(t)/Q_s \, . \tag{5.9}$$

Representative values in transformer oil of mobilities and charge densities of positive and negative ions and electrons are $\mu_p \approx \mu_n \approx 1\times10^{-9}$ m^{2}V^{-1}s^{-1}, $\mu_e \approx 1\times10^{-4}$ m^{2}V^{-1}s^{-1} and $\rho_p \approx -\rho_n \approx 1000$ C/m^3 and $\rho_e \approx -1000$ C/m^3. The effective conductivities of ions are then $\sigma_{p,n} = \rho_p\mu_p = -\rho_n\mu_n \approx 1\times10^{-6}$ S/m while electrons have a much higher effective ohmic conductivity of $\sigma_e = -\rho_e\mu_e \approx 1\times10^{-1}$S/m. With the much lower transformer oil ohmic conductivity of $\sigma_1 \approx 1\times10^{-12}$S/m, the dominant charge carriers that charge the nanoparticles are the electrons so that the nanoparticle charging current for angles $0<\theta<\theta_c$ is

$$\begin{aligned} J_r(r=R,\theta) &= -\rho_e\mu_e E_r(r=R,\theta) \\ &= -3\rho_e\mu_e E_0\left[\cos\theta - \frac{Q(t)}{Q_s}\right] \end{aligned} \tag{5.10}$$

where $\rho_e<0$ and $\mu_e>0$. The nanoparticle charging current is

$$\frac{dQ(t)}{dt} = -\int_{\theta=0}^{\theta_c} J_r 2\pi R^2 \sin\theta d\theta = \frac{Q_s}{\tau_{pc}}\left[1-\frac{Q(t)}{Q_s}\right]^2 \tag{5.11}$$

where the time constant for nanoparticle charging τ_{pc} is

$$\tau_{pc} = \frac{4\epsilon_1}{|\rho_e|\mu_e}\,. \tag{5.12}$$

By time integrating the nanoparticle charging current of Eq. (5.11) the charge of the perfectly conducting nanoparticle with respect to time can be found. Therefore, the charge on a perfectly conductive nanoparticle by electron scavenging is

$$Q(t) = \frac{Q_s\frac{t}{\tau_{pc}}}{1+\frac{t}{\tau_{pc}}} \tag{5.13}$$

where the initial condition is $Q(t=0)=0$.

For the purposes of evaluating the values of Q_s and τ_{pc}, the following additional parameter values are used: $q=1.6\times10^{-19}$C, $E_0=1\times10^8$V/m, $\epsilon_1=2.2\epsilon_0$ and $R=5\times10^{-9}$m. These values are reasonable estimates for the parameter values at the tip of a streamer in a transformer oil-based nanofluid [25]. The resulting values for Q_s and τ_{pc} are -1.836×10^{-18} C ($\approx$ 11 electrons) and 7.79×10^{-10} s, respectively. Figure 5.2 shows the nanoparticle charging dynamics. At early times, where the charging window is maximum with $\theta_c=\pi/2$, the charging occurs rapidly; however, at later time, as the charge capture window is reduced by the negative surface charge, the charging rate decreases until the nanoparticle's charge saturates at Q_s. As the particle captures electrons the repulsion increases between the negatively charged nanoparticles and the mobile free electrons in the surrounding oil.

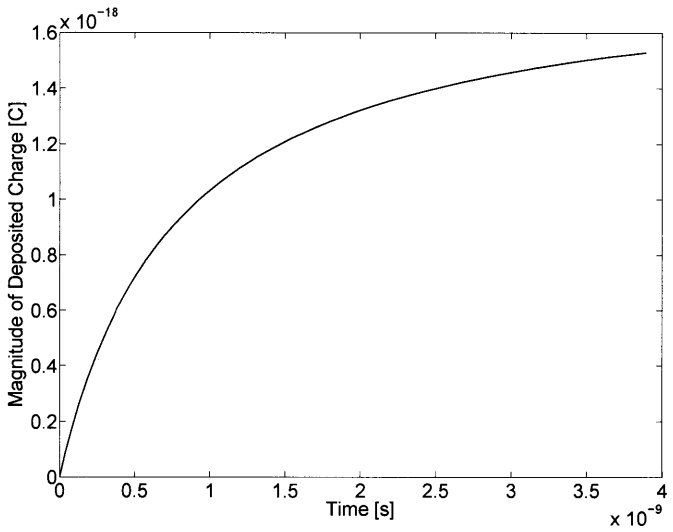

Figure 5.2: Charging dynamics, $|Q(t)|$, of a perfectly conducting nanoparticle versus time in transformer oil as given by (5.13) with $Q_s = -1.836 \times 10^{-18}$ C (approximately equals 11 electrons) and $\tau_{pc} = 7.79 \times 10^{-10}$ s.

Free charge carriers in the nanofluid will tend to move along the electric field lines that converge on the relaxed nanoparticle, depositing negative charge on the top surface and positive charge on the bottom surface of the particle in Fig. 5.1. Because electron mobility is much higher than positive ion mobility, the nanoparticles trap electrons at a much faster rate than positive ions, meaning that the nanoparticles effectively become slow negative ions. The mobility of such a charged spherical particle in transformer oil is given by Eq. (5.14) [148], where the viscosity of transformer oil is approximately $\eta = 0.02$ Pa·s.

$$\mu_{np} = \frac{|Q_s|}{6\pi\eta R} = 9.7 \times 10^{-10} \text{ m}^2\text{V}^{-1}\text{s}^{-1} \ . \tag{5.14}$$

5.2.2 Finitely Conducting Nanoparticle

In expanding the analysis to finitely conducting nanoparticles, it cannot be assumed that at $t = 0^+$ the nanoparticle is perfectly relaxed since σ_2 is not equal to infinity the surface charge distribution at $t{=}0^+$ on the nanoparticle is zero. Therefore, there will be some finite time to surface charge the nanoparticles, that is dependent on the particle and fluid conductivities and permittivities, in which the nanoparticle relaxes and polarizes to the applied electric field, such that the steady-state the field lines terminate and emanate perpendicular to the nanoparticle surface.

Negative charge deposition on a particle takes place where the radial component of the electric field distribution on the particle surface is positive. Initially, when the particle is uncharged the radial electric field on the particle is positive for $0<\theta<\pi/2$. However, once charge deposition occurs this situation changes and the area of the particle's surface with a positive radial field component decreases, ultimately going to $\theta = 0$ when the particle becomes fully charged and $Q = Q_s$. As charging occurs the section of the surface that can accept charge is defined by the polar angle θ. The critical angle, θ_c, demarcates the boundary position where the radial electric field is zero. For $0 < \theta < \theta_c$ the radial electric field is positive, while for $\theta_c < \theta < \pi$ the radial electric field is negative. For the perfectly conducting case illustrated in Fig. 5.1, at time $t=0^+$, negative charge can be deposited at all points from $\theta = 0$ to $\pi/2$, where $\theta_c = \pi/2$. As negative charge is deposited the critical angle θ_c decreases, which reduces the cylindrical radius of the charge collection window at $z \rightarrow +\infty$, $R_a(t)$, and increases the cylindrical radius at $z \rightarrow -\infty$, $R_b(t)$. Also, $\theta_c \rightarrow 0$ as $t \rightarrow \infty$, at which point the particle is fully charged and the radial electric field component is negative at every point on the particle's surface preventing any further electron charging of the nanoparticle.

To develop an expression for the charging dynamics of a particle of arbitrary material in transformer oil, the effect of the deposited charge on the electric field distribution outside the nanoparticle, $r > R$, must be accounted for. The deposited charge does not affect the electric field polar component Eq. (5.2), however it adds a point charge-like component to the radial component of the electric field of Eq. (5.1) that modifies it as

$$E_r(r,\theta) = E_0\left[1+\frac{2R^3}{r^3}\Upsilon_c\exp\left(-\frac{t}{\tau_r}\right)+\frac{2R^3}{r^3}\Sigma_c\left(1-\exp\left(-\frac{t}{\tau_r}\right)\right)\right]\cos\theta + \frac{Q(t)}{4\pi\epsilon_1 r^2}, \quad (5.15)$$

$$E_\theta(r,\theta) = E_0\left[-1+\frac{R^3}{r^3}\Upsilon_c\exp\left(-\frac{t}{\tau_r}\right)+\frac{R^3}{r^3}\Sigma_c\left(1-\exp\left(-\frac{t}{\tau_r}\right)\right)\right]\sin\theta. \quad (5.16)$$

As the relaxation time is non-zero, the charging angle has a stronger dependency on time compared to Eqs. (5.7)-(5.9). Once again, electrons are deposited on the nanoparticle where $E_r(r=R,\theta)\geq 0$ and the window for electron charging over a range of angles can be determined. The critical angle, θ_c, occurs exactly at $E_r(r=R,\theta)=0$ and is

$$\cos\theta_c = \frac{3Q(t)}{Q_s A(t)} \quad (5.17)$$

where Q_s is the nanoparticle's electron saturation charge of Eq. (5.8) and

$$A(t) = 1 + 2\Upsilon_c \exp\left(-\frac{t}{\tau_r}\right) + 2\Sigma_c\left[1 - \exp\left(-\frac{t}{\tau_r}\right)\right] . \tag{5.18}$$

The current density charging the nanoparticle for $0<\theta<\theta_c$ is

$$J_r = -\rho_e\mu_e E_r(r=R) = -3\rho_e\mu_e E_0\left[A(t)\cos\theta - \frac{Q(t)}{Q_s}\right] \tag{5.19}$$

and the nanoparticle charging rate is thus

$$\frac{dQ(t)}{dt} = -\int_{\theta=0}^{\theta_c} J_r 2\pi R^2 \sin\theta d\theta = \frac{3Q_s}{\tau_{pc}A(t)}\left[\frac{Q(t)}{Q_s} - \frac{A(t)}{3}\right]^2 \tag{5.20}$$

where Q_s, τ_{pc}, and $A(t)$ are given in equations Eqs. (5.8), (5.12), and (5.18) respectively. Note that for a perfectly conducting particle, $\sigma_2 \to \infty$, $\Sigma_c = 1$, $\tau_r \to 0$, and $A(t) = 3$. Then Eq. (5.20) reduces to Eq. (5.11).

5.2.3 Solution for the Electric Field Lines

Analysis is also facilitated through the use of a vector potential $\vec{A}$ for the electric field when the electric field due to the space charge density is small compared to the electric field due to the applied voltage such that $\nabla\cdot\vec{E}\approx 0$. Then with no dependence on the angle ϕ, the vector potential $\vec{A}=A_\phi(r,\theta)\vec{i}_\phi$ and the electric field are related as

$$\begin{aligned}\vec{E}(r,\theta) &= \nabla\times\vec{A}(r,\theta) \\ &= \frac{1}{r\sin\theta}\frac{\partial}{\partial\theta}(\sin\theta A_\phi)\vec{i}_r - \frac{1}{r}\frac{\partial}{\partial r}(rA_\phi)\vec{i}_\theta .\end{aligned} \tag{5.21}$$

From Eqs. (5.15) and (5.16) with Eq. (5.21) the vector potential is

$$A_\phi(r,\theta) = \frac{E_0 r\sin\theta}{2}\left[1 + \frac{2R^3}{r^3}\Upsilon_c\exp\left(-\frac{t}{\tau_r}\right) + \frac{2R^3}{r^3}\Sigma_c\left(1-\exp\left(-\frac{t}{\tau_r}\right)\right)\right] - \frac{Q(t)\cos\theta}{4\pi\epsilon_1 r\sin\theta} . \tag{5.22}$$

Electric field lines are everywhere tangent to the electric field and related to the vector potential in Eq. (5.21) as

$$\frac{dr}{rd\theta} = \frac{E_r}{E_\theta} = \frac{\frac{1}{r\sin\theta}\frac{\partial}{\partial\theta}(\sin\theta A_\phi)}{-\frac{1}{r}\frac{\partial}{\partial r}(rA_\phi)} . \tag{5.23}$$

After cross multiplication and reduction, the electric field lines are lines of constant $r\sin\theta A_\phi(r,\theta)$ because

$$d(r\sin\theta A_\phi(r,\theta)) = \frac{\partial}{\partial r}(r\sin\theta A_\phi)dr + \frac{\partial}{\partial\theta}(r\sin\theta A_\phi)d\theta = 0 \tag{5.24}$$

where the constant for a given electric field line is found by specifying one (r,θ) value of a point that the field line goes through.

5.2.3.1 Perfectly Conducting Nanoparticle

A perfectly conducting nanoparticle has $\tau_r = 0$ so that $e^{-t/\tau_r} = 0$, $\Sigma_c = 1$, and $A(t) = 3$. The field lines are obtained from Eq. (5.22) as

$$\begin{aligned}\Lambda_1(r,\theta) &= r\sin\theta A_\phi(r,\theta)\\ &= \frac{E_0 r^2\sin^2\theta}{2}\left[1+\frac{2R^3}{r^3}\right] - \frac{Q(t)\cos\theta}{4\pi\epsilon_1}\\ &= \text{constant}\,.\end{aligned} \tag{5.25}$$

The separation field line that demarcates the region where electrons charge a nanoparticle is shown by the thicker field line in Fig. 5.1 and terminates on the nanoparticle at $r = R$, $\theta = \theta_c$ where θ_c is given in Eq. (5.9). This field line obeys the equation

$$\begin{aligned}\Lambda_1(r=R,\theta=\theta_c) &= \frac{3E_0R^2\sin^2\theta_c}{2} - \frac{Q(t)\cos\theta_c}{4\pi\epsilon_1}\\ &= \frac{3E_0R^2}{2}\left[1+\left(\frac{Q(t)}{Q_s}\right)^2\right]\,.\end{aligned} \tag{5.26}$$

Evaluating Eq. (5.25) at $r\to\infty$, $\theta\to 0$ and equating it to Eq. (5.26) gives the cylindrical radius $R_a(t)$ of the electron charging demarcation field line of the upper hemisphere. The cylindrical radius is

$$R_a(t) = \lim_{\substack{r\to\infty\\ \theta\to 0}}(r\sin\theta) = \sqrt{3}R\left[1-\frac{Q(t)}{Q_s}\right] = \frac{\sqrt{3}R}{1+\dfrac{t}{\tau_{pc}}} \tag{5.27}$$

where Eq. (5.13) is used and $R_a(t)$ decreases with time as the particle charges up.

Similarly, there is a separation field line that passes through $(r=R,\ \theta=\theta_c)$ but terminates in the lower region at $r\to\infty$, $\theta\to\pi$ with cylindrical radius

$$R_b(t) = \lim_{\substack{r\to\infty\\ \theta\to\pi}}(r\sin\theta) = \sqrt{3}R\left[1+\frac{Q(t)}{Q_s}\right] = \sqrt{3}R\frac{2t+\tau_{pc}}{t+\tau_{pc}} \tag{5.28}$$

which separates field lines that terminate on the spherical nanoparticle for $\theta_c < \theta < \pi$ from field lines that go around the nanoparticle. The combined separation field line that passes through ($r=R$, $\theta=\theta_c$) and $r \to \infty$ and $\theta=0$ or π are drawn as thicker lines in Fig. 5.1.

The total current at $r \to \infty$ passing through the area $\pi R_a^2(t)$ is the total current incident onto the nanoparticle

$$I(t) = \rho_e \mu_e E_0 \pi R_a^2(t) = \frac{Q_s}{\tau_{pc}} \left[1 - \frac{Q(t)}{Q_s}\right]^2 \tag{5.29}$$

which matches the right-hand side of Eq. (5.11).

5.2.3.2 Finitely Conducting Nanoparticle

Similarly, the electric field lines for a finitely conducting nanoparticle are described by Eq. (5.30) which is also obtained from Eq. (5.22).

$$\begin{aligned} \Lambda_2(r,\theta) &= r \sin\theta A_\phi(r,\theta) \\ &= \frac{E_0 r^2 \sin^2\theta}{2}\left[1 + \frac{2R^3}{r^3}\Upsilon_c \exp\left(-\frac{t}{\tau_r}\right) + \frac{2R^3}{r^3}\Sigma_c\left(1 - \exp\left(-\frac{t}{\tau_r}\right)\right)\right] - \frac{Q(t)\cos\theta}{4\pi\epsilon_1} \\ &= \text{constant} \end{aligned} \tag{5.30}$$

The separation field line, which divides the field lines terminating on the nanoparticle from those going around the nanoparticles, terminates at $r = R$, $\theta = \theta_c$ where θ_c is given in Eq. (5.17) and is defined by

$$\begin{aligned} \Lambda_2(r=R,\, \theta=\theta_c) &= \frac{E_0 R^2 \sin^2\theta_c}{2} A(t) - \frac{Q(t)\cos\theta_c}{4\pi\epsilon_1} \\ &= \frac{E_0 R^2}{2} A(t)\left[1 + \left(\frac{3Q(t)}{Q_s A(t)}\right)^2\right]. \end{aligned} \tag{5.31}$$

At $r \to \infty$, $\theta \to 0$ this demarcation field line has a cylindrical radius of

$$R_a(t) = \lim_{\substack{r\to\infty \\ \theta\to 0}} (r\sin\theta) = \frac{3R}{\sqrt{A(t)}}\left|\frac{Q(t)}{Q_s} - \frac{A(t)}{3}\right|. \tag{5.32}$$

As was performed in Eq. (5.28), we evaluate Eq. (5.30) at $r \to \infty$, $\theta \to \pi$ to find the separation field line that passes through ($r=R$, $\theta=\theta_c$) from below with cylindrical radius at $z \to -\infty$

of

$$R_b(t) = \lim_{\substack{r\to\infty \\ \theta\to\pi}} (r\sin\theta) = \frac{3R}{\sqrt{A(t)}}\left|\frac{Q(t)}{Q_s} + \frac{A(t)}{3}\right| . \tag{5.33}$$

As a check, note that for a perfect conductor $A(t)=3$ so that Eq. (5.32) reduces to Eq. (5.27) and Eq. (5.33) reduces to Eq. (5.28).

Note that at $t=0$, $Q(t=0) = 0$ and

$$A(t=0) = 1 + 2\Upsilon_c = \frac{3\epsilon_2}{2\epsilon_1 + \epsilon_2} \tag{5.34}$$

so that

$$R_a(t=0) = R_b(t=0) = R\sqrt{A(t=0)} = R\sqrt{\frac{3\epsilon_2}{2\epsilon_1 + \epsilon_2}} . \tag{5.35}$$

If $\epsilon_2 \to \infty$, Eq. (5.35) reduces to $R_a(t=0) = \sqrt{3}R$ which is the same as for a perfectly conducting nanoparticle.

The total current at $r \to \infty$ passing through the area $\pi R_a^2(t)$ is the total current incident onto the nanoparticle

$$I(t) = \rho_e \mu_e E_0 \pi R_a^2(t) = \frac{3Q_s}{\tau_{pc} A(t)}\left[\frac{Q(t)}{Q_s} - \frac{A(t)}{3}\right]^2 \tag{5.36}$$

which matches the right-hand side of Eq. (5.20).

5.2.4 Evaluating Nanoparticle Charging

The solution to Eq. (5.20), which gives the temporal dynamics of the charge trapped on a nanoparticle in transformer oil, is not easily solved for analytically. As such, the symbolic solver from the software *Mathematica* [151] was used to obtain the solution. A closed form solution for $Q(t)$ does exist; however, its form is exceptionally long and complicated with numerous hypergeometric functions with complex number arguments. These factors mean that it is not possible to develop an intuitive feel for the time dependent charging dynamics. Surprisingly, by replacing general variables with numerical values (*e.g.*, $\epsilon_1 = 2.2\epsilon_0$, $\sigma_1 = 10^{-12}$ S/m, $\epsilon_2 = \epsilon_0$, $\sigma_2 = 0.01$ S/m, $\rho_e = -10^3$ C/m^3, $\mu_e = 10^{-4}$ m^{2}V^{-1}s^{-1}, $\tau_r = 4.78 \times 10^{-9}$ s, $\Upsilon_c = -0.222$, $\Sigma_c = 1$, $\tau_{pc} = 7.79 \times 10^{-10}$ s), the general solution reduces to Fig. 5.3.

Utilizing the general solution for $Q(t)$ the charging dynamics of particles manufactured with materials of varying electrical characteristics is explored. A number of interesting insights

```
q[t]

-(0.136364 e^-t (-2.44444 + 3. e^t)
    ((-1678.56 + 1264.37 i) Hypergeometric2F1[0.5 - 2.42618 i, 0.5 - 2.42618 i,
        1. - 4.85237 i, 1.22727 e^t] + (89.6397 - 106.441 i) (e^t)^(0.+4.85237 i)
      Hypergeometric2F1[0.5 + 2.42618 i, 0.5 + 2.42618 i, 1. + 4.85237 i, 1.22727 e^t] -
     (390.686 + 344.031 i) e^t Hypergeometric2F1[1.5 - 2.42618 i, 1.5 - 2.42618 i,
      2. - 4.85237 i, 1.22727 e^t] - (21.3425 + 27.0703 i) (e^t)^(1.+4.85237 i)
      Hypergeometric2F1[1.5 + 2.42618 i, 1.5 + 2.42618 i, 2. + 4.85237 i, 1.22727 e^t]))/
 ((426.225 - 746.594 i) Hypergeometric2F1[0.5 - 2.42618 i, 0.5 - 2.42618 i,
    1. - 4.85237 i, 1.22727 e^t] - (50.8991 - 25.4971 i) (e^t)^(0.+4.85237 i)
   Hypergeometric2F1[0.5 + 2.42618 i, 0.5 + 2.42618 i, 1. + 4.85237 i, 1.22727 e^t])
```

Figure 5.3: Screen-shot of the the closed form solution for $Q(t)$ in Eq. (5.20) generated by *Mathematica* when numerical values are given to each variable (*e.g.*, $\epsilon_1 = 2.2\epsilon_0$, $\sigma_1 = 10^{-12}$ S/m, $\rho_e = -10^3$ C/m^3, $\mu_e = 10^{-4}$ m^{2}V^{-1}s^{-1}, $\epsilon_2 = \epsilon_0$, $\sigma_2 = 0.01$ S/m, $\tau_r = 4.78 \times 10^{-9}$ s, $\Upsilon_c = -0.222$, $\Sigma_c = 1$, $\tau_{pc} = 7.79 \times 10^{-10}$ s).

into the charging dynamics of particles in transformer oil can be gained from analyzing $Q(t)$ for several values of nanoparticle permittivity and conductivity. For example, in Fig. 5.4 three particle conductivity values ($\sigma_2 = 0.01$, 0.1, 1 S/m) and permittivity values ($\epsilon_2 = \epsilon_0$, $10\epsilon_0$, $100\epsilon_0$) are examined, nine cases in all. The three conductivity values are chosen to highlight the large change in nanoparticle charging dynamics for a relatively small change in conductivity (*i.e.*, poor insulator ($\sigma_2 = 0.01$ S/m) to a poor conductor ($\sigma_2 = 1$ S/m)). The three permittivity values were chosen as most materials, such as those in Table 5.1, have permittivities that range between ϵ_0 and $100\epsilon_0$. Note, the values used for E_0, ρ_e, μ_e, R, ϵ_1, and σ_1 in Fig. 5.4 were the same as given in Section 5.2.1 (*i.e.*, $E_0 = 1 \times 10^8$ V/m, $\rho_e = -1000$ C/m^3, $\mu_e = 1 \times 10^{-4}$ m^{2}V^{-1}s^{-1}, $R = 5 \times 10^{-9}$ m, $\epsilon_1 = 2.2\epsilon_0$, and $\sigma_1 = 1 \times 10^{-12}$ S/m).

The results of Fig. 5.4 distinctly show that there is an upper limit to the nanoparticle charging rate in transformer oil. This limit appears to be linked to the particle's conductivity, with the upper limit being the perfect conductor case. Also, the nanoparticle charging dynamics appear to be less sensitive to variations in particle permittivity, where the permittivity insensitivity is particularly evident for particles whose conductivity is greater than 1 S/m.

For less conductive particles the initial charging rate is higher for particles with higher permittivity. This behavior is shown in Figs. 5.4(a) and 5.5, where the charging dynamics of a particle with a conductivity of 0.01 S/m are plotted. The explanation for this behavior is that at early times high permittivity particles will direct field lines to the particle, much like a good conducting particle, which will cause it to charge up quickly. However, from Eq. (5.3) it is likely that the charging rate of a higher permittivity particle would be lower than that of a low permittivity particle because a higher permittivity particle will have a

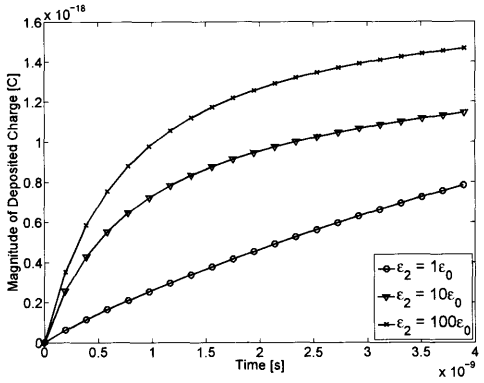

(a) $\sigma_2 = 0.01$ S/m

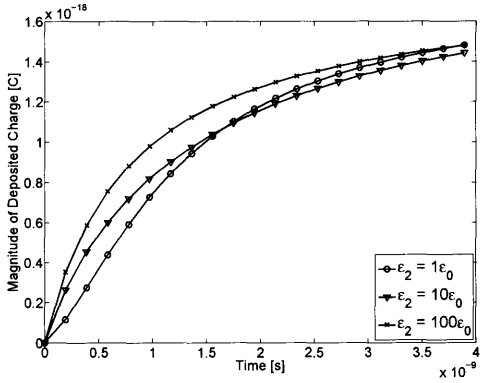

(b) $\sigma_2 = 0.1$ S/m

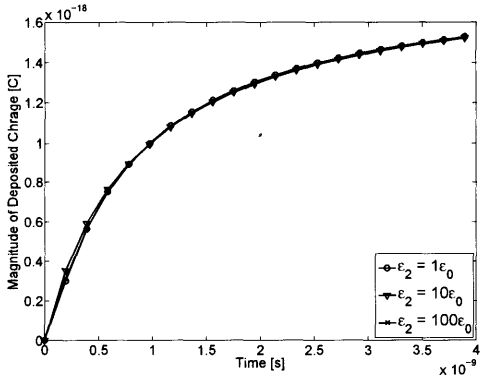

(c) $\sigma_2 = 1$ S/m

Figure 5.4: Charging dynamics, $|Q(t)|$, of a nanoparticle with constant conductivity σ_2 and varying permittivity $\epsilon_2 = 1\epsilon_0$ ($\bigcirc$), $10\epsilon_0$ ($\triangledown$), and $100\epsilon_0$ ($\times$) in transformer oil ($\sigma_1 = 1\times10^{-12}$ S/m, $\epsilon_1 = 2.2\epsilon_0$). The other charging parameter values used, such as E_0, ρ_e, μ_e, R, ϵ_1, and σ_1, are the same as given in Section 5.2.1 (*i.e.*, $E_0 = 1\times10^8$ V/m, $\rho_e = -1000$ C/m^3, $\mu_e = 1\times10^{-4}$ m^{2}V^{-1}s^{-1}, $R = 5\times10^{-9}$ m, $\epsilon_1 = 2.2\epsilon_0$, and $\sigma_1 = 1\times10^{-12}$ S/m).

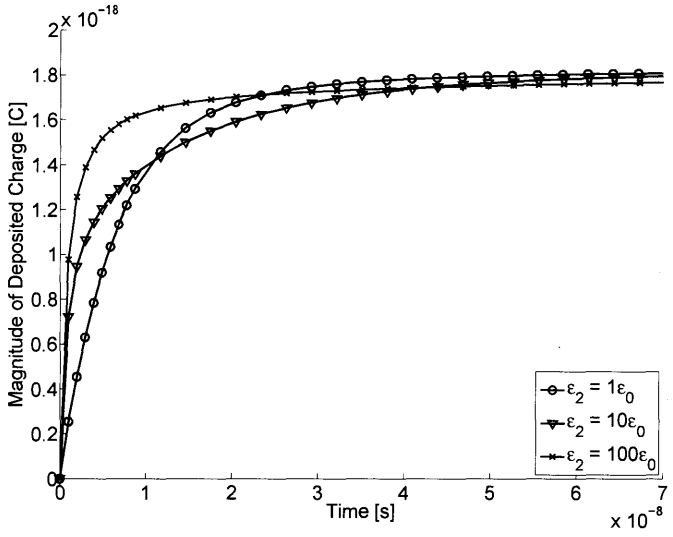

Figure 5.5: Initial 70 ns of the charging dynamics, $|Q(t)|$, for particles with conductivity $\sigma_2 = 0.01$ S/m and varying permittivity ϵ_2.

longer relaxation time τ_r for any given value of conductivity. Investigating the charging rate solution $Q(t)$ for a given conductivity value, a particle of higher permittivity will have a faster initial charging rate; however, particles of lower permittivity will ultimately reach charge saturation more quickly. Figure 5.5 shows the charging dynamics of a nanoparticle in transformer oil, where the nanoparticle conductivity is 0.01 S/m, for several different nanoparticle permittivities over a longer timescale than in Fig. 5.4. It is evident that the $100\epsilon_0$ nanoparticle has the fastest initial charging rate; however, after about 20 ns the $1\epsilon_0$ nanoparticle starts to charge faster and reaches saturation more quickly.

In the context of streamer development in a nanofluid, such as transformer oil with nanoparticle suspensions, the nanoparticle charging times must be fast to influence the creation of net space charge in the ionization zone, which creates the electric field enhancement in the fluid and drives streamers. Therefore, the nanoparticle charging times must be commensurate or shorter than the time needed for electrons to leave the ionization zone, such that the highly mobile electron is converted into a slow negative particle and the creation of net positive space charge is hindered. To assess the nanoparticle's ability to scavenge electrons and impact the electrodynamics in the high field ionization zone of the streamer tip, a preliminary calculation of the ion-electron separation is determined using representative values for streamers. For example, for streamers in transformer oil an electric field level of $E_0 = 1 \times 10^8$ V/m and a length of $d = 10\,\mu$m are typical for the ionization zone, while electron mobility $\mu_e = 1 \times 10^{-4}$ m^{2}V^{-1}s^{-1} is appropriate. Consequently, the electron velocity in the ionization zone is approximately $v_e = -\mu_e E_0 = -1 \times 10^4$ m/s and the corresponding time

required for the electrons to exit the ionization zone is $t_e = d/|v_e| = 1 \times 10^{-9}$ s. This exit time indicates the required nanoparticle charging time, such that nanoparticle charging effects the electrodynamics involved in the development of an electric field wave in a transformer oil-based nanofluid.

The charging dynamics of highly conductive particles (*i.e.*, those with a conductivity greater than 1 S/m) plotted in Fig. 5.4(c) indicate that during the electron sweep out time t_e a nanoparticle in the ionization zone can capture approximately $Q(t = t_e) \approx 1 \times 10^{-18}$ C or approximately six electrons. Therefore, the charging rate of conductive nanoparticles in transformer oil is enough to ensure the capture or trapping of six free electrons per nanoparticle in the ionization zone. Therefore, conductive nanoparticles, such as magnetite particles, which have been used to manufacture transformer oil-based nanofluids [23, 74–79], have the capability to capture free charge carriers at a sufficient rate to significantly modify the electrodynamic processes that drive streamer development in transformer oil-based nanofluids.

5.3 Bipolar Charging Dynamics of a Spherical Nanoparticle

We consider the charging of an isolated perfectly conducting sphere in an applied uniform electric field. At $t = 0$, the uniform z-directed dc electric field $\vec{E} = E_0 \vec{i}_z$ at infinity is turned on within a lossy dielectric with permittivity ϵ and conductivity σ where we take E_0 to be positive. The perfectly conducting sphere of radius R centered at $r = 0$ distorts the applied uniform electric field by instantaneously adding a dipole electric field due to positive surface charging on the upper $0 < \theta < \pi/2$ hemisphere and to negative surface charging on the lower $\pi/2 < \theta < \pi$ hemisphere. We assume that the electric field also ionizes the dielectric region surrounding the sphere with positive charge carriers with charge density ρ_+ and mobility μ_+ and negative charge carriers with charge density ρ_-, which is a negative quantity, and mobility μ_-. These two mobile charge carriers will be driven by the electric field to charge the sphere with total charge $Q(t)$ to be determined by this analysis.

We assume that the volume charge density from ρ_+ and ρ_- outside the perfectly conducting sphere for $r > R$ is small so that the electric field due to the volume charge density is much less than the applied electric field strength E_0. The electric field for $t > 0$ and $r > R$ is determined from solutions to Laplace's equation in spherical coordinates for the electrostatic scalar potential $\Phi(r, \theta, t)$. The total electric field, $\vec{E}(r, \theta, t) = -\nabla\Phi(r, \theta, t)$, is then due to the superposition of the imposed uniform electric field, the induced dipole field from the sphere surface charge with effective dipole moment $\vec{p} = 4\pi\epsilon R^3 E_0 \vec{i}_z$, and the Coulomb field from the net charge $Q(t)$ flowing onto the sphere from the mobile positive and negative charges. The

electric field for $t>0$ is then

$$\vec{E}(r,\theta,t) = \left[E_0\left(1+\frac{2R^3}{r^3}\right)\cos\theta + \frac{Q(t)}{4\pi\epsilon r^2}\right]\vec{i}_r - E_0\left[1-\frac{R^3}{r^3}\right]\sin\theta\,\vec{i}_\theta \quad r>R,\ t>0 \quad (5.37)$$

where $Q(t)$ will be determined in Section 5.3.3.

5.3.1 Solution for the Electric Field Lines

With the assumption of small volume charge density so that the resulting electric field from the volume charge is small compared to the applied electric field, $\vec{E} = E_0\vec{i}_z$, then $\nabla\cdot\vec{E}\approx 0$. The electric field can then be represented by the curl of a vector potential. With no dependence of the electric field on angle ϕ, the vector potential is of the form $\vec{A}(r,\theta)=A_\phi(r,\theta)\vec{i}_\phi$ and is related to the electric field as

$$\begin{aligned}\vec{E}(r,\theta) &= \nabla\times\vec{A}(r,\theta)\\ &= \frac{1}{r\sin\theta}\frac{\partial}{\partial\theta}(\sin\theta A_\phi)\vec{i}_r - \frac{1}{r}\frac{\partial}{\partial r}(rA_\phi)\vec{i}_\theta\ .\end{aligned} \quad (5.38)$$

From Eqs. (5.37) and (5.38), the vector potential is then

$$A_\phi(r,\theta) = \frac{E_0 r\sin\theta}{2}\left[1+\frac{2R^3}{r^3}\right] - \frac{Q(t)\cos\theta}{4\pi\epsilon r\sin\theta}\ . \quad (5.39)$$

Electric field lines are everywhere tangent to the electric field and related to the vector potential of Eq. (5.39) as

$$\frac{dr}{rd\theta} = \frac{E_r}{E_\theta} = \frac{\frac{1}{r\sin\theta}\frac{\partial}{\partial\theta}(\sin\theta A_\phi)}{-\frac{1}{r}\frac{\partial}{\partial r}(rA_\phi)}\ . \quad (5.40)$$

After cross multiplication and algebraic reduction of Eq. (5.40), the electric field lines are lines of constant $\Lambda(r,\theta)$ of the form

$$\begin{aligned}\Lambda(r,\theta) &= r\sin\theta A_\phi(r,\theta)\\ &= \frac{E_0 r^2\sin^2\theta}{2}\left[1+\frac{2R^3}{r^3}\right] - \frac{Q(t)\cos\theta}{4\pi\epsilon}\end{aligned} \quad (5.41)$$

where $\Lambda(r,\theta)$ is called the stream function with

$$d(\Lambda(r,\theta)) = d(r\sin\theta A_\phi(r,\theta)) = \frac{\partial}{\partial r}(r\sin\theta A_\phi)dr + \frac{\partial}{\partial\theta}(r\sin\theta A_\phi)d\theta = 0 \quad (5.42)$$

The solution to Eq. (5.42) is

$$\Lambda(r,\theta) = r\sin\theta A_\phi(r,\theta) = \text{constant} = \Lambda(r_0,\theta_0) = r_0\sin\theta_0 A_\phi(r_0,\theta_0) \tag{5.43}$$

where (r_0,θ_0) is a specified point that the field line, also called a streamline, passes through. The electric field line passing through the specified point (r_0,θ_0) is then

$$\begin{aligned}\Lambda(r,\theta) &= \frac{E_0 r^2\sin^2\theta}{2}\left[1+\frac{2R^3}{r^3}\right] - \frac{Q(t)\cos\theta}{4\pi\epsilon} \\ &= \Lambda(r_0,\theta_0) = \frac{E_0 r_0^2\sin^2\theta_0}{2}\left[1+\frac{2R^3}{r_0^3}\right] - \frac{Q(t)\cos\theta_0}{4\pi\epsilon}\,.\end{aligned} \tag{5.44}$$

5.3.2 Critical Points

Positive charge can only be deposited on the sphere where the radial component of electric field is negative, due to negative surface charge on the sphere, while negative charge can only be deposited on the sphere where the radial component of electric field is positive, due to positive surface charge on the sphere. The two adjacent charging regions then connect on the sphere at coordinate $(r=R,\theta=\theta_c)$ where the radial electric field is zero $E_r(r=R,\theta=\theta_c)=0$. θ_c is the critical polar angle on the sphere and is defined as

$$\cos\theta_c = -\frac{Q(t)}{Q_{s0}} \tag{5.45}$$

where

$$Q_{s0} = 12\pi\epsilon E_0 R^2 \tag{5.46}$$

and Q_{s0} is taken to be positive. The point at coordinate $(r=R,\theta=\theta_c)$ is called a critical point because both $E_r(r=R,\theta=\theta_c)$ and $E_\theta(r=R,\theta=\theta_c)$ are zero. Thus with $E_0>0$, the sphere charges negatively for $0<\theta<\theta_c$, where $E_r(r=R,\theta)>0$, and charges positively for $\theta_c<\theta<\pi$, where $E_r(r=R,\theta)<0$.

Letting $(r_0=R,\theta_0=\theta_c)$ be the specified point that the field line passes through, the equation of this special separation field line is

$$\begin{aligned}\Lambda(r,\theta) = \Lambda(r=R,\theta=\theta_c) &= \frac{E_0 r^2\sin^2\theta}{2}\left[1+\frac{2R^3}{r^3}\right] - \frac{Q(t)\cos\theta}{4\pi\epsilon} \\ &= \frac{3E_0R^2\sin^2\theta_c}{2} - \frac{Q(t)\cos\theta_c}{4\pi\epsilon} \\ &= \frac{3E_0R^2}{2}\left[1+\left(\frac{Q(t)}{Q_{s0}}\right)^2\right]\end{aligned} \tag{5.47}$$

where the last equality is obtained using Eqs. (5.45) and (5.46). This field line separates field lines starting at $z \to \pm\infty$ that terminate on the sphere from field lines that go around the sphere.

Evaluating Eq. (5.47) at $r \to \infty$, $\theta \to 0$ (*i.e.*, $\Lambda(r=R, \theta=\theta_c) = \Lambda(r \to \infty, \theta \to 0)$) gives the cylindrical radius $R_a(t)$ for negative charges at $z \to +\infty$ which terminate on the upper part of the sphere for $0 < \theta < \theta_c$.

$$R_a(t) = \lim_{\substack{r\to\infty \\ \theta\to 0}} (r \sin\theta) = \sqrt{3}R \left[1 + \frac{Q(t)}{Q_{s0}}\right] \tag{5.48}$$

Similarly, evaluating Eq. (5.47) at $r \to \infty$, $\theta \to \pi$ (*i.e.*, $\Lambda(r=R, \theta=\theta_c) = \Lambda(r \to \infty, \theta \to \pi)$) gives the cylindrical radius $R_b(t)$ for positive charges at $z \to -\infty$ which terminate on the lower part of the sphere for $\theta_c < \theta < \pi$.

$$R_b(t) = \lim_{\substack{r\to\infty \\ \theta\to \pi}} (r \sin\theta) = \sqrt{3}R \left[1 - \frac{Q(t)}{Q_{s0}}\right] \tag{5.49}$$

At $t=0$ when $Q(t=0)=0$ such that the sphere is initially uncharged then

$$R_a(t=0) = R_b(t=0) = \sqrt{3}R \; . \tag{5.50}$$

5.3.3 Total Current that Charges the Sphere

The total current due to positive and negative mobile ions and ohmic conduction that charges the sphere is then

$$\begin{aligned} I &= \frac{dQ(t)}{dt} \\ &= 2\pi R^2 \left\{ \int_{\theta=0}^{\theta_c} \rho_- \mu_- E_r(r=R) \sin\theta d\theta - \int_{\theta=\theta_c}^{\pi} \rho_+ \mu_+ E_r(r=R) \sin\theta d\theta - \int_{\theta=0}^{\pi} \sigma E_r(r=R) \sin\theta d\theta \right\} \\ &= \frac{Q_{s0}}{4\epsilon} \left\{ (\rho_+\mu_+ + \rho_-\mu_-) \left[1 + \left(\frac{Q(t)}{Q_{s0}}\right)^2\right] - 2(\rho_+\mu_+ - \rho_-\mu_-) \frac{Q(t)}{Q_{s0}} - \frac{4\sigma Q(t)}{Q_{s0}} \right\} \end{aligned} \tag{5.51}$$

where

$$E_r(r=R) = 3E_0 \cos\theta + \frac{Q(t)}{4\pi\epsilon R^2} \tag{5.52}$$

is obtained from Eq. (5.37). Then Eq. (5.51) can be re-written as

$$\frac{d}{dt}\left(\frac{Q(t)}{Q_{s0}}\right) = A \left\{ B \left[1 + \left(\frac{Q(t)}{Q_{s0}}\right)^2\right] - 2\left(\frac{Q(t)}{Q_{s0}}\right) \right\} \tag{5.53}$$

where

$$A = \frac{\rho_+\mu_+ - \rho_-\mu_- + 2\sigma}{4\epsilon}, \tag{5.54a}$$

$$B = \frac{\rho_+\mu_+ + \rho_-\mu_-}{\rho_+\mu_+ - \rho_-\mu_- + 2\sigma}. \tag{5.54b}$$

Note that $A>0$ and $-1\leq B\leq 1$. The non-dimensional charge $(Q(t)/Q_{s0})$ can then be found by integrating Eq. (5.53) subject to the initial condition that $Q(t=0)=0$

$$\frac{Q(t)}{Q_{s0}} = \frac{1}{B}\left\{1 - \sqrt{1-B^2}\tanh\left[At\sqrt{1-B^2} + \operatorname{arctanh}\left(\frac{1}{\sqrt{1-B^2}}\right)\right]\right\}. \tag{5.55}$$

Note, in Eq. (5.55) that the initial and steady-state solutions are

$$\frac{Q(t=0)}{Q_{s0}} = 0, \tag{5.56a}$$

$$\frac{Q(t\to\infty)}{Q_{s0}} = \frac{1-\sqrt{1-B^2}}{B}. \tag{5.56b}$$

The steady-state sphere charge is positive if B is positive $(\rho_+\mu_+ > -\rho_-\mu_-)$ and is negative if B is negative $(-\rho_-\mu_- > \rho_+\mu_+)$. Using Eq. (5.56) in Eqs. (5.48) and (5.49), the steady-state (*i.e.*, $t\to\infty$) cylindrical radii at $z\to\pm\infty$ are

$$R_a(t\to\infty) = \sqrt{3}R\left(\frac{B+1-\sqrt{1-B^2}}{B}\right), \tag{5.57a}$$

$$R_b(t\to\infty) = \sqrt{3}R\left(\frac{B-1+\sqrt{1-B^2}}{B}\right), \tag{5.57b}$$

where B is given in Eq. (5.54b).

5.3.4 Method to Check the Sphere Charging Current

The difference in the current that charges the sphere at $z\to-\infty$ for $0<r\sin\theta<R_b(t)$ and at $z\to+\infty$ for $0<r\sin\theta<R_a(t)$ must equal the current of Eq. (5.51) that charges the sphere. This provides a simple check of Eq. (5.51) because at $z\to\pm\infty$ the electric field is uniform, $\vec{E}=E_0\vec{i}_z$ so the current densities for sphere positive charging, $J_+(z\to-\infty)$, and sphere negative charging, $J_-(z\to+\infty)$, including ohmic current contributions are also uniform.

$$J_+(z\to-\infty) = (\rho_+\mu_+ + \sigma)E_0, \tag{5.58a}$$

$$J_-(z\to+\infty) = -(-\rho_+\mu_+ + \sigma)E_0. \tag{5.58b}$$

Then the total charging current is obtained by multiplying the current density $J_+(z\rightarrow-\infty)$ by the area $\pi R_b^2(t)$ and multiplying the current density $J_-(z\rightarrow+\infty)$ by $\pi R_a^2(t)$. Then summing the two current contributions using Eqs. (5.48) and (5.49) yields

$$\begin{aligned} I &= \frac{dQ(t)}{dt} \\ &= J_+(z\rightarrow-\infty)\pi R_b^2(t) + J_-(z\rightarrow+\infty)\pi R_a^2(t) \\ &= 3\pi R^2 E_0 \left\{ (\rho_+\mu_+ + \rho_-\mu_-)\left[1+\left(\frac{Q(t)}{Q_{s0}}\right)^2\right] - 2(\rho_+\mu_+ - \rho_-\mu_-)\frac{Q(t)}{Q_{s0}} - \frac{4\sigma Q(t)}{Q_{s0}} \right\}. \end{aligned} \tag{5.59}$$

The charging current given in Eq. (5.59) matches that in Eq. (5.51) where we recognize that

$$3\pi R^2 E_0 = \frac{Q_{s0}}{4\epsilon}. \tag{5.60}$$

5.3.5 Unipolar Charging of the Sphere

5.3.5.1 Positive Charging

The negative charge does not contribute to the charging current of the sphere if either ρ_- or μ_- is zero. Then for positive charging Eq. (5.54) reduces to

$$A = \frac{1}{\tau_+} + \frac{1}{2\tau_s}, \tag{5.61a}$$

$$B = \frac{2\tau_s}{\tau_+ + 2\tau_s}, \tag{5.61b}$$

where

$$\tau_+ = \frac{4\epsilon}{\rho_+\mu_+}, \tag{5.62a}$$

$$\tau_s = \frac{\epsilon}{\sigma}, \tag{5.62b}$$

are the positive mobile charge and ohmic relaxation time constants. If the dielectric medium is perfectly insulating, $\sigma=0$, then $\tau_s\rightarrow\infty$ so that Eqs. (5.55) and (5.61) greatly reduce to

$$A = \frac{1}{\tau_+}, \tag{5.63a}$$

$$B = 1, \tag{5.63b}$$

$$\frac{Q(t)}{Q_{s0}} = \frac{t}{t+\tau_+} \,. \tag{5.64}$$

5.3.5.2 Negative Charging

The positive charge does not contribute to the charging current of the sphere if either ρ_+ or μ_+ is zero. Then for negative charging Eq. (5.54) reduces to

$$A = \frac{1}{\tau_-} + \frac{1}{2\tau_s}, \tag{5.65a}$$

$$B = \frac{-2\tau_s}{\tau_- + 2\tau_s}, \tag{5.65b}$$

where

$$\tau_- = \frac{-4\epsilon}{\rho_-\mu_-} = \frac{4\epsilon}{|\rho_-|\mu_-}, \tag{5.66a}$$

$$\tau_s = \frac{\epsilon}{\sigma}, \tag{5.66b}$$

are the negative mobile charge and ohmic relaxation time constants. Note, the magnitude of negative charge density, $|\rho_-|$, is used in Eq. (5.66a) because ρ_- is a negative number so that τ_- is positive. If the dielectric medium is perfectly insulating, $\sigma = 0$, then $\tau_s \to \infty$ so that Eqs. (5.55) and (5.65) greatly reduce to

$$A = \frac{1}{\tau_-}, \tag{5.67a}$$

$$B = -1, \tag{5.67b}$$

$$\frac{Q(t)}{Q_{s0}} = \frac{-t}{t+\tau_-} \tag{5.68}$$

which agrees with unipolar electron charging of Eq. (5.13) with $\tau_- = \tau_{pc}$ and $Q_{s0} = -Q_s$.

Figure 5.6 plots unipolar positive charging described by Eqs. (5.61)-(5.64) for various values of τ_s/τ_+ and unipolar negative charging described by Eqs. (5.65)-(5.68) for various values of τ_s/τ_-. When $\tau_s \to \infty$ the positive charging is given by Eq. (5.64) and the negative charging is given by Eq. (5.68).

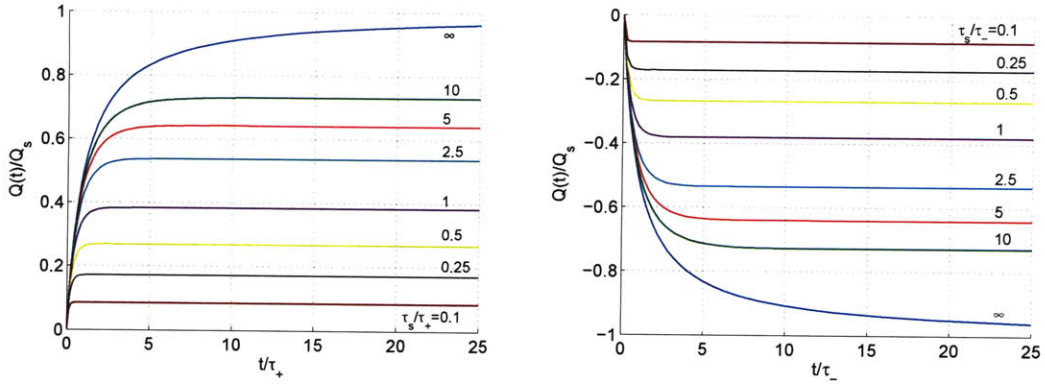

(a) $\rho_-\mu_- = 0$, $\tau_+ = \frac{4\epsilon}{\rho_+\mu_+}$ (b) $\rho_+\mu_+ = 0$, $\tau_- = \frac{-4\epsilon}{\rho_-\mu_-} = \frac{4\epsilon}{|\rho_-|\mu_-}$

Figure 5.6: Unipolar charging of a perfectly conducting sphere versus time for (a) positive mobile charge ($\rho_-\mu_- = 0$ for various values τ_s/τ_+) and for (b) negative mobile charge ($\rho_+\mu_+ = 0$ for various values of τ_s/τ_-). Note that the (a) positive charge plot has $Q(t) > 0$ for all time with time constant $\tau = \tau_+ = 4\epsilon/(\rho_+\mu_+)$ while the (b) negative charge half plot has $Q(t) < 0$ for all time with time constant $\tau = \tau_- = -4\epsilon/(\rho_-\mu_-) = 4\epsilon/(|\rho_-|\mu_-)$.

5.3.6 Bipolar Charging of the Sphere

We here consider in Fig. 5.7 the charge on the perfectly conducting sphere as a function of time assuming a lossless dielectric, $\sigma = 0$, for bipolar charging versus time for various values of $\rho_+\mu_+ > -\rho_-\mu_-$ for positive charging (Fig. 5.7(a)) and $-\rho_-\mu_- > \rho_+\mu_+$ for negative charging (Fig. 5.7(b)). With $\sigma = 0$, Eq. (5.54) reduces to

$$A = \frac{\rho_+\mu_+ - \rho_-\mu_-}{4\epsilon}, \tag{5.69a}$$

$$B = \frac{\rho_+\mu_+ + \rho_-\mu_-}{\rho_+\mu_+ - \rho_-\mu_-}. \tag{5.69b}$$

Note that the upper positive charge half of the plot has $\rho_+\mu_+ > -\rho_-\mu_-$ so that $Q(t) > 0$ for all time with time constant $\tau_+ = 4\epsilon/(\rho_+\mu_+)$ while the lower negative charge half of the plot has $-\rho_-\mu_- > \rho_+\mu_+$ so that $Q(t) < 0$ for all time with time constant $\tau_- = -4\epsilon/(\rho_-\mu_-) = 4\epsilon/(|\rho_-|\mu_-)$.

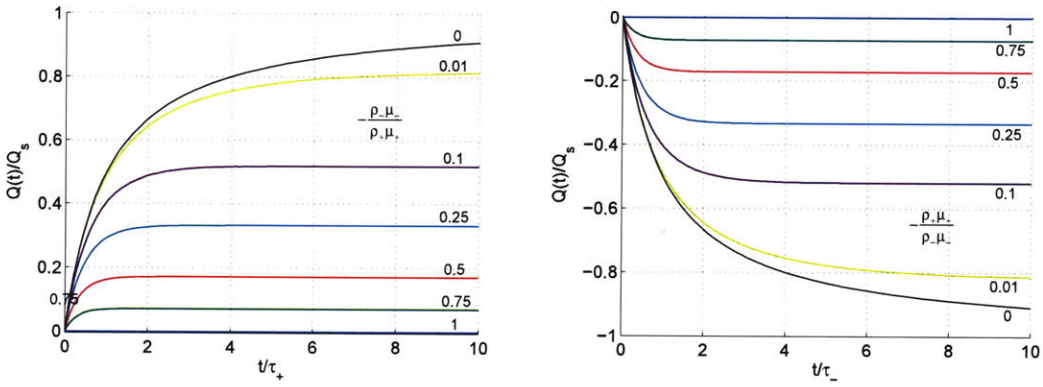

(a) $\rho_+\mu_+ > \rho_-\mu_-$, $\tau_+ = \frac{4\epsilon}{\rho_+\mu_+}$ (b) $-\rho_-\mu_- > \rho_+\mu_+$, $\tau_- = \frac{-4\epsilon}{\rho_-\mu_-} = \frac{4\epsilon}{|\rho_-|\mu_-}$

Figure 5.7: Perfectly conducting sphere in a perfectly insulating dielectric ($\tau_s \to \infty$) for bipolar charging versus time for various values of (a) $\rho_+\mu_+ > -\rho_-\mu_-$ for positive charging and (b) $-\rho_-\mu_- > \rho_+\mu_+$ for negative charging. Note that (a) the upper positive charge plot has $\rho_+\mu_+ > -\rho_-\mu_-$ so that $Q(t) > 0$ for all time with time constant $\tau = \tau_+ = 4\epsilon/(\rho_+\mu_+)$ while (b) the negative charge plot has $-\rho_-\mu_- > \rho_+\mu_+$ so that $Q(t) < 0$ for all time with time constant $\tau = \tau_- = -4\epsilon/(\rho_-\mu_-) = 4\epsilon/(|\rho_-|\mu_-)$.

5.4 Model of Streamer Propagation in Transformer Oil-Based Nanofluids

In Chapter 4, it was shown that field ionization is a key mechanism behind positive streamer development in transformer oil [25, 53, 73]. By ionizing oil molecules into slow positive ions and fast electrons, an area of net positive space charge quickly develops because the highly mobile electrons are swept away to the positive electrode from the ionization zone leaving behind the low mobility positive ions. The net homocharge modifies the electric field distribution in the oil such that the electric field at the positive electrode decreases while the electric field ahead of the positive charge in the oil increases. The new field distribution leads to ionization occurring further away from the positive electrode, which in turn causes further modification of the electric field distribution. The ultimate result of these electrodynamic processes is the development of an ionizing electric field wave, which is a moving dissipative source that raises the temperature to vaporize transformer oil and create a gas phase. This oil vaporization leads to the formation of the low density streamer channel in transformer oil [25, 53].

Streamer propagation in a transformer oil-based nanofluid is still dependent on field ionization in the same manner as it is in pure oil. However, the dynamics that take place in the nanofluid subsequent to this differ from those in pure oil, depending upon the nanoparticle

material's characteristics that determine the rate of nanoparticle charging. For a nanofluid manufactured using magnetite, the extremely short charging time of the nanoparticles, as shown by the analysis in Section 5.2, indicate that they are excellent electron trapping particles. Therefore, many of the mobile electrons produced by ionization are trapped before they can be swept away from the ionization zone. This alters the electrodynamics involved in the development of an electric field wave in the nanofluid such that they are significantly slower from those in pure oil.

5.4.1 Governing Equations and Model Parameters

The governing equations that contain the physics to model streamer development are based on the drift dominated charge continuity equations Eqs. (5.71)-(5.74) for positive ion (ρ_p), negative ion (ρ_n), electron (ρ_e), and charged nanoparticle (ρ_{np}) densities which are coupled through Gauss' Law Eq. (5.70) and include the thermal diffusion equation Eq. (5.75) to model temperature rise in oil. The negative ion, electron, and charged nanoparticle densities are negative quantities.

$$\nabla \cdot (\epsilon \vec{E}) = \rho_p + \rho_n + \rho_e + \rho_{np} \tag{5.70}$$

$$\frac{\partial \rho_p}{\partial t} + \nabla \cdot (\rho_p \mu_p \vec{E}) = G_F(|\vec{E}|) + \frac{\rho_p \rho_e R_{pe}}{q} + \frac{\rho_p(\rho_n + \rho_{np}) R_{pn}}{q} \tag{5.71}$$

$$\frac{\partial \rho_n}{\partial t} - \nabla \cdot (\rho_n \mu_n \vec{E}) = \frac{\rho_e}{\tau_a} - \frac{\rho_p \rho_n R_{pn}}{q} \tag{5.72}$$

$$\frac{\partial \rho_e}{\partial t} - \nabla \cdot (\rho_e \mu_e \vec{E}) = -G_F(|\vec{E}|) - \frac{\rho_p \rho_e R_{pe}}{q} - \frac{\rho_e}{\tau_a} - \frac{\rho_e}{\tau_{np}}(1 - H(\rho_{np,sat} - \rho_{np})) \tag{5.73}$$

$$\frac{\partial \rho_{np}}{\partial t} - \nabla \cdot (\rho_{np} \mu_{np} \vec{E}) = \frac{\rho_e}{\tau_{np}}(1 - H(\rho_{np,sat} - \rho_{np})) - \frac{\rho_p \rho_{np} R_{pn}}{q} \tag{5.74}$$

$$\frac{\partial T}{\partial t} + \vec{v} \cdot \nabla T = \frac{1}{\rho_l c_v}(k_T \nabla^2 T + \vec{E} \cdot \vec{J}\,) \tag{5.75}$$

As a check of correctness of signs in Eqs. (5.71)-(5.74), conservation of charge requires that the sum of the right-hand sides of Eqs. (5.71)-(5.74) must be zero. The $H(x)$ function in Eqs. (5.73) and (5.74) is the unit step defined as

$$H(x) = \begin{cases} 0 & x \leq 0 \\ 1 & x > 0\,. \end{cases} \tag{5.76}$$

Parameters μ_p, μ_n, μ_e, and μ_{np} are the mobilities of the positive ions (1×10^{-9} $\mathrm{m^2V^{-1}s^{-1}}$) [96], negative ions (1×10^{-9} $\mathrm{m^2V^{-1}s^{-1}}$) [96], electrons (1×10^{-4} $\mathrm{m^2V^{-1}s^{-1}}$) [97, 98] and charged nanoparticles ($\sim 1 \times 10^{-9}$ $\mathrm{m^2V^{-1}s^{-1}}$) from Eq. (5.14). For more information on

carrier mobility please refer to Section 3.4. R_{pn} and R_{pe} are the positive ion-negative ion and positive ion-electron recombination rates, respectively, and $R_{pn}=R_{pe}=1.64\times10^{-17}$ m^3/s as discussed in Section 3.5. The electron attachment time τ_a is 200 ns and is detailed in Section 3.6.

The electrodynamics are coupled to the oil's temperature through the $\vec{E}\cdot\vec{J}$ dissipation term in Eq. (5.75), where $\vec{J}=(\rho_p\mu_p-\rho_n\mu_n-\rho_e\mu_e-\rho_{np}\mu_{np})\vec{E}$ is the total current density. This term reflects the electrical power dissipation or Joule heating that takes place in the oil as a result of the motion of free charge carriers under the influence of the local electric field. Parameters ϵ, k_T, c_v, and ρ_l are the oil's permittivity ($2.2\epsilon_0$), thermal conductivity ($0.13\,\mathrm{Wm^{-1}K^{-1}}$), specific heat ($1.7\times10^3\,\mathrm{Jkg^{-1}K^{-1}}$), and mass density (880 kg/m^3), respectively, and these values are representative for transformer oil. In the time scales of interest for streamer formation, that is nanoseconds to microseconds, the oil's velocity is negligible such that no effects of fluid convection are included in Eqs. (5.71)-(5.75). The pertinent model parameters and their respective values are summarized in Table 3.1.

The charge generation term, $G_F(|\vec{E}|)$, models field ionization using the Zener model discussed in Section 3.7. The field ionization model is

$$G_F(|\vec{E}|)=\frac{q^2n_0a|\vec{E}|}{h}\exp\left(-\frac{\pi^2m^*a\Delta^2}{qh^2|\vec{E}|}\right). \tag{5.77}$$

The parameter values in the field ionization model correspond to those for low number density, low ionization potential aromatic molecules summarized in Table 4.1.

The boundary conditions applied to the streamer model of Eqs. (3.1)-(3.5) are:

- Gauss' Law Eq. (3.1): The sharp needle electrode is set to a V_0 step voltage at $t=0$ with respect to the grounded large sphere. The symmetry z-axis and the top, bottom and side insulating walls have the boundary condition of zero normal electric field components (*i.e.*, $\vec{n}\cdot\vec{E}=0$).
- Charge Transport Continuity Equations Eqs. (3.2)-(3.4): The boundary condition along the outer boundaries is zero normal flux ($\vec{n}\cdot\vec{J}_p=0$, $\vec{n}\cdot\vec{J}_n=0$, $\vec{n}\cdot\vec{J}_e=0$). In addition, the boundary condition at the electrodes is zero diffusive flux ($\vec{n}\cdot\nabla\rho_p=0$, $\vec{n}\cdot\nabla\rho_n=0$, $\vec{n}\cdot\nabla\rho_e=0$) where only free migration currents are permitted.
- Thermal Equation Eq. (3.5): All boundaries are set to zero normal thermal diffusive flux (*i.e.*, $\vec{n}\cdot\nabla T=0$) approximating the system to be adiabatic on the timescales of interest.

The mathematical model described by the set of equations above is solved numerically using the finite element method software package COMSOL Multiphysics [54]. The model

is analogous to that described in detail in Chapter 3 for transformer oil, however with the added nanoparticle species of Eq. (5.74) and its associated charge dynamics. In particular, the setup corresponds to the needle-sphere electrode geometry, as shown previously for the transformer oil case in Fig. 3.1 in Section 3.2. The applied voltage to the needle electrode is a 130 kV step voltage. The electrothermal model equations (5.70)-(5.75) are solved in their two dimensional form with azimuthal symmetry.

5.4.2 Modeling Nanoparticle Charging

The analytical solution for the charging dynamics of a perfectly conducting nanoparticle in a transformer oil-based nanofluid is given by Eq. (5.13). In practical terms, modeling the charging dynamics of the nanoparticles is approximated by a nanoparticle attachment time constant τ_{np}. As the electrons are captured by the nanoparticles they are converted into slowly moving negatively charged carriers. Therefore, this is reflected in the electron continuity equation (5.73), where the last right-hand side term accounts for the free electron reduction due to nanoparticle charging. Consequently, there is an increase in the concentration of negatively charged nanoparticles, which is modeled by the first right-hand side term of the nanoparticle continuity equation (5.74).

The nanoparticle attachment time constant, τ_{np}, defines the time scale over which the nanoparticle charging takes place. The analysis presented in Section 5.2.4 demonstrates that, in general, more conductive particles tend to charge faster, however there is an upper limit to the nanoparticle charging rate as shown in Fig. 5.4. The upper limit is approximated with $\tau_{np} = 2$ ns for highly conductive particles such as magnetite. Case studies for longer τ_{np} values, such as 5 and 50 ns, will also be presented as they provide insight into how the streamer dynamics change for more insulating nanoparticle materials.

To include nanoparticle charging in the electrodynamic model of Eqs. (5.70)-(5.75), it is necessary to account for the upper limit of free electrons that can be deposited on the nanoparticles. The nanoparticle charge density limit is $\rho_{np,sat} = n_{np} Q_s$, where n_{np} is the number density of nanoparticles and Q_s is given in Eq. (5.8). The unit step function, $H(\rho_{np,sat} - \rho_{np})$, is used in Eqs. (5.73) and (5.74), to model this charging limit, where

$$H(\rho_{np,sat} - \rho_{np}) = \begin{cases} 0 & |\rho_{np}| \leq |\rho_{np,sat}| \\ 1 & |\rho_{np}| > |\rho_{np,sat}| \,. \end{cases} \tag{5.78}$$

Note that ρ_{np} and $\rho_{np,sat}$ are both negative quantities. A reasonable value of $\rho_{np,sat} = -500$ C/m^3 was chosen, which correlates to a nanoparticle number density of $n_{np} \approx 2.7 \times 10^{20}$ m^{-3} with $Q_s = -1.836 \times 10^{-18}$ C. This $\rho_{np,sat}$ value is derived from the nanopar-

ticle charging analysis discussed in Section 5.2.4 along with assumptions regarding the composition of the transformer oil-based nanofluid. For example, assuming the magnetite nanoparticles have a radius $R = 5$ nm and the diluted nanofluid has a saturation magnetization $\mu_0 M_s = 10^{-4}$ T or 1 Gauss, where $\mu_0 = 4\pi \times 10^{-7}$ H/m, the magnetite volume is $V_{np} = 4\pi R^3/3 \approx 5.236 \times 10^{-25}$ m^3 and the volume fraction ϕ of magnetite nanoparticles in the nanofluid is

$$\phi = \frac{M_s}{M_d} = 1.79 \times 10^{-4} \tag{5.79}$$

where the domain magnetization $\mu_0 M_d$ of magnetite is 0.56T [152]. The nanoparticle charge density upper limit for trapping electrons $\rho^{\infty}_{np,sat}$ is then

$$\rho^{\infty}_{np,sat} = 11 \text{ electrons} \times \frac{-q}{V_{np}/\phi} = -600 \text{ C/m}^3 \tag{5.80}$$

but this assumes that the charging time is infinite. From Fig. 5.2, the perfectly conducting nanoparticle has charged to slightly under 80% of its total charge by $\tau_{np} = 2$ ns. Therefore, $\rho_{np,sat}$ is reduced from $\rho^{\infty}_{np,sat}$ and is chosen to be -500 C/m^3 corresponding to $\phi = 1.5 \times 10^{-4}$ to model the finite charging time of highly conductive nanoparticles such as magnetite.

5.5 Results and Discussion of Streamer Propagation in Transformer Oil-Based Nanofluids

The streamer model is modified for use in modeling the dynamics in transformer oil-based nanofluids by adding the extra nanoparticle attachment term in the electron charge continuity equation of Eq. (5.73) and adding the nanoparticle charge continuity equation of Eq. (5.74). This nanoparticle attachment term models the trapping of free electrons onto nanoparticles in the nanofluid. However, by setting the nanoparticle attachment time constant to $\tau_{np} \to \infty$ the presence of perfectly insulating nanoparticles can also be studied. The $\tau_{np} \to \infty$ simulation results give electric field, space charge and temperature dynamics that are identical to the pure oil case in Section 4.2 and confirms that insulating nanoparticles do not affect streamer propagation. The results also reveal that field ionization is a key contributor to the initiation and propagation of positive streamers in dielectric liquids.

5.5.1 Electric Field Dynamics

For nanoparticles made of conducting materials, whether poorly or perfectly conducting, the temporal dynamics will differ from those of pure oil. In Fig. 5.8, the electric field distributions along the needle-sphere electrode axis are plotted for the cases where $\tau_{np} = 2$,

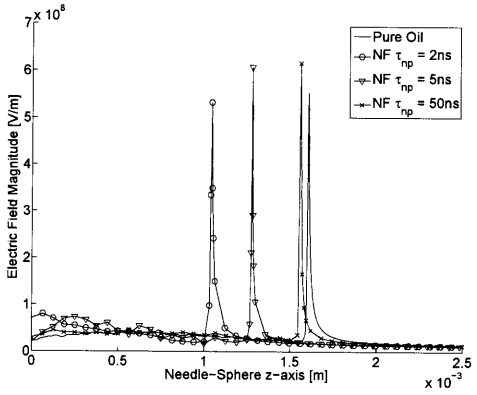

Figure 5.8: Electric field distribution along the needle-sphere z-axis at $t = 1$ μs given by the solutions to the streamer model of Eqs. (5.70)-(5.75) for the three nanofluid (NF) case studies with different nanoparticle attachment time constants τ_{np} and the pure transformer oil.

5, and 50 ns plus the pure oil case. The streamer propagation velocity for each of the three nanofluids is slower than that of pure transformer oil. This result reinforces the results of Segal *et al.* [23] in Table 2.3 , that the presence of conductive nanoparticles in transformer oil reduces positive streamer propagation velocity. Also, Fig. 5.8 shows that the most significant reduction in propagation velocity occurs in the nanofluid with $\tau_{np} = 2$ ns. This charging time constant represents the limiting case for highly conductive nanoparticles, such as those manufactured from magnetite.

The velocity of the electric field wave generated by the $\tau_{np} = 2$ ns nanofluid model case study after 1 μs is about 36% slower than the velocity of the electric field wave generated in pure oil [53]. This result confirms that the presence of conductive nanoparticles in transformer oil would reduce the velocity of the electric field wave generated by field ionization in the liquid and thereby decrease streamer velocity. The model results in an average positive streamer velocity decrease from 1.65km/s in pure transformer oil to 1.05km/s in the nanofluid. These velocities are extremely close to the average velocities obtained by Segal *et al.* [23] that are summarized in Table 2.3.

The electric field dynamics generated by the $\tau_{np} = 5$ and 50 ns case studies, shown in Fig. 5.8, illustrate that for increased nanoparticle charging times, and therefore decreased nanoparticle conductivities, the differences between the electric field dynamics in the pure oil and the oil-based nanofluid become less pronounced. This behavior shows that in order for nanoparticles to have an impact upon the electric field dynamics in transformers, the nanoparticles have to trap electrons on the nanosecond timescale associated with the sweep out of electrons from the ionization zone at the streamer tip. This requires highly conductive nanoparticles.

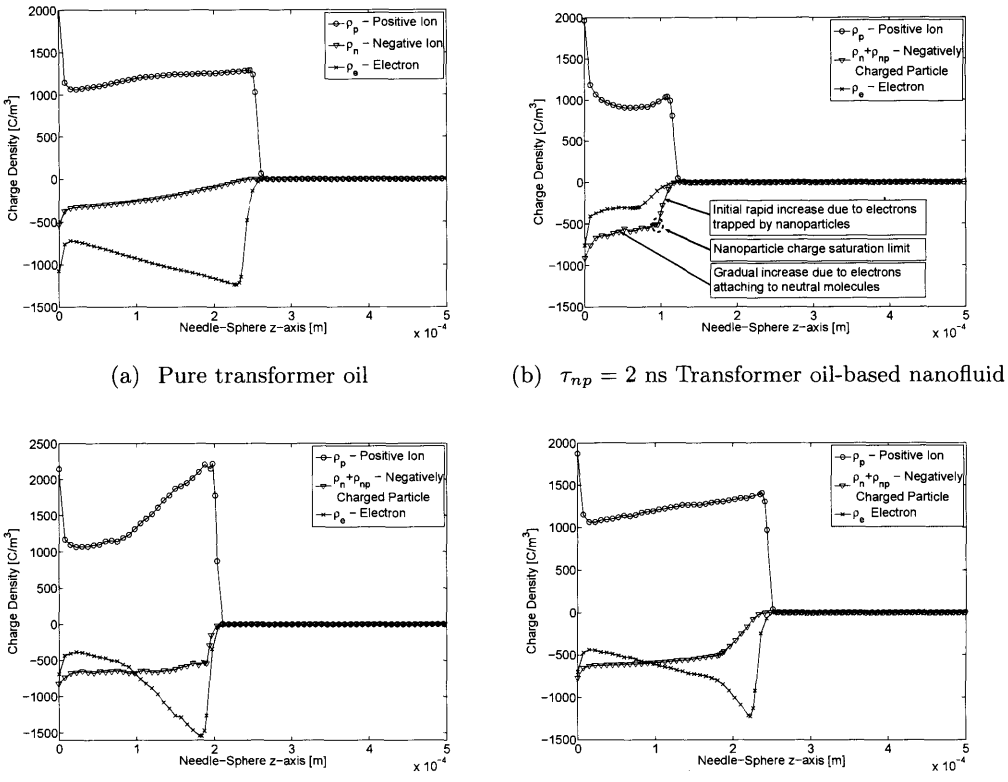

(a) Pure transformer oil

(b) $\tau_{np} = 2$ ns Transformer oil-based nanofluid

(c) $\tau_{np} = 5$ ns Transformer oil-based nanofluid

(d) $\tau_{np} = 50$ ns Transformer oil-based nanofluid

Figure 5.9: Charge density distributions along the needle-sphere z-axis at time $t = 0.1$ μs given by the solution to the streamer model for transformer oil and transformer oil-based nanofluid with $\rho_{np,sat} = -500$ C/m^3 and varying τ_{np}.

5.5.2 Charge Density Dynamics

Figure 5.9 plots the positive ion, negative charged particles (negative ions plus nanoparticles), and electron density distributions along the needle-sphere z-axis given by the solutions to the streamer model for the three nanofluid case studies ($\tau_{np} = 2$, 5 and 50 ns) and the pure oil case. These plots highlight the differences between the charge density dynamics in nanofluids and those in pure transformer oil, along with the differences which exist between nanofluids that are manufactured using nanoparticles with differing conductivities and permittivities that change the charge relaxation time constant τ_r in Eq. (5.3) and the nanoparticle attachment time constant τ_{np}.

The charge density distributions given by the solutions to the nanofluid case studies differ from those in pure oil. Figures 5.9(b), 5.9(c), and 5.9(d) illustrate the rapid creation of

negatively charged particles via the electron scavenging of conductive nanoparticles. This is in contrast with the pure oil case of Fig. 5.9(a), where the magnitude of the negative ion charge density distribution increases slowly from the streamer tip towards the needle electrode tip via electron attachment to neutral molecules. In contrast, for transformer oil with conductive nanoparticles the negatively charged particle density rises rapidly at first due to the trapping of electrons onto nanoparticles. Afterwards, as the nanoparticle saturation limit of $\rho_{np,sat} = -500$ C/m^3 is reached the negatively charged particle density transitions to a more gradual increase, which is attributed once again to the trapping of electrons onto neutral molecules creating negative ions.

The effectiveness of the nanofluid comprised of magnetite nanoparticles, where $\tau_{np} = 2$ ns, to trap electrons is illustrated and labeled in Fig. 5.9(b). Unlike the pure oil case, the magnitude of the negatively charged particle density rises rapidly at first in the ionization zone, thereby significantly decreasing the electron density. Afterwards, it transitions to a more gradual increase after the nanofluid charge density saturation is reached. Due to the efficient trapping of the fast electrons by the low mobility nanoparticles the development of a net space charge zone at the streamer tip is hindered, suppressing the propagating electric field wave that drives field ionization. This behavior results in a major reduction in the velocity of the electric field wave for the nanofluids compared to the pure oil case, as seen in Fig. 5.8.

In the previous section it was shown that nanoparticles must effectively trap electrons generated in the ionization zone to have an affect on the electrodynamics involved in streamer propagation. Interestingly though, the electrodynamics may still differ from the pure oil for nanofluids where the nanoparticle attachment time constants are longer than the electron exit time. This results because any additional generation of negatively charged nanoparticles at the expense of electrons above the normal level (*i.e.*, pure oil without nanoparticles) results in an increased potential drop in the streamer tail. Subsequently, the increase in potential drop will deprive the streamer tip of driving potential, ultimately resulting in the streamer slowing or even stopping.

For example, in Fig. 5.9(d) the longer attachment time constant $\tau_{np} = 50$ ns results in a differing nanoparticle charging dynamic than for $\tau_{np} = 2$ ns. In particular, the generation and exiting of electrons from the ionization zone is similar to pure oil due to the long time constant, however, the nanoparticle-electron attachment resembles a faster version of the electron attachment to neutral molecules. The maximum magnitude of the electron charge density distribution in the ionization zone is not reduced by nanoparticle charge attachment, rather the attachment modifies the electron charge density distribution in the streamer tail where its magnitude value is higher than compared to the pure oil case. The

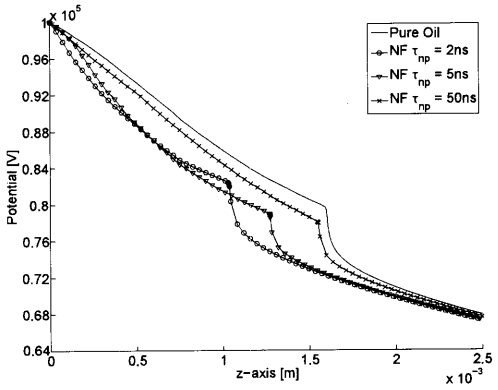

Figure 5.10: Electric potential distribution along the needle-sphere z-axis at $t=1$ μs given by the solution of the nanofluid field ionization case studies and the equivalent solution in pure oil. The needle tip is at $z=0$ and the streamer tail is to the left of the knee, where the slope changes dramatically, in each electric potential plot. The location of the streamer tip is at the knee in each electric potential plot.

reduced electron number density and subsequently higher number density of slow negatively charged nanoparticles in the streamer body results in a lower tail conductivity.

5.5.3 Electric Potential

Figure 5.10 plots the potential distributions along the needle-sphere z-axis given by the solutions to the field ionization model for the three nanofluids case studies and the pure transformer oil case, at $t=1$ μs after the application of the 130 kV step voltage excitation. The key observation is that within the streamer channel region the potential drop per unit distance is greater for all nanofluid cases when compared to pure oil. This result reinforces the argument in Section 5.5.2, that even for nanofluids manufactured with insulating nanoparticles, such as the $\tau_{np}=5$ and 50 ns cases, the electrodynamics are still altered due to the slower scavenging of electrons by the nanoparticles in the streamer tail, which is to the left of the knee where the slope changes dramatically in each electric potential plot of Fig. 5.10, and hence the decrease in tail conductivity.

Generally, any nanoparticle-electron attachment in nanofluids traps highly mobile electrons and hinders space charge development via the production of low mobility negatively charged nanoparticles. Not only does this decrease field enhancement at the streamer tip due to lower space charge levels, but it also reduces the electrical conductivity thereby increasing the potential drop along the streamer channel. This greater potential drop results in less drive potential and field enhancement at the streamer tip in a nanofluid than in pure oil.

Therefore, the level of ionization at the streamer tip in a nanofluid is less than that of pure oil, which results in slower streamer propagation velocity in the nanofluid.

5.6 Summary and Key Results

This chapter extends a theory to explain the differences observed between the electrical breakdown characteristics of transformer oil and transformer oil-based nanofluids. A general expression for the charging of nanoparticles in a dielectric liquid is presented and it is shown that the charge relaxation time constant τ_r and the charging time constant τ_{pc} from Eqs. (5.3) and (5.12) of conductive nanoparticles, such as magnetite ($\tau_r = 7.47 \times 10^{-14}$ s, $\tau_{pc} = 7.79 \times 10^{-10}$s), in transformer oil is much faster than the microsecond timescale involved in streamer development in transformer oil. Therefore, for the purposes of streamer analysis assuming approximately infinite conductivity for conductive magnetite nanoparticles is justified.

The generalized analysis of the unipolar and bipolar charging dynamics for spherical conducting nanoparticles including ohmic loss of the surrounding dielectric liquid is derived. Applying the nanoparticle charging models, a complete electrodynamic streamer model in a transformer oil-based nanofluid is developed. The simulation study shows that streamer propagation is hindered because the charging of slow conductive nanoparticles by electrons in the ionization zone changes fast electrons into slow negatively charged nanoparticles that modifies the electrodynamics in the oil and slows the propagation of positive streamers.

The key property of nanoparticle material is that it must be highly conductive, rather than magnetic like magnetite, such that when added to the oil they effectively trap electrons, which results in a significant reduction in streamer speed offering improved high voltage performance and reliability. Therefore, the analysis of this chapter can be generalized to many different materials and have broader implications, when extended from the magnetite material studied by early oil-based nanofluid researchers [23, 74–79].

Chapter 6

General Electrodynamic Models for Multi-Dielectric Systems

A SIGNIFICANT portion of power transformers, transmission cables, and other high voltage equipment have composite insulation systems, that is they are insulated with several different types of insulators. Often these insulators comprise both solid and fluid insulating materials. A common solid insulator for power transformers and cables is oil-impregnated paper like cellulose, which is often called pressboard. Liquid-solid systems such as transformer oil-pressboard systems constitute the major composite insulation system that is used to improve the insulation capability of power transformers. Therefore, it is important to understand the influence of adding solid insulation to dielectric liquid systems, such as transformer oil, and how streamer dynamics are affected.

6.1 Modeling Solid Insulators

Adding solid insulation to the liquid model of Chapter 3 may seem trivial, however there are many fine details that must be considered and investigated. One particular example of this is that by adding solid insulation to the liquid model, a two-region system is formed that requires equations that govern the relationship at the liquid-solid interface. Complicating the issue further is, unlike the liquid model that uses a migration model where charge carriers and their dynamics are specifically modeled via charge densities and mobilities, there are several ways to model solid insulation. These model types are:

- Migration Model: Based upon charge transport continuity equations for each carrier coupled through Gauss' Law.
- Ohmic Model: Based upon bulk conductivity and permittivity of dielectric material.
- Insulator Model: The bulk conductivity is zero and the material is only characterized by a permittivity only.

Each model of the solid insulator requires unique governing equations and special consideration for the liquid-solid interface. The focus of modeling liquid-solid insulation systems is to investigate streamers that form in the dielectric liquid and tend to travel near or along the liquid-solid interface. Therefore, puncturing or breakdown of the solid insulation is not considered and consequently the modeling of complex charge generation and recombination mechanisms in the solid insulation bulk is ignored. On the other hand, the interface between the liquid and solid will be examined closely and shown to play an important role in streamer development.

This section gives a detailed description of each model's governing equations. In subsequent sections, these models will be used with the migration liquid model presented in Chapter 3 to develop a complete composite liquid-solid insulation model with correct interfacial boundary conditions.

Within this section, variables appended with a superscript "s" and "l" denote that the variable exists in the solid and liquid insulation, respectively.

6.1.1 Migration Model

During the discourse of modeling streamer development in dielectric liquids, two main types of equations were used to model the electrodynamic system:

- Gauss' Law (Poisson's equation)
- Drift-dominated charge transport continuity equation for each charge carrier

The same type of modeling can be used for solid insulation with several modifications.

The generalized migration model equations for a solid insulator are based upon a three charge carrier system (6.2)-(6.4) of positive ion (ρ_p), negative ion (ρ_n) and electron (ρ_e) charge densities coupled through Gauss' Law (6.1). The negative ion and electron charge densities are negative quantities. The continuity equations (6.2)-(6.4) have no charge generation and recombination source terms on their right-hand sides since we are interested in the phenomenon at the interface as the streamer approaches the solid insulator from the

liquid.

$$\nabla \cdot \epsilon_r^s \epsilon_0 \vec{E}^s = \rho_p^s + \rho_n^s + \rho_e^s \tag{6.1}$$

$$\frac{\partial \rho_p^s}{\partial t} + \nabla \cdot \vec{J_p}^s = 0 \tag{6.2}$$

$$\frac{\partial \rho_n^s}{\partial t} + \nabla \cdot \vec{J_n}^s = 0 \tag{6.3}$$

$$\frac{\partial \rho_e^s}{\partial t} + \nabla \cdot \vec{J_e}^s = 0 \tag{6.4}$$

Note that

$$\vec{J_p}^s = \rho_p^s \mu_p^s \vec{E}^s, \tag{6.5}$$

$$\vec{J_n}^s = -\rho_n^s \mu_n^s \vec{E}^s, \tag{6.6}$$

$$\vec{J_e}^s = -\rho_e^s \mu_e^s \vec{E}^s \tag{6.7}$$

are the charge carrier current densities. The charge transport equations define total conduction current density as a function of charge densities ρ_p^s, ρ_n^s and ρ_e^s, carrier mobilities μ_p^s, μ_n^s and μ_e^s, and electric field $\vec{E}^s$.

$$\begin{aligned} \vec{J}^s &= \vec{J_p}^s + \vec{J_n}^s + \vec{J_e}^s \\ &= \left(\rho_p^s \mu_p^s + \rho_n^s \mu_n^s + \rho_e^s \mu_e^s\right) \vec{E}^s \end{aligned} \tag{6.8}$$

The superscript "s" in the relative permittivity ϵ_r^s and carrier mobilities (positive ion μ_p^s, negative ion μ_n^s and electron μ_e^s) is a reminder that these parameter values are for the solid insulation.

Since free charge carriers are not generated in the solid insulator bulk (*i.e.*, there are no charge generation mechanisms modeled), they exist only when charge carriers are transported from the liquid dielectric across the interface into the solid. The boundary conditions at the interface are chosen such that no surface charge build up is assumed and Maxwell's equations are satisfied. In particular, the potential V is continuous across the boundary and the normal components of positive ion, negative ion and electron current densities are

$$\vec{n} \cdot \left(\rho_p^l \mu_p^l \vec{E}^l\right) = \vec{n} \cdot \left(\rho_p^s \mu_p^s \vec{E}^s\right), \tag{6.9}$$

$$\vec{n} \cdot \left(\rho_n^l \mu_n^l \vec{E}^l\right) = \vec{n} \cdot \left(\rho_n^s \mu_n^s \vec{E}^s\right), \tag{6.10}$$

$$\vec{n} \cdot \left(\rho_e^l \mu_e^l \vec{E}^l\right) = \vec{n} \cdot \left(\rho_e^s \mu_e^s \vec{E}^s\right), \tag{6.11}$$

such that they are forced to be continuous across the interface. The vector $\vec{n}$ is the unit vector normal to the liquid-solid interface from the liquid side. Note, the superscript "l"

is used to denote and differentiate the dielectric liquid variables and the total conduction current in the dielectric liquid volume is

$$\vec{J}^l = \left(\rho_p^l \mu_p^l - \rho_n^l \mu_n^l - \rho_e^l \mu_e^l\right) \vec{E}^l. \tag{6.12}$$

The interfacial boundary condition equations (6.9)-(6.11) assume there is no surface charge density ρ_s at the interface

$$\begin{aligned} \rho_s &= \int_{-\infty}^{t} \vec{n} \cdot \left(\vec{J}^l - \vec{J}^s\right) d\tau \\ &= \int_{-\infty}^{t} \vec{n} \cdot \left[\left(\vec{J}_p^l + \vec{J}_n^l + \vec{J}_e^l\right) - \left(\vec{J}_p^s + \vec{J}_n^s + \vec{J}_e^s\right)\right] d\tau \\ &= \int_{-\infty}^{t} \vec{n} \cdot \left[\left(\rho_p^l \mu_p^l - \rho_n^l \mu_n^l - \rho_e^l \mu_e^l\right) \vec{E}^l - \left(\rho_p^s \mu_p^s - \rho_n^s \mu_n^s - \rho_e^s \mu_e^s\right) \vec{E}^s\right] d\tau \\ &= 0\,. \end{aligned} \tag{6.13}$$

This boundary condition ensures all ions and electrons that come to the surface are "swept" across the interface. This assumption will be further discussed in Section 6.2.1.

From here on, a dielectric modeled with governing equations similar to equations (6.1)-(6.4) will be referred to as a migration model, as they explicitly describe the migration transport of charge carriers.

6.1.2 Ohmic Model

In most dielectrics, where electric field levels are not high enough to cause pre-breakdown phenomena, the total free charge carrier density is small and in equilibrium such that there is no net space charge. Consequently, such a dielectric can be simplified to an ohmic model. To contrast this, for transformer oil under extreme voltage stress conditions the net space charge density in the dielectric is a function of space and time making a constant ohmic conductivity model not suitable. In the highly stressed transformer oil, there are large variations in conductivity due to the generation of charge carriers near the streamer tip via ionization as described in Chapter 4. Conversely, dielectrics where pre-breakdown phenomena does not occur within the bulk medium, for example the solid insulation we have discussed, can readily be modeled using a bulk conductivity and permittivity.

The conduction current is derived from the equal magnitude positive and negative charge carrier concentrations $|\rho_0|$ and their respective carrier mobilities μ_+^s and μ_-^s such that

$$\begin{aligned} \vec{J}^s &= \vec{J_+}^s + \vec{J_-}^s \\ &= |\rho_0| \left(\mu_+^s + \mu_-^s\right) \vec{E}^s \\ &= \sigma^s \vec{E}^s \end{aligned} \tag{6.14}$$

where the solid insulator's conductivity is

$$\sigma^s = |\rho_0|(\mu_+^s + \mu_-^s). \tag{6.15}$$

This type of modeling combines the separate charge transport equations into one. The following is the electrodynamic system equations for a material defined by constant conductivity σ^s.

$$\nabla \cdot \epsilon_r^s \epsilon_0 \vec{E}^s = \rho \tag{6.16}$$

$$\frac{\partial \rho}{\partial t} + \nabla \cdot \left(\sigma \vec{E}^s\right) = 0 \tag{6.17}$$

The two system equations can be combined, by substituting for the total charge density ρ, to give the governing equation

$$\nabla \cdot \epsilon_r^s \epsilon_0 \frac{\partial \vec{E}^s}{\partial t} + \nabla \cdot \left(\sigma^s \vec{E}^s\right) = 0 \tag{6.18}$$

In this system description, the notion of charge density is lost. There is a direct relation between the electric field and current density from Ohm's law such that (6.14)-(6.18) will be referred to as the ohmic model.

Unlike the migration model, the interfacial boundary condition for the ohmic model, which links the liquid and solid volumes, is such that the normal component of the conduction current density in the liquid and solid are not modeled to be equal.

$$\begin{aligned} \vec{n} \cdot \vec{J}^l &= \vec{n} \cdot \left(\rho_p^l \mu_p^l - \rho_n^l \mu_n^l - \rho_e^l \mu_e^l\right) \vec{E}^l \\ &\neq \vec{n} \cdot \vec{J}^s \\ &= \sigma^s \vec{E}^s \ . \end{aligned} \tag{6.19}$$

This ultimately means a surface charge density ρ_s builds up at the interface

$$\begin{aligned} \rho_s &= \int_{-\infty}^{t} \vec{n} \cdot \left(\vec{J}^l - \vec{J}^s \right) d\tau \\ &= \int_{-\infty}^{t} \vec{n} \cdot \left[\left(\rho_p^l \mu_p^l - \rho_n^l \mu_n^l - \rho_e^l \mu_e^l \right) \vec{E}^l - \sigma^s \vec{E}^s \right] d\tau. \end{aligned} \tag{6.20}$$

The other boundary condition is that the potential V is continuous at the liquid-solid interface. By applying these boundary conditions the following current continuity is upheld

$$\vec{n} \cdot \left[\vec{J}^l + \epsilon_r^l \epsilon_0 \frac{\partial \vec{E}^l}{\partial t} \right] = \vec{n} \cdot \left[\vec{J}^s + \epsilon_r^s \epsilon_0 \frac{\partial \vec{E}^s}{\partial t} \right]. \tag{6.21}$$

6.1.3 Insulator Model

Investigating the literature, there has been little or no past work done on modeling liquid-solid insulation systems to better understand the interesting phenomena that occurs during streamer development. However, there is a large body of modeling work related to dielectric barrier discharge (DBD) systems. These models investigate the interaction between an electrical discharge in a highly insulating gas (*i.e.*, air, nitrogen, xenon) with a solid dielectric barrier [135,153–156]. Applications of this work are for DBD actuators that modify/control the flow of a gas near the interface [135,153,154] and excimer lamps [155]. In [135,153,154], all volume charge in the dielectric liquid that travel toward the interface is converted to surface charge. Conversely, in [156] the solid is perfectly insulating such that all charge in the liquid coming towards the interface is impeded at the interface, eventually migrating or diffusing back into the volume or traveling along the interface. Adsorption of volume charge from the fluid to the dielectric interface, desorption of the surface charge to the fluid volume, and recombination of surface charges are taken into consideration in [155]. Unfortunately, the rate constants for adsorption, desorption, and recombination need to be known, which is not often the case. All these works model the solid dielectric as a perfect insulator, and therefore all the current density in the solid dielectric is displacement current.

These models assume that for timescales related to plasma discharges (*i.e.*, nanosecond to microsecond timescales), there is no penetration and flow of charge carriers within the volume of the solid dielectric. Also, puncturing of the solid dielectric is not considered. This type of modeling for the solid dielectric has merit as the liquid-solid studies in this thesis are focused on streamer propagation along or near the interface and the interactions that occur at the interface itself, rather than direct puncturing of the solid insulator.

The governing equation for the insulator model is

$$\nabla \cdot (\epsilon_r^s \epsilon_0 \vec{E}) = 0, \tag{6.22}$$

where there is no conduction of charge carriers (*i.e.*, $\mu_p^s = 0$, $\mu_n^s = 0$, $\mu_e^s = 0$) and zero conductivity (*i.e.*, $\sigma^s = 0$). Consequently, the conduction current in the solid insulator is zero and the total current density is only displacement current.

Due to the zero conductivity of the solid insulator, the boundary condition at the liquid-solid interface is such that two extreme cases can occur:

1. All volume charges (positive ion ρ_p^l, negative ion ρ_n^l, and electron ρ_e^l) in the liquid that travel to the interface are impeded by the solid and remain as volume charge in the dielectric liquid bulk, albeit very near to the surface.
2. All volume charges (positive ion ρ_p^l, negative ion ρ_n^l, and electron ρ_e^l) in the liquid that travel to the interface are converted to a surface charge density ρ_s.

There can be cases in between these two extremes, where only a percentage of the volume charge is converted to surface charge. However, since the two extremes listed above are the limiting cases, their dynamics encompass the others.

The surface charge density of case 2 can be calculated as:

$$\begin{aligned} \rho_s &= \int_{-\infty}^{t} \vec{n} \cdot \left(\vec{J}^l - \vec{J}^s \right) d\tau \\ &= \int_{-\infty}^{t} \vec{n} \cdot \left[\left(\rho_p^l \mu_p^l - \rho_n^l \mu_n^l - \rho_e^l \mu_e^l \right) \vec{E}^l - 0 \right] d\tau \\ &= \int_{-\infty}^{t} \vec{n} \cdot \left(\rho_p^l \mu_p^l - \rho_n^l \mu_n^l - \rho_e^l \mu_e^l \right) \vec{E}^l \, d\tau, \end{aligned} \tag{6.23}$$

where the volume charges (positive ion ρ_p^l, negative ion ρ_n^l, and electron ρ_e^l) in the liquid travel to the interface and are converted into surface charge. The other boundary condition is that the potential V is continuous at the liquid-solid interface.

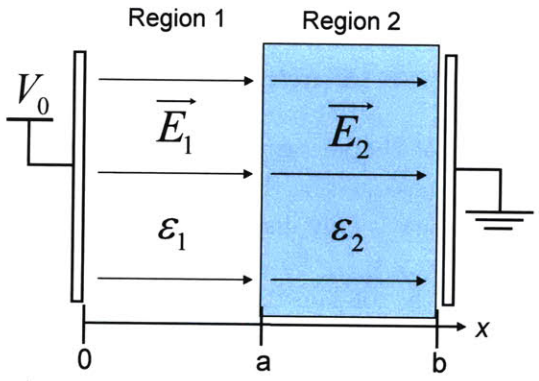

Figure 6.1: Two series dielectric parallel plane geometry to represent a simplified liquid-solid insulation system.

6.2 Preliminary Studies of Simplified Multi-Dielectric Insulation Systems

The following sections describe the analytical and numerical results for a two series dielectric parallel plane model, as shown in Fig. 6.1, which represents a simplified liquid-solid insulation system. The analytical results are compared to numerical results obtained for the same governing equations, parameter values, and geometry to prove both the validity of the mathematical modeling and the numerical solver. The Migration-Migration Model of Section 6.2.1 models both dielectric regions via two separate migration models. The Migration-Ohmic Model of Section 6.2.2 models the first region via the migration model and the second region via the ohmic model.

The models presented in this section represent simplified liquid-solid insulation systems, where regions 1 and 2 in Fig. 6.1 are the dielectric liquid and solid regions respectively, and fringing field effects are ignored. The solid region 2 is modeled by a migration model in Section 6.2.1 and ohmic model in Section 6.2.2.

The liquid region 1 is modeled via a migration model with a positive charge carrier density ρ_1, which is injected at the $x=0$ electrode by the following linear charge injection law

$$\rho_1(x=0) = A \cdot E_1(x=0). \tag{6.24}$$

The linear coefficient A in Eq. (6.24) is chosen to be very large, approaching infinity in the limiting case, such that the electric field at $x=0$, that is $E_1(x=0)$, is zero. In the numerical

simulation, the linear coefficient was made large (*i.e.*, $A = 1000$) to approximate the space charge limited injection source ($A \rightarrow \infty$) such that $E_1 \rightarrow 0$ keeping J_1 finite.

Due to the zero electric field at $x = 0$ a finite current density J_1 will flow even though $\rho_1(x = 0) \rightarrow \infty$.

$$J_1(x = 0) = \rho_1(x = 0)\mu_1 E_1(x = 0) = \mu_1 A\,[E_1(x = 0)]^2 \tag{6.25}$$

In Eq. (6.25) the variable μ_1 is the mobility of the positive charge carriers in the dielectric liquid. Note that unipolar positive charge injection was assumed to simplify the equations by neglecting the negative signs that accompany negative charge injection.

The model parameter values used for both the analytical and numerical studies of this section are summarized in Table 6.1.

Table 6.1: Parameter Values for Simplified Two Series Dielectric Parallel Plane Model

Parameter	**Symbol**	**Value**
Permittivity in Region 1	ϵ_1	1 F/m
Permittivity in Region 2	ϵ_2	2 F/m
Applied Voltage	V_0	1 V
Length of Region 1	a	0.5 m
Total Length	b	1.0 m

The motivation behind the simplified liquid-solid models is to gain a better understanding on how the model representation of the solid dielectric affects the solutions, especially those at the liquid-solid interface. Also, there is a lack of knowledge on how to best connect two dielectric regions with different material characteristics (*i.e.*, permittivity, conductivity, carrier mobilities) and model types (*i.e.*, migration, ohmic, insulator). This section deals with both these issues, as well as to validate the effectiveness of COMSOL Multiphysics to model pre-breakdown phenomena in multi-dielectric systems, which is accomplished by comparing analytical and numerical solutions.

6.2.1 Steady-State Study of Migration-Migration Model

6.2.1.1 Analytical Model

For the parallel plane geometry, shown in Fig 6.2, a migration-migration model is used, where the positive charge carriers (*i.e.*, those injected at $x = 0$ via the linear injection law of Eq. (6.1)) have a mobility of μ_1 and μ_2 for regions 1 and 2, respectively.

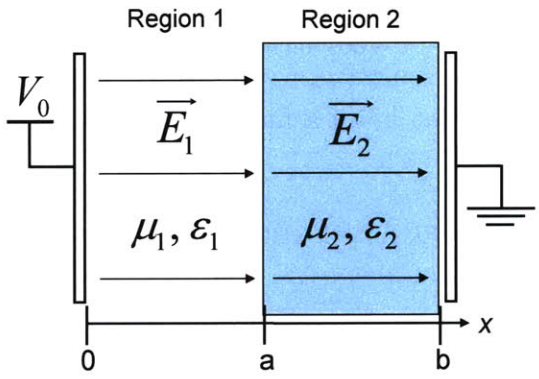

Figure 6.2: Two series dielectric parallel plane model where Regions 1 and 2 are defined by unique permittivities (ϵ_1, ϵ_2) and carrier mobilities (μ_1, μ_2).

In region 1, where $0<x<a$, the current density is

$$J_1 = \rho_1 \mu_1 E_1 \tag{6.26}$$

and from Gauss' Law:

$$\frac{\partial E_1}{\partial x} = \frac{\rho_1}{\epsilon_1}. \tag{6.27}$$

Utilizing Eq. (6.27), the current density can be written as

$$J_1 = \frac{\partial}{\partial x}\left(\frac{1}{2}\epsilon_1 \mu_1 E_1^2\right). \tag{6.28}$$

Integrating Eq. (6.28) and using the space charge limited condition, where the electric field at $x=0$ is zero (*i.e.*, $E(x=0)=0$), the electric field throughout all of region 1 is

$$E_1 = \sqrt{\frac{2Jx}{\epsilon_1 \mu_1}} \tag{6.29}$$

where J_1 has been replaced with J as we are assuming steady-state and the current density throughout the structure is uniform.

Now looking at region 2, where $a<x<b$, and following the same methodology the current density in the region is

$$J_2 = \rho_2 \mu_2 E_2 \tag{6.30}$$

where $J = J_1 = J_2$. Through the use of Gauss' Law, which states

$$\frac{\partial E_2}{\partial x} = \frac{\rho_2}{\epsilon_2}, \tag{6.31}$$

the current density in region 2 can be written as

$$J = \frac{\partial}{\partial x}\left(\frac{1}{2}\epsilon_2\mu_2 E_2^2\right). \tag{6.32}$$

Now integrating Eq. (6.32), the electric field in region 2 is found within a constant of integration C.

$$E_2 = \sqrt{\frac{2}{\epsilon_2\mu_2}(Jx + C)} \tag{6.33}$$

The voltage across the parallel plates can be found by integrating the electric field along the x-axis from $x=0$ to b and equated to V_0.

$$V_0 = \int_0^a E_1 dx + \int_a^b E_2 dx \tag{6.34}$$

Completing the integration there are two unknowns to solve for, the current density J and the integration constant C. A relation that may help solve for these unknowns is the surface charge density ρ_s at the interface between dielectric 1 and 2, which is

$$\rho_s = \epsilon_2 E_2(x = a_+) - \epsilon_1 E_1(x = a_-). \tag{6.35}$$

Unfortunately, using (6.34) introduces another unknown, the interfacial surface charge density ρ_s itself. If the surface charge density is known or chosen, then a solution to the steady-state system can be found. An argument can be made that for all time zero surface charge density exists in a fully two-dielectric migrational model unless there are trapping mechanisms at the interface. In the migration-migration model described above we assume no trapping mechanisms exist, which bound incoming charges to the interface. Consequently, the surface charge density at the interface is always zero. Applying this argument, that is $\rho_s = 0$, it is possible to solve for a closed-form analytical solution for all unknowns (*i.e.*, J and C) such that

$$J = \frac{9\epsilon_1\mu_1 V_0^2}{8b^3} \tag{6.36}$$

$$C = Ja\left(\frac{\epsilon_1\mu_2}{\epsilon_2\mu_1} - 1\right) \tag{6.37}$$

6.2.1.2 Numerical Model

The Migration-Migration Model was investigated by modeling the two dielectric regions, as shown in Fig. 6.2, with differing permittivities and charge mobilities.

The governing equations for the migration-migration model are based on the drift-dominated charge continuity equations (6.39), (6.41) for a positive charge density in region 1 (ρ_1) and region 2 (ρ_2), respectively. Each density is coupled to a region specific Gauss' Law (6.38), (6.40), where $\vec{E}_1$ and $\vec{E}_2$ are the electric field in regions 1 and 2, respectively.

$$\nabla \cdot (\epsilon_1 \vec{E}_1) = \rho_1 \tag{6.38}$$

$$\nabla \cdot (\rho_1 \mu_1 \vec{E}_1) = 0 \tag{6.39}$$

$$\nabla \cdot (\epsilon_2 \vec{E}_2) = \rho_2 \tag{6.40}$$

$$\nabla \cdot (\rho_2 \mu_2 \vec{E}_2) = 0 \tag{6.41}$$

The region specific charge mobilities used in this study are given in Table 6.2.

Table 6.2: Mobility Values for the Simplified Migration-Migration Model

Parameter	**Symbol**	**Value**
Charge Mobility in Region 1	μ_1	1.0 $m^2V^{-1}s^{-1}$
Charge Mobility in Region 2	μ_2	0.1 $m^2V^{-1}s^{-1}$

Due to the injection of a non-trivial positive charge density at $x=0$, which is accompanied by large positive charge velocities and negligible diffusion, there exists numerical instability in the numerical solver. Therefore, a small amount of artificial streamline diffusion is employed to avoid spurious oscillations in the solutions to the convection and diffusion equations (6.39), (6.41) and assist in solver stability [102, 104, 156].

The external boundary conditions applied to the model of Eqs. (6.38)-(6.41) are:

- Gauss' Law Region 1 Eq. (6.38): The electrode at $x=0$ is set to an applied voltage V_0.
- Charge Transport Continuity Equation Region 1 Eq. (6.39): The electrode at $x=0$ is set to the linear charge injection law of Eq. (6.24).
- Gauss' Law Region 2 Eq. (6.40): The electrode at $x=b$ is grounded.
- Charge Transport Continuity Equation Region 2 Eq. (6.41): The electrode at $x=b$ is set for zero diffusive flux ($\vec{n} \cdot \nabla \rho_2 = 0$) where only migration currents are permitted.

The steady-state interfacial boundary conditions that connect Eq. (6.38) to (6.40) and Eq. (6.39) to (6.41) are:

- Gauss' Law Regions 1 and 2 Eqs. (6.38), (6.40): The difference in the normal components of the displacement field at the interface is equal to the surface charge density ($\vec{n} \cdot (\vec{D}_2 - \vec{D}_1) = \rho_s$).
- Charge Transport Continuity Equation Regions 1 and 2 Eqs. (6.39), (6.41): The normal component of the positive charge conduction current density is continuous ($\vec{n} \cdot (\rho_2 \mu_2 \vec{E}_2 - \rho_2 \mu_2 \vec{E}_1) = 0$), such that there is no surface charge.

6.2.1.3 Results and Discussion

In the mathematical study of the Migration-Migration Model in Section 6.2.1.1, it was shown that the surface charge density ρ_s needed to be selected *a priori* to have a complete closed-form solution. Therefore, in Figs. 6.3, 6.4, and 6.5 the charge concentration, current density and electric displacement field are shown for three different surface charge densities (*i.e.*, $\rho_s = 0$, 2, and $3.52\,\mathrm{C/m^2}$ respectively). For all four cases, the analytical and numerical solutions are in good agreement for the charge concentration, current density and electric displacement field.

In the electric displacement field figures for the three cases, there is a discontinuity at the interface of the two dielectrics, where the step discontinuity of the electric displacement fields is equal to the free surface charge density for each case. For example, in Fig. 6.4(a) the electric displacement discontinuity is $2\,\mathrm{C/m^2}$ at the interface. This value is equal to the surface charge density chosen for this case. Similar results can be seen for the cases where $\rho_s = 0$ and $3.52\,\mathrm{C/m^2}$.

In the current density figures there exists a small deviation in the numerical results from those of the analytical current density near the anode at $x = 0$. This occurs due to the linear injection law used at this electrode such that significant charge is injected there. By further refining the discretization of the geometry near this electrode the numerical result approaches the analytical one in this area.

The numerical migration-migration model accurately captures the physics involved in pre-breakdown and charge transport phenomena. Unfortunately, the migration-migration model has been dismissed as a viable modeling method for liquid-solid insulation systems because of two major drawbacks:

- A lack of understanding and characterization of the charge capturing, releasing and generating mechanisms at the dielectric interface to model surface charging at the interface

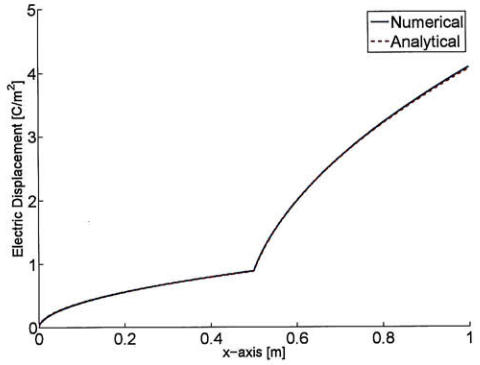

(a) Displacement field

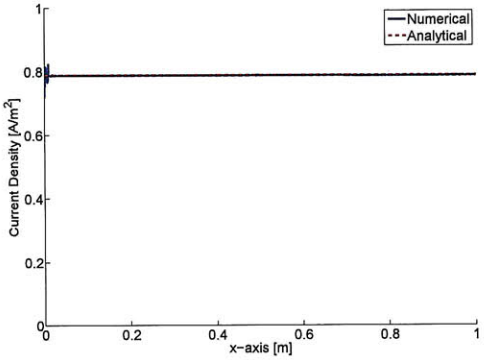

(b) Current density

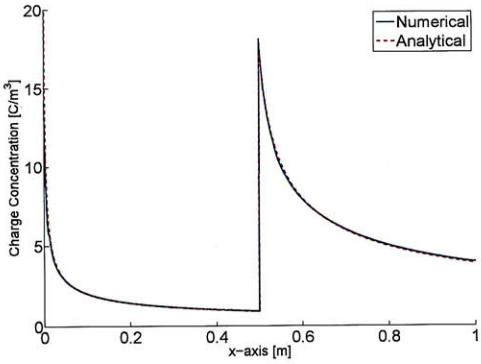

(c) Charge concentration

Figure 6.3: Analytical and numerical results for migration-migration model of two series dielectric parallel plane system (Fig. 6.2) where the surface charge density at the interface is set to $\rho_s = 0$.

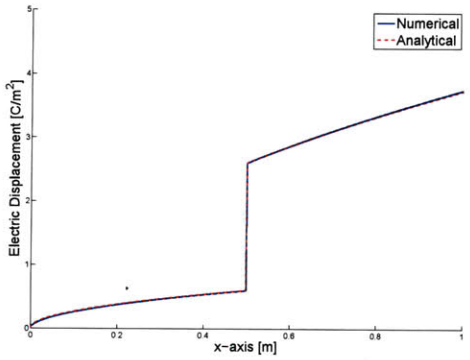

(a) Displacement field

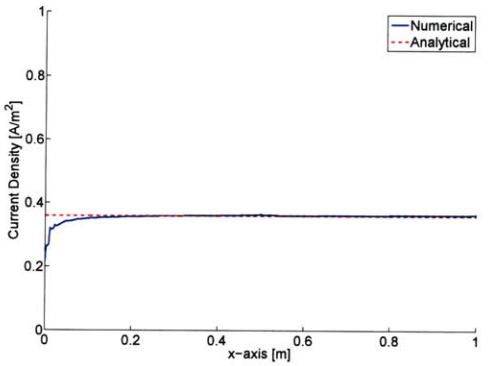

(b) Current density

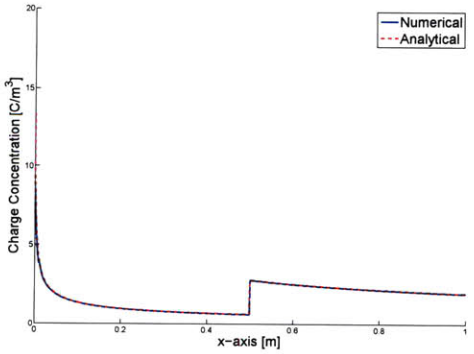

(c) Charge concentration

Figure 6.4: Analytical and numerical results for migration-migration model of two series dielectric parallel plane system (Fig. 6.2) where the surface charge density at the interface is set to $\rho_s = 2\,\mathrm{C/m^2}$.

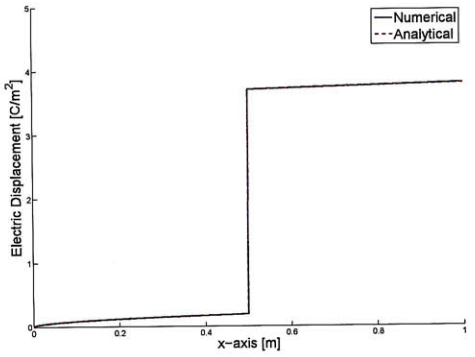

(a) Displacement field

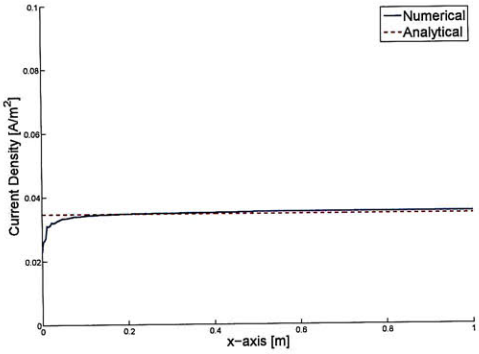

(b) Current density

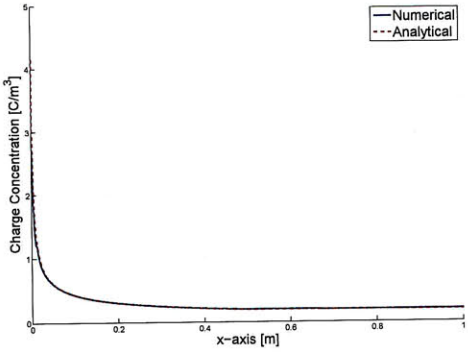

(c) Charge concentration

Figure 6.5: Analytical and numerical results for migration-migration model of two series dielectric parallel plane system (Fig. 6.2) where the surface charge density at the interface is set to $\rho_s = 3.52\ \mathrm{C/m^2}$.

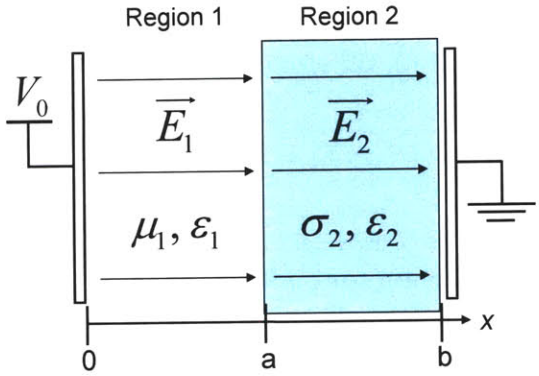

Figure 6.6: Two series dielectric parallel plane model where Region 1 is defined by a permittivity ϵ_1 and carrier mobility μ_1 and Region 2 is defined by a different permittivity ϵ_2 and conductivity σ_2.

- The model is computationally expensive due to the need for a finely discretized interface and the continual determination of upstream flow to ensure charge continuity.

6.2.2 Steady-State Study of Migration-Ohmic Model

6.2.2.1 Analytical Model

For the parallel plane geometry, shown in Fig 6.6, a migration-ohmic model is used, where in region 1 the positive charge carriers (*i.e.*, those injected at $x=0$ via the linear injection law of Eq. (6.24)) have a mobility of μ_1, and region 2 is characterized by a bulk conductivity σ_2.

The current density in region 1, where $0<x<a$

$$J_1 = \rho_1 \mu_1 E_1. \tag{6.42}$$

Using Gauss' Law, the change in electric field in region 1 is

$$\frac{\partial E_1}{\partial x} = \frac{\rho_1}{\epsilon_1}, \tag{6.43}$$

which when used in Eq. (6.42) gives

$$J_1 = \frac{\partial}{\partial x}\left(\frac{1}{2}\epsilon_1 \mu_1 E_1^2\right). \tag{6.44}$$

Integrating Eq. (6.44) and using the space charge limited condition, where the electric field at $x=0$ is zero (*i.e.*, $E_1(x=0)=0$), the electric field throughout all of region 1 is

$$E_1 = \sqrt{\frac{2Jx}{\epsilon_1 \mu_1}} \tag{6.45}$$

where J_1 has been replaced with J as we are assuming steady-state and the current density throughout the structure is uniform (*i.e.*, $J=J_1=J_2$).

In modeling region 2, where $a<x<b$, the electric field in this region is

$$E_2 = \frac{J}{\sigma_2}. \tag{6.46}$$

By integrating the electric field E along the x-axis from $x=0$ to b and equating this to the voltage V_0 a closed form solution for the steady-state current density J can be found.

$$J = \left[\frac{\frac{-1}{3}\sqrt{\frac{2a^3}{\epsilon_1\mu_1}} + \sqrt{\frac{2a^3}{9\epsilon_1\mu_1} + \frac{(b-a)V_0}{\sigma_2}}}{\frac{b-a}{\sigma_2}} \right]^2 \tag{6.47}$$

Using this current density and the electric fields E_1 and E_2 in Eqs. (6.45) and (6.46), the steady-state surface charge density ρ_s is

$$\begin{aligned} \rho_s &= \epsilon_2 E_2(x=a_+) - \epsilon_1 E_1(x=a_-) \\ &= \epsilon_2 \frac{J}{\sigma} - \epsilon_1 \sqrt{\frac{2Ja}{\epsilon_1 \mu}} \end{aligned} \tag{6.48}$$

6.2.2.2 Numerical Model

The steady-state governing equations for the migration-ohmic model are region specific. For the liquid region 1, the modeling is based upon the drift-dominated charge continuity equation (6.50), where a positive charge density (ρ_1) is coupled to Gauss' Law (6.49). For the solid region 2, a bulk conductivity ohmic model (6.51) is used.

$$\nabla \cdot (\epsilon_1 \vec{E}_1) = \rho_1 \tag{6.49}$$

$$\nabla \cdot (\rho_1 \mu_1 \vec{E}_1) = 0 \tag{6.50}$$

$$\nabla \cdot (\sigma_2 \vec{E}_2) = 0 \tag{6.51}$$

The charge mobility for region 1 and conductivity for region 2 are given in Table 6.3.

Table 6.3: Mobility and Conductivity Values for the Simplified Migration-Ohmic Model

Parameter	Symbol	Value
Charge Mobility in Region 1	μ_1	$1.0\,\mathrm{m^2V^{-1}s^{-1}}$
Conductivity in Region 2	σ_2	$0.32\,\Omega^{-1}\mathrm{m}^{-1}$

Due to the injection of a large positive charge density, and the associated large velocity and negligible diffusion for this positive charge density, there exists numerical instability in the numerical solver. Therefore, a small amount of artificial streamline diffusion is employed to avoid spurious oscillations in the solutions to the convection and diffusion equation (6.50) and assist in solver stability [102, 104, 156].

The external boundary conditions applied to the model of Eqs. (6.49)-(6.51) are:

- Gauss' Law Region 1 Eq. (6.49): The electrode at $x=0$ is set to an applied voltage V_0.
- Charge Transport Continuity Equation Region 1 Eq. (6.50): The electrode at $x=0$ is set to the linear charge injection law of Eq. (6.24).
- Ohm's Law Region 2 Eq. (6.51): The electrode at $x=b$ is grounded.

The steady-state interfacial boundary conditions that connect Eqs. (6.49) and (6.50) to Eq. (6.51) are:

- Gauss' Law Region 1 Eq. (6.49) and Ohm's Law Region 2 Eq. (6.51): The difference in the normal components of the displacement field at the interface $x=a$ is equal to the surface charge density ($\vec{n}\cdot(\vec{D}_2-\vec{D}_1)=\rho_s$). Also, the potential at the $x=a$ interface is continuous ($V_1=V_2$).
- Charge Transport Continuity Equation Region 1 Eq. (6.50): The normal component of the conduction current densities is continuous ($\vec{n}\cdot(\sigma_2\vec{E}_2-\rho_1\mu_1\vec{E}_1)=0$) at the $x=a$ interface.

6.2.2.3 Results and Discussion

Numerically modeling the steady-state behavior is accomplished by using methods similar to the migration-migration model in the previous section. In particular, the continuity of current density is enforced at the interface and the jump in displacement field is equal to the surface charge density. Figure 6.7 shows the analytical and numerical results for

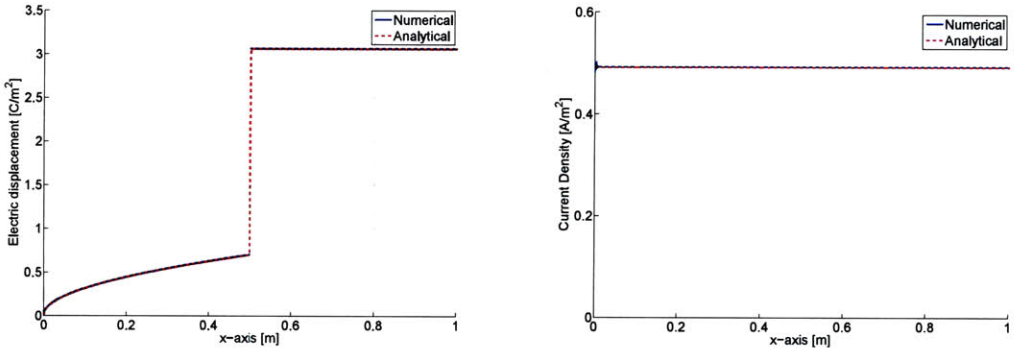

(a) Displacement field

(b) Current density

Figure 6.7: Analytical and numerical results for migration-migration model of two series dielectric parallel plane system (Fig. 6.6).

the migration-ohmic model, which are in good agreement for both the current density and electric displacement field.

The discontinuity in the electric displacement at the interface $x=0.5\text{m}$ is equal to 2.36C/m^2, which is equal to the surface charge density derived analytically in Eq. (6.48). The numerical migration-ohmic model captures the physics involved in pre-breakdown and charge transport phenomena with relative computational efficiency. Furthermore, it does not suffer from the problems associated with the migration-migration model. As such, the transient response of migration-ohmic model to a step current will be investigated in the next section.

6.2.3 Step Current Transient Study of Migration-Ohmic Model

6.2.3.1 Analytical Model

For the parallel plane geometry, shown in Fig. 6.8, a migration-ohmic model is used, where in region 1 the positive charge carriers have a mobility μ_1 and region 2 is characterized by a bulk conductivity σ_2. The system is excited by a step current with I_0 at $t=0$ applied to an initially unexcited system. The surface area of each parallel plate is A such that the total current density applied at $t=0$ into the two series dielectric system is $J_0=I_0/A$. For an initially unexcited system with space charge limited conditions, we have

$$E(x,t=0)=0 \qquad E_1(x=0,t)=0 \qquad \rho_1(0<x<a,t=0)=0. \tag{6.52}$$

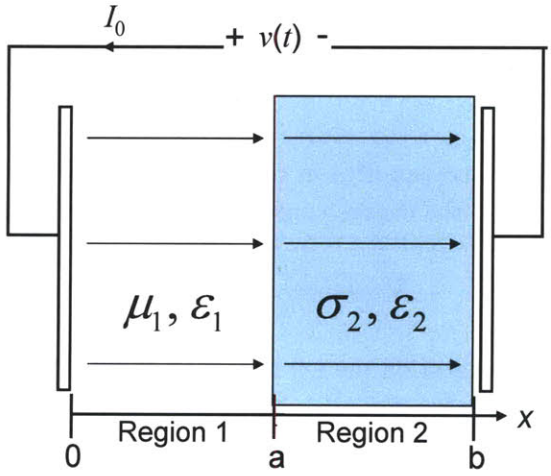

Figure 6.8: Two series dielectric parallel plane model where Region 1 is defined by a permittivity ϵ_1 and charge carrier mobility μ_1 and Region 2 is defined by a different permittivity ϵ_2 and ohmic conductivity σ_2.

In the migration modeled liquid region 1, where $0 < x < a$, the conduction current density is J is

$$J_1 = \rho_1 \mu_1 E_1 = \mu_1 E_1 \epsilon_1 \frac{\partial E_1}{\partial x}, \tag{6.53}$$

where Gauss' Law has been applied in the last equality. The total current density, conduction and displacement, is then equal to J_{t0}.

$$\begin{aligned} J_{t0} &= \frac{\partial D_1}{\partial t} + J_1 \\ &= \epsilon_1 \frac{\partial E_1}{\partial t} + \mu_1 \epsilon_1 E_1 \frac{\partial E_1}{\partial x} \end{aligned} \tag{6.54}$$

Equation (6.54) is a quasi-linear partial differential equation of the first order, which can be solved using the method of characteristics [20] . The solutions of (6.54) are also the simultaneous solutions of the subsidiary equations:

$$v_1 = \frac{dx}{dt} = \mu_1 E_1 \tag{6.55}$$

$$\frac{dE_1}{dt} = \frac{\partial E_1}{\partial t} + v_1 \frac{\partial E_1}{\partial x} = \frac{J_{t0}}{\epsilon_1}. \tag{6.56}$$

Equation (6.55) gives the trajectories of families of curves which represent the actual paths that the injected charge travels, while the solutions of Eq. (6.56) yield the electric field along these trajectories.

The charge density along the trajectories in region 1 can be derived from the charge conservation equation. Generally, the charge conservation equation is

$$\nabla \cdot \vec{J} + \frac{\partial \rho}{\partial t} = 0. \tag{6.57}$$

Utilizing $\vec{J} = \rho\mu\vec{E}$ from the migration model, the divergence of the conduction current can be expanded to

$$\begin{aligned} \nabla \cdot \vec{J} &= \nabla \cdot (\rho\mu\vec{E}) \\ &= \mu\vec{E} \cdot \nabla\rho + \rho\mu\nabla \cdot \vec{E} \\ &= \mu\vec{E} \cdot \nabla\rho + \frac{\rho^2\mu}{\epsilon}, \end{aligned} \tag{6.58}$$

where Gauss' Law is used in the last equality. By substituting and rearranging Eq. (6.58) into the charge conservation equation (6.57), we obtain

$$\begin{aligned} -\frac{\rho^2\mu}{\epsilon} &= \frac{\partial \rho}{\partial t} + (\mu\vec{E}) \cdot \nabla\rho \\ &= \frac{\partial \rho}{\partial t} + \vec{v} \cdot \nabla\rho \\ &= \frac{d\rho}{dt}, \end{aligned} \tag{6.59}$$

where a similar manipulation as done in Eq. (6.55) has been utilized. By manipulating and integrating Eq. (6.59), the resulting charge concentration profile relation in region 1 is

$$\rho_1 = \frac{1}{\frac{\mu_1 t}{\epsilon_1} + C}, \tag{6.60}$$

where C is an integration constant and is determined via the initial and boundary conditions.

In the x-t plane, the solutions of (6.55) and (6.56) divide into those characteristic curves emanating from $t = 0$ for all x and those emanating from $x = 0$ for all t, separated by the demarcation curve emanating from the point $x = 0$, $t = 0$, as shown in Fig. 6.9 for the charging transient. By integrating (6.55) and (6.56) and using (6.60) and the space charge limited conditions, we obtain

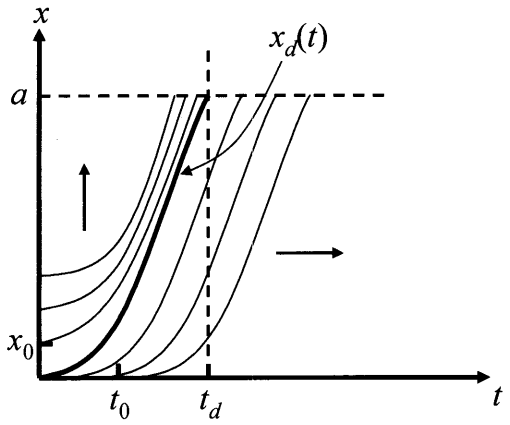

Figure 6.9: Characteristic trajectories in the x-t space under space charge limited conditions for the charging transient to a step current.

- Below the demarcation line $x_d(t)$ emanating from $(x=0,\ t=0)$

$$E_1(t) = \frac{J_{t0}}{\epsilon_1}(t - t_0) = \sqrt{\frac{2J_{t0}x}{\mu_1\epsilon_1}} \tag{6.61}$$

$$\rho_1(t) = \frac{\epsilon_1}{\mu_1(t - t_0)} \tag{6.62}$$

$$\text{on } x = \frac{\mu_1 J_{t0}}{2\epsilon_1}(t - t_0)^2 \tag{6.63}$$

- Above the demarcation line $x_d(t)$ $(x=x_0,\ t_0=0)$

$$E_1(t) = \frac{J_{t0}t}{\epsilon_1} \tag{6.64}$$

$$\rho_1(t) = 0 \tag{6.65}$$

$$\text{on } x = \frac{\mu_1 J_{t0}t^2}{2\epsilon_1} + x_0,\ x_0 = x(t=0) \tag{6.66}$$

The demarcation line, which is characterized by $(x = 0,\ t_0 = 0)$ is given from (6.63) with $t_0=0$ or from (6.66) with $x_0=0$

$$x_d = \frac{\mu_1 J_{t0}t^2}{2\epsilon_1}, \tag{6.67}$$

where the demarcation time when $x_d(t=t_d)=a$ is

$$t_d = \sqrt{\frac{2\epsilon_1 a}{\mu_1 J_{t0}}}. \tag{6.68}$$

In the ohmic modeled solid region 2, where $a<x<b$, we can characterize the electrodynamics more easily. From the total current density equation

$$\epsilon_2 \frac{\partial E_2}{\partial t} + \sigma_2 E_2 = J_{t0}, \tag{6.69}$$

the electric field in region 2 is

$$E_2 = \frac{J_{t0}}{\sigma_2}\left(1 - e^{-t/\tau}\right) \quad \text{where} \quad \tau = \frac{\epsilon_2}{\sigma_2}. \tag{6.70}$$

The surface charge density ρ_s at the interface is

$$\begin{aligned} \rho_s(x=a,t) &= \epsilon_2 E_2(x=a_+) - \epsilon_1 E_1(x=a_-) \\ &= \begin{cases} J_{t0}\left[\tau\left(1-e^{-t/\tau}\right) - t\right], & 0 \le t < t_d \\ J_{t0}\left[\tau\left(1-e^{-t/\tau}\right) - t_d\right], & t \ge t_d. \end{cases} \end{aligned} \tag{6.71}$$

The voltage across the the whole parallel plate structure is

$$\begin{aligned} v(t) &= \int_0^a E_1 dx \int_a^b E_2 dx \\ &= \begin{cases} \int_0^{x_d} \sqrt{\frac{2J_{t0}x}{\mu_1\epsilon_1}}dx + \int_{x_d}^a \frac{J_{t0}t}{\epsilon_1}dx + \int_a^b \frac{J_{t0}}{\sigma_2}\left(1-e^{-t/\tau}\right)dx, & 0 \le t < t_d \\ \int_0^a \sqrt{\frac{2J_{t0}x}{\mu_1\epsilon_1}}dx + \int_a^b \frac{J_{t0}}{\sigma_2}\left(1-e^{-t/\tau}\right)dx, & t \ge t_d \end{cases} \\ &= \begin{cases} \frac{J_{t0}at}{\epsilon_1}\left[1 - \frac{1}{3}\left(\frac{t}{t_d}\right)^2\right] + \frac{J_{t0}(b-a)}{\sigma_2}\left(1-e^{-t/\tau}\right), & 0 \le t < t_d \\ \frac{2J_{t0}at_d}{3\epsilon_1} + \frac{J_{t0}(b-a)}{\sigma_2}\left(1-e^{-t_d/\tau}\right), & t \ge t_d. \end{cases} \end{aligned} \tag{6.72}$$

6.2.3.2 Numerical Model

The governing equations for the step current excited migration-ohmic model are region specific, where for the liquid region 1 the modeling is based upon the drift-dominated charge continuity equation (6.74), for a positive charge density (ρ_1) coupled through Gauss' Law (6.73). For the solid region 2, a bulk conductivity ohmic model (6.75) is used.

$$\nabla \cdot (\epsilon_1 \vec{E}_1) = \rho_1 \tag{6.73}$$

$$\frac{\partial \rho_1}{\partial t} + \nabla \cdot (\rho_1 \mu_1 \vec{E}_1) = 0 \tag{6.74}$$

$$\epsilon_2 \frac{\partial \vec{E}_2}{\partial t} + \nabla \cdot (\sigma_2 \vec{E}_2) = 0 \tag{6.75}$$

At the interface, there is a boundary condition equation to account for the difference in normal conduction currents equaling the surface charge ρ_s

$$\begin{aligned} \frac{\partial \rho_s}{\partial t} &= \vec{n} \cdot \left(\vec{J}_1 - \vec{J}_2 \right) \\ &= \vec{n} \cdot \left(\rho \mu_1 \vec{E}(x=a_-) - \sigma_2 \vec{E}(x=a_+) \right). \end{aligned} \tag{6.76}$$

The charge mobility for region 1 is $\mu_1 = 1.0\,\mathrm{m^2 V^{-1} s^{-1}}$ and conductivity for region 2 is $\sigma_2 = 0.32\,\Omega^{-1}\mathrm{m}^{-1}$. They are the same as those used in the previous section and are summarized in Table 6.3. As in the previous numerical models, a small amount of artificial streamline diffusion is employed to avoid spurious oscillations in the solutions to the convection and diffusion equation (6.74) and assist in solver stability [102, 104, 156].

The external boundary conditions applied to the model of Eqs. (6.73)-(6.75) are:

- Gauss' Law Region 1 Eq. (6.73): The electrode at $x=0$ is grounded.
- Charge Transport Continuity Equation Region 1 Eq. (6.74): The electrode at $x=0$ is set to the linear charge injection law of Eq. (6.24).
- Ohm's Law Region 2 Eq. (6.75): At the $x=b$ electrode an outward current flow of $J_{t0} = 0.492\ \mathrm{A/m^2}$ is set.

The interfacial boundary conditions applied to the model of Eqs. (6.73)-(6.75) are:

- Gauss' Law Region 1 Eq. (6.73): The normal displacement field is set to

$$\vec{n} \cdot \vec{D}_1(x=a_-) = \vec{n} \cdot \vec{D}_2(x=a_+) - \rho_s.$$

- Charge Transport Continuity Region 1 Eq. (6.74): The $x=a$ interface is set to zero diffusive flux ($\vec{n} \cdot \nabla \rho_1 = 0$) such that only migration currents are permitted.
- Current Continuity Eq. (6.75): The total current density flow across the boundary is continuous

$$\vec{n} \cdot \left(\frac{\partial \vec{D}_1}{\partial t} + \rho_1 \mu_1 \vec{E}_1 \right) \Bigg|_{x=a_-} = \vec{n} \cdot \left(\frac{\partial \vec{D}_2}{\partial t} + \sigma_2 \vec{E}_2 \right) \Bigg|_{x=a_+}.$$

Also, the potential is set to be continuous across the $x=a$ interface.

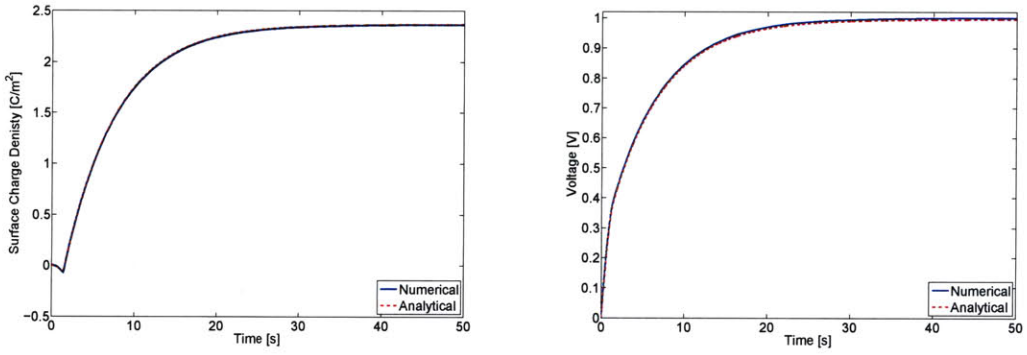

(a) Surface charge density ρ_s

(b) Voltage across electrode terminals $v(t)$

Figure 6.10: Analytical and numerical results for step current excited migration-ohmic model of two series dielectric parallel plane geometry (Fig. 6.8).

6.2.3.3 Results and Discussion

The analytical and numerical results of the step current excited migration-ohmic two series dielectric system are shown in Fig. 6.10. The results show good agreement between the analytical and numerical solutions for the surface charge density at the interface and the potential distribution between the terminals. A step current density of $J_{t0}=0.492\ \mathrm{A/m^2}$ is used such that the steady state voltage across the structure is $v(t\to\infty)=1\ \mathrm{V}$ (Fig. 6.10(b)) leading to a steady-state solution that should match the stationary results of Section 6.2.2. Ultimately the steady-state current density of $J_0 = 0.492\ \mathrm{A/m^2}$ matches that obtained in the previous section, as shown in Fig. 6.7(b). Also, the stationary surface charge density in Fig. 6.10(a) matches $\rho_s = 2.36\ \mathrm{C/m^2}$ from the last section.

The modeling and results of this section have shown that the migration-ohmic model effectively models both the bulk and interfacial dynamics. In particular, this method is superior at determining surface charging of the interface, which is of importance in streamer phenomena where the interface greatly affects their propagation [13, 14, 21].

6.3 Complete Models for Liquid-Solid Insulation Systems

A detailed description of the governing equations for an electrohydrodynamic model of a dielectric liquid, such as transformer oil, is given in Chapter 3. The same migration model governing equations is used for the dielectric liquid in the liquid-solid insulation system so

much of the discussion will focus on the solid and interfacial governing equations and the reader should refer to Chapter 3 for more details on the liquid modeling.

The motivation of modeling and studying of liquid-solid insulation systems is to better understand the impact of solid insulation on the propagation of streamers in dielectric liquids or along the liquid-solid interface. To that extent, the focus will be on how the presence of solid insulation affects the electrodynamics (*i.e.*, charge transport, ionization mechanisms, etc.). Puncturing or breakdown of the solid insulation and consequently, the modeling of complex charge generation and recombination mechanisms in the solid insulation bulk is neglected. From Section 6.1, both the ohmic and insulator models of the solid insulation are given. Due to the drawbacks discussed in Section 6.2, the migration model is not used as a modeling method for solid insulation.

6.3.1 Governing Equations for the Migration Model of the Liquid Dielectric

The governing equations for the dielectric liquid, which contain the physics to model streamer development are based on the drift-dominated charge continuity equations (6.78)-(6.80) for positive ion (ρ_p), negative ion (ρ_n) and electron (ρ_e) charge densities which are coupled through Gauss' Law (6.77). The negative ion and electron charge densities are both negative quantities. The three carrier continuum model is utilized to account for the charge generation and capture mechanisms, which are critical in the study of streamers.

$$\nabla \cdot (\epsilon_r \epsilon_0 \vec{E}) = \rho_p + \rho_n + \rho_e \tag{6.77}$$

$$\frac{\partial \rho_p}{\partial t} + \nabla \cdot (\rho_p \mu_p \vec{E}) = G(|\vec{E}|) + \frac{\rho_p \rho_e R_{pe}}{q} + \frac{\rho_p \rho_n R_{pn}}{q} \tag{6.78}$$

$$\frac{\partial \rho_n}{\partial t} - \nabla \cdot (\rho_n \mu_n \vec{E}) = \frac{\rho_e}{\tau_a} - \frac{\rho_p \rho_n R_{pn}}{q} \tag{6.79}$$

$$\frac{\partial \rho_e}{\partial t} - \nabla \cdot (\rho_e \mu_e \vec{E}) = -G(|\vec{E}|) - \frac{\rho_p \rho_e R_{pe}}{q} - \frac{\rho_e}{\tau_a} \tag{6.80}$$

In (6.77)-(6.80), μ_p, μ_n and μ_e are the mobilities of the positive ions, negative ions, and electrons, respectively, and ϵ_r is the liquid's relative permittivity. The charge generation source term $G(|\vec{E}|)$ can model an ionization source discussed in Section 3.7. A detailed discussion of the model and parameters can be found in Chapter 3.

The total conduction current in the dielectric liquid is

$$\begin{aligned} \vec{J}^l &= \vec{J}_p + \vec{J}_n + \vec{J}_e \\ &= (\rho_p \mu_p - \rho_n \mu_n - \rho_e \mu_e)\vec{E}^l, \end{aligned} \tag{6.81}$$

where the superscript "l" denotes liquid.

Due to the high field levels and accompanying large carrier velocities, especially the electrons, the drift component of the current density strongly dominates over the diffusion component leading to instability in the numerical solver. Therefore, artificial streamline diffusion is employed to avoid spurious oscillations in the solutions to the convection and diffusion equations (6.78)-(6.80) and assist in solver stability [102, 104].

The external boundary conditions applied to the streamer model of Eqs. (6.77)-(6.80) are:

- Gauss' Law Eq. (6.77): The sharp needle electrode is set to a V_0 step voltage at $t=0$ with respect to the grounded large sphere. The symmetry z-axis and the top, bottom and side insulating walls have the boundary condition of zero normal electric field components (*i.e.*, $\vec{n}\cdot\vec{E} = 0$).
- Charge Transport Continuity Equations Eqs. (6.78)-(6.80): The boundary condition along the outer boundaries is zero normal flux ($\vec{n}\cdot\vec{J}_p=0$, $\vec{n}\cdot\vec{J}_n=0$, $\vec{n}\cdot\vec{J}_e=0$). In addition, the boundary condition at the electrodes is zero diffusive flux ($\vec{n}\cdot\nabla\rho_p = 0$, $\vec{n}\cdot\nabla\rho_n = 0$, $\vec{n}\cdot\nabla\rho_e=0$) where only migration currents are permitted.

6.3.2 Governing Equations for the Ohmic Model of the Solid Dielectric

The governing equation for dielectric solid, which is based on current continuity (Kirchoff's current law), is

$$\nabla\cdot\left[\frac{\partial\epsilon_r\epsilon_0\vec{E}}{\partial t} + \sigma\vec{E}\right] = 0, \tag{6.82}$$

where σ and ϵ_r are the bulk conductivity and relative permittivity, respectively, of the solid and $\vec{E}$ is the local electric field. The total conduction current in the dielectric liquid is

$$\vec{J}^s = \sigma\vec{E}^s, \tag{6.83}$$

where the superscript "s" denotes solid.

Also, at the liquid-solid interface an added governing equation accounts for the time derivative of the surface charge density ρ_s, which is equal to the difference in normal conduction currents on either side of the interface

$$\begin{aligned} \frac{\partial \rho_s}{\partial t} &= \vec{n} \cdot \left(\vec{J}^l - \vec{J}^s \right) \\ &= \vec{n} \cdot \left[\left(\rho_p \mu_p - \rho_n \mu_n - \rho_e \mu_e \right) \vec{E}^l - \sigma \vec{E}^s \right], \end{aligned} \tag{6.84}$$

where $\vec{n}$ is the outward normal vector from the liquid side.

The liquid-solid interface boundary conditions applied to the migration-ohmic model of Eqs. (6.77)-(6.80), and (6.82) are:

- Gauss' Law Eq. (6.77): The normal displacement field in the dielectric liquid is set to

$$\vec{n} \cdot \vec{D}^l = \vec{n} \cdot \vec{D}^s - \rho_s.$$

- Charge Transport Continuity Eqs. (6.78)-(6.80): Only migration currents are permitted across the interface such that $\vec{n} \cdot \nabla \rho_p = 0$, $\vec{n} \cdot \nabla \rho_n = 0$, and $\vec{n} \cdot \nabla \rho_e = 0$. For further detail on implementing these boundary conditions in COMSOL Multiphysics please refer to Appendix B.

- Current Continuity Eq. (6.82): The normal total current (conduction plus displacement) is continuous

$$\vec{n} \cdot \left[\frac{\partial \epsilon^s \vec{E}^s}{\partial t} + \vec{J}^s \right] = \vec{n} \cdot \left[\frac{\partial \epsilon^l \vec{E}^l}{\partial t} + \vec{J}^l \right].$$

Also, the potential is set to be continuous across the interface.

6.3.3 Governing Equations for the Insulator Model of the Solid Dielectric

The governing equation for the perfect insulator model of the solid dielectric is Gauss' Law with zero space charge (*i.e.*, Laplace's equation).

$$\nabla \cdot (\epsilon_r \epsilon_0 \vec{E}) = 0. \tag{6.85}$$

This model assumes the solid has zero conductivity (*i.e.*, $\sigma = 0$) and relative permittivity ϵ_r. Consequently, the conduction current in the dielectric solid is

$$\vec{J}^s = 0, \tag{6.86}$$

and the total current density is only displacement current.

Also, at the liquid-solid interface, an added governing equation accounts for the surface charge density ρ_s, which is equal to the difference in normal conduction currents on either side of the interface

$$\begin{aligned} \frac{\partial \rho_s}{\partial t} &= \vec{n} \cdot \left(\vec{J}^l - \vec{J}^s \right) \\ &= \vec{n} \cdot \left(\rho_p \mu_p - \rho_n \mu_n - \rho_e \mu_e \right) \vec{E}^l, \end{aligned} \tag{6.87}$$

where $\vec{n}$ is the outward normal vector from the liquid side.

The liquid-solid interface boundary conditions applied to the migration-insulator model of Eqs. (6.77)-(6.80), and (6.85) are:

- Gauss' Law Eqs. (6.77), (6.85): The difference in normal displacement fields on either side of the interface is equal to the surface charge density.

$$\rho_s = \vec{n} \cdot \left(\vec{D}^s - \vec{D}^l \right).$$

- Charge Transport Continuity Eqs. (6.78)-(6.80): Only migration currents are permitted across the interface such that $\vec{n} \cdot \nabla \rho_p = 0$, $\vec{n} \cdot \nabla \rho_n = 0$, and $\vec{n} \cdot \nabla \rho_e = 0$. For further detail on implementing these boundary conditions in COMSOL Multiphysics please refer to Appendix B.

6.3.4 Artificial Diffusion

For streamer models the charge transport continuity equations (6.78)-(6.80) are strongly drift dominated. Applying the Einstein relation [19] to determine the diffusion coefficients from the charge carrier mobilities in Table 3.1 results in the following diffusion coefficients:

$$D_p = \frac{kT}{q} \mu_p = 2.6 \times 10^{-11} \mathrm{m}^2/\mathrm{s} \tag{6.88}$$

$$D_n = \frac{kT}{q} \mu_n = 2.6 \times 10^{-11} \mathrm{m}^2/\mathrm{s} \tag{6.89}$$

$$D_e = \frac{kT}{q} \mu_e = 2.6 \times 10^{-6} \mathrm{m}^2/\mathrm{s} \tag{6.90}$$

where k is Boltzmann's constant (1.38×10^{-23} J/K), T is room temperature (300 K), and q is the magnitude of the electron charge (1.6×10^{-19} C). The positive ion, negative ion and

electron diffusion coefficients are extremely small and this makes the charge transport continuity equations (6.78)-(6.80) unstable. In the finite element method, artificial or numerical diffusion is often added to the drift-dominated charge transport continuity equations to fix the instability issue. In COMSOL Multiphysics, there are three types of artificial diffusion. The three types of artificial diffusion are:

1. Isotropic Diffusion
2. Streamline Diffusion
3. Crosswind Diffusion

More about each type of artificial diffusion can be found in the COMSOL Modeling Guide [157]. In short, streamline diffusion adds diffusion only in the direction of the flow, while crosswind adds diffusion orthogonal to flow. Isotropic adds the same amount of diffusion both along and orthogonal to the flow. Throughout the thesis, we have used streamline diffusion to help dampen the sharp charge density gradients that exist due to the ionization. However, when the streamer comes in contact with the solid dielectric at the interface large oscillations occur in the positive ion and electron charge densities due to instability issues. To remedy this a crosswind type of diffusion is required. Unfortunately, crosswind diffusion is extremely non-linear and coupled with the streamer physics causes the model to come to a standstill. Therefore, isotropic diffusion is used to remedy both of these issues. While isotropic diffusion may be the least accurate, we choose a small tuning parameter δ in COMSOL Multiphysics, such that $\delta \leq 0.1$, to minimize the amount of numerical diffusion added to the problem. The nominal value of the isotropic tuning parameter is $\delta = 0.5$. This type of diffusion was also used by Kumara, Serdyuk, and Gubanski [156] and showed reasonable results.

Chapter 7

The Influence of Solid Insulation on Streamer Development in Dielectric Liquids

---

THIS CHAPTER details the results of streamer development within liquid-solid insulation, such as oil-pressboard and oil-polytetrafluoroethylene systems. Significant effort has been taken to understand the effects solid insulation has on streamer development with a focus on propagation along the liquid-solid interface. Utilizing the liquid-solid models of Chapter 6, the propagation of positive streamers along solid surfaces that are oriented parallel and perpendicular to the main electric field component is thoroughly examined. This chapter also investigates the effect of the permittivity differences of the liquid and solid dielectrics on streamer propagation.

7.1 Streamers in Oil with Solid Insulation Oriented Parallel and Perpendicular to the Primary Electric Field Direction

Experimental evidence has shown that streamer propagation is dramatically altered when the streamer comes in contact with a solid surface. The surface can either assist or impede streamer propagation depending on the orientation of the solid surface with respect to the direction of the main electric field component. For the case where the surface orientation is parallel to the primary direction of the main electric field component, the interface accelerates streamer propagation and aids in breakdown [13, 14, 21, 22, 59, 85]. However, the opposite is true when the surface orientation is perpendicular to the direction of the main electric field component such that streamer growth towards the negative electrode is impeded, as it travels along the surface [15, 16, 85].

7.1.1 Governing Equations of the Oil-Solid Insulation System

To identify the physical phenomena that affects streamer propagation in various oil-solid systems, the numerical models of the previous chapter are utilized. The oil-solid numerical model is based upon the liquid migration and solid insulator model discussed in Sections 6.3.1 and 6.3.3, respectively. While Chapter 6 should be referred to for in depth discussion on liquid-solid modeling, this section briefly outlines the model's governing equations and important parameter values in each dielectric region and at the interface.

7.1.1.1 Oil Governing Equations

The governing equations for transformer oil are based on the drift-dominated charge transport continuity equations (7.2)-(7.4) for positive ion (ρ_p), negative ion (ρ_n) and electron (ρ_e) charge densities which are coupled through Gauss' Law (7.1). The negative ion and electron charge densities are both negative quantities. The three carrier continuum model is utilized to account for the charge generation and capture mechanisms, which are critical in the study of streamers.

$$\nabla \cdot (\epsilon_r \epsilon_0 \vec{E}) = \rho_p + \rho_n + \rho_e \tag{7.1}$$

$$\frac{\partial \rho_p}{\partial t} + \nabla \cdot (\rho_p \mu_p \vec{E}) = G_F(|\vec{E}|) + \frac{\rho_p \rho_e R_{pe}}{q} + \frac{\rho_p \rho_n R_{pn}}{q} \tag{7.2}$$

$$\frac{\partial \rho_n}{\partial t} - \nabla \cdot (\rho_n \mu_n \vec{E}) = \frac{\rho_e}{\tau_a} - \frac{\rho_p \rho_n R_{pn}}{q} \tag{7.3}$$

$$\frac{\partial \rho_e}{\partial t} - \nabla \cdot (\rho_e \mu_e \vec{E}) = -G_F(|\vec{E}|) - \frac{\rho_p \rho_e R_{pe}}{q} - \frac{\rho_e}{\tau_a} \tag{7.4}$$

In (7.1)-(7.4), μ_p, μ_n and μ_e are the mobilities of the positive ions, negative ions, and electrons, respectively, and ϵ_r is the oil's relative permittivity and are outlined in Table 3.1. A detailed discussion of the model and parameters can be found in Chapter 3.

The field ionization charge generation term

$$G_F(|\vec{E}|) = \frac{q^2 n_0 a |\vec{E}|}{h} \exp\left(-\frac{\pi^2 m^* a \Delta^2}{q h^2 |\vec{E}|}\right) \tag{7.5}$$

is based on the Zener model [11, 121] as discussed in Section 3.7. This field ionization mechanism models the ionization of low concentration, low ionization potential aromatic molecules with parameter values identical to those in Table 4.1. In Section 4.2, it is shown that for over-voltage conditions the ionization of these molecules leads to the formation of slow 2$^{\text{nd}}$ mode streamers that travel at average velocities in the range of $2-5$ km/s.

The total conduction current in the dielectric liquid is

$$\begin{aligned} \vec{J}^l &= \vec{J}_p + \vec{J}_n + \vec{J}_e \\ &= (\rho_p \mu_p - \rho_n \mu_n - \rho_e \mu_e)\vec{E}. \end{aligned} \tag{7.6}$$

7.1.1.2 Solid Insulation Governing Equation

The governing equation for the perfect insulator model of the solid dielectric is Gauss' Law with zero space charge (*i.e.*, Laplace's equation).

$$\nabla \cdot (\epsilon_r \epsilon_0 \vec{E}) = 0. \tag{7.7}$$

A detailed discussion of the model parameters can be found in Sections 6.1 and 6.3.3.

In Eq. (7.7), ϵ_r is the solid's relative permittivity. In this chapter, several different relative permittivity values (*e.g.*, 1.0, 2.2, 3.3, and 4.4) for the solid insulation will be used to investigate the effect of oil-solid permittivity differences on streamer propagation (see Section 7.4). The relative permittivities of 2.2 and 4.4 model polytetrafluoroethylene (PTFE) and pressboard, respectively. These two solid insulators are used extensively in high voltage equipment and streamer studies [13, 15, 16, 91].

The underlying assumption for the model equation (7.7) is that the solid insulator has zero conductivity (*i.e.*, $\sigma = 0$), as discussed in Section 6.1. Consequently, the conduction current in the dielectric solid is

$$\vec{J}^s = 0, \tag{7.8}$$

and the total current density is only displacement current.

7.1.1.3 Oil-Solid Interface Governing Equation

At the liquid-solid interface, an added governing equation accounts for the surface charge density ρ_s, whose time derivative is equal to the difference in normal conduction currents on either side of the interface

$$\begin{aligned} \frac{\partial \rho_s}{\partial t} &= \vec{n} \cdot \left(\vec{J}^l - \vec{J}^s \right) \\ &= \vec{n} \cdot (\rho_p \mu_p - \rho_n \mu_n - \rho_e \mu_e)\, \vec{E}, \end{aligned} \tag{7.9}$$

where $\vec{n}$ is the outward normal vector from the liquid side.

7.1.2 Parallel Oriented Interface – PTFE Cylindrical Tube

The experimental results from the literature have shown that surfaces oriented parallel to the direction of the main electric field component aid streamer development at voltages above the breakdown voltage V_b such that the acceleration voltage V_a is substantially lowered when compared to an oil-only system [13, 14, 21, 22, 59, 85]. Massala and Lesaint [13] observed that by confining the radial growth of streamers within polytetrafluoroethylene (PTFE) cylindrical tubes, where the surface is oriented parallel to the main electric field component, there were significant changes to the streamer behavior, shape and velocity. The key observation was that the streamer velocity was greatly increased when the applied voltage was above V_b and below V_a, which is unlike the oil-only case where the streamers accelerate from the slow 2^{nd} to fast 3^{rd} mode at V_a. Massala and Lesaint reasoned that the lower acceleration voltage is due to the presence of the tube surface, which confines the streamer growth to along the cylinder's main axis restricting its radial growth. In fact, as the diameter of the tube was lowered, the streamers tended to accelerate to faster velocities at much lower voltages than the oil-only case.

To determine the mechanisms that affect streamer propagation in liquid-solid insulation systems, where the interface is oriented parallel to the main electric field component, the oil-solid cylindrical tube system is modeled. The solid cylindrical tube is placed in the oil within the needle-sphere electrode geometry discussed in Section 3.2, as shown in Fig. 7.1. The apex of the needle tip electrode is placed inside the inner radius of the tube, as shown Fig. 7.1(b), confining streamer development to be within the tube. Furthermore, the setup of the oil-tube system is such that the interface at the oil and inner radius tube surface is parallel to the main applied electric field component, which is in the z-direction. This allows the numerical results obtained from the model to be qualitatively compared to the results of Massala and Lesaint [13] who performed similar experiments with PTFE tubes, which has a relative permittivity of $\sim$2.2 [158].

7.1.3 Perpendicular Oriented Interface – Pressboard Barrier

The experimental results from the literature have shown that surfaces oriented perpendicular to the direction of the main electric field component impedes streamer development. As the streamer comes in contact with the surface, its propagation direction is altered as it is forced to travel along the surface. Due to the increased propagation length, the potential drop along the streamer channel also increases, thereby increasing the breakdown voltage [15, 16, 85].

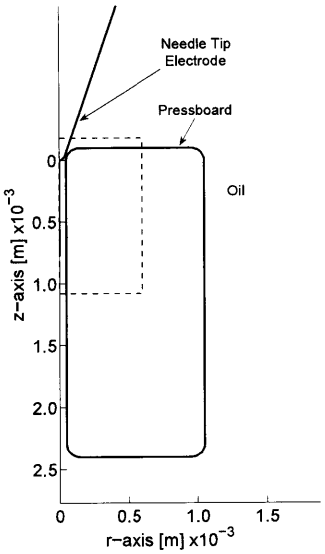

(a) Oil-solid cylindrical tube system.

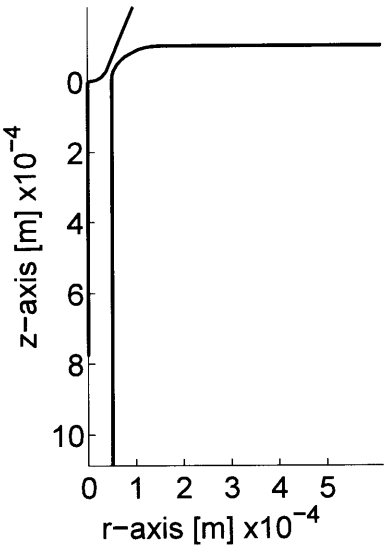

(b) Enlargement of square dashed area in Fig. 7.1(a).

Figure 7.1: 2D-axisymmetrical oil-solid tube system, where the main z-directed electric field component is parallel to the inner tube surface, within the needle-sphere electrode geometry outlined in Section 3.2.

Lesaint and Massala [91] and Liu *et al.* [15,16] observed that once streamers initiated in oil they propagated to the solid pressboard surface, which was oriented perpendicular to the main electric field direction. However, once in contact with the pressboard the streamer began to creep along and deposit charge onto the surface, which redistributed the electric field in the insulation and left noticeable discharge markings. These studies were restricted to voltages where the pressboard was not punctured, such that the streamer needed to propagate the full length of the pressboard before continuing towards the counter-electrode. Otherwise, the streamer would stop along the surface and lead to partial discharge. As a result of the increased streamer propagation length along the surface, an increase in breakdown voltage and time to breakdown was recorded, thereby significantly decreasing the streamer's average breakdown velocity. These results suggest that solid insulation in the perpendicular field configuration plays a critical role in hindering the development of streamers and decreases the probability of breakdown in oil-insulated systems.

To understand these experimental observations for streamer propagation in liquid-solid insulation systems, where the interface is oriented perpendicular to the main electric field component, the oil-solid barrier system is modeled. The needle-sphere electrode geometry, as detailed in Section 3.2, is utilized for the oil-solid barrier system. The solid barrier is placed in the oil as shown in Fig. 7.2. The distance of the needle tip electrode from the

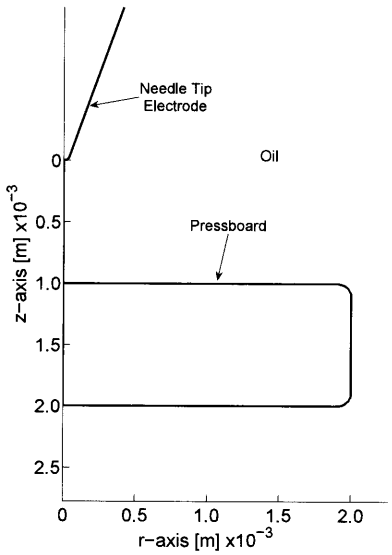

Figure 7.2: 2D-axisymmetrical oil-solid barrier system, where the main z-directed electric field component is perpendicular to the interface, within the needle-sphere electrode geometry outlined in Section 3.2.

top of the solid barrier is 1.0 mm. The setup of the oil-solid barrier allows the streamer at earlier times to travel along the symmetry z-axis, however, as the streamer comes in contact with the top surface its propagation is confined to travel in radial direction, like many experimental studies [13, 15, 16, 91]. This allows the numerical results obtained from the model to be qualitatively compared to their experimental results, such as those of Liu *et al.* [15, 16] who performed experiments with a similar oil-pressboard barrier setup. The relative permittivity of pressboard is 4.4 [92].

7.2 Oil-PTFE Tube System with the Interface Oriented Parallel to the Primary Electric Field Direction

This section discusses the streamer modeling results for the oil-PTFE tube system reported in Section 7.1.2. The streamer initially develops in the oil due to field ionization of aromatic hydrocarbon molecules, which have a low number density and low ionization potential as modeled by the parameters in Table 4.1. For an oil-only system, these types of molecules result in the formation of slow 2^{nd} mode streamers, which was discussed in Sections 4.2 and 4.4. The solid insulator permittivity is $2.2\epsilon_0$ like that of PTFE, while the oil permittivity is $2.2\epsilon_0$.

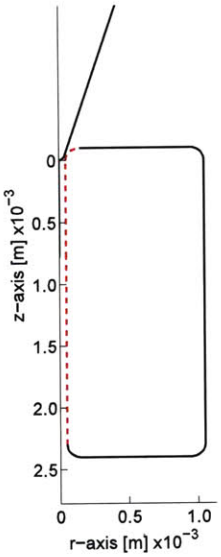

Figure 7.3: Portion of the inner oil-tube interface along which the electric field magnitude and surface charge density line distributions are measured from the top of the line to the bottom (*e.g.*, see Fig. 7.4).

As in earlier chapters, the streamers in the oil-tube system will be investigated by examining the spatial electric field distribution. However, unlike the earlier studies, the oil-tube results of this section plot the electric field and surface charge line distributions along the inner tube radius as shown in Fig. 7.3 from top to bottom, rather than along the z-axis.

7.2.1 $V_{app} = 130\,\mathbf{kV}$ – Figures 7.4(a), 7.4(b) and 7.5

The numerical results for the oil-cylindrical tube system of Fig. 7.1 and model equations (7.1)-(7.9) are presented in this section. The applied voltage to the needle electrode is $V_{app} = 130$ kV and the field ionization mechanism of (7.5) is utilized with parameter values corresponding to aromatic hydrocarbon molecules summarized in Table 4.1. Furthermore, the cylindrical solid tube has a relative permittivity of 2.2, like that of PTFE, and is oriented such that tube's inner radius surface is parallel to the direction of the main z-directed electric field component. In Figs. 7.4(a) and 7.4(b), the electric field and surface charge density profile distributions along the liquid-solid interface (see Fig 7.3) are given at several time instances. Figure 7.5 shows the rz-plane spatial distribution of the electric field magnitude.

Figure 7.4(a) shows temporal dynamics in the electric field magnitude along the liquid-solid interface, however, the peak field does not move or increase considerably over the 100 ns

duration. Also, examining Fig. 7.4(b) the level of surface charging is extremely small, such that the minuscule erratic spikes seen in the figure are due to numerical error and have little effect on the results at such low levels. From these line plots alone, it could be assumed that either i) a streamer does not develop in the oil at all or ii) it forms far away from the interface such that the streamer that develops does not affect the field and charge near the solid. The former is not likely plausible as a streamer develops for the oil-only model under the same applied voltage stress of $V_{app} = 130\,\text{kV}$ in Section 4.2.1. In that oil-only case the streamer traveled along the needle-sphere z-axis, as seen in Figs. 4.1 and 4.2. The latter hypothesis is likely, especially after examining the electric field spatial distributions of Fig. 4.2 in Section 4.2.1 for the oil-only system. From these figures, it is seen that the streamer which develops in the oil has a channel radius of $\sim 10\,\mu\text{m}$. This is much smaller than the cylindrical tube's inner radius of 50 μm such that if a streamer with similar dimensions were to develop in the oil-tube system, it would not come in contact with solid surface. But is this a fair comparison? Would not the presence of the solid tube effect streamer development such that streamers produced in the oil-tube system of Fig. 7.1 would be completely different from the streamers that develop in the oil-only system?

The electric field magnitude spatial distributions shown in Fig. 7.5 illustrates the streamer dynamics for the oil-tube system, especially near the oil-tube interface. From this figure it is evident that a streamer does form in the oil. Therefore, the stagnant electric field and low level surface charge along the liquid-solid interface illustrated in Figs. 7.4(a) and 7.4(b), respectively, results because the streamer develops and propagates along the needle-sphere z-axis. The streamer body and tip does not come in contact with the solid. Consequently, this results in the low field levels and negligible surface charging at the interface.

From Figs. 7.5(a)-7.5(c), at early times the electric field enhancement is localized near the sharp needle electrode due to the low applied voltage, near the breakdown voltage, and low space charge level in the oil. As time progresses, an extremely large field enhancement occurs further out in the oil along the z-axis (Fig. 7.5(d)). At even later times the electric field distribution shows a cylindrical-like streamer that is adjacent to the z-axis (Figs. 7.5(e) and 7.5(f)). The cylindrical streamer is enveloped by a field enhancement at its boundary, with the greatest enhancement occurring along the z-axis at the streamer tip. Like the oil-only system, the maximum electric field enhancement peak occurs along the z-axis in the oil and is approximately 3.5×10^8 V/m.

By approximating the dimensions of the streamer to be equal to the volume enclosed by the electric field enhancement, the radius of the streamer near the field enhanced streamer tip is $5 - 10\,\mu\text{m}$. The average streamer velocity, as it travels along the z-axis, is $3.0 - 4.0\,\text{km/s}$ after 100 ns. The streamer is nearly identical to the one reported in Section 4.2.1 for the oil-only system, for an oil streamer model identical to (7.1)-(7.6) used in this section. Consequently,

a puzzling question plagues these observations: why for the oil-tube system of Fig. 7.1, which is driven by an applied voltage of $V_{app} = 130$ kV, where the oil and solid insulators have equal permittivities of $2.2\epsilon_0$, does the presence of the solid tube not severely impact streamer development?

The answer to this troubling question is linked to

- the oil and solid's relative permittivity being equal $\epsilon_r = 2.2$,
- the streamer channel radius being smaller than the tube's inner radius.

Once again, streamer development occurs as if it would in the oil-only system of Section 4.2.1 and the presence of the cylindrical solid insulating tube has little effect. The fact that the oil and solid have the same relative permittivity means that there are no additional polarization forces, when compared to the oil-only system, to distort fields. The lack of the added polarization forces, coupled with the streamer radius being smaller than the tube radius results in space charge developing in a manner similar to the oil-only results. Thus, the space charge distribution is not altered by polarization charge or confined by the solid tube, as the streamer radius is smaller than the tube's. If this were not the case then the space charge profile would be different from the oil-only case, changing the electric field distribution and altering the field dependent charge generation mechanisms like field ionization. Ultimately, this would alter streamer development due to the interaction of the solid tube with the space charge in the oil resulting in different streamer dynamics than the oil-only case.

7.2.2 $V_{app} = 200$ kV – Figures 7.4(c), 7.4(d) and 7.6

The numerical results for the oil-cylindrical tube system of Fig. 7.1 and model equations (7.1)-(7.9) are presented in this section. The applied voltage to the needle electrode is $V_{app} = 200$ kV and the field ionization mechanism of (7.5) is utilized with parameter values corresponding to aromatic hydrocarbon molecules summarized in Table 4.1. Furthermore, the cylindrical solid tube has a relative permittivity of 2.2, like that of PTFE, and is oriented such that tube's inner radius surface is parallel to the direction of the main z-directed electric field component. In Figs. 7.4(c) and 7.4(d), the electric field and surface charge density profile distributions along the liquid-solid interface (see Fig 7.3) are given at several time instances. Figure 7.6 shows the rz-plane spatial distribution of the electric field magnitude.

Figures 7.4(c) and 7.4(d) show significant temporal dynamics in the electric field magnitude and surface charge density, respectively, along the liquid-solid interface. Compared to the $V_{app} = 130$ kV case presented in the previous section, the field and surface charge levels are much higher (*i.e.*, two times and at least three orders of magnitude with respect to the field and surface charge levels). Also, the electric field peak and surface charge front, which coincide at the same position along the liquid-solid interface for each time instance, are traveling along the interface at a velocity exceeding 7.0 km/s. To contrast this, the velocity with the streamer in the oil-only system presented in Section 4.2.2, which is also driven by $V_{app} = 200$ kV, the electric field and space charge peaks for the oil-only case travel at the much slower velocity of 2.0 km/s and slow down as time progresses, as shown in Figs. 4.3 and 4.4.

The electric field peak and surface charge front in Figs. 7.4(c) and 7.4(d) suggest that the streamer is traveling near or along the tube's inner radius, possibly to the extent that the tube is confining the branched radial growth of the streamer. This is confirmed by the electric field spatial distributions in Fig. 7.6, where even at early times the field level is significant (*i.e.*,$> 3.0 \times 10^8$ V/m) within the solid tube. From Figs. 7.6(a) and 7.6(b), at early times the electric field enhancement is localized near the sharp needle electrode along the liquid-solid interface. As time progresses an extremely large field enhancement of approximately 4.0×10^8 V/m occurs much further out into the inner tube along the liquid-solid interface (Figs. 7.6(c)-7.6(f)). At all times the peak electric field occurs along the liquid-solid interface such that the radial growth of the streamer channel is confined by the solid tube. By approximating the dimensions of the streamer to be equal to the volume enclosed by the electric field enhancement level, the radius of the streamer is 50 μm, which is equal to the inner radius of the solid tube.

The streamer of Fig. 7.6 is extremely different to the one reported in Section 4.2.2 for the oil-only system (Fig. 4.4), driven by the same applied voltage of $V_{app} = 200$ kV and for an oil liquid streamer model identical to (7.1)-(7.6) which is used in this section. Thus, the presence of the solid tube must play a significant role in altering the electrodynamics and field ionization mechanism responsible for streamer development in oil.

By further examining the oil-only system positive streamer of Fig. 4.4, the maximum electric field peak is $\sim 2.0 \times 10^8$ V/m and the maximum streamer channel radius is $\sim 150\,\mu$m. However, with the solid tube present the streamer radius is restricted from ~ 150 μm to 50 μm. This alters the positive space charge density distribution profile from the oil-only case by confining the free charge carriers from ionization within a smaller volume. This results in higher space charge density levels than the oil-only case at the streamer tip. Consequently, the field enhancement level is two times greater than the oil-only case at 4.0×10^8 V/m (Fig. 7.6(c)-7.6(f)). The higher field level can be explained from a simplified

one-dimensional analysis of Gauss' Law in integral form:

$$E_x(l) - E_x(0) = \int_0^l \frac{\rho_{\text{net}}}{\epsilon}\, dx, \tag{7.10}$$

where ρ_{net} is the net space charge density and E_x is the 1-D electric field. Notice that in (7.10) the greater the positive space charge density, the greater the electric field. The higher field level subsequently leads to more ionization and efficient streamer propagation. The overall result is a streamer that propagates at a fast velocity (*i.e.*, near the velocity of a fast 3$^{\text{rd}}$ mode streamer) for an applied voltage where slow 2$^{\text{nd}}$ mode streamers would be produced in transformer oil.

7.2.3 $V_{app} = 300\,\text{kV}$ – Figures 7.4(e), 7.4(f) and 7.7

The numerical results for the oil-cylindrical tube system of Fig. 7.1 and model equations (7.1)-(7.9) are presented in this section. The applied voltage to the needle electrode is $V_{app} = 300$ kV and the field ionization mechanism of (7.5) is utilized with parameter values corresponding to aromatic hydrocarbon molecules summarized in Table 4.1. Furthermore, the cylindrical solid tube has a relative permittivity of 2.2, like that of PTFE, and is oriented such that tube's inner radius surface is parallel to the direction of the main z-directed electric field component. In Figs. 7.4(e) and 7.4(f), the electric field and surface charge density profile distributions along the liquid-solid interface (see Fig 7.3) are given at several time instances. Figure 7.7 shows the rz-plane spatial distribution of the electric field magnitude.

Figures 7.4(e) and 7.4(f) show significant temporal dynamics in the electric field magnitude and surface charge density, respectively, along the liquid-solid interface. The results are similar to the $V_{app} = 200$ kV case presented in the previous section with similar values for the field and surface charge levels. Also, the electric field peak and surface charge front, which coincide at the same position along the liquid-solid interface for each time instance, are traveling along the interface at a velocity exceeding 11.0 km/s. Comparing this velocity with the streamer in the oil-only system presented in Section 4.2.3, which is also driven by $V_{app} = 300$ kV, the electric field and space charge peaks for the oil-only case travel at the much slower velocity of 3.0 km/s and slow down as time progresses, as shown in Figs. 4.5 and 4.6.

The electric field spatial distributions in Fig. 7.7 illustrate that the streamer channel radius is equal to the tube's inner radius, such that the tube restricts the streamer's radial growth. Even at early times (Figs. 7.7(a) and 7.7(b)), there is significant streamer development such that the large electric field enhancement of $\sim 4.0 \times 10^8$ V/m is not localized near the

sharp needle electrode but has traveled far into the tube. As time progresses, the streamer and associated electric field enhancement travel much further out into the tube along the liquid-solid interface (Fig. 7.7(c)-7.7(f)). At all times the peak electric field occurs along the liquid-solid interface and the streamer channel's radius is 50 μm, which is equal to the solid tube's inner radius.

Just like in the $V_{app} = 200$ kV case presented in the previous section, the streamer that develops in the oil-only system for a $V_{app} = 300$ kV drive voltage (Fig. 4.6 in Section 4.2.3) is extremely different to the one reported here for the oil-tube system. By further examining the oil-only system positive streamer of Fig. 4.6 the maximum electric field peak is approximately 2.0×10^8 V/m and the maximum streamer channel radius is ~ 250 μm. Therefore, with the solid tube present the streamer radius is restricted from ~ 250 μm to 50 μm.

It was shown in Section 4.2 that the field ionization of low number density, low ionization potential aromatic molecules results in the development of slow 2$^{\text{nd}}$ mode streamers with velocities ranging from 2–5 km/s, even at an extremely high voltages, such as $V_{app} = 300$ kV. However, as we have seen from the results of this section, by forcing the field ionization of the same molecules within a thin solid tube, whose surface is parallel to the direction of the main z-directed electric field component, a fast 3$^{\text{rd}}$ mode streamer with velocity exceeding 10 km/s develops inside the tube. By constricting field ionization within the tube a substantial amount of space charge, that would have otherwise had a more diffusive distribution in the radial direction, is confined to a narrow volume inside the tube. This produces a higher field within the inner tube ionizing more aromatic molecules and sustains fast streamer development. Thus, the presence of the solid tube in Fig. 7.1 significantly alters the electrodynamics and field ionization mechanism responsible for streamer development in oil by restricting the streamer's radial growth and space charge distribution. This results in the formation of fast 3$^{\text{rd}}$ mode streamers from the ionization of low number density, low ionization potential aromatic molecules.

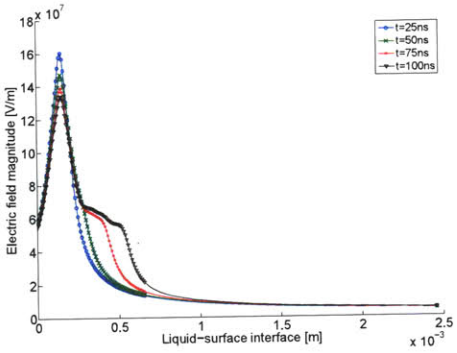

(a) $V_{app} = 130$ kV, Electric field magnitude above surface in transformer oil.

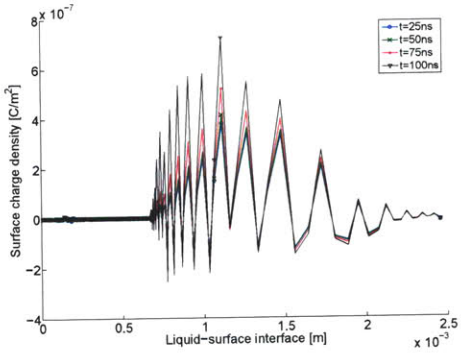

(b) $V_{app} = 130$ kV, Surface charge density along surface.

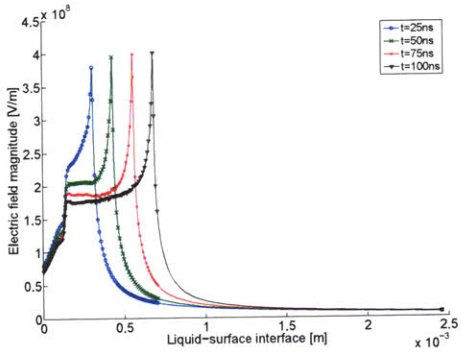

(c) $V_{app} = 200$ kV, Electric field magnitude above surface in transformer oil.

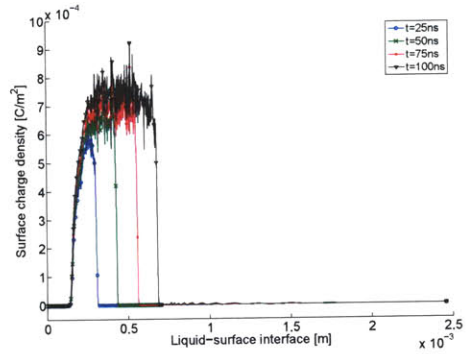

(d) $V_{app} = 200$ kV, Surface charge density along surface.

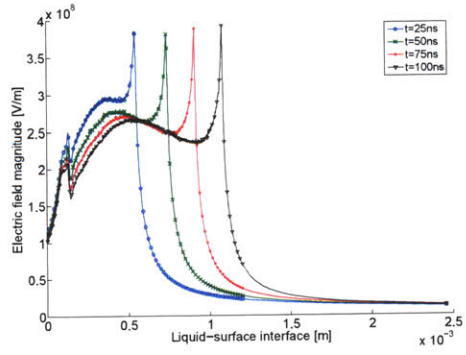

(e) $V_{app} = 300$ kV, Electric field magnitude above surface in transformer oil.

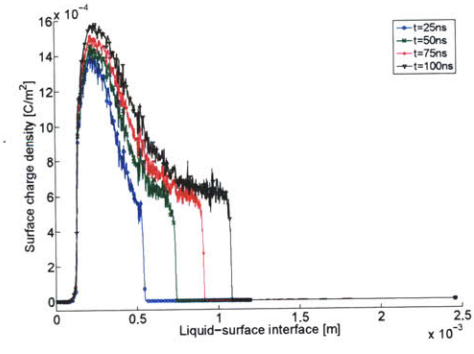

(f) $V_{app} = 300$ kV, Surface charge density along surface.

Figure 7.4: Temporal dynamics along the liquid-solid interface shown in Fig 7.3 at 25 ns intervals from $t = 25 - 100$ ns given by the solution to the oil-solid insulation model of (7.1)-(7.9) for the field ionization mechanism of (7.5) and varying applied voltage (*e.g.*, 130 kV, 200 kV, and 300 kV). The oil is comprised of low number density, low ionization potential aromatic hydrocarbon molecules only with parameter values summarized in Table 4.1. The solid insulator's permittivity is $2.2\epsilon_0$.

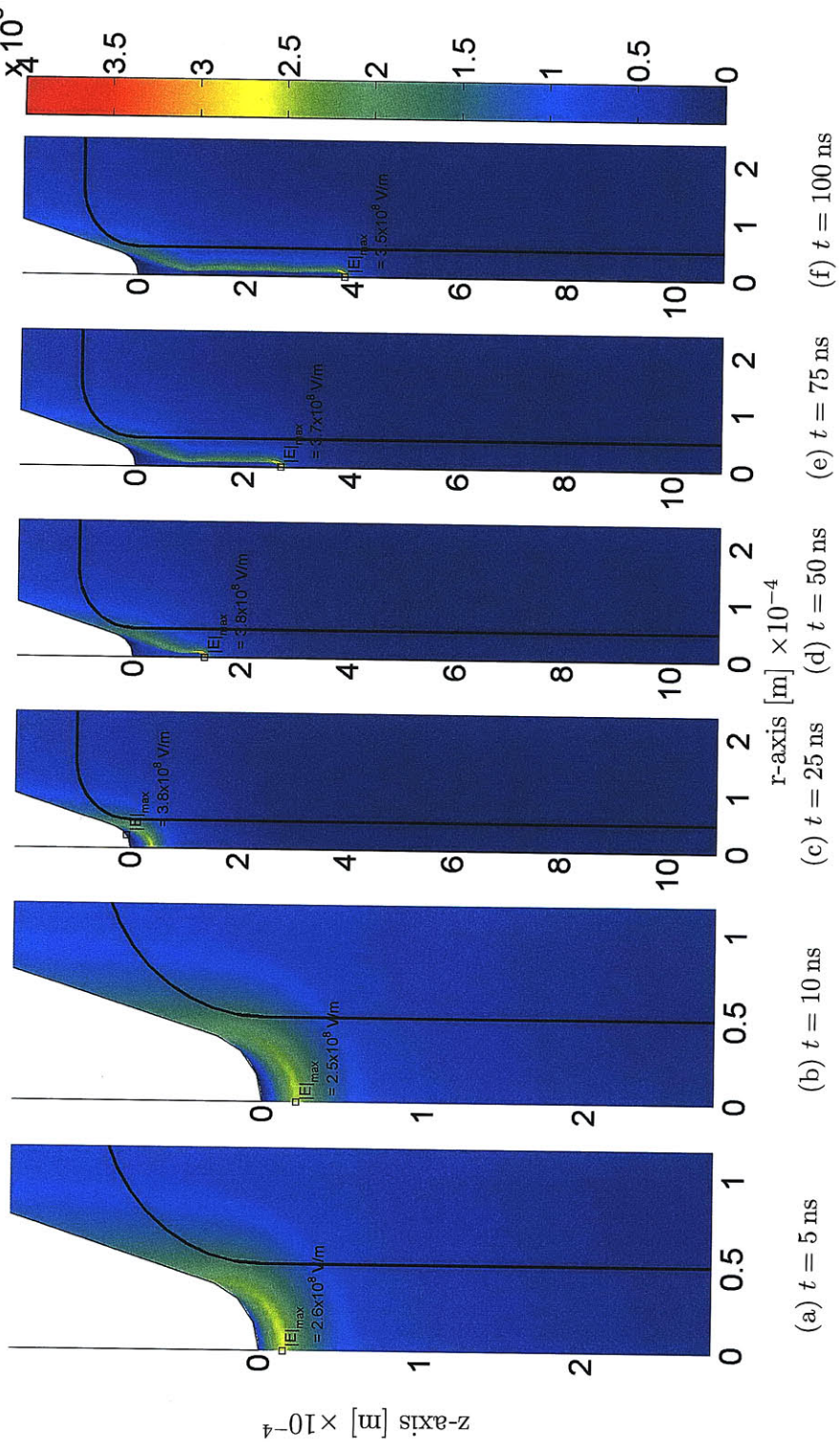

(a) $t = 5$ ns (b) $t = 10$ ns (c) $t = 25$ ns (d) $t = 50$ ns (e) $t = 75$ ns (f) $t = 100$ ns

Figure 7.5: Electric field magnitude [V/m] spatial distributions (as a function of r and z in the electrode geometry) from $t = 5 - 100$ ns given by the solution to the oil-solid insulation model (7.1)-(7.9) for an applied voltage of $V_{app} = 130$ kV and the field ionization mechanism of (7.5). The oil is composed of low number density, low ionization potential aromatic hydrocarbon molecules only with parameter values summarized in Table 4.1. The solid insulator's permittivity is $2.2\epsilon_0$.

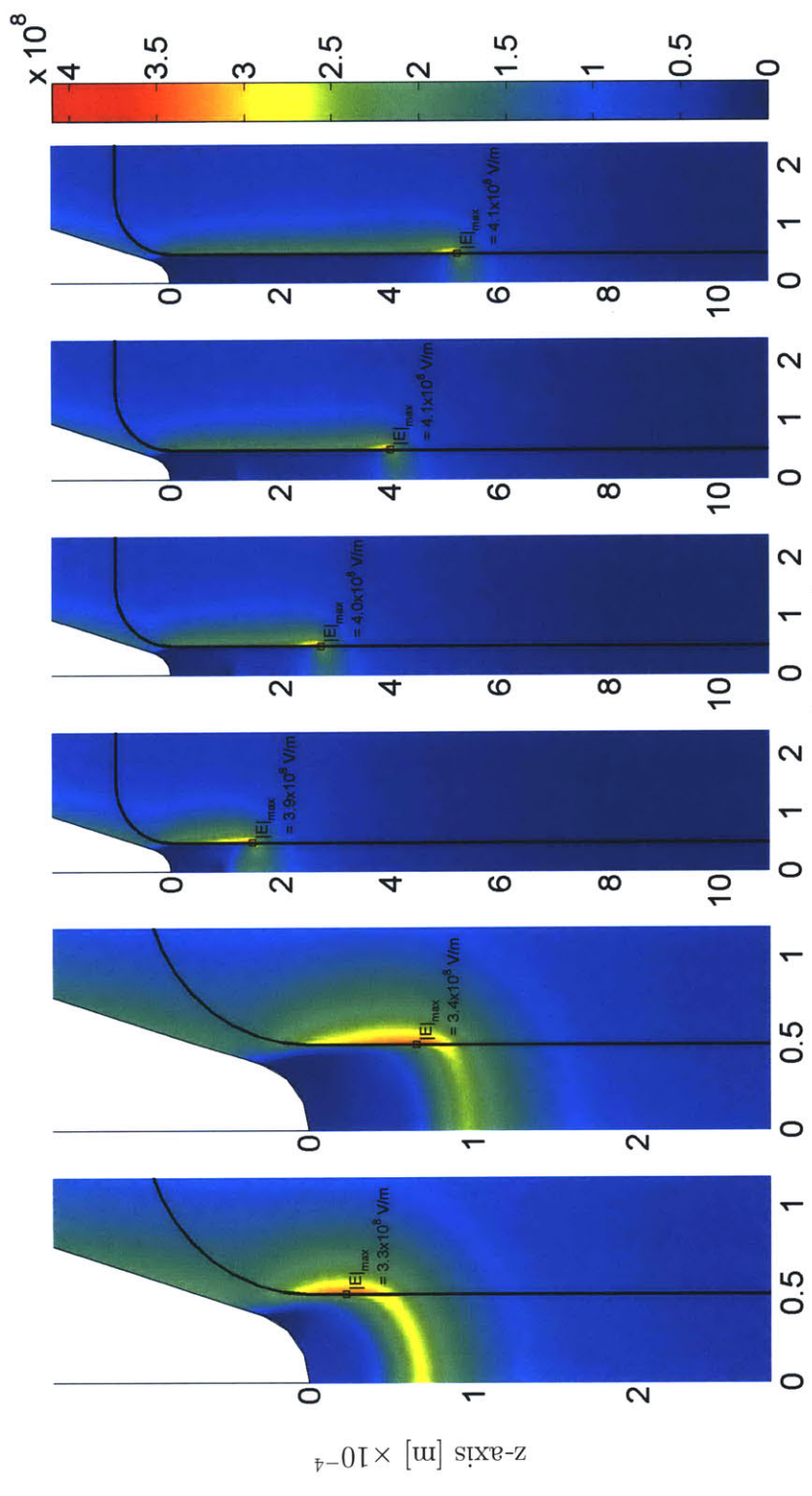

(a) $t = 5$ ns (b) $t = 10$ ns (c) $t = 25$ ns (d) $t = 50$ ns (e) $t = 75$ ns (f) $t = 100$ ns

Figure 7.6: Electric field magnitude [V/m] spatial distributions (as a function of r and z in the electrode geometry) from $t = 5 - 100$ ns given by the solution to the oil-solid insulation model (7.1)-(7.9) for an applied voltage of $V_{app} = 200$ kV and the field ionization mechanism of (7.5). The oil is composed of low number density, low ionization potential aromatic hydrocarbon molecules only with parameter values summarized in Table 4.1. The solid insulator's permittivity is $2.2\epsilon_0$.

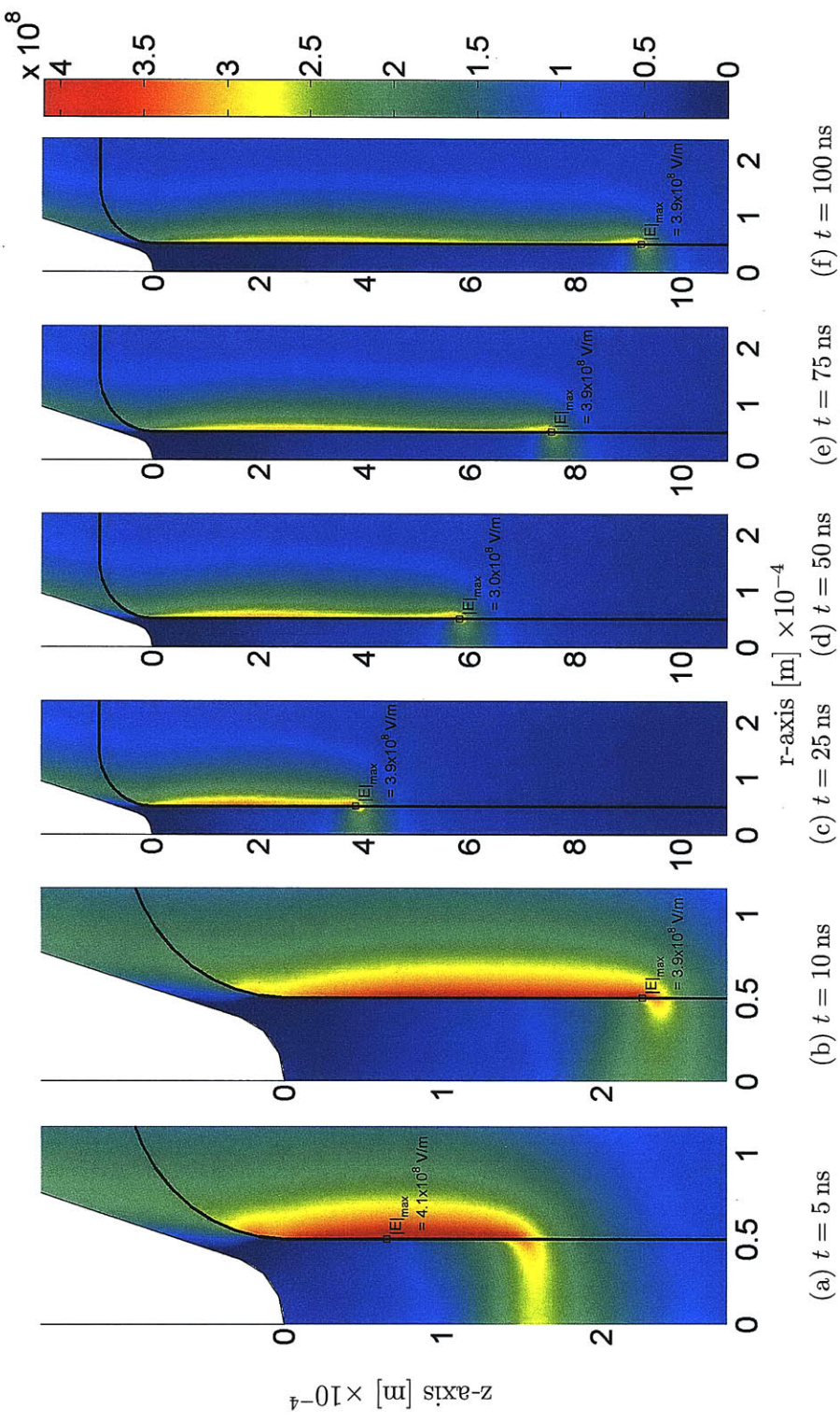

(a) $t = 5$ ns (b) $t = 10$ ns (c) $t = 25$ ns (d) $t = 50$ ns (e) $t = 75$ ns (f) $t = 100$ ns

Figure 7.7: Electric field magnitude [V/m] spatial distributions (as a function of r and z in the electrode geometry) from $t = 5 - 100$ ns given by the solution to the oil-solid insulation model (7.1)-(7.9) for an applied voltage of $V_{app} = 300$ kV and the field ionization mechanism of (7.5). The oil is composed of low number density, low ionization potential aromatic hydrocarbon molecules only with parameter values summarized in Table 4.1. The solid insulator's permittivity is $2.2\epsilon_0$.

7.2.4 Summary

The numerical results obtained for oil-tube system of Fig. 7.1, where the interface is oriented parallel to the direction of the main z-directed electric field component, have shown that the effect of the solid insulation is strongly dependent on the extent to which the surface alters the streamer shape and electric field by modifying and confining the space charge distribution. The modification of the streamer shape leads to a change in the space charge electric field that, when superimposed with the Laplacian field, leads to a larger field enhancement in the oil. The higher field allows for greater ionization which expedites streamer growth and assists in breakdown since the main field component is parallel with the solid surface.

These results corroborate the geometric field regulation hypothesis of Lundgaard *et al.* [14], where the geometry of the streamer regulates the electric field generated during streamer propagation such that in the presence of a solid insulation surface, which alters the streamer shape, the geometrical field regulation is lost and streamers tend to propagate faster and at lower voltages. Moreover, the results of streamers in oil-tube systems is supported by experimental evidence from the literature [13, 14, 21, 59]. The results also explain the experimental observations of Massala and Lesaint [13], where insulating PTFE tubes were used to confine and guide streamer growth within the cylinder. They observed a lower breakdown voltage, a significant change in the streamer shape and an increase in streamer velocity at lower voltages.

7.3 Oil-Pressboard Barrier System with the Interface Oriented Perpendicular to the Primary Electric Field Direction

This section discusses the streamer modeling results for the oil-pressboard barrier system reported in Section 7.1.3. The streamer initially develops in the oil due to field ionization of aromatic hydrocarbon molecules, which have a low concentration and low ionization potential as modeled by the parameters in Table 4.1. For an oil-only system, these types of molecules result in the formation of slow 2^{nd} mode streamers, which was discussed in Sections 4.2 and 4.4. The solid insulator permittivity is $4.4\epsilon_0$ like that of pressboard, while the oil permittivity is $2.2\epsilon_0$.

As in earlier chapters, the streamers in the oil-barrier system will be investigated by examining the spatial electric field distribution. However, the oil-barrier results of this section

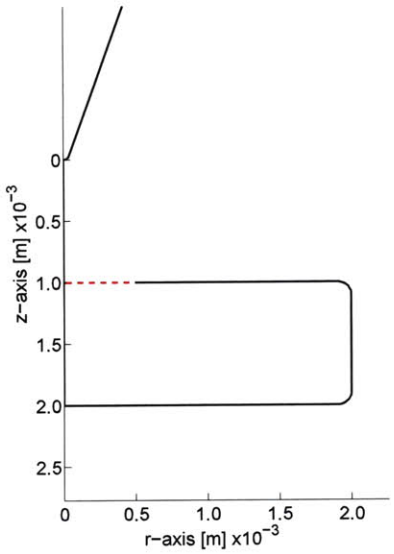

Figure 7.8: Portion of the oil-solid barrier interface along which the electric field magnitude and surface charge density line distributions are measured from the z-axis radially outwards (*e.g.*, see Fig. 7.9).

plot the electric field and surface charge line distributions along the top barrier interface, as shown in Fig. 7.3, from the z-axis radially outwards.

7.3.1 Results – Figures 7.9 and 7.10

The numerical results to the oil-solid barrier system of Fig. 7.2 and model equations (7.1)-(7.9) are presented in this section. The applied voltage to the needle electrode is $V_{app} = 130$ kV and the field ionization mechanism of (7.5) is utilized with parameter values corresponding to aromatic hydrocarbon molecules summarized in Table 4.1. Furthermore, the solid barrier has a relative permittivity of 4.4, like that of pressboard, and is oriented such that its top surface is perpendicular to the direction of the main z-directed electric field component. In Fig. 7.9, the electric field and surface charge density profile distributions along the liquid-solid interface (see Fig 7.8) are given at several time instances after the streamer comes in contact with the solid insulation. Figure 7.10 shows the rz-plane spatial distribution of the electric field magnitude.

The electric field spatial distributions in Fig. 7.10 illustrate the streamer dynamics in the oil-solid barrier system before and after it comes in contact with solid barrier. Figures 7.10(a) and 7.10(b) document the streamer propagation along the z-axis before it comes in contact with the solid barrier. Figure 7.10(c) shows the streamer immediately after it comes in

contact with the solid barrier at $t = 260$ ns. Afterward the streamer travels along the solid surface in a direction that is perpendicular to its original trajectory along the z-axis due to the transverse orientation of the solid barrier (Figs. 7.10(d)-7.10(f)).

7.3.1.1 Streamer Prior to Contacting Interface – Figs. 7.10(a) and 7.10(b)

Investigating the streamer along the z-axis before it comes in contact with the barrier it looks similar to the streamer discussed in Section 4.2.1 for the oil-only system that is also driven by $V_{app} = 130$ kV. However, on closer inspection by comparing Figs. 7.10(b) and 4.2(e) the streamer in the oil-solid barrier system travels considerably faster and reaches $z = 1$ mm, where the top of the barrier surface is, in ~ 250 ns. In contrast, in the oil-only case it takes ~ 325 ns to reach the same position along the z-axis. Thus, we can conclude that presence of the solid barrier with relative permittivity of 4.4 accelerates the streamer, such that it travels with an average velocity of 4.0 km/s before it hits the surface compared to 3.0 km/s streamer in the oil-only case. This phenomenon results from the permittivity difference between the oil, where the streamer forms and propagates, and the solid barrier, whose relative permittivity is two times greater than that of oil. Due to the solid barrier having a higher permittivity, the polarization charge developed along the top surface at $z = 1$ mm, in response to the electric field generated by the positive streamer and needle tip, is of opposite polarity to the positive space charge comprising the streamer. Therefore, this negative polarization charge produces an added polarization force on the positive streamer which accelerates it towards the barrier's top surface. More on the effect of permittivity differences between oil and solid insulation will be discussed in Section 7.4.

7.3.1.2 Streamer Immediately After Contacting Interface – Fig. 7.10(c)

At $t = 260$ ns, the streamer, which was previously propagating unimpeded along the z-axis, comes in contact with the solid barrier surface and its course is altered to travel along the perpendicular oriented interface. Of special interest here is what happens to the electric field enhancement as the streamer propagation goes from the z-axis to along the barrier surface. Note that in Figs. 7.10(a) and 7.10(b), before the streamer makes contact with the barrier, the maximum field enhancement is 3.8×10^8 V/m in the oil. However, immediately after the streamer touches the surface, its maximum field enhancement almost doubles to 6.7×10^8 V/m. This large field enhancement is a result of two phenomena: i) the polarization charge and force induced at the interface by the positive streamer and the difference in oil-solid permittivities and ii) the compression of the space charge at the streamer tip into a small volume adjacent to and along the surface by the presence of the barrier. The permittivity mismatch effect is similar to that discussed previously and is

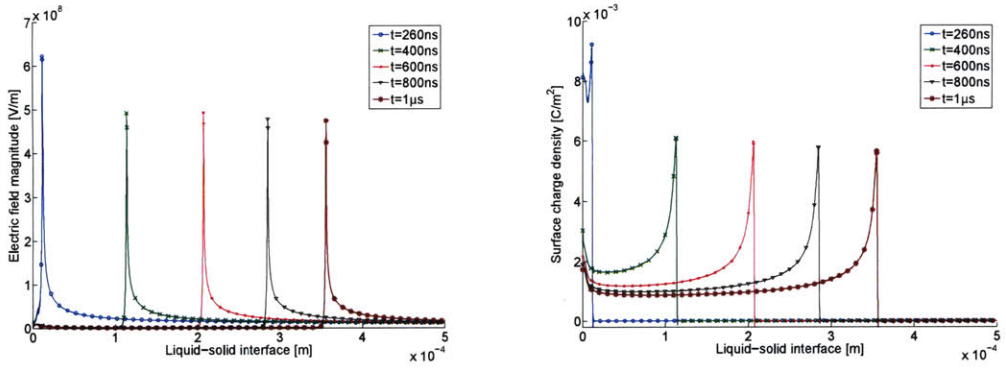

(a) Electric field magnitude above surface in transformer oil.

(b) Surface charge density along surface.

Figure 7.9: Temporal dynamics along the liquid-solid interface in Fig 7.8 at several time instances after the streamer makes contact with the perpendicular surface. Results given by the solution to the oil-solid insulation model of (7.1)-(7.9) for an applied voltage of $V_{app} = 130\,\text{kV}$ and the field ionization mechanism of (7.5). The oil is composed of low number density, low ionization potential aromatic hydrocarbon molecules only with parameter values summarized in Table 4.1. The solid insulator's permittivity is $4.4\epsilon_0$.

discussed in detail in Section 7.4. However, one special note regarding the effect of the permittivity difference is that the induced polarization charge also assists the compression of the streamer tip's free space charge into a small volume along the barrier surface, thereby creating a larger field enhancement.

Regarding the compression of space charge into a small volume, this phenomenon is similar to the oil-tube over-voltage case in Sections 7.2.2 and 7.2.3, where the streamer radial growth was restricted by the tube causing the space charge to be confined within the small inner tube volume. The result was an increase in the field enhancement and more ionization. Similarly, as the streamer tip, which was previously traveling unobstructed in the $+z$-direction, is stopped at the solid barrier, all the positive space charge is confined to a small volume near the surface. The high space charge results in an increase in field enhancement at the oil-barrier interface as seen in the electric field line plot of Fig. 7.9(a) at $t = 260\,\text{ns}$. Also, due to the high space charge density and electric field near the surface at $t = 260\,\text{ns}$, a large surface charge density forms on the liquid-solid interface near the z-axis (Fig. 7.9(b)).

7.3.1.3 Streamer Traveling along Perpendicular Interface - Figs. 7.9 and 7.10(d)-7.10(f)

Just after $t = 250$ ns, the streamer comes in contact with the solid barrier. Since the barrier surface is perpendicular to the streamers original propagation path and the dominant field direction, it impedes further growth of the streamer along the z-axis. As such, the streamer travels along the pressboard surface in the radial direction (Figs. 7.10(d)-7.10(f)). As in the oil-tube system in Section 7.2, the barrier surface alters the streamer shape when the two come in contact. The modification of the streamer shape once again leads to an increase in the electric field enhancement at the streamer tip to greater than 5×10^8 V/m. However, since the main electric field component of the streamer tip is perpendicular to the barrier surface, the streamer velocity does not increase. Rather the streamer velocity decreases because there is only a small field component that is parallel to the surface in the radial direction, such that the migration of charge along the surface is decreased when compared to the streamer propagation along the z-axis for the initial 250 ns. This can be seen when examining the large surface charge build up on the upper pressboard surface in Fig. 7.9(b).

Figure 7.9 shows significant temporal dynamics in the electric field magnitude and surface charge density along the liquid-solid interface portion in Fig. 7.8. The electric field and surface charge peaks, which coincide at the same position along the liquid-solid interface for each time instance, are traveling along the interface at a velocity of ~ 400 m/s. Comparing this velocity with 4.0 km/s velocity of the streamer as it traveled along the z-axis (before it touched the interface in Section 7.3.1.1), there is an order of magnitude decrease in the streamer velocity. Furthermore, the electric field and space charge peaks decelerate along the liquid-solid interface as time progresses.

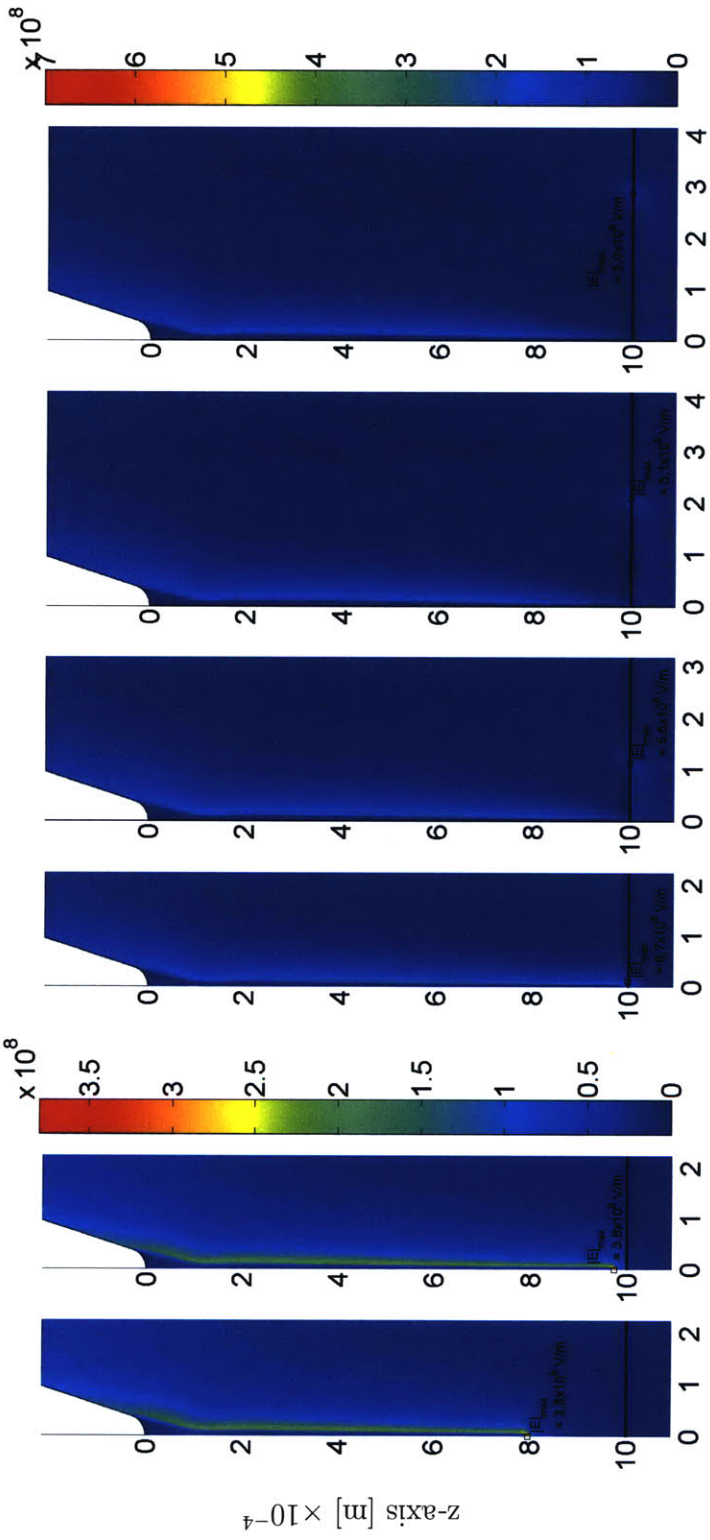

(a) $t = 200$ ns (b) $t = 250$ ns (c) $t = 260$ ns (d) $t = 400$ ns (e) $t = 600$ ns (f) $t = 800$ ns

Figure 7.10: Electric field magnitude [V/m] spatial distributions (as a function of r and z in the electrode geometry) at several time instances before (a)-(b) and after (c)-(f) the streamer makes contact with the perpendicular surface. Results given by the solution to the oil-solid insulation model of (7.1)-(7.9) for an applied voltage of $V_{app} = 130$ kV and the field ionization mechanism of (7.5). The oil is composed of low number density, low ionization potential aromatic hydrocarbon molecules only with parameter values summarized in Table 4.1. The solid insulator's permittivity is $4.4\epsilon_0$.

7.3.2 Summary

The numerical results obtained for the oil-barrier system of Fig. 7.2, where the interface is oriented perpendicular to the direction of the main z-directed electric field component, have shown that the solid barrier insulation impedes streamer development by obstructing its propagation path to the counter-electrode. When the streamer comes in contact with the surface, the streamer shape is modified producing a greater field enhancement at the streamer tip along the surface. But since the main electric field component is perpendicular to the surface, the streamer does not propagate in that direction. Rather the streamer travels along the solid surface extending its propagation length, which substantially increases the time to breakdown. Also, the velocity decreases due to the small electric field component parallel to the surface slowing down charge migration and streamer development.

The significant decrease in streamer velocity, as it travels along the pressboard barrier, is directly related to the increase in the time to breakdown as recorded for similar experimental systems in the literature [13, 15, 16, 85, 91]. The numerical results for the oil-pressboard barrier system are validated by the experimental results of Liu *et al.* [15, 16] and help to explain the observations for systems where the solid interface is oriented perpendicular to the main electric field component.

7.4 The Effects of Permittivity Differences of Oil and Solid Insulation on Streamer Propagation

The effect of permittivity differences between oil and solid insulation on streamer propagation has been well documented in the literature extensively. For example, researchers report that low permittivity insulating solids, such as polyethylene and polypropylene, which have relative permittivities of $\sim$2.3 almost matching that of oil, result in high flashover voltages for impulse and 60 Hz excitations [57]. On the other hand, it has been reported that larger permittivity differences between liquid and solid, such as that of oil and pressboard, can assist in discharge propagation and enhance surface irregularities [93]. Furthermore, pressboard with a relative permittivity of 4.4 [92], twice that of transformer oil at 2.2 [83], has been shown to dramatically affect streamer propagation, such that streamers in the oil are attracted towards the pressboard surface [57, 84, 93].

In other studies researchers observed that the presence of pressboard spacer objects in oil gave way to large field enhancement due to the permittivity mismatch [84]. Therefore, it was postulated that the field enhancement led to the reduction of the breakdown voltage in an oil-pressboard system compared to an oil-only system. They too were able to show

that by utilizing solid materials with relative permittivity comparable to transformer oil, the reduction in breakdown voltage was not so severe or did not exist in some cases.

The reported impact of permittivity differences of oil and solid insulation shows that it is a source of major concern for insulation designers. To better understand this permittivity difference effect we examine three test cases, where the permittivity of the solid insulation is varied and the oil permittivity is kept constant at $2.2\epsilon_0$. As was shown in the two previous sections, the orientation of the solid insulation with respect to the direction of the main electric field component has a major bearing on streamer dynamics. Therefore, three test cases for varying solid permittivity are done for both parallel and perpendicular oriented liquid-solid interfaces. For the parallel oriented interface the oil-cylindrical tube system in Fig. 7.1, which is described in Section 7.1.2, is utilized and the solid insulation's relative permittivity for three three test cases are 4.4, 3.3, and 1.0. For the perpendicular oriented interface the oil-solid barrier system in Fig. 7.2 and described in Section 7.1.3 is utilized and the solid insulation's relative permittivity for three test cases are 3.3, 2.2, and 1.0.

7.4.1 Permittivity and Polarization

The relative permittivity of a linear dielectric material describes the ability of tightly bound electrons in the material to be displaced from the positive nucleus under an applied electric field to form electric dipoles which results in a net electronic polarization [19]. The greater the relative permittivity of a material, the greater the polarization charge that develops in a region where there is a local imbalance of dipoles [19], as shown in Fig. 7.11. This polarization charge is a source of electric field that affects electrodynamics in a system such as a composite liquid-solid insulation structure. The net polarization charge produces the polarization field

$$\vec{P} = (\epsilon_r - 1)\epsilon_0 \vec{E}, \tag{7.11}$$

which is dependent on the electric field. A linear combination of the polarization field and the electric field in the form

$$\begin{aligned} \vec{D} &= \epsilon_0 \vec{E} + \vec{P} \\ &= \epsilon_r \epsilon_0 \vec{E}, \end{aligned} \tag{7.12}$$

results in the displacement field, which is a true measure of the total field from both free and polarization charges [19] that can act upon free charge. Thus, the greater a material's relative permittivity ϵ_r, the greater the total force that acts upon free charge in a system.

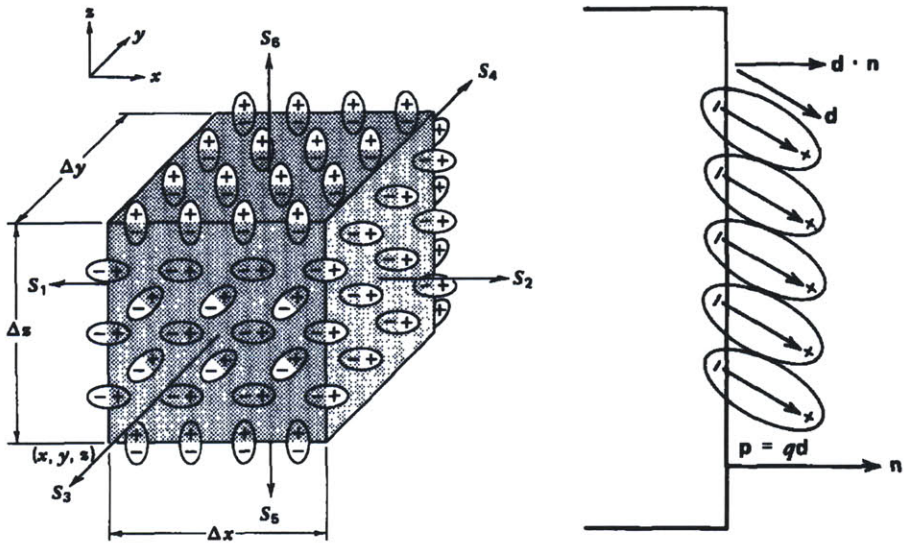

(a) (b)

Figure 7.11: (a) The net charge enclosed within a differential-sized volume of dipoles has contributions only from dipoles that are cut by the surfaces. All totally enclosed dipoles contribute no net charge. (b) Only those dipoles within a distance $\vec{d} \cdot \vec{n}$ of the surface are cut by the volume. (Figure 3-4, [19])

7.4.2 Analytical Study of the Electric Fields in a Simplified Two Dielectric System with Unique Permittivities

For the simple two series, lossless dielectric parallel plane system shown in Fig. 7.12 the voltage across the electrode plates is

$$\begin{aligned} V_0 &= \int_0^a E_1 dx + \int_a^b E_2 \, dx \\ &= E_1 a + E_2 (b - a). \end{aligned} \tag{7.13}$$

Since the two dielectrics are lossless (*i.e.*, $\sigma_1 = \sigma_2 = 0$), no surface charge builds up at the $x = a$ interface such that

$$\rho_s = \epsilon_2 E_2 (x = a_+) - \epsilon_1 E_1 (x = a_-) = 0. \tag{7.14}$$

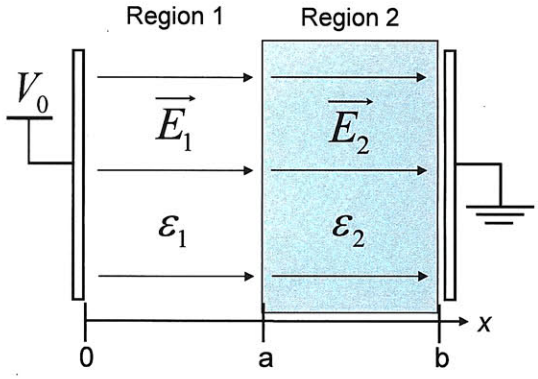

Figure 7.12: Two dielectric parallel plane geometry to represent a simplified liquid-solid insulation system.

Combining (7.13) and (7.14), the electric fields in the two regions are

$$E_1 = \frac{\epsilon_2 V_0}{\epsilon_2 a + \epsilon_1 (b-a)} = \frac{V_0}{a + \frac{\epsilon_1}{\epsilon_2}(b-a)}, \tag{7.15}$$

$$E_2 = \frac{\epsilon_1 V_0}{\epsilon_2 a + \epsilon_1 (b-a)} = \frac{V_0}{\frac{\epsilon_2}{\epsilon_1} a + (b-a)}. \tag{7.16}$$

Imagine now that Region 1 is oil with permittivity $\epsilon_1 = 2.2\epsilon_0$ and Region 2 is the solid insulation with permittivity ϵ_2. There are three cases to be examined.

1. $\epsilon_1 = \epsilon_2$:
   If the solid insulation has the same permittivity as oil, such as PTFE, then the fields E_1 and E_2 are the same, such that

$$E_0 = E_1 = E_2 = \frac{V_0}{b}. \tag{7.17}$$

   In (7.17) the field has no dependency on the permittivities and is solely dependent on the applied voltage and geometry. Therefore, for this simplified lossless system it would be equivalent to making the whole parallel plane structure $0 \leq x \leq b$ filled with transformer oil. Consider this to be the base case.

2. $\epsilon_2 > \epsilon_1$:
   For the case where the solid insulation has a higher permittivity than oil, such as pressboard, the fields in the two regions are such that

$$E_1 > E_0, \tag{7.18}$$
$$E_2 < E_0. \tag{7.19}$$

   Due to the higher permittivity of the solid insulation, the field within the oil is greater than it would otherwise be if the whole parallel plane $0 \leq x \leq b$ structure were only comprised of oil, such as in the base case 1. This greater field in the oil means that positive and negative charges in this region would experience a greater force in the $+x$ and $-x$ directions, respectively, than for an oil-only system.

3. $\epsilon_2 < \epsilon_1$:
   For the case where the solid insulation has a lower permittivity than oil, the fields in the two regions are such that

$$E_1 < E_0, \tag{7.20}$$
$$E_2 > E_0. \tag{7.21}$$

   Due to the lower permittivity of the solid insulation, the field within the oil is less than it would otherwise be if the whole parallel plane $0 \leq x \leq b$ structure were only comprised of oil such as in the base case 1. This result is the opposite of case 2. The lower field in the oil means that positive and negative charges in this region would experience a smaller force in the $+x$ and $-x$ directions, respectively, than for an oil-only system.

7.4.3 Parallel Oriented Interface – Cylindrical Tube

This section discusses the streamer modeling results for the oil-solid tube system test cases, where the permittivity of the solid insulation is varied (*e.g.*, $4.4\epsilon_0$, $3.3\epsilon_0$, and $1.0\epsilon_0$) and the oil permittivity is kept constant at $2.2\epsilon_0$. The oil-tube case, where the solid insulation's permittivity is $2.2\epsilon_0$, was presented in Section 7.2.1.

The model equations are given in (7.1)-(7.9) and the applied voltage to the needle electrode is $V_{app} = 130\,\text{kV}$. The streamer initially develops in the oil due to field ionization of aromatic hydrocarbon molecules, which have a low number density and low ionization potential as modeled by the parameter values in Table 4.1. For an oil-only system, these types of molecules result in the formation of slow 2^{nd} mode streamers, which was discussed in Sections 4.2 and 4.4.

The streamers in the oil-tube system are investigated by examining the spatial electric field distribution and the electric field magnitude and surface charge density line distributions along the inner tube radius from top to bottom, as highlighted in red in Fig. 7.3.

7.4.3.1 $\epsilon = 4.4\epsilon_0$ – Figures 7.13(a), 7.13(b) and 7.14

The numerical results for the oil-cylindrical tube system of Fig. 7.1 and model equations (7.1)-(7.9) are presented in this section. The applied voltage to the needle electrode is $V_{app} = 130$ kV and the field ionization mechanism of (7.5) is utilized with parameter values corresponding to aromatic hydrocarbon molecules in Table 4.1. The solid cylindrical tube has a relative permittivity of 4.4, like that of pressboard, and is oriented such that the tube's inner radius surface is parallel to the direction of the main z-directed electric field component. In Figs. 7.13(a) and 7.13(b), the electric field magnitude and surface charge density profile distributions along the liquid-solid interface (see Fig 7.3) are given at several time instances. Figure 7.14 shows the rz-plane spatial distribution of the electric field magnitude.

Examining the results along the liquid-solid interface and the spatial results of the electric field distribution, it is evident that these streamer dynamics for the solid tube with permittivity of $4.4\epsilon_0$ are extremely different from that of the PTFE modeled tube with permittivity $2.2\epsilon_0$ in Section 7.2.1, where the same $V_{app} = 130$ kV drive voltage was applied. In the PTFE case, the streamer was not affected by the presence of the solid tube as there were no permittivity mismatch effects between the oil and solid tube and the radial dimensions of the streamer channel were smaller than the tube's inner radius. The lack of a permittivity difference between the oil and PTFE tube results in the absence of additional polarization charge at the liquid-solid interface that alters the electric field acting on the streamer body. Since the oil and PTFE tube have the same permittivity, the field within the inner tube is the same as if the tube was not there at all, as shown by the simple analytical study in Section 7.4.2. With regards to the streamer's radial size, it was shown in Sections 7.2.2 and 7.2.3 that if the streamer size was similar to or greater than the tube's inner radius, then streamer growth and the free charge that arises from ionization of the oil molecules are confined within the inner tube. This restriction of the streamer's radial growth has a profound impact on its propagation velocity, such that fast 3$^{\text{rd}}$ mode streamers propagate under conditions (*i.e.*, applied voltage and liquid chemistry) where only slow 2$^{\text{nd}}$ mode streamers would form in oil-only systems where the solid tube was not present. Thus, by altering the normal streamer shape the electrodynamics and ionization mechanisms responsible for streamer development in oil are significantly altered.

In this section, the $2.2\epsilon_0$ and $4.4\epsilon_0$ permittivities of the oil and solid tube, respectively, or rather the 2 times greater permittivity of the solid has a severe effect on streamer propagation from an insulation and breakdown point of view. At early times, due to the solid tube's higher permittivity, there is a polarization charge produced by the solid insulation that increases the electric field within the oil-filled inner tube volume, as explained by case 2 of the simple analytical study in Section 7.4.2. The polarization charge not only increases the field within the tube but also slightly alters the field lines to point more radially towards the solid tube. Due to this change in electric field compared to the oil-only system in Section 4.2.1, immediately after the application of $V_{app} = 130$ kV step voltage, there is an increase in charge generation from ionization of the oil molecules. Also, the net positive space charge in the streamer tip is directed towards the inner surface of the solid insulation, such that even at early times the streamer travels along the inner surface and has radial dimensions that span the entire inner tube radius of 50 μm (Figs. 7.14(a) and 7.14(b)). This is in stark contrast to the streamer driven by the same $V_{app} = 130$ kV step voltage in the oil-only system that propagates straight down the z-axis (Fig. 4.1).

The streamer is driven into the solid surface by the polarization charge, similar to the oil-solid barrier system in Section 7.3. Consequently, the streamer is restricted from further radial growth, and its shape and space charge density distribution are altered like those in the 200 kV and 300 kV oil-PTFE tube cases in Section 7.2. The result is a streamer with much higher field enhancement of $\sim 7.0 \times 10^8$ V/m that travels in the tube with a velocity of ~ 9.0 km/s in 100 ns (Figs. 7.14(c)-7.14(f)).

The electric field and surface charge line distribution shown in Fig. 7.13(a) and 7.13(b) also reveal significant temporal dynamics along the liquid-solid interface. Once again, these results are unlike the results for a solid tube having permittivity of $2.2\epsilon_0$ in Section 7.2.1. In that case, there was no surface charge build up and no electric field peaks because the streamer traveled along the z-axis. In contrast, here the electric field and surface charge density peaks, which coincide at the same position along the liquid-solid interface for each time instance, are traveling along the interface at a velocity exceeding 10.0km/s. Comparing this velocity with the streamer in the oil-only system driven by the same 130kV step voltage and presented in Section 4.2.1, the electric field and space charge density peaks travel at the much slower velocity of 3.0 km/s with a peak field of 3.5×10^8 V/m, as shown in Fig. 4.1.

7.4.3.2 $\epsilon = 3.3\epsilon_0$ – Figures 7.13(c), 7.13(d) and 7.15

The numerical results for the oil-cylindrical tube system of Fig. 7.1 and model equations (7.1)-(7.9) are presented in this section. The applied voltage to the needle electrode is $V_{app} = 130$ kV and the field ionization mechanism of (7.5) is utilized with parameter values

corresponding to aromatic hydrocarbon molecules in Table 4.1. The solid cylindrical tube has a relative permittivity of 3.3 and is oriented such that the tube's inner radius surface is parallel to the direction of the main z-directed electric field component. In Figs. 7.13(c) and 7.13(d), the electric field magnitude and surface charge density profile distributions along the liquid-solid interface (see Fig 7.3) are given at several time instances. Figure 7.15 shows the rz-plane spatial distribution of the electric field magnitude.

The results of this section are analogous to the previous section, where the solid insulation has a permittivity of $4.4\epsilon_0$. Due to 1.5 times greater permittivity of the solid insulation with respect to the oil, the field within the oil-filled tube is greater than the oil-only case and slightly more directed towards the solid insulation as explained by case 2 of the simple analytical study in Section 7.4.2. However, when compared to results for the solid tube with permittivity of $4.4\epsilon_0$ in the previous section, it is clear that the maximum field enhancement ($\sim 5.8 \times 10^8$ V/m, Figs. 7.13(c) and 7.15), the maximum surface charge density ($\sim 4.0 \times 10^{-3}$ C/m^2, Fig. 7.13(d)), and the streamer velocity ($\sim$6.0 km/s, Fig. 7.15) in the tube are all lower.

The lowering of the field, surface charge density, and streamer velocity can be explained by examining the field E_1 within the oil region from the simple parallel plane model in Section 7.4.2. Due to the oil-solid permittivity mismatch, where $\epsilon_1 = 2.2\epsilon_0$ and ϵ_2 are the oil and solid permittivities, respectively, the field within the oil region is

$$\begin{aligned} E_1 &= \frac{\epsilon_2 V_0}{\epsilon_2 a + \epsilon_1 (b-a)} \\ &= \frac{V_0}{a + \frac{\epsilon_1}{\epsilon_2}(b-a)}, \end{aligned} \tag{7.22}$$

where a and $(b-a)$ are the thicknesses of the oil and solid regions, respectively. Examining (7.22), if the solid's permittivity ϵ_2 is lowered, for example from $4.4\epsilon_0$ to $3.3\epsilon_0$, then the denominator is increased and the field within the oil region is lowered. If the permittivity is lowered to $2.2\epsilon_0$, then there is no permittivity difference and the field within the whole structure is the same, as shown in case 1 in Section 7.4.2, such that from a polarization standpoint the solid does not alter fields.

Due to the solid's lower permittivity of $3.3\epsilon_0$ in the oil-tube system, the permittivity mismatch effect is less pronounced than in the previous section where it is $4.4\epsilon_0$. Therefore, the additional field generated by the polarization of the solid insulation is less and consequently, the force that drives the streamer into the inner tube surface and alters the streamer shape is lower. The overall result is a lower field in the tube and slower streamer. However the field and streamer velocity are appreciable and still larger than in the case where the solid tube's permittivity is $2.2\epsilon_0$ (Section 7.2.1).

7.4.3.3 $\epsilon = 1.0\epsilon_0$ – Figures 7.13(e), 7.13(f) and 7.16

The numerical results for the oil-cylindrical tube system of Fig. 7.1 and model equations (7.1)-(7.9) are presented in this section. The applied voltage to the needle electrode is $V_{app} = 130$ kV and the field ionization mechanism of (7.5) is utilized with parameter values corresponding to aromatic hydrocarbon molecules in Table 4.1. The solid cylindrical tube has a relative permittivity of 1.0, like that of free space, and is oriented such that the tube's inner radius surface is parallel to the direction of the main z-directed electric field component. In Figs. 7.13(e) and 7.13(f), the electric field magnitude and surface charge density profile distributions along the liquid-solid interface (see Fig 7.3) are given at several time instances. Figure 7.16 shows the rz-plane spatial distribution of the electric field magnitude.

The results of this section are noticeably different from the two previous cases where the solid's permittivities are $4.4\epsilon_0$ and $3.3\epsilon_0$, and more similar to the results of Section 7.2.1, where both the oil and solid's permittivity are $2.2\epsilon_0$. For instance, the streamer is not attracted towards the solid surface and does not travel along the liquid-solid interface, but rather propagates along the z-axis. Therefore, the level of surface charging is extremely small that the minuscule erratic spikes seen in the Fig. 7.13(f) are due to numerical error and have little effect at such low levels.

Directly comparing the electric field spatial distributions in Fig. 7.16 to the results of Fig. 7.5, for the solid tube with $2.2\epsilon_0$ permittivity, shows that at early times (*i.e.*, $t = 5-25$ ns) the field enhancement level and streamer length are approximately the same for both cases. For these early times the streamer is still at the opening of the cylindrical tube. However, at later times (*i.e.*, $t = 50-100$ ns) the field level and streamer length for the $1.0\epsilon_0$ solid is slightly greater (*i.e.*, $\sim 4.1\times10^8$ V/m compared to $\sim 3.8\times10^8$ V/m) and faster (*i.e.*, ~ 4.2km/s compared to ~ 3.9 km/s), respectively.

In the two previous sections, the polarization charge from the solid tube increased the field in the $+r$-direction towards its surface, which accelerated the streamer along the liquid-solid interface. However, for the $1.0\epsilon_0$ solid insulator, the additional electric field generated from the polarization charge is $-r$-directed, away from the solid and towards the z-axis. This can be explained from case 3 of the simple parallel plane model in Section 7.4.2. First, examining the base case 1, the electric field E_1 within the oil region of the two series parallel plane geometry in Fig. 7.12, where $\epsilon_1 = 2.2\epsilon_0$ and $\epsilon_2 = 2.2\epsilon_0$ are the oil and solid permittivities, respectively, is

$$E_1 = \frac{V_0}{b} = E_{\text{nominal}}. \tag{7.23}$$

Now, for the case where there is an oil-solid permittivity mismatch, such that $\epsilon_1 = 2.2\epsilon_0$ and $\epsilon_2 < 2.2\epsilon_0$, the field within the oil region is

$$\begin{aligned} E_1 &= \frac{\epsilon_2 V_0}{\epsilon_2 a + \epsilon_1 (b-a)} \\ &= \frac{V_0}{a + \frac{\epsilon_1}{\epsilon_2}(b-a)} \\ &= E_{\text{new}}, \end{aligned} \tag{7.24}$$

such that difference between the nominal field E_{nominal} in (7.23) and the newly altered field E_{new} in (7.24) is

$$\begin{aligned} \Delta E_1 &= E_{\text{new}} - E_{\text{nom}} \\ &= \frac{(\epsilon_2 - \epsilon_1)(b-a)V_0}{b\left[\epsilon_2 a + \epsilon_1 (b-a)\right]} \\ &< 0, \end{aligned} \tag{7.25}$$

since $\epsilon_2 < \epsilon_1$ and $b > a$. This differential field is produced by polarization charge that arises from the solid due to the lowering of its permittivity from the nominal $2.2\epsilon_0$. Furthermore, the differential field points in the $-x$-direction for the simple parallel plane example, which is analogous to the $-r$-direction for the oil-solid tube system assuming $x = 0$ electrode is the positive streamer channel. A consequence of this $-r$-directed differential field in the oil-tube system is the streamer channel radius is marginally smaller (Fig. 7.16(d)-7.16(f)) than compared to the $2.2\epsilon_0$ solid tube case because the field pushes the positive space charge that envelopes the streamer inward towards the z-axis. This reduction of space charge distribution volume ever-so-slightly increases the electric field at the streamer tip, which marginally increases ionization and streamer propagation. Thus, it is again shown that altering the streamer shape and space charge density distribution affects the electric field enhancement to increase streamer development.

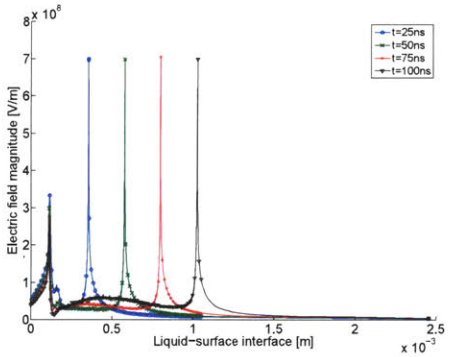

(a) $\epsilon_{solid} = 4.4\epsilon_0$, Electric field magnitude above surface in transformer oil.

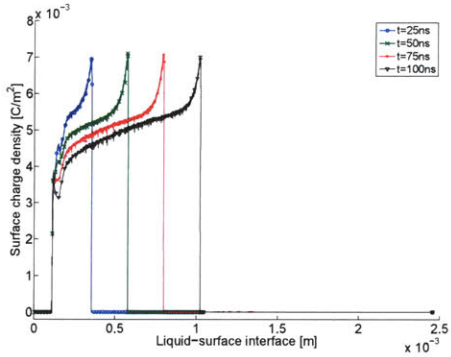

(b) $\epsilon_{solid} = 4.4\epsilon_0$, Surface charge density along surface.

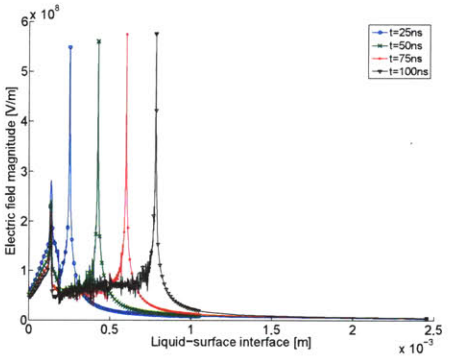

(c) $\epsilon_{solid} = 3.3\epsilon_0$, Electric field magnitude above surface in transformer oil.

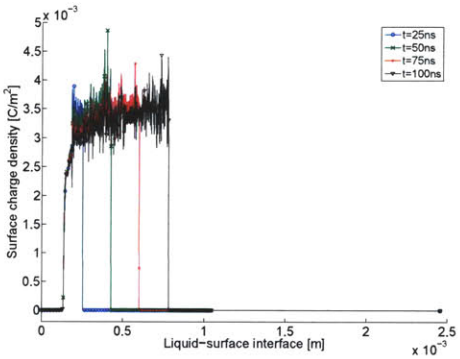

(d) $\epsilon_{solid} = 3.3\epsilon_0$, Surface charge density along surface.

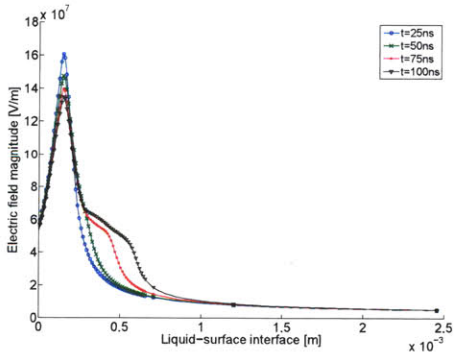

(e) $\epsilon_{solid} = 1.0\epsilon_0$, Electric field magnitude above surface in transformer oil.

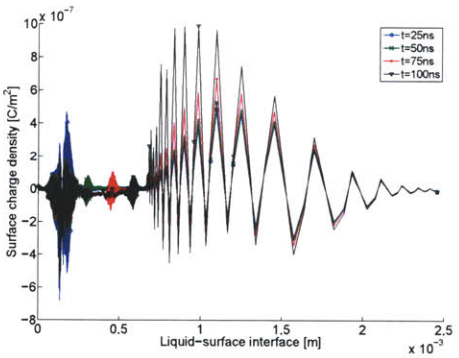

(f) $\epsilon_{solid} = 1.0\epsilon_0$, Surface charge density along surface.

Figure 7.13: Temporal dynamics along the liquid-solid interface in Fig 7.3 at 25 ns intervals from $t = 25 - 100$ ns given by the solution to the oil-solid insulation model of (7.1)-(7.9) for the field ionization mechanism of (7.5) and an applied voltage of $V_{app} = 130$ kV. The oil is comprised of low number density, low ionization potential aromatic hydrocarbon molecules only with parameter values summarized in Table 4.1. Three case studies are examined where the solid insulator's permittivity is $4.4\epsilon_0$, $3.3\epsilon_0$ and $1.0\epsilon_0$.

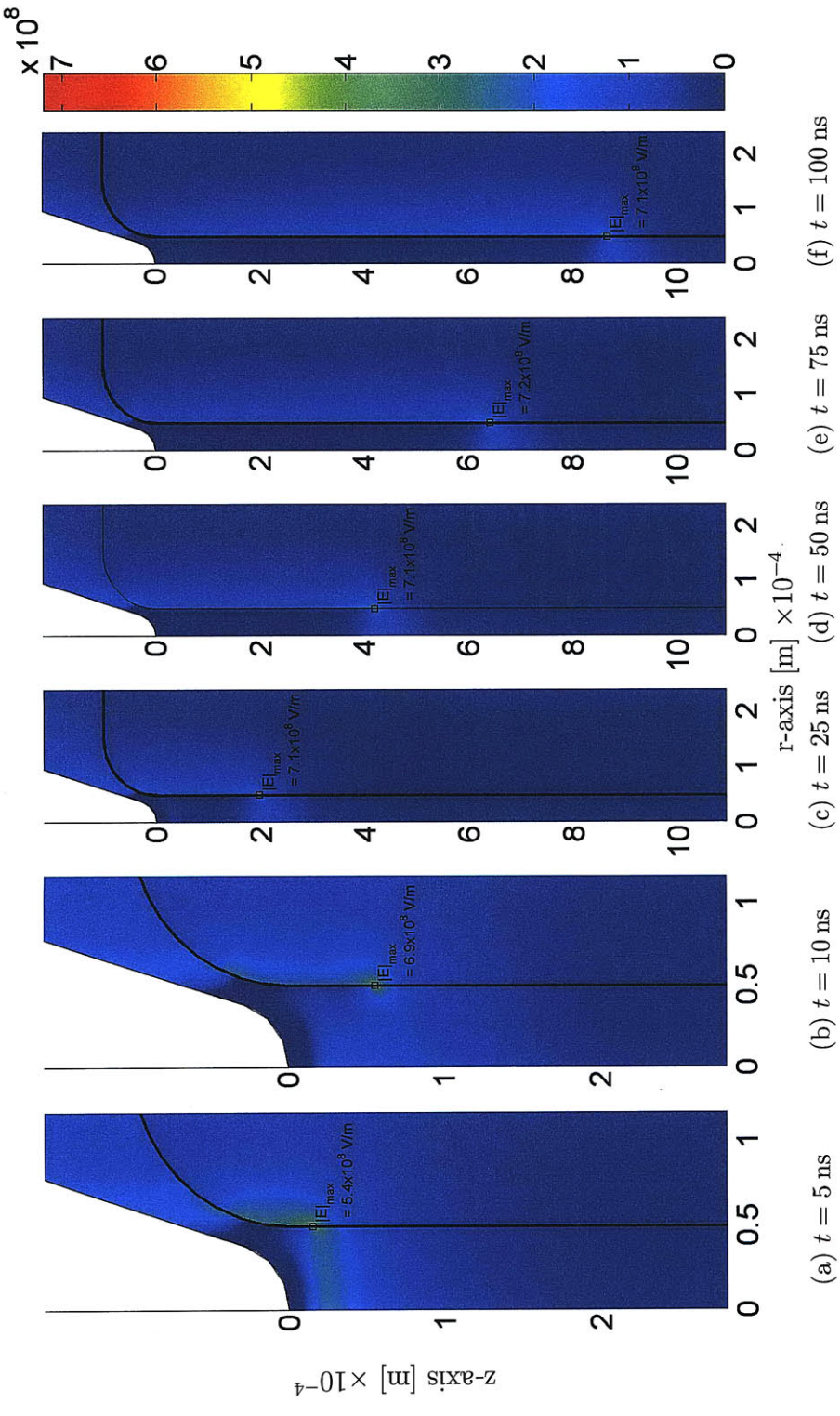

(a) $t = 5$ ns (b) $t = 10$ ns (c) $t = 25$ ns (d) $t = 50$ ns (e) $t = 75$ ns (f) $t = 100$ ns

Figure 7.14: Electric field magnitude [V/m] spatial distributions (as a function of r and z in the electrode geometry) from $t = 5 - 100$ ns given by the solution to the oil-solid insulation model (7.1)-(7.9) for an applied voltage of $V_{app} = 130$ kV and the field ionization mechanism of (7.5). The oil is composed of low number density, low ionization potential aromatic hydrocarbon molecules only with parameter values summarized in Table 4.1. The solid insulator's permittivity is $4.4\epsilon_0$.

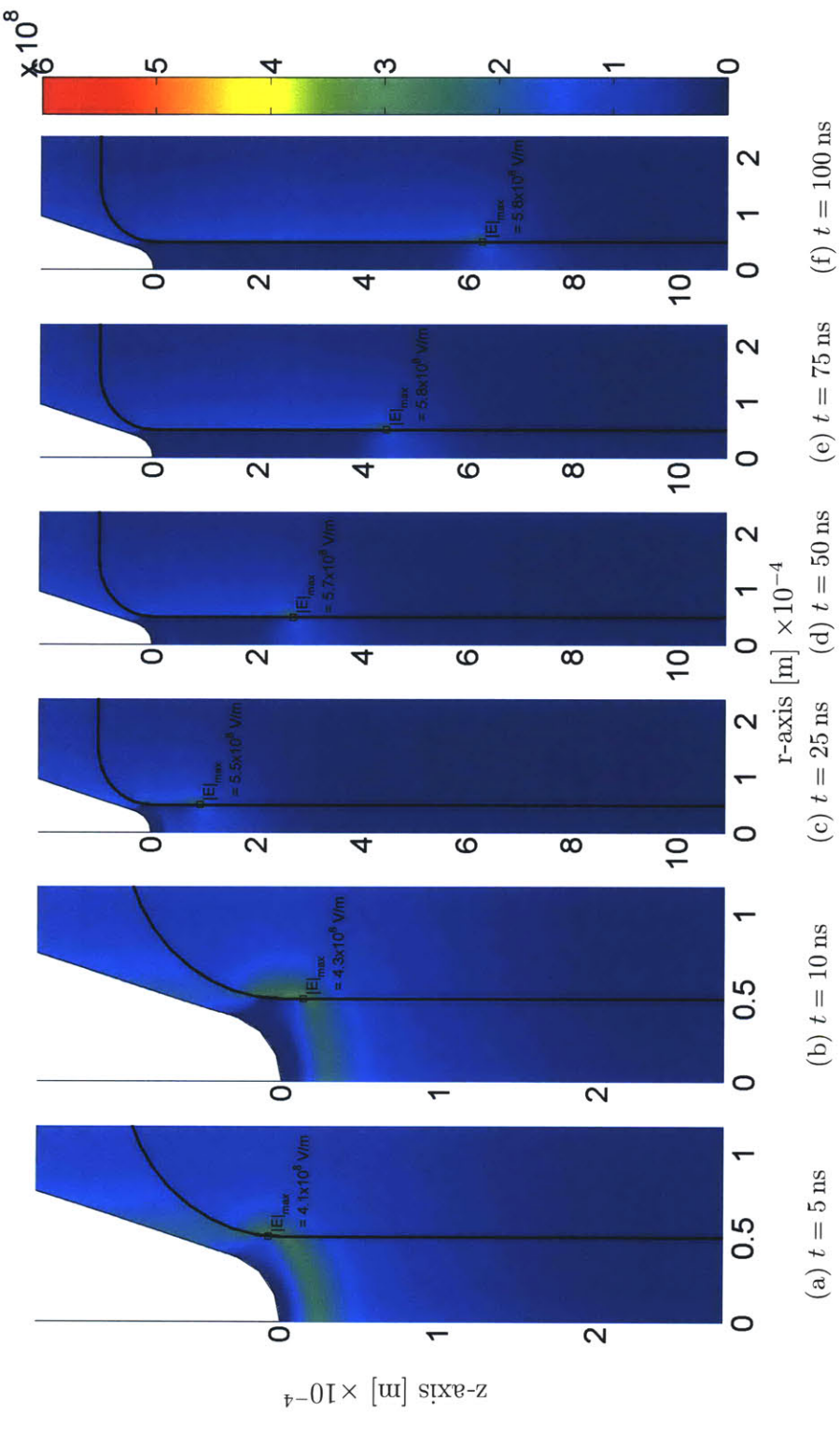

(a) $t = 5$ ns (b) $t = 10$ ns (c) $t = 25$ ns (d) $t = 50$ ns (e) $t = 75$ ns (f) $t = 100$ ns

Figure 7.15: Electric field magnitude [V/m] spatial distributions (as a function of r and z in the electrode geometry) from $t = 5 - 100$ ns given by the solution to the oil-solid insulation model (7.1)-(7.9) for an applied voltage of $V_{app} = 130$ kV and the field ionization mechanism of (7.5). The oil is composed of low number density, low ionization potential aromatic hydrocarbon molecules only with parameter values summarized in Table 4.1. The solid insulator's permittivity is $3.3\epsilon_0$.

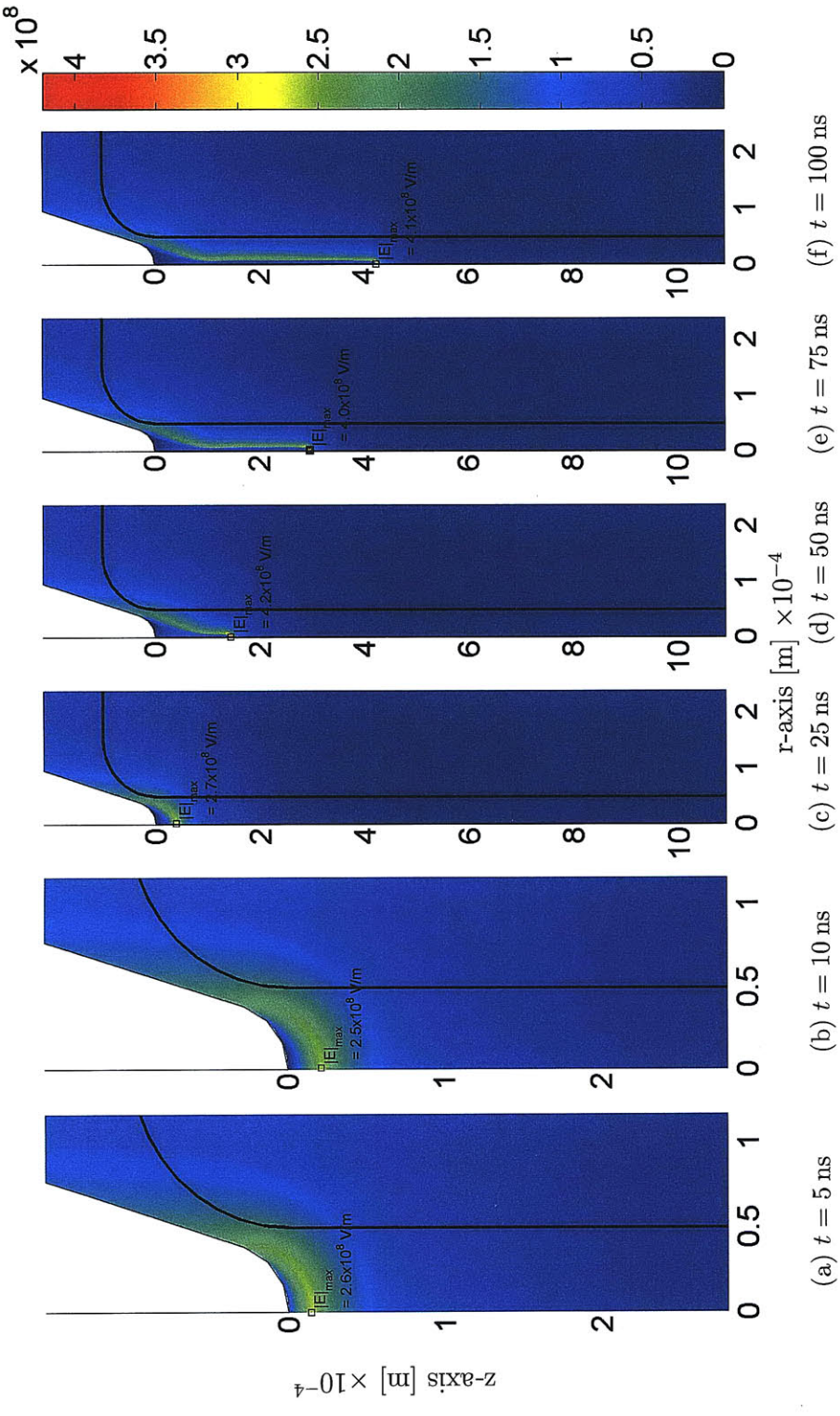

(a) $t = 5$ ns (b) $t = 10$ ns (c) $t = 25$ ns (d) $t = 50$ ns (e) $t = 75$ ns (f) $t = 100$ ns

Figure 7.16: Electric field magnitude [V/m] spatial distributions (as a function of r and z in the electrode geometry) from $t = 5 - 100$ ns given by the solution to the oil-solid insulation model (7.1)-(7.9) for an applied voltage of $V_{app} = 130$ kV and the field ionization mechanism of (7.5). The oil is composed of low number density, low ionization potential aromatic hydrocarbon molecules only with parameter values summarized in Table 4.1. The solid insulator's permittivity is $1.0\epsilon_0$.

7.4.4 Perpendicular Oriented Interface – Solid Barrier

This section discusses the streamer modeling results for the oil-solid barrier system test cases, where the permittivity of the solid insulation is varied (*e.g.*, $3.3\epsilon_0$, $2.2\epsilon_0$, and $1.0\epsilon_0$) and the oil permittivity is kept constant at $2.2\epsilon_0$. The model equations are given in (7.1)-(7.9) and the applied voltage to the needle electrode is $V_{app} = 130\,\text{kV}$. The oil-barrier case, where the solid insulation's permittivity is $4.4\epsilon_0$, was presented in Section 7.3.

The streamer initially develops in the oil due to field ionization of aromatic hydrocarbon molecules, which have a low number density and low ionization potential as modeled by the parameter values in Table 4.1. For an oil-only system, these types of molecules result in the formation of slow 2^{nd} mode streamers, which was discussed in Sections 4.2 and 4.4.

The streamers in the oil-barrier system are investigated by examining the spatial electric field distribution and the electric field and surface charge line distributions along the inner tube radius as shown in Fig. 7.8 from the z-axis radially outwards.

7.4.4.1 $\epsilon = 3.3\epsilon_0$ – Figures 7.17(a), 7.17(b) and 7.18

The numerical results for the oil-solid barrier system of Fig. 7.2 and model equations (7.1)-(7.9) are presented in this section. The applied voltage to the needle electrode is $V_{app} = 130\,\text{kV}$ and the field ionization mechanism of (7.5) is utilized with parameter values corresponding to aromatic hydrocarbon molecules in Table 4.1. The solid barrier has a relative permittivity of 3.3 and is oriented such that its top surface is perpendicular to the direction of the main z-directed electric field component. In Figs. 7.17(a) and 7.17(b), the electric field magnitude and surface charge density profile distributions along the liquid-solid interface (see Fig 7.8) are given at several time instances after the streamer comes in contact with the solid insulation. Figure 7.18 shows the rz-plane spatial distribution of the electric field magnitude.

The results of this section are analogous to Section 7.3.1, where the solid insulation has a permittivity of $4.4\epsilon_0$. For example, due to 1.5 times greater permittivity of the solid insulation with respect to the oil, the field in the oil region is greater, especially between the needle tip and barrier's top surface, than the oil-only system in Section 4.2.1, as explained by case 2 of the simple analytical study in Section 7.4.2. The higher field level in this area, which is created by the polarization charge from the solid, produces a streamer that travels considerably faster and reaches $z = 1\,\text{mm}$, where the top of the barrier surface is, in $\sim 270\,\text{ns}$ (Figs. 7.18(a) and 7.18(b)). In contrast, the streamer in the oil-only system traverses the same distance in $\sim 325\,\text{ns}$ to reach the same position along the z-axis. However, it is slower

when compared to the streamer produced in Section 7.3.1 for the $4.4\epsilon_0$ solid, which quickly traverses this gap in ~ 250 ns due to the even higher field created by the greater oil-solid barrier permittivity difference.

As the streamer comes in contact with the surface, its shape is modified, producing a greater field enhancement at the streamer tip from 3.8×10^8 V/m (along the z-axis before it made contact with the surface in Fig. 7.18(b)) to 5.7×10^8 V/m (directly after the streamer touches the surface in Fig. 7.18(c)). In Section 7.3.1, it was shown that the large field enhancement is a result of two phenomena: i) the polarization charge and force induced at the interface by the difference in oil-solid permittivities and ii) the compression of the space charge density at the streamer tip into a small volume adjacent to and along the surface. With the reduction of the solid barrier permittivity from $4.4\epsilon_0$ in Section 7.3.1 to $3.3\epsilon_0$, the polarization forces acting upon the streamer tip are subsequently reduced. Thus, the field enhancement decreases from 6.7×10^8 V/m in the $4.4\epsilon_0$ solid barrier case to 5.7×10^8 V/m here for the $3.3\epsilon_0$ solid barrier, as stated previously. Also, due to the lower polarization force exerted on the streamer and the lower field enhancement for the $3.3\epsilon_0$ solid barrier, the surface charging of the interface is lowered from a peak surface charge density of 6.0×10^{-3} C/m^2 for the $4.4\epsilon_0$ solid barrier (Fig. 7.9(b)) to 3.5×10^{-3} C/m^2 here (Fig. 7.17(b)).

Once the streamer reaches the solid barrier at approximately $t=270$ ns, it cannot propagate in the $+z$-direction anymore, which would have been the shortest path to the counter-electrode. Rather, the streamer travels along the solid surface in the $+r$-direction (Figs. 7.18(d)-7.18(f)), which extends its propagation length substantially increasing the time to breakdown. Even though the polarization forces with modification of the streamer shape leads to greater field enhancement at the streamer tip ($\sim 5\times10^8$ V/m), since the main z-directed electric field component is perpendicular to the barrier surface, the streamer velocity does not increase. Rather, the streamer velocity decreases due to the relatively small field component in the $+r$-direction parallel to the surface. Thus, the streamer velocity along the surface is decreased to ~ 450 m/s compared to 3.8 km/s along the z-axis for the initial 260 ns.

7.4.4.2 $\epsilon = 2.2\epsilon_0$ – Figures 7.17(c), 7.17(d) and 7.19

The numerical results for the oil-solid barrier system of Fig. 7.2 and model equations (7.1)-(7.9) are presented in this section. The applied voltage to the needle electrode is $V_{app} = 130$ kV and the field ionization mechanism of (7.5) is utilized with parameter values corresponding to aromatic hydrocarbon molecules in Table 4.1. The solid barrier has a relative permittivity of 2.2, like that of PTFE, and is oriented such that its top sur-

face is perpendicular to the direction of the main z-directed electric field component. In Figs. 7.17(c) and 7.17(d), the electric field magnitude and surface charge density profile distributions along the liquid-solid interface (see Fig 7.8) are given at several time instances after the streamer comes in contact with the solid insulation. Figure 7.19 shows the rz-plane spatial distribution of the electric field magnitude.

Due to the absence of a permittivity difference between the oil and solid barrier and the polarization charges that accompany it, the streamer travels to the barrier's top surface in $t = 280$ ns, which is similar to the oil-only case. Therefore, the streamer is not perturbed/accelerated by polarization forces that would result if there was a permittivity difference. Once the streamer reaches the surface at $t = 290$ ns, the field enhancement at the streamer tip is increased from 3.8×10^8 V/m (along the z-axis before it made contact with the surface in Fig. 7.19(b)) to 5.0×10^8 V/m (directly after the streamer touches the surface in Fig. 7.19(c)). The enhancement is reduced from the $4.4\epsilon_0$ and 3.3ϵ solid barriers because there is no additional polarization force driving the streamer into the surface, which would have compressed the space charge distribution further into the surface. This lack of driving polarization force is seen in the surface charge density (Fig. 7.17(d)), which is relatively constant as the streamer travels along the liquid-solid interface and does not have a definitive peak like the $4.4\epsilon_0$ and 3.3ϵ solid barriers, seen in Figs. 7.9(b) and 7.17(b).

As the streamer transitions to traveling along the solid interface and moves out in the $+r$-direction, the space charge spreads out from the z-axis and the electric field enhancement returns to its original value of 3.8×10^8 V/m that it had when it was traveling along the z-axis, since there is no induced polarization charge that drives the streamer body into the surface. However, the main z-directed electric field component is perpendicular to the surface, and the surface impedes streamer propagation in that direction. The small r-directed electric field component parallel to the surface slows streamer propagation from 3.5 km/s along the z-axis to 350 m/s along the barrier surface. Thus, the presence of the barrier forces the streamer to travel along the barrier surface, increasing the streamer propagation length, time to breakdown, and the breakdown voltage of the system compared to the oil-only system.

7.4.4.3 $\epsilon = 1.0\epsilon_0$ – Figures 7.17(e), 7.17(f) and 7.20

The numerical results for the oil-solid barrier system of Fig. 7.2 and model equations (7.1)-(7.9) are presented in this section. The applied voltage to the needle electrode is $V_{app} = 130$ kV and the field ionization mechanism of (7.5) is utilized with parameter values corresponding to aromatic hydrocarbon molecules in Table 4.1. The solid barrier has a relative permittivity of 1.0, like that of free space, and is oriented such that its top sur-

face is perpendicular to the direction of the main z-directed electric field component. In Figs. 7.17(e) and 7.17(f), the electric field magnitude and surface charge density profile distributions along the liquid-solid interface (see Fig 7.8) are given at several time instances after the streamer comes in contact with the solid insulation. Figure 7.20 shows the rz-plane spatial distribution of the electric field magnitude.

During the first 320 ns the streamer propagates along the z-axis similarly to the previous cases, however due to the solid's lower permittivity with respect to the oil, the field in the oil region between the needle tip and top barrier surface is lower than all the other previous cases and the nominal oil-only system as well. This explains the longer time needed for the streamer to propagate from the needle tip to top surface compared to the $4.4\epsilon_0$, $3.3\epsilon_0$, and $2.2\epsilon_0$ solid barrier cases. As explained via the simple parallel-plane two-series dielectric model in Section 7.4.3.3, for the $4.4\epsilon_0$ and $3.3\epsilon_0$ solid barrier cases, the applied voltage produces a polarization charge that increases the field towards the barrier surface in the $+z$-direction, thereby accelerating the streamer along the z-axis. However, for the $1.0\epsilon_0$ case the additional electric field generated from the polarization charge of the solid is $-z$-directed and reduces the field from its nominal oil-only value.

As the streamer reaches the top barrier surface at $z = 1$ mm the results differ from those of previous sections. The induced negative polarization charge from the solid reduces the electric field enhancement at the positive streamer tip from $3.8{\times}10^8$ V/m to $< 3.3{\times}10^8$ V/m. As a result of the increasingly negative polarization charge that is induced by the positive streamer from the lower permittivity solid, as the streamer begins to propagate along the surface, the dominant field direction changes from the $+z$-direction to the $-z$-direction. Consequently, the streamer is repelled from the barrier surface (Figs. 7.20(e) and 7.20(f)) and does not propagate along the surface, but rather in the $+r$, $-z$ direction. away from the counter-electrode. Since the streamer does not travel along the liquid-solid interface the level of surface charging is negligible and the erratic distribution in Fig. 7.13(f) is due to numerical error that has no bearing on the overall dynamics, as in Sections 7.2.1 and 7.4.3.3.

This phenomena can be explained via the simple parallel plane system in Fig. 7.12, where Region 1 is oil with permittivity $\epsilon_1 = 2.2\epsilon_0$ and Region 2 is the solid insulation with permittivity $\epsilon_2 = 1.0\epsilon_0$. In the nominal base case, where $\epsilon_2 = 2.2\epsilon_0$ similar to an all oil-only system, the field in the oil region is

$$E_1 = \frac{V_0}{b} = E_{\text{nominal}}. \tag{7.26}$$

However, for a system with oil and solid having unique permittivities, such that $\epsilon_1 = 2.2\epsilon_0$ and $\epsilon_2 < 2.2\epsilon_0$, the field within the oil region changes to

$$\begin{aligned} E_1 &= \frac{\epsilon_2 V_0}{\epsilon_2 a + \epsilon_1 (b-a)} \\ &= \frac{V_0}{a + \frac{\epsilon_1}{\epsilon_2}(b-a)} \\ &= E_{\text{new}}, \end{aligned} \tag{7.27}$$

such that difference between the nominal field E_{nominal} in (7.26) and the newly altered field E_{new} in (7.27) is

$$\begin{aligned} \Delta E_1 &= E_{\text{new}} - E_{\text{nom}} \\ &= \frac{(\epsilon_2 - \epsilon_1) c V_0}{b\left[\epsilon_2 a + \epsilon_1 c\right]} \\ &< 0, \end{aligned} \tag{7.28}$$

since $\epsilon_2 = 1.0\epsilon_0 < \epsilon_1$ and $b > a$. Also, note in (7.28) we use $c = (b-a)$, which is the thickness of solid insulation. The differential field ΔE_1 is produced by polarization charge that arises from the solid due to the lowering of its permittivity from the nominal $2.2\epsilon_0$. Furthermore, the differential field points in the $-x$-direction for the simple parallel plane example.

Imagine that the $x = 0$ electrode is the streamer tip and c is constant because it is the thickness of the solid insulation. As the streamer propagates in the $+x$-direction towards the interface $a \to 0$ and $b \to c$, the differential field of (7.28) becomes more negative and applies a stronger force on the electrode-modeled positive streamer in the $-x$-direction. Analogously, as the positive streamer in the oil-solid barrier system approaches and touches the solid surface, the polarization charge from the lower permittivity solid exerts an increasingly stronger force in the $-z$-direction opposing the streamer's propagation toward the solid insulation barrier.

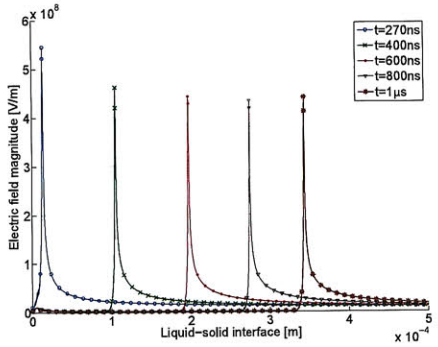

(a) $\epsilon_{solid} = 3.3\epsilon_0$, Electric field magnitude above surface in transformer oil.

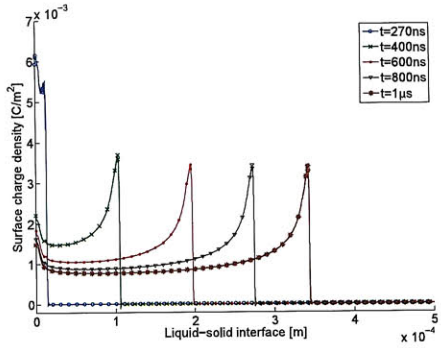

(b) $\epsilon_{solid} = 3.3\epsilon_0$, Surface charge density along surface.

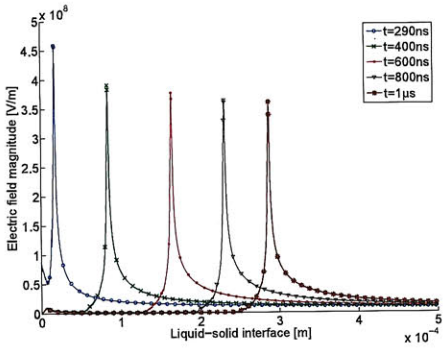

(c) $\epsilon_{solid} = 2.2\epsilon_0$, Electric field magnitude above surface in transformer oil.

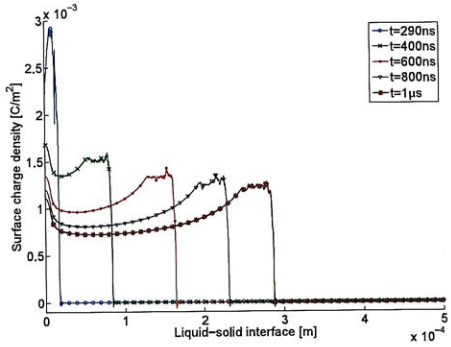

(d) $\epsilon_{solid} = 2.2\epsilon_0$, Surface charge density along surface.

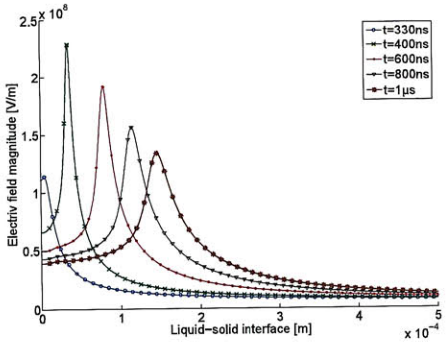

(e) $\epsilon_{solid} = 1.0\epsilon_0$, Electric field magnitude above surface in transformer oil.

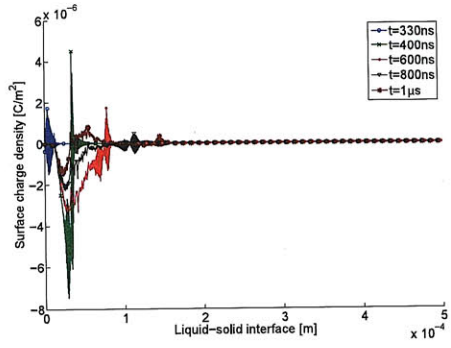

(f) $\epsilon_{solid} = 1.0\epsilon_0$, Surface charge density along surface.

Figure 7.17: Temporal dynamics along the liquid-solid interface in Fig 7.8 at several time instances after the streamer makes contact with the perpendicular surface. Results given by the solution to the oil-solid insulation model of (7.1)-(7.9) for an applied voltage of $V_{app} = 130\,\text{kV}$ and the field ionization mechanism of (7.5). The oil is composed of low number density, low ionization potential aromatic hydrocarbon molecules only with parameter values summarized in Table 4.1. The solid insulator's permittivity is $3.3\epsilon_0$, $2.2\epsilon_0$ and $1.0\epsilon_0$.

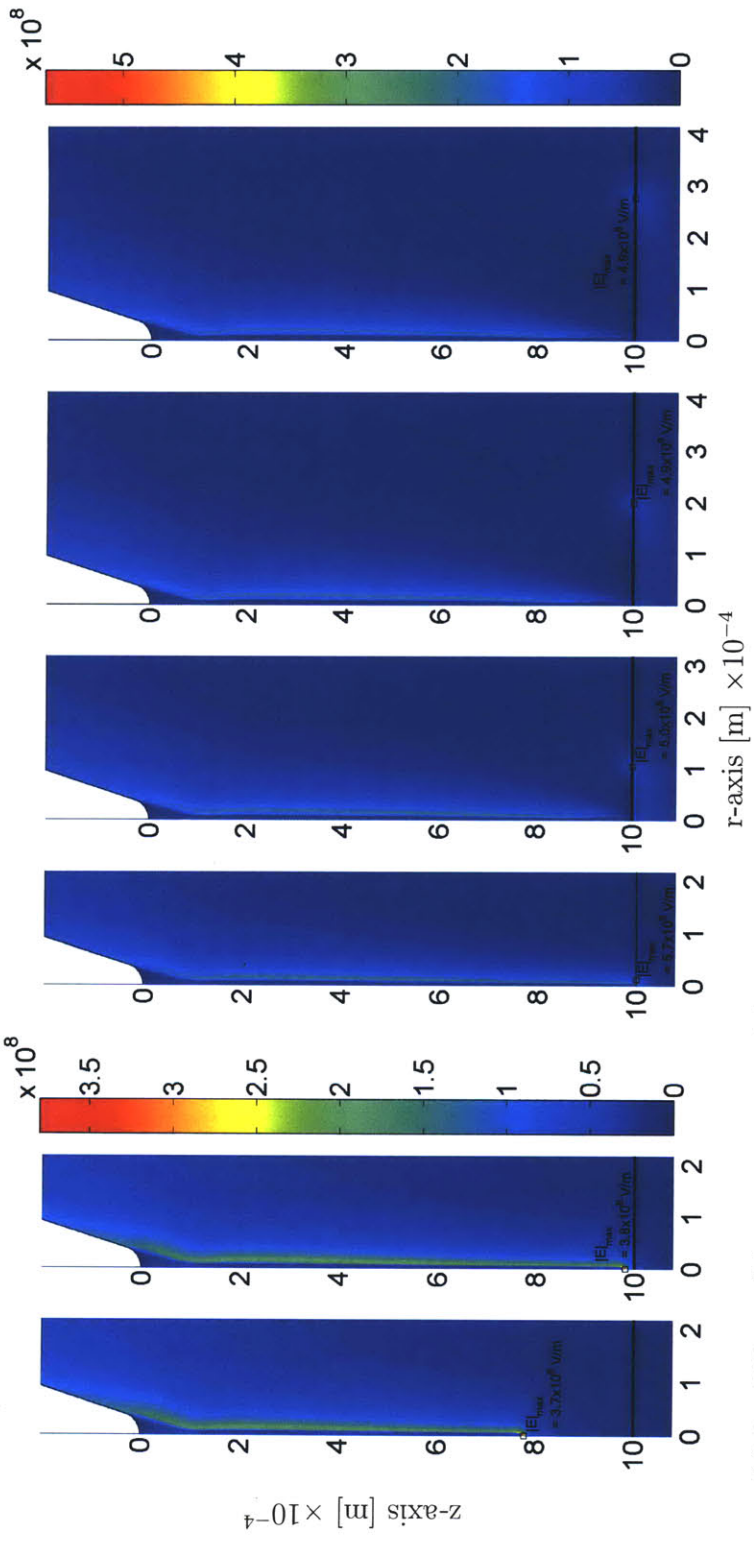

(a) $t = 200$ ns (b) $t = 260$ ns (c) $t = 270$ ns (d) $t = 400$ ns (e) $t = 600$ ns (f) $t = 800$ ns

Figure 7.18: Electric field magnitude [V/m] spatial distributions (as a function of r and z in the electrode geometry) at several time instances before (a)-(b) and after (c)-(f) the streamer makes contact with the perpendicular surface. Results given by the solution to the oil-solid insulation model of (7.1)-(7.9) for an applied voltage of $V_{app} = 130$ kV and the field ionization mechanism of (7.5). The oil is composed of low number density, low ionization potential aromatic hydrocarbon molecules only with parameter values summarized in Table 4.1. The solid insulator's permittivity is $3.3\epsilon_0$.

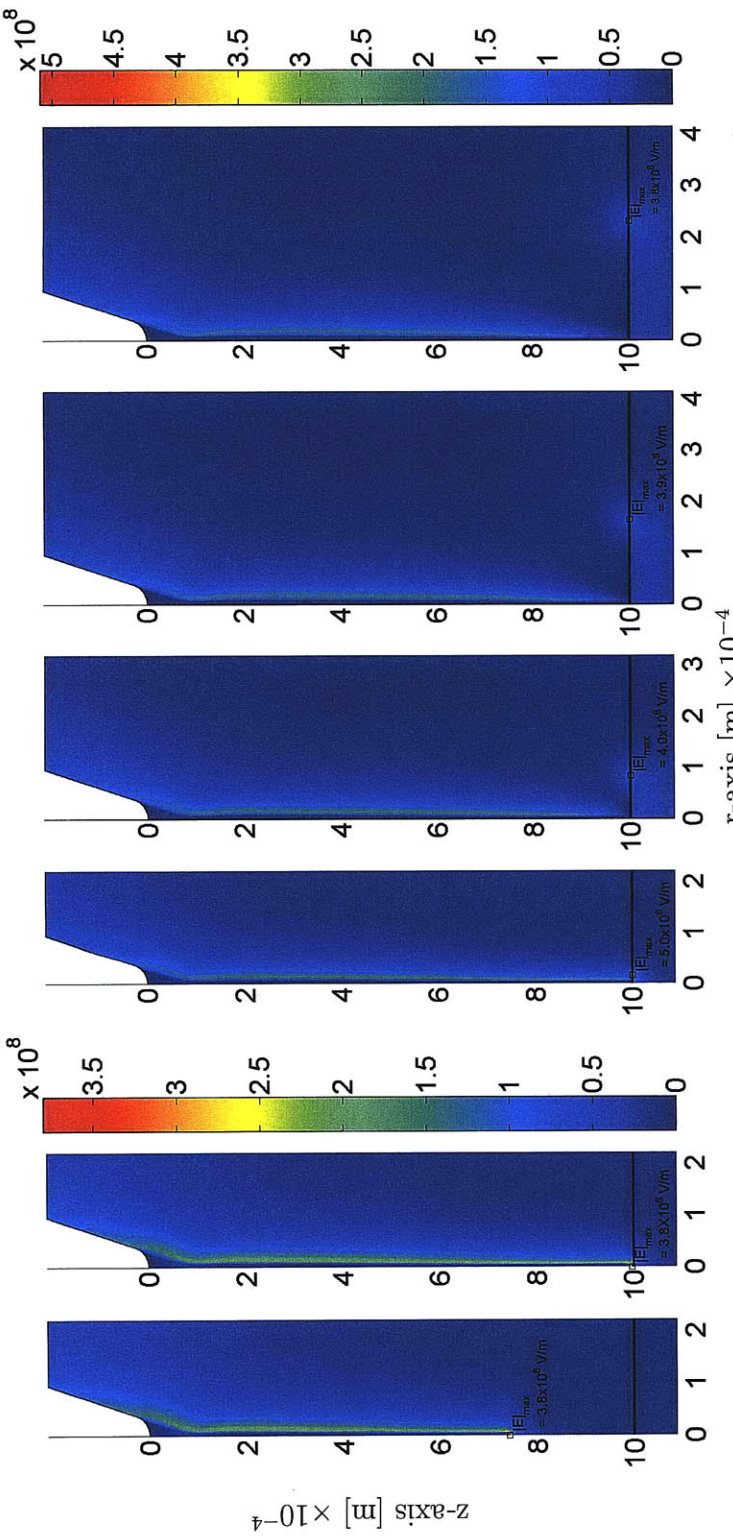

(a) $t = 200$ ns (b) $t = 280$ ns (c) $t = 290$ ns (d) $t = 400$ ns (e) $t = 600$ ns (f) $t = 800$ ns

Figure 7.19: Electric field magnitude [V/m] spatial distributions (as a function of r and z in the electrode geometry) at several time instances before (a)-(b) and after (c)-(f) the streamer makes contact with the perpendicular surface. Results given by the solution to the oil-solid insulation model of (7.1)-(7.9) for an applied voltage of $V_{app} = 130$ kV and the field ionization mechanism of (7.5). The oil is composed of low number density, low ionization potential aromatic hydrocarbon molecules only with parameter values summarized in Table 4.1. The solid insulator's permittivity is $2.2\varepsilon_0$.

(a) $t = 200$ ns (b) $t = 320$ ns (c) $t = 330$ ns (d) $t = 400$ ns (e) $t = 600$ ns (f) $t = 800$ ns

Figure 7.20: Electric field magnitude [V/m] spatial distributions (as a function of r and z in the electrode geometry) at several time instances before (a)-(b) and after (c)-(f) the streamer makes contact with the perpendicular surface. Results given by the solution to the oil-solid insulation model of (7.1)-(7.9) for an applied voltage of $V_{app} = 130$ kV and the field ionization mechanism of (7.5). The oil is composed of low number density, low ionization potential aromatic hydrocarbon molecules only with parameter values summarized in Table 4.1. The solid insulator's permittivity is $1.0\epsilon_0$.

7.4.5 Summary

In summary, the oil-solid permittivity difference alters the electrodynamics via polarization forces that act upon the streamer. For the case where the solid insulation's permittivity is greater than the liquid's, the streamer is driven into the solid, such that its growth is impeded and its shape is dramatically altered. Due to restriction of the streamer's growth by the presence of the solid insulation (*i.e.*, in radial direction by solid tube and in the axial direction by the solid barrier), the streamer is forced to change direction, which can have a severe impact on streamer propagation. When the liquid-solid interface is oriented parallel to the direction of the main z-directed electric field component, as the streamer is driven into the surface it travels along the interface. The streamer quickly accelerates to extremely fast velocities at lower applied voltages, which would normally result in slow 2^{nd} mode streamers in an oil-only system. When the liquid-solid interface is oriented perpendicular to the direction of the main z-directed electric field component, the streamer is driven into the solid insulation surface and is forced to slowly travel along the interface due to the lower field levels parallel to the interface. This increases the propagation length of the streamer, the time to breakdown, and the breakdown voltage.

For the case where the permittivity of the solid insulation is lower than the dielectric liquid, the streamer is repelled away from the solid insulator. For the oil-tube system, this results in the compression of the streamer channel within the oil-filled solid tube along the z-axis, such that the streamer shape and space charge distribution are altered. Due to compression of the streamer channel by the repulsive polarization force the streamer propagates down the z-axis with velocity that is marginally greater than in an oil-only system discussed in Section 4.2.1. On the other hand, for the oil-solid barrier system, the streamer is driven away from the liquid-solid interface due to the repulsive polarization charges induced by the solid insulation. Thus, streamer development is brought to a halt as it slowly propagates away from the interface in a direction opposite of the counter-electrode.

From these two cases, we conclude that the combination of

1. the polarization charge induced by the oil-solid permittivity differences
2. the restriction of the streamer's growth along field lines by the presence of a solid insulation surface
3. the altering or compression of the streamer shape and space charge density distribution by a solid insulation surface or polarization induced field

increases the electric field enhancement within an oil-solid insulation system. This can often result in greater ionization in the oil and a streamer that propagates at higher velocities for lower applied voltages.

These results corroborate the observation of [57, 84, 93], where it was recorded that for solid insulation with greater permittivity than oil

- streamers were attracted to the solid surface,
- solid insulation produced large field enhancements and assisted in discharge propagation,
- a reduction in the breakdown voltage occurs.

The results also help to explain the experimental observations for solid materials with permittivity comparable to transformer oil, where the reduction in breakdown voltage is not as severe or does not exist. Therefore, from the results and observations of this section, an improved solid insulator would have good insulating capability, a resistance to puncturing, and a permittivity identical or very close to the oil that surrounds it.

7.5 Summary and Key Results

The key results and observations for oil-solid insulation systems, where the interface is oriented parallel to the main electric field component direction, are:

- The surface aids streamer development and increases the probability of breakdown.
- The presence of the surface restricts the radial growth of the streamer resulting in streamers that propagate at much higher velocities for lower voltages than in the oil-only case.
- Results corroborate the geometrical field regulation hypothesis put forth by Lundgaard *et al.* [14], whereby the electric field associated with the space charge within the streamer branches (those that grow more radial when compared to the main filament that bridges the gap) regulates the electric field magnitude and ionization, which drives streamer development at the streamer tip.
- The results of streamers in oil-solid tube systems are supported by and help to explain the experimental data in the literature [13, 14, 21, 59], especially those of Massala and Lesaint [13] where insulating tubes were used to confine and guide streamer growth within the cylinder.

The key results and observations for oil-solid insulation systems, where the interface is oriented perpendicular to the main electric field component direction, are:

- The surface hinders streamer development and increases the breakdown voltage.
- As the streamer travels along the surface it deposits electric charges onto the solid surface which redistributes the electric field in the insulation.
- As the streamer is restricted to traveling along the surface, the time to breakdown is increased considerably thereby decreasing the streamer's average breakdown velocity.
- The solid acts as a barrier for streamers, hindering streamers from reaching the counter-electrode and causing breakdown.
- The numerical results for the oil-solid barrier system are validated by the experimental results of Liu *et al.* [15,16].

Chapter 8

Conclusion

THIS CHAPTER highlights the major contributions of this work to the understanding of dielectric breakdown in insulating liquids, insulating liquids with conductive nanoparticle suspensions, and liquid-solid insulation systems. The chapter concludes with suggested future work to extend the theoretical work developed in this thesis, including several suggested experiments that would help deepen the understanding of breakdown in dielectric liquids and validate several of the conclusions from this body of work.

8.1 Thesis Summary and Contributions

Chapter 1 motivates the study of dielectric materials, especially insulating liquids, and the importance of modeling the mechanisms that lead to their breakdown in an effort to engineer materials with superior insulating characteristics. The chapter continues by discussing pre-breakdown phenomena and streamer formation in dielectric liquids via reference to experimental work in the literature, describing macroscopic streamer characteristics, and utilizing a lumped circuit analogy for better visualization of such high-energy systems. The chapter concludes by referencing and discussing other work on liquid breakdown modeling and the results of these studies. The objective of this work has been to develop a set of mathematical models and parameter values which contain the physics to elucidate pre-breakdown phenomena in transformer oil and other oil-based systems.

Chapter 2 gives a review of several dielectric liquids used to insulate electrical equipment and their over-voltage or streamer characteristics. In particular, transformer oil is discussed in length and a thorough literature review on the experimental work of many research groups is detailed. From [14, 21, 29], the four streamer propagation modes are defined and their unique characteristics (*i.e.*, velocity, shape, applied voltage, etc.) are outlined. The chapter continues with the effects of additives, such as low ionization potential molecules and conductive nanoparticles, on the breakdown characteristics of transformer oil. From the literature, it is shown that these additives greatly influence positive streamer characteristics, often improving the insulating characteristics of transformer oil. The chapter concludes with a discussion on the experimental observations in the literature of the effects of solid

insulation on streamers that initiate in liquids and come in contact with the solid. It is noted that the orientation of the liquid-solid interface, with respect to the primary electric field direction, plays a key role in either aiding or hindering fast streamer propagation when the solid insulation barrier surface respectively is either along or transverse to the primary electric field direction.

8.1.1 Transformer Oil

In Chapter 3, all components of the dielectric liquid continuum model are discussed including system geometry, governing equations, boundary conditions, and model parameters. A derivation of the electron mobility, based on the classical electron radius, is given and closely matches the value used with the continuum model. A section is devoted to three charge generation mechanisms discussed in this thesis: field ionization, impact ionization and photo-ionization. Their respective models and the experimental observations from the literature, which show their influence in dielectric liquids, are given. The chapter concludes with an investigation of the molecular characteristics (*e.g.*, density, ionization, molecular separation) that affect field ionization. It is shown that there is a positive correlation between increasing density of ionizable species and charge generation, while the inverse is true for increasing ionization potential and charge generation at a constant applied voltage.

Chapter 4 is devoted to the results of the model setup in Chapter 3. Positive streamer growth is investigated via several different mechanisms and it is shown that the positive streamer propagation modes that lead to transformer oil breakdown are caused by

- Slow 2^{nd} mode ($v = 1-5$ km/s, $V_{inc} = 130$ kV): Field ionization of low number density molecules with lower ionization potentials (*i.e.*, aromatic molecules).
- Fast 3^{rd} mode ($v = 10$–25km/s, $V_{inc} = 300$kV): Field ionization of the high number density molecules with higher ionization potentials (*i.e.*, naphthenic/paraffinic molecules).
- Fast event 4^{th} mode ($v > 100$ km/s, $V_{inc} > 300$ kV): Impact ionization by seed electrons created from photo-ionization.

Yet, even though there are different mechanisms at work for these streamers, independent of the ionization mechanism, the key ingredient in streamer formation in electrically overstressed dielectrics is the disparity in mobility/velocity of the positive ions and electrons in the presence of an electric field. Transformer oil stressed by a positively charged needle electrode leads to ionization of oil molecules producing slow positive ions and fast electrons. Due to the much higher mobility of electrons, they are able to exit the ionization zone in

a small amount of time leaving behind a net positive space charge region in the oil. It is this space charge that creates an electric field enhancement away from the needle tip that continues the ionization process. Therefore, the ionization of oil molecules into slow positive ions and fast electrons creates propagating electric field and space charge waves that are the dominant mechanism behind positive streamer propagation, which leads to electrical breakdown.

The results of Chapter 4 also corroborate the hypotheses and results found in the literature regarding streamers in hydrocarbon liquids. For example, the results confirm the qualitative hypothesis of Biller [42], who reasoned that streamer propagation modes in heterogeneous dielectric liquids, like transformer oil, resulted from the ionization of different molecular species, such as the trace, easily ionizable molecules and the ordinary, bulk molecules. Also, from the numerical models, it has been shown that the molecular density, structure, and ionization potential play key roles in determining the onset of specific streamer propagation modes, which was hypothesized by Schütte [136].

A powerful discovery derived from the modeling of Chapter 4 is the space charge shielding effect, whereby adding low ionization potential additives to a pure dielectric liquid can considerably increase its acceleration voltage. This seemingly simple addition to the liquid can dramatically improve its over-voltage performance, such that the transition from slow 2^{nd} mode to fast 3^{rd} mode streamers occurs at higher voltages and allows for more time to extinguish devastating over-voltage situations, such as lightning impulses. In the space charge shielding effect, the low ionization potential additive ionizes at a lower voltage and initiates a streamer with a net space charge region at the streamer tip. This space charge creates a field enhancement level ahead of the charge front in the oil, which is considerably lower than the maximum Laplacian field, that supports further ionization of the same low ionization potential additive molecules, while suppressing the ionization of higher ionization potential molecules by shielding the high voltage needle tip. This prevents the inception of fast mode streamers, requiring a greater applied voltage for their formation. The space charge shielding effect explains the phenomena recorded by Lesaint and Jung [12], where the transition to fast streamers in cyclohexane is pushed to higher voltages with small concentrations of low ionization potential pyrene.

8.1.2 Dielectric Liquids with Conductive Nanoparticle Suspensions

In Chapter 5, analysis of unipolar and bipolar charging of spherical nanoparticles in a dielectric liquid is investigated. The charging models show that conductive nanoparticles electrically relax on short timescales such that they can effectively trap fast charge carriers, such as electrons, on timescales relevant to streamer propagation in dielectric liquids altering

the electrodynamics involved. From here the model is used within a comprehensive electrodynamic analysis to study the impact of nanoparticle charging on streamer development in transformer oil-based nanofluids. It is shown that trapping of electrons by conductive nanoparticles causes a decrease in positive streamer velocity resulting in higher electrical breakdown strength for transformer oil-based nanofluids. The key property of the nanoparticle material is that it must be highly conductive, rather than magnetic like magnetite, which is both conductive and magnetic and was used in experimental tests [23,74–77], such that when the nanoparticles are added to the oil they effectively trap electrons.

The charging analysis derives the electric field in the vicinity of the nanoparticles, electron trajectories on electric field lines that charge nanoparticles, and derives expressions for the charging characteristics of the nanoparticles as a function of time and dielectric permittivity and the conductivity of nanoparticles and surrounding transformer oil. Special cases treated are:

1. Unipolar positive or negative charging of nanoparticles,
2. Bipolar charging of nanoparticles.

Both cases treating zero and non-zero conductivity of the dielectric region surrounding a sphere have been studied.

8.1.3 Liquid-Solid Insulation Systems

Chapter 6 introduces the modeling and comparison of three different conduction mechanisms (*i.e.*, migration, ohmic and insulator) to model the solid insulator, where the correct interfacial boundary conditions based upon charge conservation are developed. The migration and ohmic cases are further investigated through analytical and numerical models using a simplified parallel plane geometry with a linear space charge injection law. The good agreement between the analytical and numerical results corroborate the sound modeling of the migration and ohmic modeling methods. The ohmic and insulator models are utilized to model the solid insulator and incorporated in complete electrodynamic oil-solid insulation continuum models.

In Chapter 7, the model setups in Chapters 3 and 6 are used to study the effects of oil-solid permittivity differences and different solid insulation geometries on streamer development. In summary, the oil-solid permittivity difference alters the electrodynamics via polarization forces that act upon the streamer. For the case where the solid insulation's permittivity is greater than the liquid's, the streamer is driven into the solid, such that its growth is

impeded and its shape is dramatically altered. Due to restriction of the streamer's growth by the presence of the solid insulation (*i.e.*, in radial direction by solid tube and in the axial direction by the solid barrier), the streamer is forced to change direction, which can have a severe impact on streamer propagation. When the liquid-solid interface is oriented parallel to the direction of the main electric field component, as the streamer is driven into the surface it travels along the interface. The streamer quickly accelerates to extremely fast velocities at lower applied voltages, which would normally result in slow 2^{nd} mode streamers in an oil-only system. When the liquid-solid interface is oriented perpendicular to the direction of the main electric field component, the streamer is driven into the solid insulation surface and is forced to slowly travel along the interface due to the lower field levels parallel to the interface. This increases the propagation length of the streamer, the time to breakdown, and the breakdown voltage.

For the case where the permittivity of the solid insulation is lower than the dielectric liquid, the streamer is repelled away from the solid insulator. For the oil-tube system, this results in the compression of the streamer channel within the oil-filled solid tube along the z-axis, such that the streamer shape and space charge distribution are altered. Due to compression of the streamer channel by the repulsive polarization force the streamer propagates down the z-axis with velocity that is marginally greater than in an oil-only system discussed in Section 4.2.1. On the other hand, for the oil-solid barrier system, the streamer is driven away from the liquid-solid interface due to the repulsive polarization charges induced by the solid insulation. Thus, streamer development is brought to a halt as it slowly propagates away from the interface in a direction opposite of the counter-electrode.

From these two cases, we conclude that the combination of

1. the polarization charge induced by the oil-solid permittivity differences
2. the restriction of the streamer's growth along field lines by the presence of a solid insulation surface
3. the altering or compression of the streamer shape and space charge density distribution by a solid insulation surface or polarization induced field

increases the electric field enhancement within an oil-solid insulation system. This can often result in greater ionization in the oil and a streamer that propagates at higher velocities for lower applied voltages.

These results corroborate the observation of [57,84,93], where it was recorded that for solid insulation with greater permittivity than oil

- streamers were attracted to the solid surface,
- solid insulation produced large field enhancements and assisted in discharge propagation,
- a reduction in the breakdown voltage occurs.

The results also help to explain the experimental observations for solid materials with permittivity comparable to transformer oil, where the reduction in breakdown voltage is not as severe or does not exist. Therefore, from the results and observations of Section 7.4, an improved solid insulator, especially compared to pressboard, would have good insulating capability, a resistance to puncturing, and a permittivity identical or very close to the oil that surrounds it.

Chapter 7 also investigates the impact of the oil-solid interface orientation, with respect to the primary electric field direction, on streamer propagation and development. The key results and observations for oil-solid insulation systems, where the interface is oriented parallel to the main electric field component direction, are:

- The surface aids streamer development and increases the probability of breakdown.
- The presence of the surface restricts the radial growth of the streamer resulting in streamers that propagate at much higher velocities for lower voltages than in the oil-only case.
- Results corroborate the geometrical field regulation hypothesis put forth by Lundgaard *et al.* [14], whereby the electric field associated with the space charge within the streamer branches (those that grow more radial when compared to the main filament that bridges the gap) regulates the electric field magnitude and ionization, which drives streamer development at the streamer tip.
- The results of streamers in oil-solid tube systems are supported by and help to explain the experimental data in the literature [13, 14, 21, 59], especially those of Massala and Lesaint [13] where insulating tubes were used to confine and guide streamer growth within the cylinder.

The key results and observations for oil-solid insulation systems, where the interface is oriented perpendicular to the main electric field component direction, are:

- The surface hinders streamer development and increases the breakdown voltage.
- As the streamer travels along the surface it deposits electric charges onto the solid surface which redistributes the electric field in the insulation.

- As the streamer is restricted to traveling along the surface, the time to breakdown is increased considerably thereby decreasing the streamer's average breakdown velocity.
- The solid acts as a barrier for streamers, hindering streamers from reaching the counter-electrode and causing breakdown.
- The numerical results for the oil-solid barrier system are validated by the experimental results of Liu *et al.* [15, 16].

8.2 Future Work

8.2.1 Expanding the Streamer Model

This thesis has mainly focused on positive streamers because they travel faster and develop at lower applied voltages than their negative counterparts [1, 29]. However, negative streamers are still important and do pose as major threats to transformer oil insulated systems. Building on the work presented in this thesis, studying negative streamers should be a relatively straightforward extension of the current models. Furthermore, it is important that the negative streamer model fully explain the occurrence of pre-breakdown phenomena in true insulation systems. As such, it is important to understand the effects of negative streamer development in the presence of solid insulation. The liquid streamer model can be expanded to explain the development of fast propagating negative streamers that travel along solid insulation material, such as pressboard.

A main objective of this work has been to gain a thorough understanding of pre-breakdown phenomena in dielectric liquids so as to develop better insulation systems for power equipment, especially power transformers. To do so, it is important to develop a model that can encompass both the microscopic elements of streamers (*e.g.*, ionization, attachment and recombination mechanisms that occur on the molecular scale) and the macroscopic details of streamers (*e.g.*, streamer velocity, streamer shape, fractal geometry, and stochastic branching). The current work has strongly focused on the microscopic details and has obtained good results. Regarding the macroscopic elements of streamer development, good results for the streamer velocity have been obtained, however there is much work to be done on the streamer shape and its stochastic branching nature. This is critical because many researchers have hypothesized that the semi-spherical shape of slow 2^{nd} mode streamers plays a strong role in regulating the streamer velocity and is responsible for the large applied voltage range over which 2^{nd} mode streamers dominate [13, 14, 21, 22]. Therefore, a good model should include both the microscopic and macroscopic details of streamers.

Future work should build upon the present models in order to fully model the directly observable features of streamers such as the liquid-to-gas phase change associated with the development of streamer channels and to incorporate the uncertain nature of streamer growth. This work will require that the model be expanded from the two-dimensional axial symmetric case to a full three-dimensional model. This modeling would use the current electrodynamic model as a foundation to examine how electrical dissipation results in the development of low-density streamer channels and how the dynamics of these observable streamer channels relate to the underlying electrodynamic driving mechanisms. The future research should continue to develop the streamer model to the point where it can be used as a design tool for electrical equipment. This would allow engineers to evaluate real world designs with regards to the likelihood of streamer formation.

8.2.2 Experimental Work

The physics of high voltage charge injection and transport is generally not well understood or controlled so that space charge and interfacial surface charge distributions are generally not known. The electric field distribution cannot then be simply calculated from knowledge of the electrode configuration and source excitation alone. The measurement and analysis of spatial and temporal variations of electric field distributions gives valuable insights into physical phenomena; provides measurement approaches for system monitoring and diagnostics; and can be used to optimize design performance of high voltage equipment [159].

Many analytical models assume that the electric field is spatially uniform. This motivates many tests to use parallel plane electrodes, but the uniform field assumption is only true in the central region between electrodes in the absence of net volume charge. Breakdown tests typically involve point-plane electrodes so as to localize the initiation of breakdown near the sharp point electrode and to have breakdown onset at reasonable voltages due to the electric field enhancement near the point. Although the space charge free solution of electric field can be approximately expressed in closed form for a hyperboloid of revolution point electrode [160], injection of charge from the point will significantly distort this electric field distribution. The work presented here uses numerical modeling to solve for charge injection, generation and recombination, and transport in high voltage stressed transformer oil with point-sphere electrodes [25,51–53,146]. Therefore, performing studies such as Kerr electro-optic field mapping measurements for various liquid dielectrics to study homocharge injection would be of great interest to validate theory and numerical results. The measurements could include high Kerr constant materials that are not a health hazard such as propylene carbonate (Kerr constant $B \approx 1 \times 10^{-12} \mathrm{m/V^2}$) [161], near that of the largest known Kerr constant material nitrobenzene, where ($B \approx 3 \times 10^{-12}\,\mathrm{m/V^2}$) [162] but difficult to work with because it is toxic. Work with low Kerr constant materials should also be undertaken,

such as transformer oil ($B \approx 3 \times 10^{-15}$ m/V^2) [163], silicon oil ($B \approx 1 \times 10^{-15}$ m/V^2) [163], and rapeseed ester oil ($B \approx 2 \times 10^{-16}$ m/V^2) [163] and other vegetable fats and oils that can potentially be used for high voltage insulation using sensitive electro-optical detectors such as a CCD camera as well as the ac modulation method using lock-in amplifiers.

Appendix A

Numerical Current Calculation Methods in COMSOL Multiphysics

In the study of high voltage phenomena, such as streamers in liquids, there are only a handful of variables that can be readily measured with the appropriate equipment. Applied voltage and terminal current are examples of common variables that are most often measured during streamer studies. As such, the ability to calculate these two electrical quantities in the streamer models are important as they can help validate the accuracy of the model by comparison with experimental data.

The terminal current is most often calculated from the total current density $\vec{J}_t$, which is

$$\begin{aligned} \vec{J}_t &= \vec{J}_c + \vec{J}_d \\ &= \sigma\vec{E} + \frac{\partial\vec{D}}{\partial t}, \end{aligned} \tag{A.1}$$

where $\vec{J}_c$ and $\vec{J}_d$ are the conduction and displacement current densities, respectively. The terminal current across a boundary, such as an electrode, can be calculated by integrating the normal component of $\vec{J}_t$ along the surface area of the closed boundary. Unfortunately, COMSOL Multiphysics does not provide a direct method for calculating the terminal current via this method. The problem is that there is no easy method in COMSOL to calculate a time derivative along a boundary, which makes it difficult to calculate the displacement current density $\vec{J}_d$ in (A.1). In the past, to circumvent this software limitation, an innovative technique was developed to calculate the terminal current based on the volume integration of power and energy densities using Poynting's theorem in a two-terminal system [25, 164]. Since then, a method has been developed to overcome COMSOL Multiphysics' deficiency in calculating displacement currents at boundaries, such that the total current can be derived from integrating the sum of the conduction and displacement current densities over a surface. This new method also allows for the generalization of the current calculation to a multi-terminal system [164].

This appendix discusses the calculation of the terminal current via the two methods discussed above: Poynting's theorem and integration of the total current density. The method

based on Poynting's theorem is revisited because there were errors found in the COMSOL Multiphysics formulation of the method for two-dimensional axial symmetric geometries described in [25].

A.1 Generalized Power Method via Poynting's Theorem

The technique, based upon Poynting's theorem, can be understood by considering any general electromagnetic field within a volume V. Within this volume the total energy of the field is distributed throughout space with an energy density W. Also, power dissipation P_d through the action of the field occurs in the same volume. The Poynting vector $\vec{S}$ describes the power flow within the volume. Therefore, the total power crossing the closed surface of area A, which encloses the volume V, is given by:

$$\oint_A \vec{S} \cdot d\vec{A}. \tag{A.2}$$

This power can be attributed to the power dissipated, the time rate of change of the stored energy in the volume V, and the mechanical work of a force density causing a material velocity $\vec{v}$, such that

$$-\oint_A \vec{S} \cdot d\vec{A} = \int_V P_d \, dV + \frac{d}{dt} \int_V W \, dV + \int \vec{F} \cdot \vec{v} \, dV, \tag{A.3}$$

where the minus sign represents the power flowing into the volume enclosed by the surface A, $\vec{F}$ is the force density, $\vec{v}$ is the velocity, and the last term on the right hand side is the power due to work. The Poynting vector $\vec{S} = \vec{E} \times \vec{H}$ [19, 148] obeys a power conservation theorem known as Poynting's theorem

$$\nabla \cdot \vec{S} = \nabla \cdot (\vec{E} \times \vec{H}) = -\vec{H} \cdot \frac{\partial \vec{B}}{\partial t} - \vec{E} \cdot \frac{\partial \vec{D}}{\partial t} - \vec{E} \cdot \vec{J}_c - \vec{F} \cdot \vec{v}, \tag{A.4}$$

where $\vec{J}_c$ is the conduction current equal to the sum of the products of the individual free charge carriers ρ_i and their velocities $\vec{v}_i$. For a linear medium with dielectric permittivity of ϵ and magnetic permeability of μ, the constitutive laws are

$$\vec{D} = \epsilon \vec{E}, \tag{A.5}$$

$$\vec{B} = \mu \vec{H}. \tag{A.6}$$

Utilizing (A.5) and (A.6), the stored energy density and power dissipation density are

$$W = \frac{1}{2}\epsilon\vec{E}\cdot\vec{E} + \frac{1}{2}\mu\vec{H}\cdot\vec{H} \tag{A.7}$$

$$P_d = \vec{E}\cdot\vec{J}_c = \vec{E}\cdot\sum\rho_i\vec{v}_i \tag{A.8}$$

and the total input power into the volume V enclosed by the area A is the volume integral of the rate of stored energy plus the the internal power dissipated:

$$\sum_{n=1}^{N} v_n i_n = \frac{d}{dt}\int_V W dV + \int_V P_d dV \tag{A.9}$$

where v_n and i_n are the applied voltage at and the current into the n^{th} terminal, respectively. Here, it is assumed that no force is applied to the medium (*i.e.*, $\vec{F} = 0$) or that the medium velocity is zero (*i.e.*, $\vec{v} = 0$) and the magnetic field intensity $\vec{H}$ is negligible as the electric field dominates for our electroquasistatic (EQS) models of charge transport. The flux of $\vec{S}$ entering the surface surrounding a circuit element with N terminals is the summation of all $v_n i_n$.

Unfortunately, it is only possible to use (A.9) to calculate the current flowing into a volume for the case of $n = 1$ (*i.e.*, a two-port system with one port as ground reference). However, this is suitable for the needle-sphere electrode geometry discussed throughout this thesis, since it is a two-port system. Therefore, this method can be used within COMSOL Multiphysics to accurately calculate the total current entering the needle-sphere electrode.

A.1.1 Implementation of Terminal Current Calculation in COMSOL Multiphysics

The form of (A.9) that is used in COMSOL Multiphysics is

$$vi = \frac{d}{dt}\int_V W dV + \int_V P_d dV, \tag{A.10}$$

where W and P_d are defined as

$$W = \frac{1}{2}\epsilon\vec{E}\cdot\vec{E}, \tag{A.11}$$

$$P_d = \vec{E}\cdot\vec{J}_c. \tag{A.12}$$

In the transformer oil streamer models, the conduction current $\vec{J}_c$ is defined as

$$\vec{J}_c = (\rho_p \mu_p - \rho_n \mu_n - \rho_e \mu_e)\, \vec{E}, \tag{A.13}$$

where ρ_p, ρ_n, and ρ_e are the positive ion, negative ion, and electron charge densities, respectively, and ρ_n and ρ_e are negative values. The variables μ_p, μ_n, and μ_e are the positive ion, negative ion, and electron mobilities, respectively, and all taken to be positive values. The left-hand side of (A.10) contains one vi product because the needle-sphere geometry used is a two-port system, with a voltage excitation applied to the needle electrode and the spherical electrode is set to the ground reference with zero voltage.

The volume integration in (A.10) of the stored energy density W and power dissipation density P_d is calculated via the subdomain integration coupling variables in COMSOL Multiphysics. The needle-sphere model is a 2D-axisymmetric model such that the subdomain integration coupling variables perform an area integration in the rz-plane, rather than a volume integration in the $r\phi z$ volume. Therefore, the formulation of the integrands of (A.11) and (A.12) must be handled with extra care due to the 2D-axisymmetrical nature of the system geometry and model.

In Cartesian coordinates, the volume integration, L, of a variable $M(x, y, z)$ is

$$L = \int_{z_1}^{z_2} \int_{y_1}^{y_2} \int_{x_1}^{x_2} M(x, y, z)\; dxdydz. \tag{A.14}$$

The same integration in cylindrical coordinates is

$$L = \int_{z_1}^{z_2} \int_{\phi_1}^{\phi_2} \int_{r_1}^{r_2} M(r\cos\phi, r\sin\phi, z)\; rdrd\phi dz. \tag{A.15}$$

Therefore, in a 2D-axisymmetrical system, where there is no ϕ-dependence, the correct formulation of (A.10) is

$$\begin{aligned} vi &= \frac{d}{dt} \int_{z_1}^{z_2} \int_{0}^{2\pi} \int_{r_1}^{r_2} \left(\frac{1}{2} \epsilon \vec{E}(r,z) \cdot \vec{E}(r,z) \right) rdrd\phi dz \\ &\quad + \int_{z_1}^{z_2} \int_{0}^{2\pi} \int_{r_1}^{r_2} \left(\vec{E}(r,z) \cdot \vec{J}_c(r,z) \right) rdrd\phi dz \\ &= \frac{d}{dt} \int_{z_1}^{z_2} \int_{r_1}^{r_2} \left(\frac{1}{2} \epsilon \vec{E} \cdot \vec{E} \right) (2\pi r)\; drdz + \int_{z_1}^{z_2} \int_{r_1}^{r_2} \left(\vec{E} \cdot \vec{J}_c \right) (2\pi r)\; drdz \end{aligned} \tag{A.16}$$

In the 2D-axisymmetrical mode, the $2\pi r$ contribution in each integrand, as shown in (A.16), must not be neglected in order to derive the correct results. Figure A.1 shows the formulation of the integrands for stored energy and power dissipation densities in COMSOL

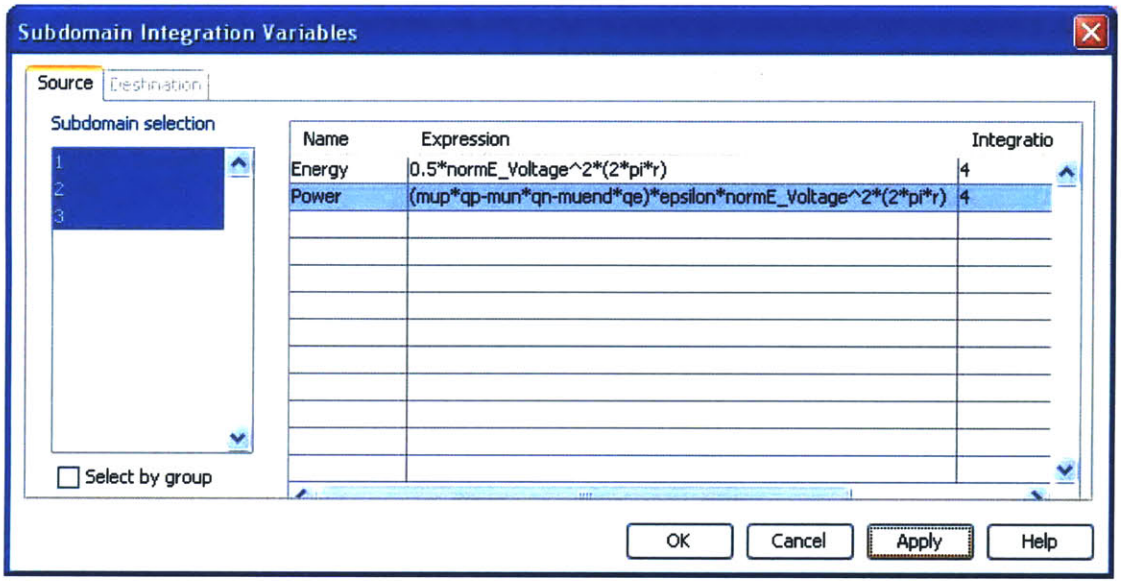

Figure A.1: Formulation of the integrands for stored energy density W of (A.11) and power dissipation P_d density of (A.12) in COMSOL Multiphysics 2D-axisymmetrical mode within the subdomain integration coupling variables.

Multiphysics, where `qp`, `qn`, and `qe` are the positive ion, negative ion, and electron densities, `mup`, `mun`, and `mue` are the positive ion, negative ion, and electron mobilities, `epsilon` is permittivity ϵ, `normE_Voltage` is $|\vec{E}|$, and `pi` is π.

A.1.2 Results

The formulation of the current i is greatly affected by the addition of $2\pi r$ in the integrands. To compare the current results with and without the $2\pi r$ contribution in the integrands, a simple co-axial cylindrical parallel plate model of Fig. A.2 is used with only one positive charge species. The carrier mobility is $\mu = 1\ \mathrm{m^2V^{-1}s^{-1}}$ and dielectric permittivity is $\epsilon = 1\mathrm{F/m}$ for simplicity. The linear space charge injection law $|\vec{J}| = A\mu|\vec{E}|^2$ [20] of Eq. (6.24) is applied to the top electrode, such that $A \to \infty$ and $|\vec{E}| \to 0$ at the top electrode. The bottom electrode is grounded. Other values are $V_0 = 1\mathrm{V}$, $d = 1\mathrm{m}$ and $a = 20\mathrm{mm}$. In Fig. A.3, the current is calculated with and without the $2\pi r$ contribution in the integrand expressions seen in Fig. A.2, where the $2\pi r$ contribution was inadvertently neglected previously by O'Sullivan [25]. The glaring difference in the two results shows the major impact that ignoring $2\pi r$ has on the true current value.

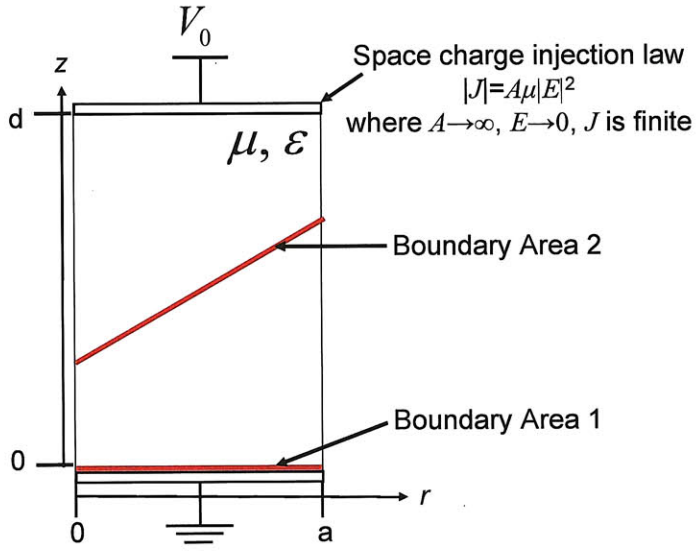

Figure A.2: Simple co-axial cylindrical parallel plane geometry test case with positive space charge injection at top electrode using a linear space charge injection law $\rho = A|\vec{E}|$ [20]. The carrier mobility is $\mu = 1\ \mathrm{m^2V^{-1}s^{-1}}$ and dielectric permittivity is $\epsilon = 1\ \mathrm{F/m}$. Other values are $V(t) = V_0 u(t)$ with $V_0 = 1\ \mathrm{V}$, $d = 1\ \mathrm{m}$ and $a = 20\ \mathrm{mm}$. The closed boundary areas 1 and 2 are used to calculate the current using the boundary area integration of the total current density, as discussed in Section A.2.

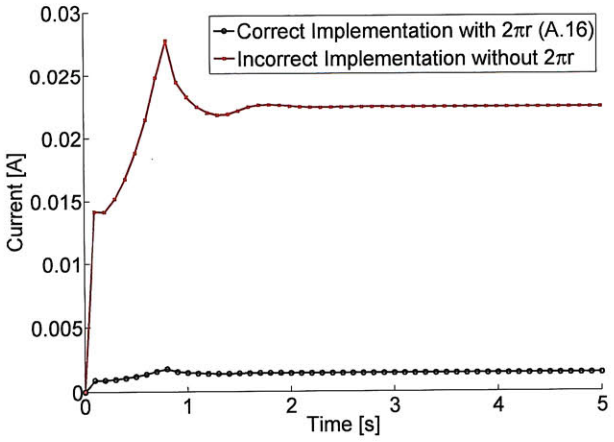

Figure A.3: Terminal current derived from generalized power method via Poynting's theorem. Results are shown for the two cases when the $2\pi r$ contribution in the integrands of Fig.A.2 are included, as in (A.16), and not included.

A.2 Boundary Area Integration of Total Current Density

A method has been found to take the time derivative along a boundary for specific field variables in COMSOL Multiphysics. COMSOL only allows the calculation of time and spatial derivatives along a boundary for the electric potential variable, $V(r,z)$, and not the field variable directly. Therefore, to calculate the electric field, displacement field, displacement current density, etc., they must be manually derived from the voltage along the boundary. Therefore, in a 2D-axisymmetrical system, these variables are calculated as follows:

$$E_r = -\frac{\partial V}{\partial r} \qquad E_z = -\frac{\partial V}{\partial z} \tag{A.17}$$

$$D_r = -\epsilon\frac{\partial V}{\partial r} \qquad D_z = -\epsilon\frac{\partial V}{\partial z} \tag{A.18}$$

$$J_{dr} = -\epsilon\frac{\partial^2 V}{\partial t \partial r} \qquad J_{dz} = -\epsilon\frac{\partial^2 V}{\partial t \partial z} \tag{A.19}$$

$$J_{cr} = \rho\mu E_r \qquad J_{cz} = \rho\mu E_z. \tag{A.20}$$

The displacement current density $\vec{J}_d$ and conduction current density $\vec{J}_c$ are defined as

$$\vec{J}_d = J_{dr}\vec{i}_r + J_{dz}\vec{i}_z, \tag{A.21}$$

$$\vec{J}_c = J_{cr}\vec{i}_r + J_{cz}\vec{i}_z. \tag{A.22}$$

The total current density of (A.1) is the sum of the conduction current $\vec{J}_c$ and displacement current $\vec{J}_d$. The current is then calculated from the following surface integral

$$i = \int_A \vec{n} \cdot \vec{J}_t \, dA \tag{A.23}$$

over the area A and $\vec{n}$ is the vector normal to the surface boundary. In COMSOL Multiphysics, this surface integral is calculated using the boundary integration coupling variables. This method is not constrained to two-port systems, as the current can be calculated across any closed boundary (*i.e.*, boundaries where all flux must pass across) and electrode.

A.2.1 Implementation of Terminal Current Calculation in COMSOL Multiphysics

In a 2D-axisymmetric system, where there is no ϕ-dependence, (A.23) is simplified to

$$i = \int_{l_1}^{l_2} \left(\vec{n} \cdot \vec{J}_t\right)(2\pi r)\, dl \tag{A.24}$$

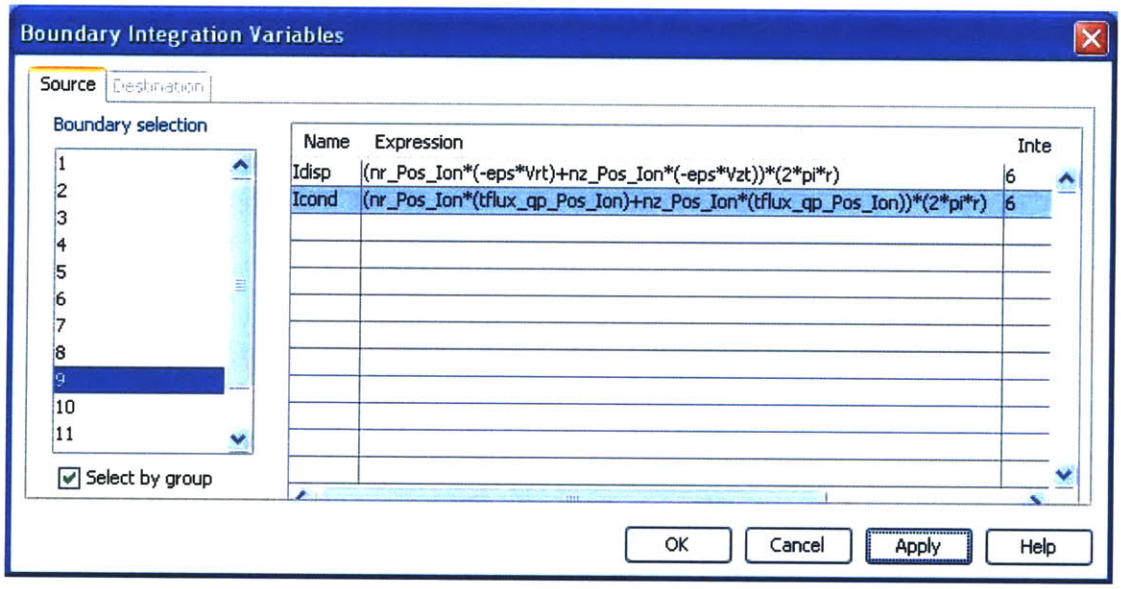

Figure A.4: Formulation of the integrands for the determination of the displacement current i_{disp} of (A.25) and conduction current i_{cond} of (A.26) in COMSOL Multiphysics 2D-axisymmetrical mode within the boundary integration coupling variables.

where l is a function of both r and z coordinates and $\vec{n}$ is the vector normal to the surface boundary. The COMSOL Multiphysics formulation of the boundary integration variables for the displacement and conduction currents is shown in Fig. A.4, where `nr_Pos_Ion` and `nz_Pos_Ion` are the r and z-directed components of the normal vector, `tflux_qp_Pos_Ion` is the conduction current density of the positive charge carrier `qp`, `eps` is permittivity ϵ, and `-eps*Vrt` and `-eps*Vzt` are the r and z-directed components of the displacement current density vector, as shown in (A.19).

The calculation of the displacement i_{disp} and conduction i_{cond} currents in a 2D-axisymmetric geometry, where there is no ϕ-dependence, are

$$\begin{aligned} i_{\text{disp}} &= \int_{z_1}^{z_2}\int_{r_1}^{r_2}\left(\vec{n}\cdot\vec{J}_d\right)(2\pi r)\,drdz \\ &= \int_{z_1}^{z_2}\int_{r_1}^{r_2}\left[\left(n_r\vec{i}_r + n_z\vec{i}_z\right)\cdot\left(J_{dr}\vec{i}_r + J_{dz}\vec{i}_z\right)\right](2\pi r)\,drdz \\ &= \int_{z_1}^{z_2}\int_{r_1}^{r_2}\left[\left(-n_r\epsilon\frac{\partial^2 V}{\partial t\partial r}\right) + \left(-n_z\epsilon\frac{\partial^2 V}{\partial t\partial z}\right)\right](2\pi r)\,drdz \end{aligned} \tag{A.25}$$

$$
\begin{aligned}
i_{\text{cond}} &= \int_{z_1}^{z_2}\int_{r_1}^{r_2}\left(\vec{n}\cdot\vec{J_c}\right)(2\pi r)\,drdz \\
&= \int_{z_1}^{z_2}\int_{r_1}^{r_2}\left[\left(n_r\vec{i_r}+n_z\vec{i_z}\right)\cdot\left(J_{cr}\vec{i_r}+J_{cz}\vec{i_z}\right)\right](2\pi r)\,drdz \\
&= \int_{z_1}^{z_2}\int_{r_1}^{r_2}\left[(n_r\rho\mu E_r)+(n_z\rho\mu E_z)\right](2\pi r)\,drdz
\end{aligned}
\tag{A.26}
$$

where $\vec{n}=n_r\vec{i_r}+n_z\vec{i_z}$ is the unit vector normal to the surface and the displacement and conduction current densities are obtained from (A.19) and (A.20), respectively.

A.2.2 Results

Consider the same co-axial cylindrical parallel plane problem as in the last section, where the geometry is shown in Fig. A.2. The calculation of the terminal current using (A.24) can be done at any closed boundary. In Fig. A.2, there are two closed boundaries where the current can be calculated. Using the COMSOL Multiphysics boundary integration variables, shown in Fig. A.4, the current at both boundaries are plotted in Fig. A.5, as well as the current calculated from the generalized power method derived from Poynting's theorem. The results show that both methods, boundary integration of the total current density and Poynting's theorem, give the same results. Furthermore, the current can be calculated across any closed boundary which allows the user to determine the boundary that results in simplest computations.

A.3 Summary

Two methods for calculating the terminal current are presented. The generalized power method based upon Poynting's theorem was shown to give correct results for two-port systems. Also, special notice was taken of the correct formulation of the equations in the 2D-axisymmetrical mode of COMSOL Multiphysics in order to obtain the correct results. Also, a new method to determine the terminal current is presented, based upon the integration of the total current density across a closed boundary. The method results in a current that is identical to the one derived via Poynting's theorem. This new method is based on a scheme in COMSOL Multiphysics to calculate the displacement current density, which is the time derivative of the displacement field, at the boundary. This is significant as it was previously believed not possible to calculate time and space derivatives of electromagnetic field values along boundaries in COMSOL Multiphysics.

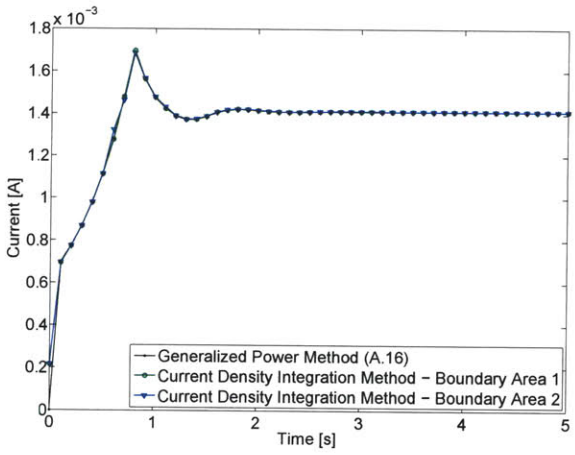

Figure A.5: Terminal current derived from the integration of current density across two different closed boundaries and the generalized power method via Poynting's theorem (same as the correct formulation (A.16) plotted in black in Fig. A.3). All three currents are nearly identical showing that the total current density integration method gives correct results and that it may be more powerful to use in multi-port systems and systems with awkward geometries.

Appendix B

Implementation of Internal Boundary Conditions at the Liquid-Solid Interface

---

By modeling pressboard as a perfect insulator all the current that flows through the pressboard is displacement current. Therefore, to ensure continuity across the interface of the total current density's normal component, there must be a build up of surface charge, σ_s, at the interface. Modeling surface charge is done using the "Weak Form Boundary" application mode in COMSOL Multiphysics [157]. The governing equation is

$$\begin{aligned} \frac{\partial \sigma_s}{\partial t} &= \vec{n} \cdot \vec{J}_{c,oil} \\ &= \vec{n} \cdot \left(\vec{J}_p + \vec{J}_n + \vec{J}_e \right) \\ &= \vec{n} \cdot \left(\rho_p \mu_p - \rho_n \mu_n - \rho_e \mu_e \right) \vec{E}, \end{aligned} \tag{B.1}$$

since the conduction current in the pressboard volume is zero. Note that $\vec{n}$ is the outward unit normal vector from the oil volume to the solid insulation volume.

To fully incorporate the surface charge within the model, it must be explicitly used within the boundary condition at the interface for Gauss' Law (6.77) and the correct boundary conditions for the charge transport continuity equations (6.78)-(6.80). The boundary condition for Eqs. (6.77)-(6.80) at the oil-solid interface are:

- Gauss' Law Eq. (6.77):

$$\vec{n} \cdot \left(\vec{D}_{solid} - \vec{D}_{oil} \right) = \sigma_s \tag{B.2}$$

- Positive Ion Transport Continuity Eq. (6.78): The normal component of the total positive ion current density, $\vec{J}_{p,total}$, is

$$\vec{n} \cdot \vec{J}_{p,total} = \begin{cases} 0 & \text{if } \vec{n} \cdot \vec{E} < 0 \\ \vec{n} \cdot \vec{J}_p & \text{if } \vec{n} \cdot \vec{E} \geq 0 \end{cases} \tag{B.3}$$

- Negative Ion Transport Continuity Eq. (6.79): The normal component of the total negative ion current density, $\vec{J}_{n,total}$, is

$$\vec{n} \cdot \vec{J}_{n,total} = \begin{cases} \vec{n} \cdot \vec{J}_n & \text{if } \vec{n} \cdot \vec{E} \leq 0 \\ 0 & \text{if } \vec{n} \cdot \vec{E} > 0 \end{cases} \tag{B.4}$$

- Electron Transport Continuity Eq. (6.80): The normal component of the total electron current density, $\vec{J}_{e,total}$, is

$$\vec{n} \cdot \vec{J}_{e,total} = \begin{cases} \vec{n} \cdot \vec{J}_e & \text{if } \vec{n} \cdot \vec{E} \leq 0 \\ 0 & \text{if } \vec{n} \cdot \vec{E} > 0 \end{cases} \tag{B.5}$$

It was discovered that the conditional boundary conditions for the charge transport continuity equations in Eqs. (B.3)-(B.5) are required because of an inherent error in COMSOL Multiphysics. In COMSOL's literature (*i.e.*, user guides) and their example models, the boundary condition often used between two media for the charge transport continuity equation is

$$\vec{n} \cdot D \nabla \rho_x = 0, \tag{B.6}$$

where in our model the subscript x is equal to p, n or e. This boundary condition is called zero diffusive flux and only free convection flow, or migration current, is permitted between the two media through the interface. COMSOL Multiphysics' modeling guide ambiguously states the zero diffusive flux boundary condition as [54]

> "This boundary condition typically applies at outlets, where you can assume that mass is transported out of the domain by convection only."

The error in applying the zero diffusive flux boundary condition of (B.6) to an interface that is <u>not</u> an outlet is that COMSOL Multiphysics places numerical "ghost" charges across the interface in the solid insulator to uphold the zero diffusive current density boundary condition. The numerical ghost charges are needed to ensure no diffusion across the boundary, when the boundary is an outlet. However, when the boundary is not an outlet for the charge density, the ghost charges in the solid volume are swept across the interface into the oil, becoming real charge and contributing to the total charge density. At first these ghost charges are only a numerical modeling concept that helps COMSOL Multiphysics enforce the boundary condition. Unfortunately, the numerical ghost charges are convected across the boundary from the solid to the oil due to the electric field and subsequently the interface becomes an inlet for these ghost charges. Once these ghost charges enter the oil volume they contribute to the electric field via Gauss' Law (6.77) and affect the simulation leading

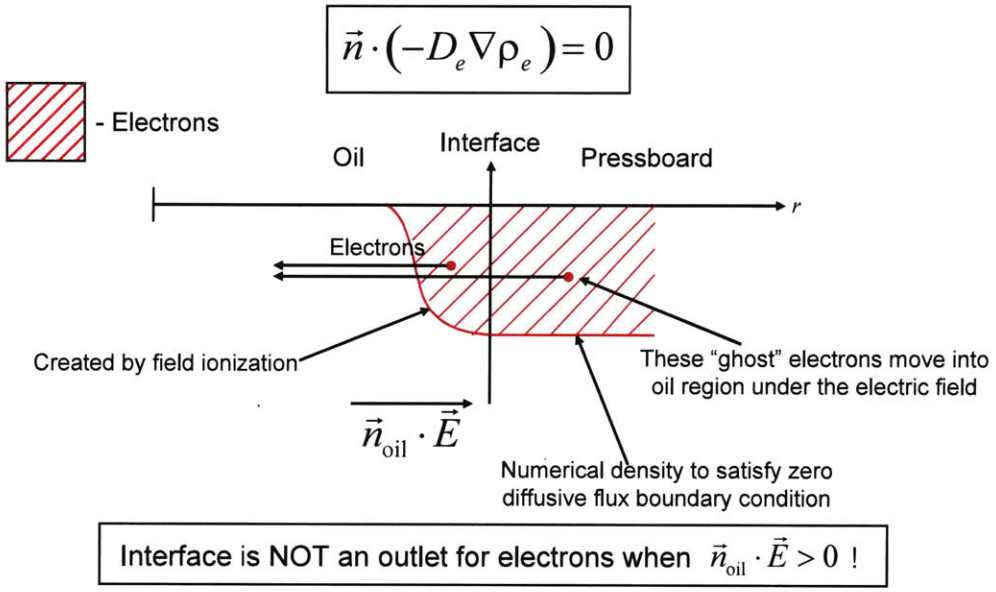

Figure B.1: Pictorial example of how COMSOL Multiphysics enforces a zero diffusive boundary condition at the oil-pressboard interface by creating and subsequently injecting numerical "ghost" numerical electrons from the pressboard into the transformer oil. These ghost charge carriers give incorrect results. By applying the new conditional interface boundary conditions of (B.2)-(B.5), this error in COMSOL Multiphysics is resolved.

to erroneous results. A pictorial description of the transport of ghost electron charges from the pressboard volume to the oil volume is shown in Fig. B.1.

By applying the new conditional boundary conditions of (B.2)-(B.5) with the surface charge density calculation of (B.1), the model gives correct results and accounts for surface charge at the oil-solid interface. Unlike the work of Kumara *et al.* [156], who set the oil-pressboard interface boundary condition for the charge transport continuity equations of (6.77)-(6.80) as insulating (*i.e.*, zero normal flux $\vec{n} \cdot \vec{J}_x = 0$ where the subscript x is equal to p, n or e), such that the oil's normal conduction current is zero at the interface, we model the flow of conduction current into the interface. As stated above, the charge from the conduction current then becomes surface charge as it comes in contact with the surface.

Appendix C

A Low Ionization Potential Additive Method to Increase the Electric Breakdown Strength of Insulation Materials

---

THIS SECTION includes a United States provisional patent application filed on the 23rd of March 2010 entitled "A Low Ionization Potential Additive Method to Increase the Electric Breakdown Strength of Insulation Materials" [165]. The patent describes a method to increase the inception voltage for fast streamers of vegetable-based oils composed of natural or synthetic esters by adding low ionization potential additives in small concentrations.

The majority of high voltage components, such as paper insulated oil impregnated cables and high voltage power transformers in use today, rely on mineral oil, also called transformer oil, as a vital piece of their electrical insulation system [1,55]. Within the past decade there has been considerable interest in finding a green, environmentally friendly replacement for transformer oil. In particular, much of the research has focused on vegetable-based oils composed of natural or synthetic esters [4, 5, 59, 65] that are biodegradable. Unfortunately, ester liquids have shown to have electrical insulation characteristics that are greatly inferior to transformer oil at extremely high voltages [4, 5, 59]. For ester liquids to be considered as a viable replacement to transformer oils, their electrical insulating strength at extremely high voltages must be improved. Specifically, their inception voltage for fast discharge velocities ($>10\,\mathrm{km/s}$) (also known as fast streamers) must be increased such that the time to breakdown is also increased, which is significant because a slow streamer requires more time to traverse the liquid gap between electrodes to cause breakdown. This allows more time for the applied impulse voltage to be extinguished. This patent presents a method to increase the inception voltage for fast streamers of vegetable-based oils composed of natural or synthetic esters by adding low ionization potential additives in small concentrations that inhibit fast streamers by space charge shielding at the high voltage electrode. The additive must have an ionization potential that is lower than that of molecules comprising the majority of the base liquid.

IN THE UNITED STATES PATENT AND TRADEMARK OFFICE

Provisional Patent Application for

A LOW IONIZATION POTENTIAL ADDITIVE METHOD TO INCREASE THE ELECTRIC BREAKDOWN STRENGTH OF INSULATION MATERIALS

MIT Case No. 14099

Attorney Docket: 14099.109034

Sam (Bo) Pasternack
Registration Number 29,576
5 Cambridge Center
Room NE25-230
Cambridge, MA 021412

A LOW IONIZATION POTENTIAL ADDITIVE METHOD TO INCREASE THE ELECTRIC BREAKDOWN STRENGTH OF INSULATION MATERIALS

Background of the Invention

This invention relates to dielectric liquids for use in high voltage transformers, oil-insulated cables, and other oil-insulated high voltage devices.

The majority of high voltage components, such as paper insulated oil impregnated cables and high voltage power transformers in use today rely on mineral oil, also called transformer oil, as a vital piece of their electrical insulation system [1, 2]. The numbers in brackets refer to the references appended hereto. The contents of all of these references are incorporated by reference herein. The widespread use of transformer oil for high voltage insulation and power apparatus cooling is due to their greater electrical breakdown strength and thermal conductivity than gaseous insulators, while their ability to conform to complex geometries and self-heal means that they are often of more practical use than solid insulators. As such, the electrical insulation strength and characteristics of transformer oil has become the *de facto* standard for high voltage liquid insulation.

Due to the major implications which an insulation failure in electric power apparatus can have, scientists and engineers have for many years studied the insulating properties of dielectric liquids, particularly transformer oils, with a view to understanding the mechanisms behind electrical breakdown in an effort to reduce their likelihood [1]. Much of their work has focused on the formation of electrical streamers. These are low density conductive structures that form in regions of oil that are over-stressed by electric fields on the order of $1x10^8$ V/m or greater [10]. Once a streamer forms it tends to elongate, growing from the point of initiation towards a grounding point. The extent of a streamer's development and velocity depends upon the nature of the electrical excitation (i.e., magnitude, duration, rise time, etc.) which caused it. Sustained over-excitation can result in a streamer short circuiting the oil gap between electrodes. When this happens an arc will form and electrical breakdown will occur.

The important role which streamers play in the electrical breakdown of dielectric liquids has meant that they have been the subject of significant scientific investigation. Much of the

research on streamers in dielectric liquids has been empirical in nature and has led to the formation of a large literature on the subject of which the references [1, 7-19] are representative.

Within the past decade there has been considerable interest in finding a green, environmentally friendly replacement for transformer oil. In particular, much of the work has focused on vegetable-based oils composed of natural or synthetic esters [3-6] that are biodegradable. Unfortunately, ester liquids have been shown to have electrical insulation characteristics that greatly differ from transformer oil at extremely high voltages [4-6]. While ester liquids have similar breakdown voltage Vb (50% probability) as transformer oil, their breakdown time delay (i.e., the time between voltage application and breakdown) at slightly higher applied voltages in lightning impulse tests are extremely short or conversely the average streamer propagation velocity is very high (>>10 km/s) [4-6]. This differs from transformer oil where above its breakdown voltage Vb the average streamer velocity is low (i.e., 1-5 km/s) over a wide voltage range [6-9]. For example, it has been experimentally recorded in the literature that streamers in transformer oil travel 1-5 km/s for an applied voltage Vapp that ranges between Vb < Vapp < 2Vb [7, 9]. Above a certain voltage, called the acceleration voltage Va, the streamer in transformer oil accelerates and travels at average velocities greater than 10 km/s [7].

For ester liquids to be considered as a viable replacement to transformer oils, their electrical insulating strength at high voltages must be improved. Specifically, their transition to fast streamer velocities (> 10 km/s) must be pushed to higher voltages such that the time to breakdown is increased, which is significant because a slower streamer requires more time to traverse the liquid gap between electrodes to cause breakdown. This allows more time for the applied impulse voltage to be extinguished.

The work by Lesaint and Jung [32] with cyclohexane with a pyrene additive has shown that the addition of low ionization potential additives to these materials will create a space charge shielding effect whereby the additives will ionize and create a slow 2^{nd} mode streamer at a lower inception voltage. The creation of these streamers and their associated space charge shield the higher applied lightning impulse voltage levels and regulate the electric field enhancement at the streamer tip. Therefore, a greater applied voltage is needed to generate fast traveling streamers such as 3^{rd} and 4^{th} mode streamers such that the acceleration voltage occurs at high voltages in these non-ester liquids.

An object of this invention is a method to increase the inception voltage for fast streamers of vegetable-based oils composed of natural or synthetic esters by adding low ionization potential additives in small concentrations that inhibit fast streamers by space charge shielding at the high voltage electrode.

Summary of the Invention

The insulating liquid according to the invention includes an ester liquid, and an additive to the ester liquid having a lower ionization potential than the ionization potential of the ester liquid. In a preferred embodiment, the ester liquid is rapeseed oil, and a suitable additive is pinoresinol. Other suitable esters are sunflower, soybean, corn, cottonseed and sesame oils. Other suitable additives for use with the ester liquids are low ionization potential phenolic compounds such as 1-acetoxypinoresinol.

In another aspect, the invention includes the further addition of conducting nanoparticles to offset the lower breakdown voltage caused by the addition of the low ionization potential additive.

Brief Description of the Drawing

Fig. 1a is a graph of stopping length versus applied voltage in rapeseed oil comprising natural esters.

Fig. 1b is a graph of average velocity versus applied voltage in rapeseed oil.

Fig. 1c is a graph of streamer charge versus applied voltage in rapeseed oil.

Fig. 2 is a graph of average streamer velocity versus voltage in natural and synthetic esters and transformer oil.

Description of the Preferred Embodiment

Ester liquids, whether natural or synthetic, have pre-breakdown characteristics that are extremely different from transformer oil. This should not come as a surprise as esters have very different chemical compositions than transformer oil.

As in transformer oil, the onset of the streamer modes in ester liquids is dependent on the magnitude of the voltage excitation. Once again, the 2^{nd} mode initiates at the breakdown voltage

Vb which denotes 50% probability of breakdown, while the 3rd mode initiates at the acceleration voltage Va where the streamer propagation velocity rises dramatically [7]. The 2nd, 3rd, and 4th modes have velocities on the order of 1 km/s, 10 km/s, and 100 km/s, like in transformer oil [4-6]. Furthermore, the breakdown voltage Vb of ester liquids and transformer oil, where 2nd mode streamers initiate, has been shown to be very close in magnitude for the same experimental setup [4-6].

The key difference between ester liquids and transformer oil is the acceleration voltage Va level where streamers transition to very fast 3rd and 4th mode streamers. For transformer oil the acceleration voltage is much higher than the breakdown voltage. Therefore, in transformer oil the applied voltage range, where the slower 2nd mode streamers dominate, is large and the voltage at which the dangerous 3rd and 4th mode streamers propagate is pushed to exceedingly high voltages. This ensures a lower probability for propagation of fast streamers that quickly traverse the oil gap to the cathode causing electrical breakdown before the applied voltage impulse can be extinguished.

For ester liquids, the acceleration voltage Va occurs almost directly above the breakdown voltage as shown by the two different experimental results from Duy et al. [4, 5, 34] and ABB [6] in Figs. 1 and 2. Therefore, when the breakdown voltage is reached the streamers easily transition to streamers that propagate at average velocities greater than 10km/s since $Vb \approx Va$ for ester liquids and are not well-suited to insulate high-voltage systems.

According to the invention, the acceleration voltage of a pure ester liquid such as rapeseed oil is increased by adding a secondary molecule in low concentrations. The secondary molecule has an ionization potential that is lower than the main family of molecules comprising the ester liquid.

Many ester liquids are largely composed of oleic acid which has an ionization potential of 8.6 eV. Thus, additives such as pinoresinol with an ionization potential of 6.6 eV and other low ionization potential phenolic compounds such as 1-acetoxypinoresinol with an ionization potential of 6.8 eV are suitable additives according to some embodiments of the invention.

While the acceleration voltage Va of esters is increased by adding the lower ionization potential additive according to this aspect of the invention, the breakdown voltage Vb is decreased. This lower breakdown strength of an insulating dielectric liquid due to the addition of a low ionization potential additive can be offset by the further addition of conducting

nanoparticles of typical diameter around 10 nm, that raises the breakdown strength of a dielectric liquid and decreases positive streamer velocity [37,38]. This breakdown strength increase is due to the conversion of fast electrons produced by ionization of the dielectric liquids to slow negatively charged nanoparticle charge carriers with effective mobility reduction by a factor of about 10^5 [38]. This also raises the acceleration voltage. Therefore, the use of conducting nanoparticles together with a low ionization potential additive can result in both an increased breakdown voltage for slow 2nd mode streamers and an increased acceleration voltage for fast 3rd and 4th mode streamers.

Example one

A mixture of rapeseed oil and pinoresinol is prepared. The concentration of the additive is five percent. The breakdown voltage of the mixture is slightly decreased while the acceleration voltage is increased as compared to pure rapeseed oil. An acceptable range of concentration for the additive is 3 to 10% percent. Other suitable esters are sunflower oil, soybean oil, corn oil, cottonseed oil and sesame oil, and other suitable additives are low ionization potential phenolic compounds such as 1-acetoxypinoresinol.

Example two

A mixture of rapeseed oil and pinoresinol is prepared. The concentration of the additive is five percent. Magnetite nanoparticles, with dielectric relaxation time of about 10^{-14} seconds, 10 nm diameter and concentration about 10^{20} nanoparticles/m^3 are also added to the rapeseed and pinoresinol additive. The breakdown voltage and acceleration voltage of the mixture is increased as compared to pure rapeseed oil. An acceptable range of concentration for the additive is 3 to 10% percent. Other suitable esters are sunflower oil, soybean oil, corn oil, cottonseed oil and sesame oil, and other suitable additives are low ionization potential phenolic compounds such as 1-acetoxypinoresinol. Other suitable nanoparticles can be any material with dielectric relaxation time less than about 50 microseconds, such as any iron oxide, zinc oxide, aluminum, copper, steel, titanium, or any metal or conducting material whose dielectric relaxation time is shorter than about 50 microseconds.

It is recognized that modifications and variations of the invention will be apparent to those of ordinary skill in the art and it is intended that all such modifications and variations be included within the scope of the appended claims.

References

[1] Beroual, M. Zahn, A. Badent, K. Kist, A. J. Schwabe, H. Yamashita, K. Yamazawa, M. Danikas, W. D. Chadband, and Y. Torshin, Propagation and structure of streamers in liquid dielectrics. IEEE Electr. Insul. Mag., 14(2): 6-17, March 1998.

[2] A. Al-Sulaiman and M. I. Qureshi. The role of methylnaphthalene in ehv cable oil as related to oil breakdown and discharge velocity. European Transactions on Electrical Power, 12(6):389-395, November/December 2002.

[3] T. V. Oommen. Vegetable oils for liquid-filled transformers. 18(1):6-11, January 2002.

[4] C. T. Duy, O. Lesaint, N. Bonifaci, A. Denat, and Y. Bertrand. High voltage breakdown and pre-breakdown properties in rape-seed insulating oil. In Proc. Annual Report - Conference on Electrical Insulation and Dielectric Phenomena CEIDP 2007, pp. 623-626, October 14-17, 2007.

[5] C. T. Duy, O. Lesaint, A. Denat, N. Bonifaci, and Y. Bertrand. Streamer propagation and breakdown in rape-seed oil at high voltage. In Proc. IEEE International Conference on Dielectric Liquids ICDL 2008, pp. 1-4, June 2008.

[6] Rongsheng Liu, Christer Tornkvist, Yijaya Chandramouli, Orlando Girlanda, and Leif A. A. Pettersson. Ester fluids as alternative for mineral oil: the difference in streamer velocity and LI breakdown voltages. In Proc. Annual Report Conference on Electrical Insulation and Dielectric Phenomena, 6 pages, Virginia Beach, VA, USA, October 2009.

[7] O. Lesaint and G. Massala. Positive streamer propagation in large oil gaps: experimental characterization of propagation modes. IEEE Trans. Dielectr. Electr. Insul., 5(3):360-370, June 1998.

[8] D. Linhjell, L. Lundgaard, and G. Berg. Streamer propagation under impulse voltage in long point-plane oil gaps. IEEE Trans. Electr. Insul., 1:447-458, 1994.

[9] L. Lundgaard, D. Linhjell, G. Berg, and S. Sigmond. Propagation of positive and negative streamers in oil with and without pressboard interfaces. IEEE Trans. Dielectr. Electr. Insul., 5(3):388-395, June 1998.

[10] R. Tobazeon. Prebreakdown phenomena in dielectric liquids. IEEE Trans. Dielectr. Electr. Insul., 1(6):1132-1147, December 1994.

[11] H. Akiyama. Streamer discharges in liquids and their applications. IEEE Trans. Dielectr. Electr. Insul., 7(5):646-653, October 2000.

[12] E. O. Forster. Critical assessment of the electrical breakdown process in dielectric fluids. IEEE Trans. Electr. Insul., (5):891-896, October 1985.

[13] R. E. Hebner. Measurements of electrical breakdown in liquids, pp. 519-537. Plenum Press, New York, 1988.

[14] Yu. V. Torshin. On the existence of leader discharges in mineral oil. IEEE Trans. Dielectr. Electr. Insul., 2(1):167-179, February 1995.

[15] G. Massala and O. Lesaint. Positive streamer propagation in large oil gaps: electrical properties of streamers. IEEE Trans. Dielectr. Electr. Insul., 5(3):371-381, June 1998.

[16] Y. Nakao, T. Yamazaki, K. Miyagi, Y. Zakai, and H. Tagashira. The effect of molecular structure on prebreakdown phenomena in dielectric liquids under nonuniform field. Electrical Engineering in Japan, 139(2):1-8, 2002.

[17] J. C. Devins, S. J. Rzad, and R. J. Schwabe. Breakdown and prebreakdown phenomena in liquids. J. Appl. Phys., 52:4531-4545, 1981.

[18] W. G. Chadband. On variations in the propagation of positive discharges between transformer oil and silicone fluids. J. Phys. D: Appl. Phys., 13:1299-1307, 1980.

[19] O. Lesaint and P. Gournay. Initiation and propagation thresholds of positive prebreakdown phenomena in hydrocarbon liquids. IEEE Trans. Dielectr. Electr. Insul., 1(4):702-708, August 1994.

[20] Nynas AB. Nynas Transformer Oil - Nytro 10XN (IEC 60296/03), 2008.

[21] L. Costeanu and O. Lesaint. On mechanisms involved in the propagation of subsonic positive streamers in cyclohexane. In Proc. IEEE 14th International Conference on Dielectric Liquids ICDL 2002, pp. 143-146, Graz, Austria, July 7-12, 2002.

[22] CEI/IEC60897:1987. Methods for the determination of the lightning impulse breakdown voltage of insulating liquids. IEC, Geneva, Switzerland, 1987.

[23] P. Biller. A simple qualitative model for the different types of streamers in dielectric liquids. In Proc. 12th International Conference on Conduction and Breakdown in Dielectric Liquids, ICDL '96, pp. 189-192, Baden-Dattwil, Switzerland, July 15-19, 1996.

[24] M. Harada, Y. Ohga, I. Watanabe, and H. Watarai. Ionization energies for solvated polycyclic aromatic hydrocarbons. Chem. Phys. Lett., 303:489-492, 1999.

[25] H. S. Smalo, P.-O. Astrand, and S. Ingebrigtsen. Calculation of ionization potentials and electron affinities for molecules relevant for streamer initiation and propagation. In Proc. IEEE International Conference on Dielectric Liquids ICDL 2008, pp. 1-4, Futuroscope-Chasseneuil, France, June 2008.

[26] D. R. Lide, editor. Physical Constants of Organic Compounds, pp. 519-537. CRC Press/Taylor and Francis, Boca Raton, 89th edition, 2009.

[27] J. George Hwang, Markus Zahn, Leif A. A. Pettersson, Olof Hjortstam, and Rongsheng Liu. Modeling streamers in transformer oil: The transitional fast 3rd mode streamer. In Proc. IEEE 9th International Conference on the Properties and Applications of Dielectric Materials ICPADM 2009, pp 573-578, July 19-23, 2009.

[28] J. Nieto-Salazar, O. Lesaint, and A. Denat. Transient current and light emission associated to the propagation of pre-breakdown phenomena in water. In Proc. Annual Report Electrical Insulation and Dielectric Phenomena Conference on, pp 542-545, 2003.

[29] J. Nieto-Salazar, N. Bonifaci, A. Denat, and O. Lesaint. Characterization and spectroscopic study of positive streamers in water. In Proc. IEEE International Conference on Dielectric Liquids ICDL 2005, pp. 91-94, 2005.

[30] F. M. J. McCluskey, O. Lesaint, and A. Denat. Breakdown processes over large distances in insulating liquids of distinct chemical compositions. In Conference Record of the 1994 IEEE International Symposium on Electrical Insulation, pp. 426-429, June 5-8, 1994.

[31] F. M. J. McCluskey, A. Denat, and O. Lesaint. Breakdown and prebreakdown phenomena in liquids under positive impulse voltages. 1(3):377-382, June 1994.

[32] O. Lesaint and M. Jung. On the relationship between streamer branching and propagation in liquids: influence of pyrene in cyclohexane. J. Phys. D: Appl. Phys., 33:1360-1368, 2000.

[33] F. M. O'Sullivan. A model for the initiation and propagation of electrical streamers in transformer oil and transformer oil based nanofluids. PhD thesis, Massachusetts Institute of Technology, 2007.

[34] C. T. Duy, O. Lesaint, A. Denat, and N. Bonifaci. Streamer propagation and breakdown in natural ester at high voltage. IEEE Trans. Dielectr. Electr. Insul., 16(6):1582-1594, December 2009.

[35] N. Nenadis, L.-F. Wang, M. Z. Tsimidou, and H.-Y. Zhang. Radical scavenging potential of phenolic compounds encountered in O. europaea products as indicated by calculation of bond dissociation enthalpy and ionization potential values. J. Agric. Food Chem., 53: 295-299, 2005.

[36] D. G. Nash, X. F. Liu, E. R. Mysak, and T. Baer. Aerosol particle mass spectrometry with low photon laser ionization. Int. J. Mass Spectrometry, 241: 89-97, 2005.

[37] US Patent No. 5,863,455, Jan. 26, 1999.

[38] J. G. Hwang, M. Zahn, F. O'Sullivan, L. A. A. Pettersson, O. Hjortstam, and R. Liu, Effects of nanoparticle charging on streamer development in transformer oil-based nanofluids, Journal of Applied Physics, Volume 107, Issue 1, pp. 014310-014310-17 (2010)

What is Claimed is:

1. Dielectric comprising:
an ester liquid; and
an additive to the ester liquid having a lower ionization potential than the ionization potential of the ester liquid.

2. The dielectric liquid according to claim 1, wherein the ester liquid is rapeseed oil.

3. The dielectric liquid according to claim 1 wherein the ester is selected from the group consisting of sunflower oil, soybean oil, corn oil, cottonseed oil and sesame oil.

4. The dielectric liquid of claim 1 wherein the additive is pinoresinol or 1-acetoxypinoresinol.

5. The dielectric liquid of claim 3 wherein the additive is other low ionization potential phenolic compounds such as pinoresinol and 1-acetoxypinoresinol.

6. Dielectric liquid comprising an ester liquid; an additive to the ester liquid having a lower ionization potential than the ionization potential of the ester liquid, and an additive to the ester liquid of conducting nanoparticles.

7. The dielectric liquid according to claim 6, wherein the ester liquid is selected from the group consisting of rapeseed oil, sunflower oil, soybean oil, corn oil, cottonseed oil and sesame oil.

8. The dielectric liquid of claim 6 wherein the low ionization potential additive is pinoresinol or other phenolic compounds such as 1-acetoxypinoresinol.

9. The dielectric liquid of claim 6 wherein the conductive nanoparticle additive is iron oxide, (magnetite,Fe_3O_4)

10. The dielectric liquid of claim 6 wherein the conductive nanoparticle additive is selected from

the group consisting of any iron oxide, zinc oxide, aluminum, copper, steel, titanium, or any metal or conducting material whose dielectric relaxation time is shorter than 50 microseconds.

11. The dielectric liquid of claim 6 wherein the conductive nanoparticle additive has diameter of 10 nm.

Abstract of the Disclosure

Insulating liquid. The liquid includes an ester liquid and an additive to the ester liquid having a lower ionization potential than the ionization potential of the ester liquid. In one aspect, conductive nanoparticles are also added.

Attorney Docket: 14099.109034

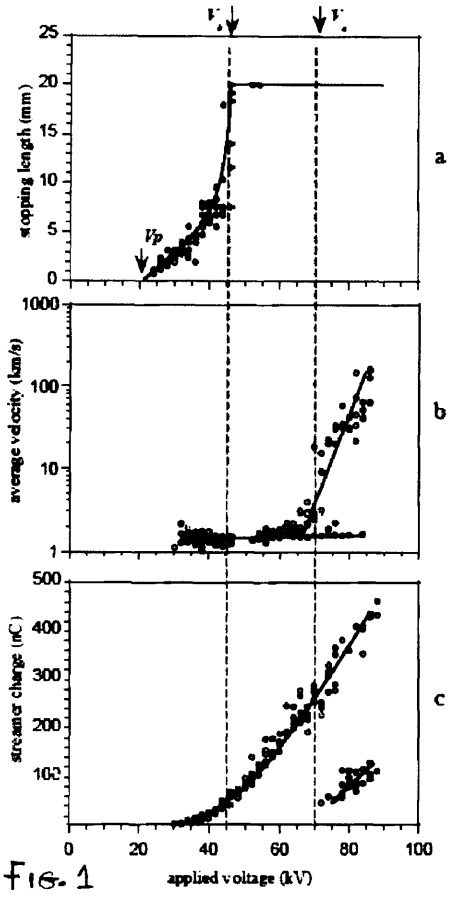

FIG. 1

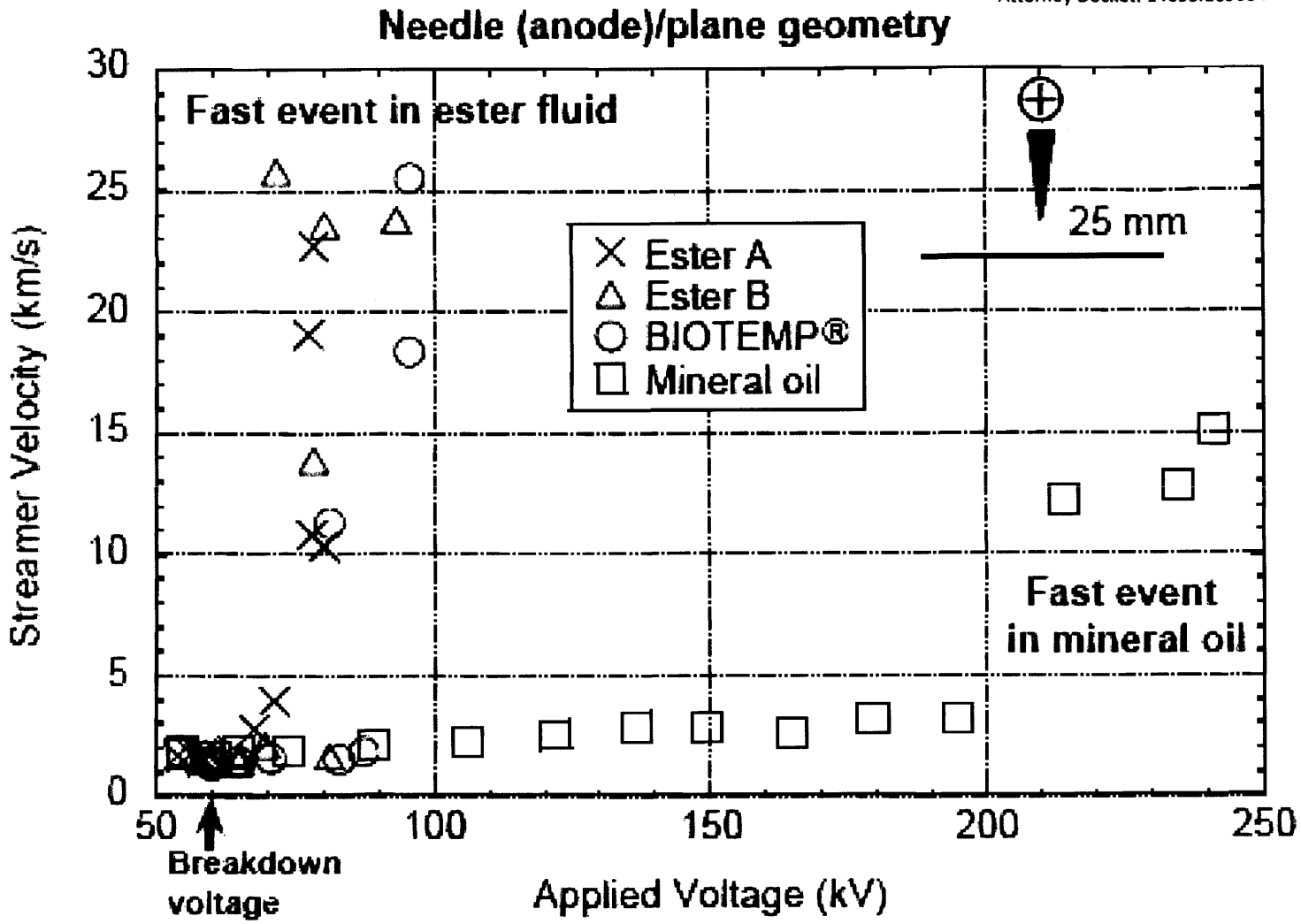
Needle (anode)/plane geometry
Fast event in ester fluid
25 mm
Ester A
Ester B
BIOTEMP®
Mineral oil
Fast event
in mineral oil
Streamer Velocity (km/s)
Applied Voltage (kV)
Breakdown
voltage
0
5
10
15
20
25
30
50
100
150
200
250

FIG. 2

Appendix D

COMSOL Multiphysics Settings for Transformer Oil Model

THE FOLLOWING is a COMSOL Multiphysics auto-generated report that corresponds to the finite element simulation results that were presented in Section 4.2 for the transformer oil model. The report provides detailed information about model properties, mesh settings, domain and boundary conditions, solver settings, solver variables, constants, etc.

Aromatic molecules, field ionization, Vapp=130kV

1. Model Properties

Property	Value
Model name	Aromatic molecules, field ionization, Vapp=130kV
Author	George Hwang
Company	MIT
Department	EECS
Reference	
URL	
Saved date	May 17, 2010 7:57:19 PM
Creation date	Aug 8, 2006 11:10:05 AM
COMSOL version	COMSOL 3.5.0.603

File name: C:\Documents and Settings\george\Desktop\Aromatic_Vapp-130kV.mph

Application modes and modules used in this model:

- Geom1 (Axial symmetry (2D))
  - Electrostatics
  - Convection and Diffusion
  - Convection and Diffusion
  - Convection and Diffusion
  - Convection and Conduction

2. Constants

Name	Expression	Value	Description
BASES	0123456789	1.234568e8	
Vb	3e5	3e5	Base voltage [V]
Lb	25e-3	0.025	Base Length [m]
mub	1e-9	1e-9	Base mobility [m^2/V-s]
epsb	epsr*eps0	1.94788e-11	Base permitivitty [F/m]
eps0	8.854e-12	8.854e-12	Permittivity of free space [F]m
epsr	2.2	2.2	Relative permittivity of transformer oil
Eb	Vb/Lb	1.2e7	Base electric field [V/m]
qNb	epsb*Vb/Lb^2	0.00935	Base charge density [C/m^3]
Gb	epsb*mub*Vb^2/Lb^4	0.004488	Base charge generation rate [C/m^3-s]
Db	mub*Vb	3e-4	Base diffusion [m^2/s]
KRb	q*mub/epsb	8.225353e-18	Base recombination rate [m^3/s]
tb	Lb^2/(mub*Vb)	2.083333	Base time [s]

Afb	(epsb*mub*Vb)/Lb^3	3.73993e-10	Base field ionization pre-exponential coefficient [F/m^2-s]
CONSTANTS	0123456789	1.234568e8	
pi	3.14159265	3.141593	PI
q	1.6022e-19	1.6022e-19	Magnitude electronic charge [C]
me	9.109e-31	9.109e-31	Free elctron mass [kg]
hp	6.626e-34	6.626e-34	Planck's constant [m^2 kg/s]
CAPTURING_MECHANISMS	0123456789	1.234568e8	
KR	1.65e-17	1.65e-17	Recombination coefficient ion-ion and ion-electron [m^3/s]
KRnd	KR/KRb	2.005993	
GENERATION_SOURCES	0123456789	1.234568e8	
MM2_VALUES	0123456789	1.234568e8	
n2	1e23	10e22	2MM density of ionizable species [m^-3]
a2	3e-10	3e-10	2MM molecular separation distance [m]
ie2	q*6.2	9.93364e-19	2MM ionization energy [J]
m2	0.1*me	9.109e-32	2MM effective electron mass [kg]
Af2	q^2*n2*a2/hp	1.16226e9	2MM pre-exponential coefficient term [F/m^2-s]
Af2nd	Af2/Afb	3.107705e18	
Bf2	pi^2*m2*a2*ie2^2/(q*hp^2)	3.783458e9	2MM exponential term [V/m]
Bf2nd	Bf2/Eb	315.288187	
MM3_VALUES	0123456789	1.234568e8	
n3	1e25	1e25	3MM density of ionizable species [m^-3]
a3	3e-10	3e-10	3MM molecular separation distance [m]
ie3	q*9.86	1.579769e-18	3MM ionization energy [J]
m3	0.1*me	9.109e-32	3MM effective electron mass [kg]
Af3	q^2*n3*a3/hp	1.16226e11	3MM pre-exponential coefficient term [F/m^2-s]
Af3nd	Af3/Afb	3.107705e20	
Bf3	pi^2*m3*a3*ie3^2/(q*hp^2)	9.568842e9	3MM exponential term [V/m]
Bf3nd	Bf3/Eb	797.403523	
SYSTEM_VALUES	0123456789	1.234568e8	
Va	1.3e5	1.3e5	Applied voltage [V]
Vand	Va/Vb	0.433333	
mui	1e-9	1e-9	Ion mobility [m^2/V-s]
muind	mui/mub	1	
mue	1e-4	1e-4	Electron mobility [m^2/V-s]
muend	mue/mub	1e5	
tnsnd	1e-9/tb	4.8e-10	Non-dimensionalized nano-second time
tea	200e-9	2e-7	Electron attachment time constant [s]
teand	tea/tb	9.6e-8	
Cv	1.67e3	1670	Specific Heat Capacity of Transformer Oil [J/kg-K]
rho	880	880	Transformer oil mass density [kg/m^3]
TT	300	300	Nominal temperature [K]
TTnd	TT/TTb	1.571794e5	
TTb	(epsb*Vb^2)/(rho*Cv*(Lb^2))	0.001909	Base temperature [K]
kT	0.13	0.13	Thermal conductivity of transformer oil [W/m-K]
kTnd	kT/(mub*Vb*rho*Cv)	2.948648e-4	

3. Geom1

Space dimensions: Axial symmetry (2D)

Independent variables: r, phi, z

3.1. Scalar Expressions

Aromatic molecules, field ionization, Vapp=130kV

Name	Expression	Unit	Description
Vapp	Vand		Non-dimensional applied voltage

3.2. Expressions

3.2.1. Subdomain Expressions

Subdomain		1-2
Particle_Velocity		0
Vp_r	V/m	Er_Voltage
Vp_z	V/m	Ez_Voltage
Vn_r	V/m	-Vp_r
Vn_z	V/m	-Vp_z
Ve_r	V/m	-muend*Er_Voltage
Ve_z	V/m	-muend*Ez_Voltage
Ve	V/m	muend*normE_Voltage
MM2		0
GF2		Af2nd*normE_Voltage*exp(-Bf2nd/normE_Voltage)
MM3		0
GF3		Af3nd*normE_Voltage*exp(-Bf3nd/normE_Voltage)
Attachment		0
alphaA		Aand*exp(-Band/normE_Voltage)
EA	mol/m^3	abs(qe)/teand
Recombination		0
Rpn	mol^2/m^6	KRnd*abs(qp*qn)
Rpe	mol^2/m^6	KRnd*abs(qp*qe)

3.3. Mesh

3.3.1. Mesh Statistics

Number of degrees of freedom	1131070
Number of mesh points	56681
Number of elements	112865
Triangular	112865
Quadrilateral	0
Number of boundary elements	1018
Number of vertex elements	18
Minimum element quality	0.699
Element area ratio	0

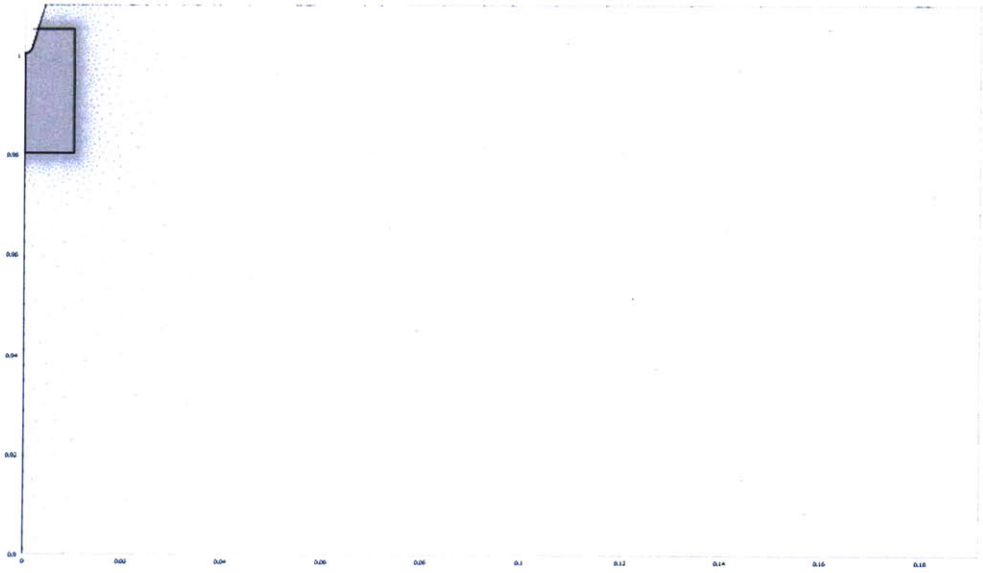

3.4. Application Mode: Electrostatics (Voltage)

Application mode type: Electrostatics

Application mode name: Voltage

3.4.1. Scalar Variables

Name	Variable	Value	Unit	Description
epsilon0	epsilon0_Voltage	8.854187817e-12	F/m	Permittivity of vacuum

3.4.2. Application Mode Properties

Property	Value
Default element type	Lagrange - Quadratic
Input property	Forced voltage
Frame	Frame (ref)
Weak constraints	Off
Constraint type	Ideal

3.4.3. Variables

Dependent variables: V

Shape functions: shlag(2,'V')

Interior boundaries not active

Aromatic molecules, field ionization, Vapp=130kV

3.4.4. Boundary Settings

Boundary		1-2	5, 7, 9, 11, 17-18	10, 13, 16, 19
Type		Axial symmetry	Electric potential	Ground
name		**SymAxis**	**Potential**	**Gnd**
Electric potential (V0)	V	0	**Vapp**	0

Boundary		12, 14-15
Type		Zero charge/Symmetry
name		**Insulation**
Electric potential (V0)	V	0

3.4.5. Subdomain Settings

Subdomain		1-2
Relative permittivity (epsilonr)	1	**{1/epsilon0_Voltage,0;0,1/epsilon0_Voltage}**
Space charge density (rho)	C/m^3	**qp+qe+qn**

Subdomain initial value		1-2
Electric potential (V)	V	1e-8*(r-z)

3.5. Application Mode: Convection and Diffusion (Pos_Ion)

Application mode type: Convection and Diffusion

Application mode name: Pos_Ion

3.5.1. Application Mode Properties

Property	Value
Default element type	Lagrange - Quadratic
Analysis type	Transient
Equation form	Conservative
Frame	Frame (ref)
Weak constraints	Off
Constraint type	Ideal

3.5.2. Variables

Dependent variables: qp

Shape functions: shlag(2,'qp')

Interior boundaries not active

3.5.3. Boundary Settings

Boundary		1-2	5, 7, 9-11, 13, 16-19	12, 14-15
Type		Axial symmetry	Convective flux	Insulation/Symmetry
name		**SymAxis**	**Electrodes**	**Insulation**

3.5.4. Subdomain Settings

Subdomain		1-2
Diffusion coefficient (D)	m^2/s	**0**
Reaction rate (R)	$mol/(m^3 \cdot s)$	**GF2-Rpn-Rpe**

r-velocity (u)	m/s	**Vp_r**
z-velocity (v)	m/s	**Vp_z**
Streamline diffusion switch (sdon)		**1**
Streamline diffusion type (sdtype)		**Anisotropic diffusion**

3.6. Application Mode: Convection and Diffusion (Electron)

Application mode type: Convection and Diffusion

Application mode name: Electron

3.6.1. Application Mode Properties

Property	Value
Default element type	Lagrange - Quadratic
Analysis type	Transient
Equation form	Conservative
Frame	Frame (ref)
Weak constraints	Off
Constraint type	Ideal

3.6.2. Variables

Dependent variables: qe

Shape functions: shlag(2,'qe')

Interior boundaries not active

3.6.3. Boundary Settings

Boundary	1-2	5, 7, 9-11, 13, 16-19	12, 14-15
Type	Axial symmetry	Convective flux	Insulation/Symmetry
name	**SymAxis**	**Electrodes**	**Insulation**

3.6.4. Subdomain Settings

Subdomain		1-2
Diffusion coefficient (D)	m^2/s	**0**
Reaction rate (R)	$mol/(m^3 \cdot s)$	**-GF2+Rpe+EA**
r-velocity (u)	m/s	**Ve_r**
z-velocity (v)	m/s	**Ve_z**
Streamline diffusion switch (sdon)		**1**
Streamline diffusion type (sdtype)		**Anisotropic diffusion**

3.7. Application Mode: Convection and Diffusion (Neg_Ion)

Application mode type: Convection and Diffusion

Application mode name: Neg_Ion

3.7.1. Application Mode Properties

Property	Value
Default element type	Lagrange - Quadratic
Analysis type	Transient
Equation form	Conservative

Aromatic molecules, field ionization, Vapp=130kV

Frame	Frame (ref)
Weak constraints	Off
Constraint type	Ideal

3.7.2. Variables

Dependent variables: qn

Shape functions: shlag(2,'qn')

Interior boundaries not active

3.7.3. Boundary Settings

Boundary	1-2	5, 7, 9-11, 13, 16-19	12, 14-15
Type	Axial symmetry	Convective flux	Insulation/Symmetry
name	**SymAxis**	**Electrodes**	**Insulation**

3.7.4. Subdomain Settings

Subdomain		1-2
Diffusion coefficient (D)	m^2/s	**0**
Reaction rate (R)	$mol/(m^3 \cdot s)$	**-EA+Rpn**
r-velocity (u)	m/s	**Vn_r**
z-velocity (v)	m/s	**Vn_z**
Streamline diffusion switch (sdon)		**1**
Streamline diffusion type (sdtype)		**Anisotropic diffusion**

3.8. Application Mode: Convection and Conduction (Temperature)

Application mode type: Convection and Conduction

Application mode name: Temperature

3.8.1. Application Mode Properties

Property	**Value**
Default element type	Lagrange - Quadratic
Analysis type	Transient
Frame	Frame (ref)
Weak constraints	Off
Constraint type	Ideal

3.8.2. Variables

Dependent variables: T

Shape functions: shlag(2,'T')

Interior boundaries not active

3.8.3. Boundary Settings

Boundary	1-2	5, 7, 9-19
Type	Axial symmetry	Thermal insulation

3.8.4. Subdomain Settings

Subdomain		1-2
Thermal conductivity (k)	W/(m·K)	**kTnd**
Density (rho)	kg/m^3	**1**
Heat capacity at constant pressure (C)	J/(kg·K)	**1**
Heat source (Q)	W/m^3	**(qp-qn-qe*muend)*(normE_Voltage^2)**
Streamline diffusion switch (sdon)		**0**

Subdomain initial value		1-2
Temperature (T)	K	TTnd

4. Integration Coupling Variables

4.1. Geom1

4.1.1. Source Subdomain: 1-2

Name	Value
Variable name	Energy
Expression	0.5*(normE_Voltage^2)
Order	4
Global	Yes

4.1.2. Source Subdomain: 1-2

Name	Value
Variable name	Power
Expression	(qp-qn-qe*muend)*(normE_Voltage^2)
Order	4
Global	Yes

5. Solver Settings

Solve using a script: off

Auto select solver	On
Solver	Time dependent
Solution form	Automatic
Symmetric	auto
Adaptive mesh refinement	Off
Optimization/Sensitivity	Off
Plot while solving	Off

5.1. Direct (PARDISO)

Solver type: Linear system solver

Parameter	Value
Preordering algorithm	Nested dissection
Row preordering	On
Bunch-Kaufmann	Off
Pivoting perturbation	1.0E-8
Relative tolerance	1.0E-6
Factor in error estimate	400.0
Check tolerances	On

Aromatic molecules, field ionization, Vapp=130kV

5.2. Time Stepping

Parameter	Value
Times	range(0,4.8e-10,4.8e-8)
Relative tolerance	1e-2
Absolute tolerance	1e-3
Times to store in output	Specified times
Time steps taken by solver	Free
Maximum BDF order	5
Singular mass matrix	Maybe
Consistent initialization of DAE systems	Backward Euler
Error estimation strategy	Include algebraic
Allow complex numbers	Off

5.3. Advanced

Parameter	Value
Constraint handling method	Elimination
Null-space function	Automatic
Automatic assembly block size	On
Assembly block size	5000
Use Hermitian transpose of constraint matrix and in symmetry detection	Off
Use complex functions with real input	Off
Stop if error due to undefined operation	On
Store solution on file	Off
Type of scaling	Automatic
Manual scaling	
Row equilibration	On
Manual control of reassembly	Off
Load constant	On
Constraint constant	On
Mass constant	On
Damping (mass) constant	On
Jacobian constant	On
Constraint Jacobian constant	On

6. Variables

6.1. Boundary

6.1.1. Boundary 1-3, 5-19

Name	Description	Unit	Expression
unTEr_Voltage	Maxwell surface stress tensor (r)	Pa	-0.5 * (up(Dr_Voltage) * up(Er_Voltage)+up(Dz_Voltage) * up (Ez_Voltage)) * dnr+(dnr * up(Dr_Voltage)+dnz * up(Dz_Voltage)) * up (Er_Voltage)
unTEz_Voltage	Maxwell surface stress tensor (z)	Pa	-0.5 * (up(Dr_Voltage) * up(Er_Voltage)+up(Dz_Voltage) * up (Ez_Voltage)) * dnz+(dnr * up(Dr_Voltage)+dnz * up(Dz_Voltage)) * up (Ez_Voltage)
dnTEr_Voltage	Maxwell surface stress tensor (r)	Pa	-0.5 * (down(Dr_Voltage) * down(Er_Voltage)+down(Dz_Voltage) * down(Ez_Voltage)) * unr+(unr * down(Dr_Voltage)+unz * down (Dz_Voltage)) * down(Er_Voltage)
dnTEz_Voltage	Maxwell surface stress tensor (z)	Pa	-0.5 * (down(Dr_Voltage) * down(Er_Voltage)+down(Dz_Voltage) * down(Ez_Voltage)) * unz+(unr * down(Dr_Voltage)+unz * down (Dz_Voltage)) * down(Ez_Voltage)
unTr_Voltage	Exterior Maxwell stress tensor (u), r	Pa	unTEr_Voltage+unTMr_Voltage

	component		
unTMr_Voltage	Exterior magnetic Maxwell stress tensor (u), r component	Pa	0
unTz_Voltage	Exterior Maxwell stress tensor (u), z component	Pa	unTEz_Voltage+unTMz_Voltage
unTMz_Voltage	Exterior magnetic Maxwell stress tensor (u), z component	Pa	0
dnTr_Voltage	Exterior Maxwell stress tensor (d), r component	Pa	dnTEr_Voltage+dnTMr_Voltage
dnTMr_Voltage	Exterior magnetic Maxwell stress tensor (d), r component	Pa	0
dnTz_Voltage	Exterior Maxwell stress tensor (d), z component	Pa	dnTEz_Voltage+dnTMz_Voltage
dnTMz_Voltage	Exterior magnetic Maxwell stress tensor (d), z component	Pa	0
dVolbnd_Voltage	Volume integration contribution	m	r
nD_Voltage	Surface charge density	C/m^2	unr * (down(Dr_Voltage)-up(Dr_Voltage))+unz * (down(Dz_Voltage)-up(Dz_Voltage))
ndflux_qp_Pos_Ion	Normal diffusive flux, qp	mol/(m^2*s)	nr_Pos_Ion * dflux_qp_r_Pos_Ion+nz_Pos_Ion * dflux_qp_z_Pos_Ion
ncflux_qp_Pos_Ion	Normal convective flux, qp	mol/(m^2*s)	nr_Pos_Ion * cflux_qp_r_Pos_Ion+nz_Pos_Ion * cflux_qp_z_Pos_Ion
ntflux_qp_Pos_Ion	Normal total flux, qp	mol/(m^2*s)	nr_Pos_Ion * tflux_qp_r_Pos_Ion+nz_Pos_Ion * tflux_qp_z_Pos_Ion
ndflux_qe_Electron	Normal diffusive flux, qe	mol/(m^2*s)	nr_Electron * dflux_qe_r_Electron+nz_Electron * dflux_qe_z_Electron
ncflux_qe_Electron	Normal convective flux, qe	mol/(m^2*s)	nr_Electron * cflux_qe_r_Electron+nz_Electron * cflux_qe_z_Electron
ntflux_qe_Electron	Normal total flux, qe	mol/(m^2*s)	nr_Electron * tflux_qe_r_Electron+nz_Electron * tflux_qe_z_Electron
ndflux_qn_Neg_Ion	Normal diffusive flux, qn	mol/(m^2*s)	nr_Neg_Ion * dflux_qn_r_Neg_Ion+nz_Neg_Ion * dflux_qn_z_Neg_Ion
ncflux_qn_Neg_Ion	Normal convective flux, qn	mol/(m^2*s)	nr_Neg_Ion * cflux_qn_r_Neg_Ion+nz_Neg_Ion * cflux_qn_z_Neg_Ion
ntflux_qn_Neg_Ion	Normal total flux, qn	mol/(m^2*s)	nr_Neg_Ion * tflux_qn_r_Neg_Ion+nz_Neg_Ion * tflux_qn_z_Neg_Ion
ndflux_T_Temperature	Normal conductive heat flux, T	W/m^2	nr_Temperature * dflux_T_r_Temperature+nz_Temperature * dflux_T_z_Temperature
ncflux_T_Temperature	Normal convective heat flux, T	W/m^2	nr_Temperature * cflux_T_r_Temperature+nz_Temperature * cflux_T_z_Temperature
ntflux_T_Temperature	Normal total heat flux, T	W/m^2	nr_Temperature * tflux_T_r_Temperature+nz_Temperature * tflux_T_z_Temperature

6.1.2. Boundary 4

Name	Description	Unit	Expression
unTEr_Voltage	Maxwell surface stress tensor (r)	Pa	
unTEz_Voltage	Maxwell surface stress tensor (z)	Pa	
dnTEr_Voltage	Maxwell surface stress tensor (r)	Pa	
dnTEz_Voltage	Maxwell surface stress tensor (z)	Pa	
unTr_Voltage	Exterior Maxwell stress tensor (u), r component	Pa	
unTMr_Voltage	Exterior magnetic Maxwell stress tensor (u), r component	Pa	

unTz_Voltage	Exterior Maxwell stress tensor (u), z component	Pa	
unTMz_Voltage	Exterior magnetic Maxwell stress tensor (u), z component	Pa	
dnTr_Voltage	Exterior Maxwell stress tensor (d), r component	Pa	
dnTMr_Voltage	Exterior magnetic Maxwell stress tensor (d), r component	Pa	
dnTz_Voltage	Exterior Maxwell stress tensor (d), z component	Pa	
dnTMz_Voltage	Exterior magnetic Maxwell stress tensor (d), z component	Pa	
dVolbnd_Voltage	Volume integration contribution	m	
nD_Voltage	Surface charge density	C/m^2	
ndflux_qp_Pos_Ion	Normal diffusive flux, qp	mol/(m^2*s)	
ncflux_qp_Pos_Ion	Normal convective flux, qp	mol/(m^2*s)	
ntflux_qp_Pos_Ion	Normal total flux, qp	mol/(m^2*s)	
ndflux_qe_Electron	Normal diffusive flux, qe	mol/(m^2*s)	
ncflux_qe_Electron	Normal convective flux, qe	mol/(m^2*s)	
ntflux_qe_Electron	Normal total flux, qe	mol/(m^2*s)	
ndflux_qn_Neg_Ion	Normal diffusive flux, qn	mol/(m^2*s)	
ncflux_qn_Neg_Ion	Normal convective flux, qn	mol/(m^2*s)	
ntflux_qn_Neg_Ion	Normal total flux, qn	mol/(m^2*s)	
ndflux_T_Temperature	Normal conductive heat flux, T	W/m^2	
ncflux_T_Temperature	Normal convective heat flux, T	W/m^2	
ntflux_T_Temperature	Normal total heat flux, T	W/m^2	

6.2. Subdomain

Name	Description	Unit	Expression
dVol_Voltage	Volume integration contribution	m	r
Dr_Voltage	Electric displacement, r component	C/m^2	epsilonrr_Voltage * Er_Voltage+epsilonrz_Voltage * Ez_Voltage
Dz_Voltage	Electric displacement, z component	C/m^2	epsilonzr_Voltage * Er_Voltage+epsilonzz_Voltage * Ez_Voltage
epsilon_Voltage	Permittivity	F/m	epsilon0_Voltage * epsilonr_Voltage
epsilonrr_Voltage	Permittivity, rr component	F/m	epsilon0_Voltage * epsilonrrr_Voltage
epsilonrz_Voltage	Permittivity, rz component	F/m	epsilon0_Voltage * epsilonrrz_Voltage
epsilonzr_Voltage	Permittivity, zr component	F/m	epsilon0_Voltage * epsilonrzr_Voltage
epsilonzz_Voltage	Permittivity, zz component	F/m	epsilon0_Voltage * epsilonrzz_Voltage
normE_Voltage	Electric field, norm	V/m	sqrt(abs(Er_Voltage)^2+abs(Ez_Voltage)^2)
normD_Voltage	Electric displacement, norm	C/m^2	sqrt(abs(Dr_Voltage)^2+abs(Dz_Voltage)^2)
normDr_Voltage	Remanent displacement, norm	C/m^2	sqrt(abs(Drr_Voltage)^2+abs(Drz_Voltage)^2)
normP_Voltage	Electric polarization, norm	C/m^2	sqrt(abs(Pr_Voltage)^2+abs(Pz_Voltage)^2)
We_Voltage	Electric energy density	J/m^3	0.5 * ((Dr_Voltage+Drr_Voltage) * Er_Voltage+(Dz_Voltage+Drz_Voltage) * Ez_Voltage)
dW_Voltage	Integrand for total energy	N/m	2 * pi * dVol_Voltage * We_Voltage
Er_Voltage	Electric field,	V/m	-Vr

	r component		
Ez_Voltage	Electric field, z component	V/m	-Vz
grad_qp_r_Pos_Ion	Concentration gradient, qp, r component	mol/m^4	qpr
dflux_qp_r_Pos_Ion	Diffusive flux, qp, r component	mol/ (m^2*s)	-Drr_qp_Pos_Ion * qpr-Drz_qp_Pos_Ion * qpz
cflux_qp_r_Pos_Ion	Convective flux, qp, r component	mol/ (m^2*s)	qp * u_qp_Pos_Ion
tflux_qp_r_Pos_Ion	Total flux, qp, r component	mol/ (m^2*s)	dflux_qp_r_Pos_Ion+cflux_qp_r_Pos_Ion
grad_qp_z_Pos_Ion	Concentration gradient, qp, z component	mol/m^4	qpz
dflux_qp_z_Pos_Ion	Diffusive flux, qp, z component	mol/ (m^2*s)	-Dzr_qp_Pos_Ion * qpr-Dzz_qp_Pos_Ion * qpz
cflux_qp_z_Pos_Ion	Convective flux, qp, z component	mol/ (m^2*s)	qp * v_qp_Pos_Ion
tflux_qp_z_Pos_Ion	Total flux, qp, z component	mol/ (m^2*s)	dflux_qp_z_Pos_Ion+cflux_qp_z_Pos_Ion
beta_qp_r_Pos_Ion	Convective field, qp, r component	m^2/s	r * u_qp_Pos_Ion
beta_qp_z_Pos_Ion	Convective field, qp, z component	m^2/s	r * v_qp_Pos_Ion
grad_qp_Pos_Ion	Concentration gradient, qp	mol/m^4	sqrt(grad_qp_r_Pos_Ion^2+grad_qp_z_Pos_Ion^2)
dflux_qp_Pos_Ion	Diffusive flux, qp	mol/ (m^2*s)	sqrt(dflux_qp_r_Pos_Ion^2+dflux_qp_z_Pos_Ion^2)
cflux_qp_Pos_Ion	Convective flux, qp	mol/ (m^2*s)	sqrt(cflux_qp_r_Pos_Ion^2+cflux_qp_z_Pos_Ion^2)
tflux_qp_Pos_Ion	Total flux, qp	mol/ (m^2*s)	sqrt(tflux_qp_r_Pos_Ion^2+tflux_qp_z_Pos_Ion^2)
cellPe_qp_Pos_Ion	Cell Peclet number, qp	1	h * sqrt(beta_qp_r_Pos_Ion^2+beta_qp_z_Pos_Ion^2)/Dm_qp_Pos_Ion
Dm_qp_Pos_Ion	Mean diffusion coefficient, qp	m^3/s	r * (Drr_qp_Pos_Ion * u_qp_Pos_Ion^2+Drz_qp_Pos_Ion * u_qp_Pos_Ion * v_qp_Pos_Ion+Dzr_qp_Pos_Ion * v_qp_Pos_Ion * u_qp_Pos_Ion+Dzz_qp_Pos_Ion * v_qp_Pos_Ion^2)/ (u_qp_Pos_Ion^2+v_qp_Pos_Ion^2+eps)
res_qp_Pos_Ion	Equation residual for qp	mol/ (m^2*s)	r * (-Drr_qp_Pos_Ion * qprr-Drz_qp_Pos_Ion * qprz+qpr * u_qp_Pos_Ion-Dzr_qp_Pos_Ion * qpzr-Dzz_qp_Pos_Ion * qpzz+qpz * v_qp_Pos_Ion-R_qp_Pos_Ion)
res_sc_qp_Pos_Ion	Shock capturing residual for qp	mol/ (m^2*s)	r * (qpr * u_qp_Pos_Ion+qpz * v_qp_Pos_Ion-R_qp_Pos_Ion)
da_qp_Pos_Ion	Total time scale factor, qp	m	r * Dts_qp_Pos_Ion
grad_qe_r_Electron	Concentration gradient, qe, r component	mol/m^4	qer
dflux_qe_r_Electron	Diffusive flux, qe, r component	mol/ (m^2*s)	-Drr_qe_Electron * qer-Drz_qe_Electron * qez
cflux_qe_r_Electron	Convective	mol/	qe * u_qe_Electron

	flux, qe, r component	(m^2*s)	
tflux_qe_r_Electron	Total flux, qe, r component	mol/(m^2*s)	dflux_qe_r_Electron+cflux_qe_r_Electron
grad_qe_z_Electron	Concentration gradient, qe, z component	mol/m^4	qez
dflux_qe_z_Electron	Diffusive flux, qe, z component	mol/(m^2*s)	-Dzr_qe_Electron * qer-Dzz_qe_Electron * qez
cflux_qe_z_Electron	Convective flux, qe, z component	mol/(m^2*s)	qe * v_qe_Electron
tflux_qe_z_Electron	Total flux, qe, z component	mol/(m^2*s)	dflux_qe_z_Electron+cflux_qe_z_Electron
beta_qe_r_Electron	Convective field, qe, r component	m^2/s	r * u_qe_Electron
beta_qe_z_Electron	Convective field, qe, z component	m^2/s	r * v_qe_Electron
grad_qe_Electron	Concentration gradient, qe	mol/m^4	sqrt(grad_qe_r_Electron^2+grad_qe_z_Electron^2)
dflux_qe_Electron	Diffusive flux, qe	mol/(m^2*s)	sqrt(dflux_qe_r_Electron^2+dflux_qe_z_Electron^2)
cflux_qe_Electron	Convective flux, qe	mol/(m^2*s)	sqrt(cflux_qe_r_Electron^2+cflux_qe_z_Electron^2)
tflux_qe_Electron	Total flux, qe	mol/(m^2*s)	sqrt(tflux_qe_r_Electron^2+tflux_qe_z_Electron^2)
cellPe_qe_Electron	Cell Peclet number, qe	1	h * sqrt(beta_qe_r_Electron^2+beta_qe_z_Electron^2)/Dm_qe_Electron
Dm_qe_Electron	Mean diffusion coefficient, qe	m^3/s	r * (Drr_qe_Electron * u_qe_Electron^2+Drz_qe_Electron * u_qe_Electron * v_qe_Electron+Dzr_qe_Electron * v_qe_Electron * u_qe_Electron+Dzz_qe_Electron * v_qe_Electron^2)/(u_qe_Electron^2+v_qe_Electron^2+eps)
res_qe_Electron	Equation residual for qe	mol/(m^2*s)	r * (-Drr_qe_Electron * qerr-Drz_qe_Electron * qerz+qer * u_qe_Electron-Dzr_qe_Electron * qezr-Dzz_qe_Electron * qezz+qez * v_qe_Electron-R_qe_Electron)
res_sc_qe_Electron	Shock capturing residual for qe	mol/(m^2*s)	r * (qer * u_qe_Electron+qez * v_qe_Electron-R_qe_Electron)
da_qe_Electron	Total time scale factor, qe	m	r * Dts_qe_Electron
grad_qn_r_Neg_Ion	Concentration gradient, qn, r component	mol/m^4	qnr
dflux_qn_r_Neg_Ion	Diffusive flux, qn, r component	mol/(m^2*s)	-Drr_qn_Neg_Ion * qnr-Drz_qn_Neg_Ion * qnz
cflux_qn_r_Neg_Ion	Convective flux, qn, r component	mol/(m^2*s)	qn * u_qn_Neg_Ion
tflux_qn_r_Neg_Ion	Total flux, qn, r component	mol/(m^2*s)	dflux_qn_r_Neg_Ion+cflux_qn_r_Neg_Ion
grad_qn_z_Neg_Ion	Concentration gradient, qn, z component	mol/m^4	qnz
dflux_qn_z_Neg_Ion	Diffusive flux, qn, z component	mol/(m^2*s)	-Dzr_qn_Neg_Ion * qnr-Dzz_qn_Neg_Ion * qnz

cflux_qn_z_Neg_Ion	Convective flux, qn, z component	mol/(m^2*s)	qn * v_qn_Neg_Ion
tflux_qn_z_Neg_Ion	Total flux, qn, z component	mol/(m^2*s)	dflux_qn_z_Neg_Ion+cflux_qn_z_Neg_Ion
beta_qn_r_Neg_Ion	Convective field, qn, r component	m^2/s	r * u_qn_Neg_Ion
beta_qn_z_Neg_Ion	Convective field, qn, z component	m^2/s	r * v_qn_Neg_Ion
grad_qn_Neg_Ion	Concentration gradient, qn	mol/m^4	sqrt(grad_qn_r_Neg_Ion^2+grad_qn_z_Neg_Ion^2)
dflux_qn_Neg_Ion	Diffusive flux, qn	mol/(m^2*s)	sqrt(dflux_qn_r_Neg_Ion^2+dflux_qn_z_Neg_Ion^2)
cflux_qn_Neg_Ion	Convective flux, qn	mol/(m^2*s)	sqrt(cflux_qn_r_Neg_Ion^2+cflux_qn_z_Neg_Ion^2)
tflux_qn_Neg_Ion	Total flux, qn	mol/(m^2*s)	sqrt(tflux_qn_r_Neg_Ion^2+tflux_qn_z_Neg_Ion^2)
cellPe_qn_Neg_Ion	Cell Peclet number, qn	1	h * sqrt(beta_qn_r_Neg_Ion^2+beta_qn_z_Neg_Ion^2)/Dm_qn_Neg_Ion
Dm_qn_Neg_Ion	Mean diffusion coefficient, qn	m^3/s	r * (Drr_qn_Neg_Ion * u_qn_Neg_Ion^2+Drz_qn_Neg_Ion * u_qn_Neg_Ion * v_qn_Neg_Ion+Dzr_qn_Neg_Ion * v_qn_Neg_Ion * u_qn_Neg_Ion+Dzz_qn_Neg_Ion * v_qn_Neg_Ion^2)/(u_qn_Neg_Ion^2+v_qn_Neg_Ion^2+eps)
res_qn_Neg_Ion	Equation residual for qn	mol/(m^2*s)	r * (-Drr_qn_Neg_Ion * qnrr-Drz_qn_Neg_Ion * qnrz+qnr * u_qn_Neg_Ion-Dzr_qn_Neg_Ion * qnzr-Dzz_qn_Neg_Ion * qnzz+qnz * v_qn_Neg_Ion-R_qn_Neg_Ion)
res_sc_qn_Neg_Ion	Shock capturing residual for qn	mol/(m^2*s)	r * (qnr * u_qn_Neg_Ion+qnz * v_qn_Neg_Ion-R_qn_Neg_Ion)
da_qn_Neg_Ion	Total time scale factor, qn	m	r * Dts_qn_Neg_Ion
grad_T_r_Temperature	Temperature gradient, T, r component	K/m	Tr
dflux_T_r_Temperature	Conductive heat flux, T, r component	W/m^2	-krr_T_Temperature * Tr-krz_T_Temperature * Tz
cflux_T_r_Temperature	Convective heat flux, T, r component	W/m^2	rho_T_Temperature * C_T_Temperature * T * u_T_Temperature
tflux_T_r_Temperature	Total heat flux, T, r component	W/m^2	dflux_T_r_Temperature+cflux_T_r_Temperature
grad_T_z_Temperature	Temperature gradient, T, z component	K/m	Tz
dflux_T_z_Temperature	Conductive heat flux, T, z component	W/m^2	-kzr_T_Temperature * Tr-kzz_T_Temperature * Tz
cflux_T_z_Temperature	Convective heat flux, T, z component	W/m^2	rho_T_Temperature * C_T_Temperature * T * v_T_Temperature
tflux_T_z_Temperature	Total heat flux, T, z component	W/m^2	dflux_T_z_Temperature+cflux_T_z_Temperature
beta_T_r_Temperature	Convective field, T, r component	W/(m*K)	r * rho_T_Temperature * C_T_Temperature * u_T_Temperature

Aromatic molecules, field ionization, Vapp=130kV

beta_T_z_Temperature	Convective field, T, z component	W/(m*K)	r * rho_T_Temperature * C_T_Temperature * v_T_Temperature
grad_T_Temperature	Temperature gradient, T	K/m	sqrt(grad_T_r_Temperature^2+grad_T_z_Temperature^2)
dflux_T_Temperature	Conductive heat flux, T	W/m^2	sqrt(dflux_T_r_Temperature^2+dflux_T_z_Temperature^2)
cflux_T_Temperature	Convective heat flux, T	W/m^2	sqrt(cflux_T_r_Temperature^2+cflux_T_z_Temperature^2)
tflux_T_Temperature	Total heat flux, T	W/m^2	sqrt(tflux_T_r_Temperature^2+tflux_T_z_Temperature^2)
cellPe_T_Temperature	Cell Peclet number, T	1	h * sqrt (beta_T_r_Temperature^2+beta_T_z_Temperature^2)/Dm_T_Temperature
kmean_T_Temperature	Mean effective thermal conductivity	W/(m*K)	k_Temperature
taue_T_Temperature	GLS time-scale	m*s^3*K/kg	0
helem_T_Temperature	Element size	m	h
Dm_T_Temperature	Mean diffusion coefficient, T	m^2*kg/(s^3*K)	r * rho_T_Temperature^2 * C_T_Temperature^2 * (krr_T_Temperature * u_T_Temperature^2+krz_T_Temperature * u_T_Temperature * v_T_Temperature+kzr_T_Temperature * v_T_Temperature * u_T_Temperature+kzz_T_Temperature * v_T_Temperature^2)/ ((rho_T_Temperature * C_T_Temperature * u_T_Temperature)^2+ (rho_T_Temperature * C_T_Temperature * v_T_Temperature)^2+eps)
res_T_Temperature	Equation residual for T	W/m^2	r * (-krr_T_Temperature * Trr-krz_T_Temperature * Trz-kzr_T_Temperature * Tzr-kzz_T_Temperature * Tzz+Tr * rho_T_Temperature * C_T_Temperature * u_T_Temperature+Tz * rho_T_Temperature * C_T_Temperature * v_T_Temperature-Q_T_Temperature)
da_T_Temperature	Total time scale factor, T	kg/(s^2*K)	r * Dts_T_Temperature * rho_T_Temperature * C_T_Temperature

Appendix E

COMSOL Multiphysics Settings for Composite Transformer Oil-Solid Cylindrical Tube Model

---

THE FOLLOWING is a COMSOL Multiphysics auto-generated report that corresponds to the finite element simulation results that were presented in Section 7.2 for the composite transformer oil-solid cylindrical tube model. The report provides detailed information about model properties, mesh settings, domain and boundary conditions, solver settings, solver variables, constants, etc.

Parallel oriented interface, aromatic molecules, field ionization, Vapp=130kV

1. Model Properties

Property	Value
Model name	Parallel oriented interface, aromatic molecules, field ionization, Vapp=130kV
Author	George Hwang
Company	MIT
Department	EECS
Reference	
URL	
Saved date	May 17, 2010 9:06:22 PM
Creation date	Aug 31, 2009 3:37:41 PM
COMSOL version	COMSOL 3.5.0.603

File name: C:\Documents and Settings\george\Desktop\Parallel-Orientation_Vapp-130kV_epsSolid-2.2.mph

Application modes and modules used in this model:

- Geom1 (Axial symmetry (2D))
  - Electrostatics (AC/DC Module)
  - Convection and Diffusion
  - Convection and Diffusion
  - Convection and Diffusion
  - Weak Form, Boundary

2. Constants

Name	Expression	Value	Description
BASES	0123456789		
Vb	3e5[V]		Base voltage [V]
Lb	25e-3[m]		Base Length [m]
mub	1e-9[m^2/V/s]		Base mobility [m^2/V-s]
epsb	epsr*eps0		Base permitivitty [F/m]
eps0	8.854e-12[F/m]		Permittivity of free space [F]m
epsr	2.2		Relative permittivity of transformer oil
Eb	Vb/Lb		Base electric field [V/m]
qNb	epsb*Vb/Lb^2		Base charge density [C/m^3]
Gb	epsb*mub*Vb^2/Lb^4		Base charge generation rate [C/m^3-s]
Db	mub*Vb		Base diffusion [m^2/s]
KRb	q*mub/epsb		Base recombination rate [m^3/s]
tb	Lb^2/(mub*Vb)		Base time [s]
Afb	(epsb*mub*Vb)/Lb^3		Base field ionization pre-exponential coefficient [F/m^2-s]
CONSTANTS	0123456789		
pi	3.14159265		PI

q	1.6022e-19[C]		Magnitude electronic charge [C]
me	9.109e-31[kg]		Free elctron mass [kg]
hp	6.626e-34[J*s]		Planck's constant [m^2 kg/s]
CAPTURING_MECHANISMS	0123456789		
KR	1.65e-17[m^3/s]		Recombination coefficient ion-ion and ion-electron [m^3/s]
KRnd	KR/KRb		
GENERATION_SOURCES	0123456789		
MM2_VALUES	0123456789		
n2	1e23[1/m^3]		2MM density of ionizable species [m^-3]
a2	2e-10[m]		2MM molecular separation distance [m]
ie2	q*7.5[V]		2MM ionization energy [J]
m2	0.1*me		2MM effective electron mass [kg]
Af2	q^2*n2*a2/hp		2MM pre-exponential coefficient term [F/m^2-s]
Af2nd	Af2/Afb		
Bf2	pi^2*m2*a2*ie2^2/(q*hp^2)		2MM exponential term [V/m]
Bf2nd	Bf2/Eb		
MM3_VALUES	0123456789		
n3	1e25[1/m^3]		3MM density of ionizable species [m^-3]
a3	3e-10[m]		3MM molecular separation distance [m]
ie3	q*9.86[V]		3MM ionization energy [J]
m3	0.1*me		3MM effective electron mass [kg]
Af3	q^2*n3*a3/hp		3MM pre-exponential coefficient term [F/m^2-s]
Af3nd	Af3/Afb		
Bf3	pi^2*m3*a3*ie3^2/(q*hp^2)		3MM exponential term [V/m]
Bf3nd	Bf3/Eb		
SYSTEM_VALUES	0123456789		
Va	1.3e5[V]		Applied voltage [V]
Vand	Va/Vb		
mui	1e-9[m^2/V/s]		Ion mobility [m^2/V-s]
muind	mui/mub		
mue	1e-4[m^2/V/s]		Electron mobility [m^2/V-s]
muend	mue/mub		
tnsnd	1e-9[s]/tb		Non-dimensionalized nano-second time
tea	200e-9[s]		Electron attachment time constant [s]
teand	tea/tb		
epsrpb	2.2		Solid insulator's relative permittivity
epspbnd	epsrpb*eps0/epsb		
gamma	0		Oil-solid interface secondary electron emission percentage

3. Geom1

Space dimensions: Axial symmetry (2D)

Independent variables: r, phi, z

3.1. Expressions

3.1.1. Boundary Expressions

Boundary		5-6, 12, 24, 27	10, 14, 23, 26
En_pb	V/m	nr_Pos_Ion*up(Er_Voltage)+nz_Pos_Ion*up (Ez_Voltage)	nr_Pos_Ion*down(Er_Voltage)+nz_Pos_Ion*down (Ez_Voltage)
nD0	V/m	nr_Pos_Ion*(epspbnd*down(-Vr)-up(-Vr)) +nz_Pos_Ion*(epspbnd*down(-Vz)-up(-Vz))	nr_Pos_Ion*(epspbnd*up(-Vr)-down(-Vr)) +nz_Pos_Ion*(epspbnd*up(-Vz)-down(-Vz))
nDt0	m*kg/ (s^4*A)	nr_Pos_Ion*(epspbnd*down(-Vrt)-up(-Vrt)) +nz_Pos_Ion*(epspbnd*down(-Vzt)-up(-Vzt))	nr_Pos_Ion*(epspbnd*up(-Vrt)-down(-Vrt)) +nz_Pos_Ion*(epspbnd*up(-Vzt)-down(-Vzt))
drhosdt_qp		qs_test*(En_pb>0)*ncflux_qp_Pos_Ion	qs_test*(En_pb>0)*ncflux_qp_Pos_Ion
drhosdt_qe		qs_test*(En_pb<0)*ncflux_qe_Electron	qs_test*(En_pb<0)*ncflux_qe_Electron

Parallel oriented interface, aromatic molecules, field ionization, Vapp=130kV

3.1.2. Subdomain Expressions

Subdomain		1-2
GF2		Af2nd*normE_Voltage*exp(-Bf2nd/normE_Voltage)
GF3		Af3nd*normE_Voltage*exp(-Bf3nd/normE_Voltage)
Rpe	mol^2/m^6	KRnd*abs(qp*qe)
Rpn	mol^2/m^6	KRnd*abs(qp*qn)
EA	mol/m^3	abs(qe)/teand

3.2. Mesh

3.2.1. Mesh Statistics

Number of degrees of freedom	1089858
Number of mesh points	83482
Number of elements	166111
Triangular	166111
Quadrilateral	0
Number of boundary elements	3931
Number of vertex elements	25
Minimum element quality	0.353
Element area ratio	0

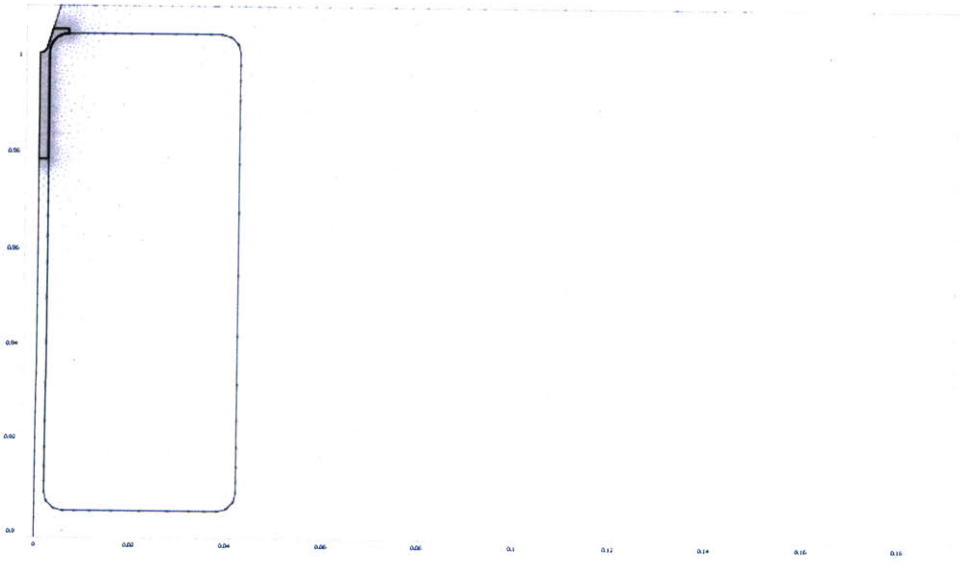

3.3. Application Mode: Electrostatics (Voltage)

Application mode type: Electrostatics (AC/DC Module)

Application mode name: Voltage

3.3.1. Scalar Variables

Name	Variable	Value	Unit	Description
epsilon0	epsilon0_Voltage	8.854187817e-12	F/m	Permittivity of vacuum

3.3.2. Application Mode Properties

Property	Value
Default element type	Lagrange - Quadratic
Input property	Forced voltage
Frame	Frame (ref)
Weak constraints	Off
Constraint type	Ideal

3.3.3. Variables

Dependent variables: V

Shape functions: shlag(2,'V')

Interior boundaries active

3.3.4. Boundary Settings

Boundary		1-2	3, 7-8, 11	4, 9, 13, 16, 22, 25
Type		Axial symmetry	Continuity	Electric potential
name		**SymAxis**		**Potential**
Surface charge density (rhos)	C/m^2	0	0	0
Electric potential (V0)	V	0	0	**Vand**

Boundary		5-6, 10, 12, 14, 23-24, 26-27	15, 18, 21, 28	17, 19-20
Type		Surface charge	Ground	Zero charge/Symmetry
name		**Interface**	**Ground**	**Insulation**
Surface charge density (rhos)	C/m^2	**qs**	0	0
Electric potential (V0)	V	0	0	0

3.3.5. Subdomain Settings

Subdomain		1-2	3
Relative permittivity (epsilonr)	1	**{1/epsilon0_Voltage,0;0,1/epsilon0_Voltage}**	**{epspbnd/epsilon0_Voltage,0;0,epspbnd/epsilon0_Voltage}**
Space charge density (rho)	C/m^3	**qp+qe+qn**	0

Subdomain initial value		1-2	3
Electric potential (V)	V	1e-2*(r-z)	1e-2*(r-z)

3.4. Application Mode: Convection and Diffusion (Pos_Ion)

Application mode type: Convection and Diffusion

Application mode name: Pos_Ion

3.4.1. Application Mode Properties

Property	Value

Parallel oriented interface, aromatic molecules, field ionization, Vapp=130kV

Default element type	Lagrange - Quadratic
Analysis type	Transient
Equation form	Conservative
Frame	Frame (ref)
Weak constraints	Off
Constraint type	Ideal

3.4.2. Variables

Dependent variables: qp

Shape functions: shlag(2,'qp')

Interior boundaries not active

3.4.3. Boundary Settings

Boundary		1-2	4, 9, 13, 15-16, 18, 21-22, 25, 28	5-6, 10, 12, 14, 23-24, 26-27
Type		Axial symmetry	Convective flux	Flux
name		**SymAxis**	**Electrode**	**Interface**
Inward flux (N)	$mol/(m^2 \cdot s)$	0	0	**(En_pb>0)*(-ncflux_qp_Pos_Ion)**

Boundary		17, 19-20
Type		Insulation/Symmetry
name		**Insulation**
Inward flux (N)	$mol/(m^2 \cdot s)$	0

3.4.4. Subdomain Settings

Subdomain		1-2
Diffusion coefficient (D)	m^2/s	**0**
Reaction rate (R)	$mol/(m^3 \cdot s)$	**GF2-Rpn-Rpe**
r-velocity (u)	m/s	**muind*Er_Voltage**
z-velocity (v)	m/s	**muind*Ez_Voltage**
Isotropic diffusion switch (idon)		**1**
Tuning parameter (delid)		**0.1**
Streamline diffusion switch (sdon)		**1**
Streamline diffusion type (sdtype)		**Anisotropic diffusion**

3.5. Application Mode: Convection and Diffusion (Electron)

Application mode type: Convection and Diffusion

Application mode name: Electron

3.5.1. Application Mode Properties

Property	Value
Default element type	Lagrange - Quadratic
Analysis type	Transient
Equation form	Conservative
Frame	Frame (ref)
Weak constraints	Off
Constraint type	Ideal

3.5.2. Variables

Dependent variables: qe

Shape functions: shlag(2,'qe')

Interior boundaries not active

3.5.3. Boundary Settings

Boundary		1-2	4, 9, 13, 15-16, 18, 21-22, 25, 28	5-6, 10, 12, 14, 23-24, 26-27
Type		Axial symmetry	Convective flux	Flux
name		**SymAxis**	**Electrode**	**Interface**
Inward flux (N)	mol/ ($m^2 \cdot s$)	0	0	**(En_pb<0)*(-ncflux_qe_Electron)+(En_pb>0)*(-gamma*ncflux_qp_Pos_Ion)**

Boundary		17, 19-20
Type		Insulation/Symmetry
name		**Insulation**
Inward flux (N)	mol/($m^2 \cdot s$)	0

3.5.4. Subdomain Settings

Subdomain		1-2
Diffusion coefficient (D)	m^2/s	**0**
Reaction rate (R)	mol/($m^3 \cdot s$)	**-GF2+Rpe+EA**
r-velocity (u)	m/s	**-muend*Er_Voltage**
z-velocity (v)	m/s	**-muend*Ez_Voltage**
Isotropic diffusion switch (idon)		**1**
Tuning parameter (delid)		**0.1**
Streamline diffusion switch (sdon)		**1**
Streamline diffusion type (sdtype)		**Anisotropic diffusion**

3.6. Application Mode: Convection and Diffusion (Neg_Ion)

Application mode type: Convection and Diffusion

Application mode name: Neg_Ion

3.6.1. Application Mode Properties

Property	**Value**
Default element type	Lagrange - Quadratic
Analysis type	Transient
Equation form	Conservative
Frame	Frame (ref)
Weak constraints	Off
Constraint type	Ideal

3.6.2. Variables

Dependent variables: qn

Shape functions: shlag(2,'qn')

Interior boundaries not active

3.6.3. Boundary Settings

Boundary		1-2	4, 9, 13, 15-16, 18, 21-22, 25, 28	5-6, 10, 12, 14, 23-24, 26-27
Type		Axial symmetry	Convective flux	Flux

name		SymAxis	Electrode	Interface
Inward flux (N)	$mol/(m^2 \cdot s)$	0	0	**(En_pb<0)*(-ncflux_qn_Neg_Ion)**

Boundary		17, 19-20
Type		Insulation/Symmetry
name		**Insulation**
Inward flux (N)	$mol/(m^2 \cdot s)$	0

3.6.4. Subdomain Settings

Subdomain		1-2
Diffusion coefficient (D)	m^2/s	**0**
Reaction rate (R)	$mol/(m^3 \cdot s)$	**-EA+Rpn**
r-velocity (u)	m/s	**-muind*Er_Voltage**
z-velocity (v)	m/s	**-muind*Ez_Voltage**
Isotropic diffusion switch (idon)		**1**
Tuning parameter (delid)		**0.1**
Streamline diffusion switch (sdon)		**1**
Streamline diffusion type (sdtype)		**Anisotropic diffusion**

3.7. Application Mode: Weak Form, Boundary (RhoS)

Application mode type: Weak Form, Boundary

Application mode name: RhoS

3.7.1. Application Mode Properties

Property	Value
Default element type	Lagrange - Quadratic
Wave extension	Off
Frame	Frame (ref)
Weak constraints	Off

3.7.2. Variables

Dependent variables: qs, qs_t

Shape functions: shlag(2,'qs')

Interior boundaries not active

3.7.3. Boundary Settings

Boundary	5-6, 10, 12, 14, 23-24, 26-27
Weak term (weak)	**qs_test*((En_pb>0)*(1+gamma)*ncflux_qp_Pos_Ion+(En_pb<0)* (ncflux_qe_Electron+ncflux_qn_Neg_Ion))**
Time-dependent weak term (dweak)	**qs_test*qs_time**

4. Solver Settings

Solve using a script: off

Auto select solver	On
Solver	Time dependent
Solution form	Automatic
Symmetric	auto

Adaptive mesh refinement	Off
Optimization/Sensitivity	Off
Plot while solving	Off

4.1. Direct (PARDISO)

Solver type: Linear system solver

Parameter	Value
Preordering algorithm	Nested dissection
Row preordering	On
Bunch-Kaufmann	Off
Pivoting perturbation	1.0E-8
Relative tolerance	1.0E-6
Factor in error estimate	400.0
Check tolerances	On

4.2. Time Stepping

Parameter	Value
Times	range(0,2.4e-9,4.8e-8)
Relative tolerance	0.01
Absolute tolerance	0.0010
Times to store in output	Specified times
Time steps taken by solver	Strict
Initial time step	1e-15
Maximum BDF order	5
Singular mass matrix	Maybe
Consistent initialization of DAE systems	Backward Euler
Error estimation strategy	Include algebraic
Allow complex numbers	Off

4.3. Advanced

Parameter	Value
Constraint handling method	Elimination
Null-space function	Automatic
Automatic assembly block size	On
Assembly block size	1000
Use Hermitian transpose of constraint matrix and in symmetry detection	Off
Use complex functions with real input	Off
Stop if error due to undefined operation	On
Store solution on file	Off
Type of scaling	Automatic
Manual scaling	
Row equilibration	On
Manual control of reassembly	Off
Load constant	On
Constraint constant	On
Mass constant	On
Damping (mass) constant	On
Jacobian constant	On
Constraint Jacobian constant	On

5. Variables

5.1. Boundary

5.1.1. Boundary 1-6, 8-28

Name	Description	Unit	Expression
unTEr_Voltage	Maxwell surface stress tensor (r)	Pa	-0.5 * (up(Dr_Voltage) * up(Er_Voltage)+up(Dz_Voltage) * up (Ez_Voltage)) * dnr+(dnr * up(Dr_Voltage)+dnz * up(Dz_Voltage)) * up (Er_Voltage)
unTEz_Voltage	Maxwell surface stress tensor (z)	Pa	-0.5 * (up(Dr_Voltage) * up(Er_Voltage)+up(Dz_Voltage) * up (Ez_Voltage)) * dnz+(dnr * up(Dr_Voltage)+dnz * up(Dz_Voltage)) * up (Ez_Voltage)
dnTEr_Voltage	Maxwell surface stress tensor (r)	Pa	-0.5 * (down(Dr_Voltage) * down(Er_Voltage)+down(Dz_Voltage) * down (Ez_Voltage)) * unr+(unr * down(Dr_Voltage)+unz * down(Dz_Voltage)) * down(Er_Voltage)
dnTEz_Voltage	Maxwell surface stress tensor (z)	Pa	-0.5 * (down(Dr_Voltage) * down(Er_Voltage)+down(Dz_Voltage) * down (Ez_Voltage)) * unz+(unr * down(Dr_Voltage)+unz * down(Dz_Voltage)) * down(Ez_Voltage)
unTr_Voltage	Exterior Maxwell stress tensor (u), r component	Pa	unTEr_Voltage+unTMr_Voltage
unTMr_Voltage	Exterior magnetic Maxwell stress tensor (u), r component	Pa	0
unTz_Voltage	Exterior Maxwell stress tensor (u), z component	Pa	unTEz_Voltage+unTMz_Voltage
unTMz_Voltage	Exterior magnetic Maxwell stress tensor (u), z component	Pa	0
dnTr_Voltage	Exterior Maxwell stress tensor (d), r component	Pa	dnTEr_Voltage+dnTMr_Voltage
dnTMr_Voltage	Exterior magnetic Maxwell stress tensor (d), r component	Pa	0
dnTz_Voltage	Exterior Maxwell stress tensor (d), z component	Pa	dnTEz_Voltage+dnTMz_Voltage
dnTMz_Voltage	Exterior magnetic Maxwell stress tensor (d), z component	Pa	0
dVolbnd_Voltage	Volume integration contribution	m	Sr_Voltage
nD_Voltage	Surface charge density	C/m^2	unr * (down(Dr_Voltage)-up(Dr_Voltage))+unz * (down(Dz_Voltage)-up (Dz_Voltage))
ndflux_qp_Pos_Ion	Normal diffusive flux, qp	mol/ (m^2*s)	nr_Pos_Ion * dflux_qp_r_Pos_Ion+nz_Pos_Ion * dflux_qp_z_Pos_Ion
ncflux_qp_Pos_Ion	Normal convective flux, qp	mol/ (m^2*s)	nr_Pos_Ion * cflux_qp_r_Pos_Ion+nz_Pos_Ion * cflux_qp_z_Pos_Ion
ntflux_qp_Pos_Ion	Normal total flux, qp	mol/ (m^2*s)	nr_Pos_Ion * tflux_qp_r_Pos_Ion+nz_Pos_Ion * tflux_qp_z_Pos_Ion
ndflux_qe_Electron	Normal diffusive flux, qe	mol/ (m^2*s)	nr_Electron * dflux_qe_r_Electron+nz_Electron * dflux_qe_z_Electron
ncflux_qe_Electron	Normal convective flux, qe	mol/ (m^2*s)	nr_Electron * cflux_qe_r_Electron+nz_Electron * cflux_qe_z_Electron
ntflux_qe_Electron	Normal total flux, qe	mol/ (m^2*s)	nr_Electron * tflux_qe_r_Electron+nz_Electron * tflux_qe_z_Electron
ndflux_qn_Neg_Ion	Normal diffusive flux, qn	mol/ (m^2*s)	nr_Neg_Ion * dflux_qn_r_Neg_Ion+nz_Neg_Ion * dflux_qn_z_Neg_Ion
ncflux_qn_Neg_Ion	Normal convective flux, qn	mol/ (m^2*s)	nr_Neg_Ion * cflux_qn_r_Neg_Ion+nz_Neg_Ion * cflux_qn_z_Neg_Ion
ntflux_qn_Neg_Ion	Normal total flux, qn	mol/ (m^2*s)	nr_Neg_Ion * tflux_qn_r_Neg_Ion+nz_Neg_Ion * tflux_qn_z_Neg_Ion

5.1.2. Boundary 7

Name	Description	Unit	Expression
unTEr_Voltage	Maxwell surface stress tensor (r)	Pa	
unTEz_Voltage	Maxwell surface stress tensor (z)	Pa	
dnTEr_Voltage	Maxwell surface stress tensor (r)	Pa	
dnTEz_Voltage	Maxwell surface stress tensor (z)	Pa	
unTr_Voltage	Exterior Maxwell stress tensor (u), r component	Pa	
unTMr_Voltage	Exterior magnetic Maxwell stress tensor (u), r component	Pa	
unTz_Voltage	Exterior Maxwell stress tensor (u), z component	Pa	
unTMz_Voltage	Exterior magnetic Maxwell stress tensor (u), z component	Pa	
dnTr_Voltage	Exterior Maxwell stress tensor (d), r component	Pa	
dnTMr_Voltage	Exterior magnetic Maxwell stress tensor (d), r component	Pa	
dnTz_Voltage	Exterior Maxwell stress tensor (d), z component	Pa	
dnTMz_Voltage	Exterior magnetic Maxwell stress tensor (d), z component	Pa	
dVolbnd_Voltage	Volume integration contribution	m	
nD_Voltage	Surface charge density	C/m^2	
ndflux_qp_Pos_Ion	Normal diffusive flux, qp	mol/(m^2*s)	
ncflux_qp_Pos_Ion	Normal convective flux, qp	mol/(m^2*s)	
ntflux_qp_Pos_Ion	Normal total flux, qp	mol/(m^2*s)	
ndflux_qe_Electron	Normal diffusive flux, qe	mol/(m^2*s)	
ncflux_qe_Electron	Normal convective flux, qe	mol/(m^2*s)	
ntflux_qe_Electron	Normal total flux, qe	mol/(m^2*s)	
ndflux_qn_Neg_Ion	Normal diffusive flux, qn	mol/(m^2*s)	
ncflux_qn_Neg_Ion	Normal convective flux, qn	mol/(m^2*s)	
ntflux_qn_Neg_Ion	Normal total flux, qn	mol/(m^2*s)	

5.2. Subdomain

5.2.1. Subdomain 1-2

Name	Description	Unit	Expression
Sr_Voltage	Infinite element r coordinate	m	r
S0r_guess_Voltage	Inner r coordinate default guess	m	0
Sdr_guess_Voltage	Width in r direction default guess	m	0
Sz_Voltage	Infinite element z coordinate	m	z
S0z_guess_Voltage	Inner z coordinate default guess	m	0
Sdz_guess_Voltage	Width in z direction default guess	m	0
dVol_Voltage	Volume integration contribution	m	Sr_Voltage * detJ_Voltage
Dr_Voltage	Electric displacement, r component	C/m^2	epsilonrr_Voltage * Er_Voltage+epsilonrz_Voltage * Ez_Voltage
Dz_Voltage	Electric displacement, z component	C/m^2	epsilonzr_Voltage * Er_Voltage+epsilonzz_Voltage * Ez_Voltage
epsilon_Voltage	Permittivity	F/m	epsilon0_Voltage * epsilonr_Voltage
epsilonrr_Voltage	Permittivity, rr component	F/m	epsilon0_Voltage * epsilonrrr_Voltage
epsilonrz_Voltage	Permittivity, rz component	F/m	epsilon0_Voltage * epsilonrrz_Voltage

epsilonzr_Voltage	Permittivity, zr component	F/m	epsilon0_Voltage * epsilonrzr_Voltage
epsilonzz_Voltage	Permittivity, zz component	F/m	epsilon0_Voltage * epsilonrzz_Voltage
normE_Voltage	Electric field, norm	V/m	sqrt(abs(Er_Voltage)^2+abs(Ez_Voltage)^2)
normD_Voltage	Electric displacement, norm	C/m^2	sqrt(abs(Dr_Voltage)^2+abs(Dz_Voltage)^2)
normDr_Voltage	Remanent displacement, norm	C/m^2	sqrt(abs(Drr_Voltage)^2+abs(Drz_Voltage)^2)
normP_Voltage	Electric polarization, norm	C/m^2	sqrt(abs(Pr_Voltage)^2+abs(Pz_Voltage)^2)
We_Voltage	Electric energy density	J/m^3	0.5 * ((Dr_Voltage+Drr_Voltage) * Er_Voltage+(Dz_Voltage+Drz_Voltage) * Ez_Voltage)
dW_Voltage	Integrand for total energy	N/m	2 * pi * dVol_Voltage * We_Voltage
Er_Voltage	Electric field, r component	V/m	-Vr
Ez_Voltage	Electric field, z component	V/m	-Vz
grad_qp_r_Pos_Ion	Concentration gradient, qp, r component	mol/m^4	qpr
dflux_qp_r_Pos_Ion	Diffusive flux, qp, r component	mol/(m^2*s)	-Drr_qp_Pos_Ion * qpr-Drz_qp_Pos_Ion * qpz
cflux_qp_r_Pos_Ion	Convective flux, qp, r component	mol/(m^2*s)	qp * u_qp_Pos_Ion
tflux_qp_r_Pos_Ion	Total flux, qp, r component	mol/(m^2*s)	dflux_qp_r_Pos_Ion+cflux_qp_r_Pos_Ion
grad_qp_z_Pos_Ion	Concentration gradient, qp, z component	mol/m^4	qpz
dflux_qp_z_Pos_Ion	Diffusive flux, qp, z component	mol/(m^2*s)	-Dzr_qp_Pos_Ion * qpr-Dzz_qp_Pos_Ion * qpz
cflux_qp_z_Pos_Ion	Convective flux, qp, z component	mol/(m^2*s)	qp * v_qp_Pos_Ion
tflux_qp_z_Pos_Ion	Total flux, qp, z component	mol/(m^2*s)	dflux_qp_z_Pos_Ion+cflux_qp_z_Pos_Ion
beta_qp_r_Pos_Ion	Convective field, qp, r component	m^2/s	r * u_qp_Pos_Ion
beta_qp_z_Pos_Ion	Convective field, qp, z component	m^2/s	r * v_qp_Pos_Ion
grad_qp_Pos_Ion	Concentration gradient, qp	mol/m^4	sqrt(grad_qp_r_Pos_Ion^2+grad_qp_z_Pos_Ion^2)
dflux_qp_Pos_Ion	Diffusive flux, qp	mol/(m^2*s)	sqrt(dflux_qp_r_Pos_Ion^2+dflux_qp_z_Pos_Ion^2)
cflux_qp_Pos_Ion	Convective flux, qp	mol/(m^2*s)	sqrt(cflux_qp_r_Pos_Ion^2+cflux_qp_z_Pos_Ion^2)
tflux_qp_Pos_Ion	Total flux, qp	mol/(m^2*s)	sqrt(tflux_qp_r_Pos_Ion^2+tflux_qp_z_Pos_Ion^2)
cellPe_qp_Pos_Ion	Cell Peclet number, qp	1	h * sqrt(beta_qp_r_Pos_Ion^2+beta_qp_z_Pos_Ion^2)/Dm_qp_Pos_Ion
Dm_qp_Pos_Ion	Mean diffusion coefficient, qp	m^3/s	r * (Drr_qp_Pos_Ion * u_qp_Pos_Ion^2+Drz_qp_Pos_Ion * u_qp_Pos_Ion * v_qp_Pos_Ion+Dzr_qp_Pos_Ion * v_qp_Pos_Ion * u_qp_Pos_Ion+Dzz_qp_Pos_Ion * v_qp_Pos_Ion^2)/(u_qp_Pos_Ion^2+v_qp_Pos_Ion^2+eps)
res_qp_Pos_Ion	Equation residual for qp	mol/(m^2*s)	r * (-Drr_qp_Pos_Ion * qprr-Drz_qp_Pos_Ion * qprz+qpr * u_qp_Pos_Ion-Dzr_qp_Pos_Ion * qpzr-Dzz_qp_Pos_Ion * qpzz+qpz * v_qp_Pos_Ion-R_qp_Pos_Ion)
res_sc_qp_Pos_Ion	Shock capturing	mol/	r * (qpr * u_qp_Pos_Ion+qpz * v_qp_Pos_Ion-R_qp_Pos_Ion)

	residual for qp	(m^2*s)	
da_qp_Pos_Ion	Total time scale factor, qp	m	r * Dts_qp_Pos_Ion
grad_qe_r_Electron	Concentration gradient, qe, r component	mol/m^4	qer
dflux_qe_r_Electron	Diffusive flux, qe, r component	mol/ (m^2*s)	-Drr_qe_Electron * qer-Drz_qe_Electron * qez
cflux_qe_r_Electron	Convective flux, qe, r component	mol/ (m^2*s)	qe * u_qe_Electron
tflux_qe_r_Electron	Total flux, qe, r component	mol/ (m^2*s)	dflux_qe_r_Electron+cflux_qe_r_Electron
grad_qe_z_Electron	Concentration gradient, qe, z component	mol/m^4	qez
dflux_qe_z_Electron	Diffusive flux, qe, z component	mol/ (m^2*s)	-Dzr_qe_Electron * qer-Dzz_qe_Electron * qez
cflux_qe_z_Electron	Convective flux, qe, z component	mol/ (m^2*s)	qe * v_qe_Electron
tflux_qe_z_Electron	Total flux, qe, z component	mol/ (m^2*s)	dflux_qe_z_Electron+cflux_qe_z_Electron
beta_qe_r_Electron	Convective field, qe, r component	m^2/s	r * u_qe_Electron
beta_qe_z_Electron	Convective field, qe, z component	m^2/s	r * v_qe_Electron
grad_qe_Electron	Concentration gradient, qe	mol/m^4	sqrt(grad_qe_r_Electron^2+grad_qe_z_Electron^2)
dflux_qe_Electron	Diffusive flux, qe	mol/ (m^2*s)	sqrt(dflux_qe_r_Electron^2+dflux_qe_z_Electron^2)
cflux_qe_Electron	Convective flux, qe	mol/ (m^2*s)	sqrt(cflux_qe_r_Electron^2+cflux_qe_z_Electron^2)
tflux_qe_Electron	Total flux, qe	mol/ (m^2*s)	sqrt(tflux_qe_r_Electron^2+tflux_qe_z_Electron^2)
cellPe_qe_Electron	Cell Peclet number, qe	1	h * sqrt(beta_qe_r_Electron^2+beta_qe_z_Electron^2)/Dm_qe_Electron
Dm_qe_Electron	Mean diffusion coefficient, qe	m^3/s	r * (Drr_qe_Electron * u_qe_Electron^2+Drz_qe_Electron * u_qe_Electron * v_qe_Electron+Dzr_qe_Electron * v_qe_Electron * u_qe_Electron+Dzz_qe_Electron * v_qe_Electron^2)/ (u_qe_Electron^2+v_qe_Electron^2+eps)
res_qe_Electron	Equation residual for qe	mol/ (m^2*s)	r * (-Drr_qe_Electron * qerr-Drz_qe_Electron * qerz+qer * u_qe_Electron-Dzr_qe_Electron * qezr-Dzz_qe_Electron * qezz+qez * v_qe_Electron-R_qe_Electron)
res_sc_qe_Electron	Shock capturing residual for qe	mol/ (m^2*s)	r * (qer * u_qe_Electron+qez * v_qe_Electron-R_qe_Electron)
da_qe_Electron	Total time scale factor, qe	m	r * Dts_qe_Electron
grad_qn_r_Neg_Ion	Concentration gradient, qn, r component	mol/m^4	qnr
dflux_qn_r_Neg_Ion	Diffusive flux, qn, r component	mol/ (m^2*s)	-Drr_qn_Neg_Ion * qnr-Drz_qn_Neg_Ion * qnz
cflux_qn_r_Neg_Ion	Convective flux, qn, r component	mol/ (m^2*s)	qn * u_qn_Neg_Ion
tflux_qn_r_Neg_Ion	Total flux, qn, r component	mol/ (m^2*s)	dflux_qn_r_Neg_Ion+cflux_qn_r_Neg_Ion
grad_qn_z_Neg_Ion	Concentration gradient, qn, z component	mol/m^4	qnz
dflux_qn_z_Neg_Ion	Diffusive flux, qn, z component	mol/ (m^2*s)	-Dzr_qn_Neg_Ion * qnr-Dzz_qn_Neg_Ion * qnz
cflux_qn_z_Neg_Ion	Convective flux, qn, z component	mol/ (m^2*s)	qn * v_qn_Neg_Ion
tflux_qn_z_Neg_Ion	Total flux, qn, z	mol/	dflux_qn_z_Neg_Ion+cflux_qn_z_Neg_Ion

	component	(m^2*s)	
beta_qn_r_Neg_Ion	Convective field, qn, r component	m^2/s	r * u_qn_Neg_Ion
beta_qn_z_Neg_Ion	Convective field, qn, z component	m^2/s	r * v_qn_Neg_Ion
grad_qn_Neg_Ion	Concentration gradient, qn	mol/m^4	sqrt(grad_qn_r_Neg_Ion^2+grad_qn_z_Neg_Ion^2)
dflux_qn_Neg_Ion	Diffusive flux, qn	mol/ (m^2*s)	sqrt(dflux_qn_r_Neg_Ion^2+dflux_qn_z_Neg_Ion^2)
cflux_qn_Neg_Ion	Convective flux, qn	mol/ (m^2*s)	sqrt(cflux_qn_r_Neg_Ion^2+cflux_qn_z_Neg_Ion^2)
tflux_qn_Neg_Ion	Total flux, qn	mol/ (m^2*s)	sqrt(tflux_qn_r_Neg_Ion^2+tflux_qn_z_Neg_Ion^2)
cellPe_qn_Neg_Ion	Cell Peclet number, qn	1	h * sqrt(beta_qn_r_Neg_Ion^2+beta_qn_z_Neg_Ion^2)/Dm_qn_Neg_Ion
Dm_qn_Neg_Ion	Mean diffusion coefficient, qn	m^3/s	r * (Drr_qn_Neg_Ion * u_qn_Neg_Ion^2+Drz_qn_Neg_Ion * u_qn_Neg_Ion * v_qn_Neg_Ion+Dzr_qn_Neg_Ion * v_qn_Neg_Ion * u_qn_Neg_Ion+Dzz_qn_Neg_Ion * v_qn_Neg_Ion^2)/ (u_qn_Neg_Ion^2+v_qn_Neg_Ion^2+eps)
res_qn_Neg_Ion	Equation residual for qn	mol/ (m^2*s)	r * (-Drr_qn_Neg_Ion * qnrr-Drz_qn_Neg_Ion * qnrz+qnr * u_qn_Neg_Ion-Dzr_qn_Neg_Ion * qnzr-Dzz_qn_Neg_Ion * qnzz+qnz * v_qn_Neg_Ion-R_qn_Neg_Ion)
res_sc_qn_Neg_Ion	Shock capturing residual for qn	mol/ (m^2*s)	r * (qnr * u_qn_Neg_Ion+qnz * v_qn_Neg_Ion-R_qn_Neg_Ion)
da_qn_Neg_Ion	Total time scale factor, qn	m	r * Dts_qn_Neg_Ion

5.2.2. Subdomain 3

Name	Description	Unit	Expression
Sr_Voltage	Infinite element r coordinate	m	r
S0r_guess_Voltage	Inner r coordinate default guess	m	0
Sdr_guess_Voltage	Width in r direction default guess	m	0
Sz_Voltage	Infinite element z coordinate	m	z
S0z_guess_Voltage	Inner z coordinate default guess	m	0
Sdz_guess_Voltage	Width in z direction default guess	m	0
dVol_Voltage	Volume integration contribution	m	Sr_Voltage * detJ_Voltage
Dr_Voltage	Electric displacement, r component	C/m^2	epsilonrr_Voltage * Er_Voltage+epsilonrz_Voltage * Ez_Voltage
Dz_Voltage	Electric displacement, z component	C/m^2	epsilonzr_Voltage * Er_Voltage+epsilonzz_Voltage * Ez_Voltage
epsilon_Voltage	Permittivity	F/m	epsilon0_Voltage * epsilonr_Voltage
epsilonrr_Voltage	Permittivity, rr component	F/m	epsilon0_Voltage * epsilonrrr_Voltage
epsilonrz_Voltage	Permittivity, rz component	F/m	epsilon0_Voltage * epsilonrrz_Voltage
epsilonzr_Voltage	Permittivity, zr component	F/m	epsilon0_Voltage * epsilonrzr_Voltage
epsilonzz_Voltage	Permittivity, zz component	F/m	epsilon0_Voltage * epsilonrzz_Voltage
normE_Voltage	Electric field, norm	V/m	sqrt(abs(Er_Voltage)^2+abs(Ez_Voltage)^2)
normD_Voltage	Electric displacement, norm	C/m^2	sqrt(abs(Dr_Voltage)^2+abs(Dz_Voltage)^2)
normDr_Voltage	Remanent displacement, norm	C/m^2	sqrt(abs(Drr_Voltage)^2+abs(Drz_Voltage)^2)
normP_Voltage	Electric polarization, norm	C/m^2	sqrt(abs(Pr_Voltage)^2+abs(Pz_Voltage)^2)
We_Voltage	Electric energy density	J/m^3	0.5 * ((Dr_Voltage+Drr_Voltage) * Er_Voltage+ (Dz_Voltage+Drz_Voltage) * Ez_Voltage)
dW_Voltage	Integrand for total energy	N/m	2 * pi * dVol_Voltage * We_Voltage
Er_Voltage	Electric field, r component	V/m	-Vr
Ez_Voltage	Electric field, z component	V/m	-Vz

grad_qp_r_Pos_Ion	Concentration gradient, qp, r component	mol/m^4	
dflux_qp_r_Pos_Ion	Diffusive flux, qp, r component	mol/(m^2*s)	
cflux_qp_r_Pos_Ion	Convective flux, qp, r component	mol/(m^2*s)	
tflux_qp_r_Pos_Ion	Total flux, qp, r component	mol/(m^2*s)	
grad_qp_z_Pos_Ion	Concentration gradient, qp, z component	mol/m^4	
dflux_qp_z_Pos_Ion	Diffusive flux, qp, z component	mol/(m^2*s)	
cflux_qp_z_Pos_Ion	Convective flux, qp, z component	mol/(m^2*s)	
tflux_qp_z_Pos_Ion	Total flux, qp, z component	mol/(m^2*s)	
beta_qp_r_Pos_Ion	Convective field, qp, r component	m^2/s	
beta_qp_z_Pos_Ion	Convective field, qp, z component	m^2/s	
grad_qp_Pos_Ion	Concentration gradient, qp	mol/m^4	
dflux_qp_Pos_Ion	Diffusive flux, qp	mol/(m^2*s)	
cflux_qp_Pos_Ion	Convective flux, qp	mol/(m^2*s)	
tflux_qp_Pos_Ion	Total flux, qp	mol/(m^2*s)	
cellPe_qp_Pos_Ion	Cell Peclet number, qp	1	
Dm_qp_Pos_Ion	Mean diffusion coefficient, qp	m^3/s	
res_qp_Pos_Ion	Equation residual for qp	mol/(m^2*s)	
res_sc_qp_Pos_Ion	Shock capturing residual for qp	mol/(m^2*s)	
da_qp_Pos_Ion	Total time scale factor, qp	m	
grad_qe_r_Electron	Concentration gradient, qe, r component	mol/m^4	
dflux_qe_r_Electron	Diffusive flux, qe, r component	mol/(m^2*s)	
cflux_qe_r_Electron	Convective flux, qe, r component	mol/(m^2*s)	
tflux_qe_r_Electron	Total flux, qe, r component	mol/(m^2*s)	
grad_qe_z_Electron	Concentration gradient, qe, z component	mol/m^4	
dflux_qe_z_Electron	Diffusive flux, qe, z component	mol/(m^2*s)	
cflux_qe_z_Electron	Convective flux, qe, z component	mol/(m^2*s)	
tflux_qe_z_Electron	Total flux, qe, z component	mol/(m^2*s)	
beta_qe_r_Electron	Convective field, qe, r component	m^2/s	
beta_qe_z_Electron	Convective field, qe, z component	m^2/s	
grad_qe_Electron	Concentration gradient, qe	mol/m^4	
dflux_qe_Electron	Diffusive flux, qe	mol/(m^2*s)	
cflux_qe_Electron	Convective flux, qe	mol/(m^2*s)	
tflux_qe_Electron	Total flux, qe	mol/(m^2*s)	
cellPe_qe_Electron	Cell Peclet number, qe	1	

Dm_qe_Electron	Mean diffusion coefficient, qe	m^3/s	
res_qe_Electron	Equation residual for qe	mol/(m^2*s)	
res_sc_qe_Electron	Shock capturing residual for qe	mol/(m^2*s)	
da_qe_Electron	Total time scale factor, qe	m	
grad_qn_r_Neg_Ion	Concentration gradient, qn, r component	mol/m^4	
dflux_qn_r_Neg_Ion	Diffusive flux, qn, r component	mol/(m^2*s)	
cflux_qn_r_Neg_Ion	Convective flux, qn, r component	mol/(m^2*s)	
tflux_qn_r_Neg_Ion	Total flux, qn, r component	mol/(m^2*s)	
grad_qn_z_Neg_Ion	Concentration gradient, qn, z component	mol/m^4	
dflux_qn_z_Neg_Ion	Diffusive flux, qn, z component	mol/(m^2*s)	
cflux_qn_z_Neg_Ion	Convective flux, qn, z component	mol/(m^2*s)	
tflux_qn_z_Neg_Ion	Total flux, qn, z component	mol/(m^2*s)	
beta_qn_r_Neg_Ion	Convective field, qn, r component	m^2/s	
beta_qn_z_Neg_Ion	Convective field, qn, z component	m^2/s	
grad_qn_Neg_Ion	Concentration gradient, qn	mol/m^4	
dflux_qn_Neg_Ion	Diffusive flux, qn	mol/(m^2*s)	
cflux_qn_Neg_Ion	Convective flux, qn	mol/(m^2*s)	
tflux_qn_Neg_Ion	Total flux, qn	mol/(m^2*s)	
cellPe_qn_Neg_Ion	Cell Peclet number, qn	1	
Dm_qn_Neg_Ion	Mean diffusion coefficient, qn	m^3/s	
res_qn_Neg_Ion	Equation residual for qn	mol/(m^2*s)	
res_sc_qn_Neg_Ion	Shock capturing residual for qn	mol/(m^2*s)	
da_qn_Neg_Ion	Total time scale factor, qn	m	

Bibliography

[1] A. Beroual, M. Zahn, A. Badent, K. Kist, A. J. Schwabe, H. Yamashita, K. Yamazawa, M. Danikas, W. D. Chadband, and Y. Torshin. Propagation and structure of streamers in liquid dielectrics. *IEEE Electr. Insul. Mag.*, 14(2):6–17, March 1998.

[2] Yu. V. Torshin. On the existence of leader discharges in mineral oil. *IEEE Trans. Dielectr. Electr. Insul.*, 2(1):167–179, February 1995.

[3] CEI/IEC60897:1987. *Methods for the determination of the lightning impulse breakdown voltage of insulating liquids.* IEC, Geneva, Switzerland, 1987.

[4] C. T. Duy, O. Lesaint, N. Bonifaci, A. Denat, and Y. Bertrand. High voltage breakdown and pre-breakdown properties in rape-seed insulating oil. In *Proc. Annual Report Conference on Electrical Insulation and Dielectric Phenomena CEIDP 2007*, pages 623–626, Vancouver, BC, Canada, October 14–17, 2007.

[5] C. T. Duy, O. Lesaint, A. Denat, N. Bonifaci, and Y. Bertrand. Streamer propagation and breakdown in rape-seed oil at high voltage. In *Proc. IEEE International Conference on Dielectric Liquids ICDL 2008*, pages 1–4, Futuroscope-Chasseneuil, France, June 2008.

[6] C. T. Duy, O. Lesaint, A. Denat, and N. Bonifaci. Streamer propagation and breakdown in natural ester at high voltage. *IEEE Trans. Dielectr. Electr. Insul.*, 16(6):1582–1594, December 2009.

[7] F. M. J. McCluskey, O. Lesaint, and A. Denat. Breakdown processes over large distances in insulating liquids of distinct chemical compositions. In *Conference Record of the 1994 IEEE International Symposium on Electrical Insulation*, pages 426–429, June 5–8, 1994.

[8] F. M. J. McCluskey, A. Denat, and O. Lesaint. Breakdown and prebreakdown phenomena in liquids under positive impulse voltages. *IEEE Trans. Dielectr. Electr. Insul.*, 1(3):377–382, June 1994.

[9] J. Nieto-Salazar, O. Lesaint, and A. Denat. Transient current and light emission associated to the propagation of pre-breakdown phenomena in water. In *Proc. Annual Report Conference on Electrical Insulation and Dielectric Phenomena CEIDP 2003*, pages 542–545, Albuquerque, NM, USA, 2003.

[10] J. Nieto-Salazar, N. Bonifaci, A. Denat, and O. Lesaint. Characterization and spectroscopic study of positive streamers in water. In *Proc. IEEE International Conference on Dielectric Liquids ICDL 2005*, pages 91–94, Coimbra, Portugal, June 26–July 1, 2005.

[11] J. C. Devins, S. J. Rzad, and R. J. Schwabe. Breakdown and prebreakdown phenomena in liquids. *J. Appl. Phys.*, 52:4531–4545, 1981.

[12] O. Lesaint and M. Jung. On the relationship between streamer branching and propagation in liquids: influence of pyrene in cyclohexane. *J. Phys. D: Appl. Phys.*, 33:1360–1368, 2000.

[13] G. Massala and O. Lesaint. Positive streamer propagation in large oil gaps: electrical properties of streamers. *IEEE Trans. Dielectr. Electr. Insul.*, 5(3):371–381, June 1998.

[14] L. Lundgaard, D. Linhjell, G. Berg, and S. Sigmond. Propagation of positive and negative streamers in oil with and without pressboard interfaces. *IEEE Trans. Dielectr. Electr. Insul.*, 5(3):388–395, June 1998.

[15] R. Liu, A. Jaksts, and T. Bengtsson. Streamer propagation in composite oil/cellulose insulation under li voltages. In *Conference Record of the 2000 IEEE International Symposium on Electrical Insulation ISEI 2000*, pages 426–430, Anaheim, CA, USA, April 2–5, 2000.

[16] R. Liu and A. Jaksts. Breakdown processes in transformer insulation under li voltages. In *Proc. IEEE International Conference on Dielectric Liquids ICDL 2005*, pages 75–78, Coimbra, Portugal, June 26–July 1, 2005.

[17] M. Zahn and J. R. Melcher. Space-charge dynamics of liquids. *Phys. Fluids*, 15(7):1197–1206, July 1972.

[18] Mathematica. http://reference.wolfram.com/mathematica/ref/streamplot.html.

[19] M. Zahn. *Electromagnetic Field Theory: A Problem Solving Approach.* Robert E. Krieger Publishing Company, Inc., 2003.

[20] M. Zahn. Transient drift-dominated unipolar conduction between concentric cylinders and spheres. *IEEE Trans. Electr. Insul.*, EI-11(4):150–157, December 1976.

[21] O. Lesaint and G. Massala. Positive streamer propagation in large oil gaps: experimental characterization of propagation modes. *IEEE Trans. Dielectr. Electr. Insul.*, 5(3):360–370, June 1998.

[22] D. Linhjell, L. Lundgaard, and G. Berg. Streamer propagation under impulse voltage in long point-plane oil gaps. *IEEE Trans. Electr. Insul.*, 1:447–458, 1994.

[23] V. Segal, A. Hjortsberg, A. Rabinovich, D. Nattrass, and K. Raj. Ac (60 hz) and impulse breakdown strength of a colloidal fluid based on transformer oil and magnetite nanoparticles. In *Conference Record of the 1998 IEEE International Symposium on Electrical Insulation ISEI 1998*, pages 619–622, Arlington, VA, USA, June 7-10, 1998.

[24] R. Bartnikas, editor. *Engineering Dielectrics: Electrical Insulating Liquids*, volume 3. American Society for Testing and Materials, Philadelphia, 1994.

[25] F. M. O'Sullivan. *A model for the initiation and propagation of electrical streamers in transformer oil and transformer oil based nanofluids.* PhD thesis, Massachusetts Institute of Technology, 2007.

[26] R. Tobazeon. Prebreakdown phenomena in dielectric liquids. *IEEE Trans. Dielectr. Electr. Insul.*, 1(6):1132–1147, December 1994.

[27] H. Akiyama. Streamer discharges in liquids and their applications. *IEEE Trans. Dielectr. Electr. Insul.*, 7(5):646–653, October 2000.

[28] E. O. Forster. Critical assessment of the electrical breakdown process in dielectric fluids. *IEEE Trans. Electr. Insul.*, (5):891–896, October 1985.

[29] R. E. Hebner. *Measurements of electrical breakdown in liquids*, pages 519–537. Plenum Press, New York, 1988.

[30] Y. Nakao, T. Yamazaki, K. Miyagi, Y. Zakai, and H. Tagashira. The effect of molecular structure on prebreakdown phenomena in dielectric liquids under nonuniform field. *Electrical Engineering in Japan*, 139(2):1–8, 2002.

[31] W. G. Chadband. On variations in the propagation of positive discharges between transformer oil and silicone fluids. *J. Phys. D: Appl. Phys.*, 13:1299–1307, 1980.

[32] O. Lesaint and P. Gournay. Initiation and propagation thresholds of positive prebreakdown phenomena in hydrocarbon liquids. *IEEE Trans. Dielectr. Electr. Insul.*, 1(4):702–708, August 1994.

[33] P. Rain and O. Lesaint. Prebreakdown phenomena in mineral oil under step and ac voltage in large-gap divergent fields. *IEEE Trans. Dielectr. Electr. Insul.*, 1(4):692–701, August 1994.

[34] S. Ingebrigtsen, L. E. Lundgaard, and P.-O. Astrand. Effects of additives on prebreakdown phenomena in liquid cyclohexane: 1. streamer initiation. *J. Phys. D: Appl. Phys.*, 40:5624–5634, 2007.

[35] S. Ingebrigtsen, L. E. Lundgaard, and P.-O. Astrand. Effects of additives on prebreakdown phenomena in liquid cyclohexane: 2. streamer propagation. *J. Phys. D: Appl. Phys.*, 40:5624–5634, 2007.

[36] N. H. Malik, A. A. Al-Arainy, and M. I. Qureshi. *Electrical Insulation in Power Systems.* Marcel Dekker Inc., New York, 1998.

[37] I. Adamczewski. *Ionization, Conductivity and Breakdown in Dielectric Liquids.* Taylor and Francis Ltd., London, 1969.

[38] V. Ya. Ushakov, V. F. Klimkin, and S. M. Korobeynikov. *Impulse Breakdown of Liquids.* Springer-Verlag, Berlin, 2007.

[39] F. M. Clark. *Insulating Materials for Design and Engineering Practice.* John Wiley and Sons Inc, New York, 1962.

[40] A. Agarwal and J. H. Lang. *Foundations of Analog and Digital Electronic Circuits.* Elsevier Inc., Amsterdam, 2005.

[41] W. G. Chadband. The ubiquitous positive streamer. *IEEE Trans. Electr. Insul.*, 23:897, 1988.

[42] P. Biller. A simple qualitative model for the different types of streamers in dielectric liquids. In *Proc. 12th International Conference on Conduction and Breakdown in Dielectric Liquids ICDL 1996*, pages 189–192, Baden-Dattwil, Switzerland, July 15–19, 1996.

[43] P. Biller. Fractal streamer models with physical time. In *Proc. IEEE 11th International Conference on Conduction and Breakdown in Dielectric Liquids ICDL 1993*, pages 199–203, Baden-Dattwil, Switzerland, July 19–23, 1993.

[44] A. L. Kupershtokh, E. I. Palchikov, D. I. Karpov, I. Vitellas, D. P. Agoris, and V. P. Charalambakos. Stochastic model of breakdown initiation in dielectric liquids. *J. Phys. D: Appl. Phys*, 35:3106–3121, 2002.

[45] H. A. Fowler, J. E. Devaney, and J. G. Hagedorn. Growth model for filamentary streamers in an ambient field. *IEEE Trans. Dielectr. Electr. Insul.*, 10(1):73–79, February 2003.

[46] M. Kim and R. E. Hebner. Initiation from a point anode in a dielectric liquid. *IEEE Trans. Dielectr. Electr. Insul.*, 13(6):1254–1260, December 2006.

[47] M. Kim, R. E. Hebner, and G. A. Hallock. Modeling the growth of streamers during liquid breakdown. *IEEE Trans. Dielectr. Electr. Insul.*, 15(2):547–553, April 2008.

[48] M. Kim, B. Murphy, and R. E. Hebner. Stochastic modeling of streamer transitions. In *Proc. Annual Report Conference on Electrical Insulation and Dielectric Phenomena CEIDP 2008*, pages 615–617, Quebec City, QC, Canada, October 26–29, 2008.

[49] I. Fofana and A. Beroual. A model for long air gap discharge using an equivalent electrical network. *IEEE Trans. Dielectr. Electr. Insul.*, 3(2):273–282, April 1996.

[50] T. Aka-Ngnui and A. Beroual. Determination of the streamers characteristics propagating in liquids using the electrical network computation. *IEEE Trans. Dielectr. Electr. Insul.*, 13(3):572–579, June 2006.

[51] F. O'Sullivan, Se-Hee Lee, M. Zahn, L. Pettersson, Rongsheng Liu, O. Hjortstam, T. Auletta, and U. Gafvert. Modeling the effect of ionic dissociation on charge transport in transformer oil. In *Proc. IEEE Conference on Electrical Insulation and Dielectric Phenomena CEIDP 2006*, pages 756–759, Kansas City, MO, USA, October 15–18, 2006.

[52] Se-Hee Lee, F. O'Sullivan, Il-Han Park, M. Zahn, L. Pettersson, Rongsheng Liu, O. Hjortstam, A. Jaksts, T. Auletta, and U. Gafvert. Finite element analysis of charge injection and transport in a dielectric liquid. In *Proc. IEEE Conference on Electrical Insulation and Dielectric Phenomena CEIDP 2006*, pages 129–132, Kansas City, MO, USA, October 15–18, 2006.

[53] F. O'Sullivan, J. G. Hwang, M. Zahn, O. Hjortstam, L. Pettersson, Rongsheng Liu, and P. Biller. A model for the initiation and propagation of positive streamers in transformer oil. In *Conference Record of the 2008 IEEE International Symposium on Electrical Insulation ISEI 2008*, pages 210–214, Vancouver, BC, Canada, June 9–12, 2008.

[54] COMSOL AB. http://www.comsol.com.

[55] A. Al-Sulaiman and M. I. Qureshi. The role of methylnaphthalene in ehv cable oil as related to oil breakdown and discharge velocity. *European Trans. Electr. Power*, 12(6):389–395, November/December 2002.

[56] M. Khalifa, editor. *High-Voltage Engineering: Theory and Practice.* Marcel Dekker, Inc., New York, 1990.

[57] M. U. Anker. Effect of test geometry, permittivity matching and metal particles on the flashover voltage of oil/solid interfaces. *IEEE Trans. Power App. Syst.*, (12):3796–3802, December 1983.

[58] E. M. Hizal and S. Dincer. Breakdown time lags and pre-breakdown phenomena in transformer oil, effects of hydrostatic pressure. *J. Electrostatics*, 12:333–343, April 1982.

[59] R. Liu, C. Tornkvist, V. Chandramouli, O. Girlanda, and L. A. A. Pettersson. Ester fluids as alternative for mineral oil: the difference in streamer velocity and li

breakdown voltages. In *Proc. Annual Report Conference on Electrical Insulation and Dielectric Phenomena CEIDP 2009*, pages 543–548, Virginia Beach, VA, USA, October 2009.

[60] L. Costeanu and O. Lesaint. On mechanisms involved in the propagation of subsonic positive streamers in cyclohexane. In *Proc. IEEE 14th International Conference on Dielectric Liquids ICDL 2002*, pages 143–146, Graz, Austria, July 7–12, 2002.

[61] M. Harada, Y. Ohga, I. Watanabe, and H. Watarai. Ionization energies for solvated polycyclic aromatic hydrocarbons. *Chem. Phys. Lett.*, 303:489–492, 1999.

[62] H. S. Smalo, P.-O. Astrand, and S. Ingebrigtsen. Calculation of ionization potentials and electron affinities for molecules relevant for streamer initiation and propagation. In *Proc. IEEE International Conference on Dielectric Liquids ICDL 2008*, pages 1–4, Futuroscope-Chasseneuil, France, June 2008.

[63] Nynas AB. *Nynas Transformer Oil - Nytro 10XN (IEC 60296/03)*, 2008.

[64] D. R. Lide, editor. *Physical Constants of Organic Compounds*, pages 519–537. CRC Press/Taylor and Francis, Boca Raton, 89th edition, 2009.

[65] T. V. Oommen. Vegetable oils for liquid-filled transformers. *IEEE Electr. Insul. Mag.*, 18(1):6–11, January 2002.

[66] S. Sakamoto and H. Yamada. Optical study of conduction and breakdown in dielectric liquids. *IEEE Trans. Electr. Insul.*, EI-15:171–181, 1980.

[67] V. M. Atrazhev, E. G. Dmitriev, and I. T. Iakubov. The impact ionization and electrical breakdown strength for atomic and molecular liquids. *IEEE Trans. Electr. Insul.*, 26(4):586–591, August 1991.

[68] L. Dumitrescu, O. Lesaint, N. Bonifaci, A. Denat, and P. Notingher. Study of streamer inception in cyclohexane with a sensitive charge measurement technique under impulse voltage. *J. Electrostatics*, 53:135–146, 2001.

[69] R. E. Hebner, E. F. Kelley, E. O. Forster, and G. J. FitzPatrick. Observation of prebreakdown and breakdown phenomena in liquid hydrocarbons 2. non-uniform field conditions. *IEEE Trans. Electr. Insul.*, EI-20(2):281–292, April 1985.

[70] O. Lesaint and M. Jung. Streamer propagation in cyclohexane: influence of a polyaromatic additive. In *Proc. Annual Report Conference on Electrical Insulation and Dielectric Phenomena CEIDP 1997*, volume 2, pages 672–675, Minneapolis, MN, USA, October 19–22, 1997.

[71] Y. Nakao, H. Itoh, S. Hoshino, Y. Sakai, and H. Tagashira. Effects of additives on pre-breakdown phenomena in n-hexane. *IEEE Trans. Dielectr. Electr. Insul.*, 1(3):383–389, June 1994.

[72] S. Ingebrigtsen, H.S. Smalo, P.-O. Astrand, and L.E. Lundgaard. Effects of electron-attaching and electron-releasing additives on streamers in liquid cyclohexane. *IEEE Trans. Dielectr. Electr. Insul.*, 16(6):1524–1535, December 2009.

[73] J. G. Hwang, M. Zahn, L. A. A. Pettersson, O. Hjortstam, and R. Liu. Modeling streamers in transformer oil: The transitional fast 3rd mode streamer. In *Proc. IEEE International Conference on the Properties and Applications of Dielectric Materials ICPADM 2009*, pages 573–578, Harbin, China, July 19–23, 2009.

[74] V. Segal and K. Raj. An investigation of power transformer cooling with magnetic fluids. *Indian J. Eng. Mater. Sci.*, 5(6):416–422, 1998.

[75] V. Segal, A. Rabinovich, D. Nattrass, K. Raj, and A. Nunes. Experimental study of magnetic colloidal fluids behavior in power transformers. *J. Magn. Magn. Mater.*, 215:513–515, 2000.

[76] V. Segal, D. Nattrass, K. Raj, and D. Leonard. Accelerated thermal aging of petroleum-based ferrofluids. *J. Magn. Magn. Mater.*, 201:70–72, 1999.

[77] V. Segal. Colloidal insulating and cooling fluid. United States Patent 5,863,455, January 26, 1999.

[78] K. Raj and R. Moskowitz. Ferrofluid-cooled electromagnetic device and improved cooling method. United States Patent 5,462,685, October 31, 1995.

[79] T. Cader, S. Bernstein, and S. Crowe. Magnetic fluid cooler transformer. United States Patent 5,898,353, April 27, 1999.

[80] J. G. Hwang, M. Zahn, F. M. O'Sullivan, L. A. A. Pettersson, O. Hjortstam, and R. Liu. Effects of nanoparticle charging on streamer development in transformer-oil based nanofluids. *J. Appl. Phys.*, 107(014310):1–17, January 2010.

[81] H. P. Moser. *Transformerboard.* H. Weidmann AG, Rapperswil, Switzerland, 1979.

[82] H. P. Moser and V. Dahinden. *Transformerboard II.* H. Weidmann AG, Rapperswil, Switzerland, 1987.

[83] *ABB Transformer Handbook.* ABB, 2004.

[84] L. Lundgaard, H. Forster, and W. Hansen. Electric breakdown in liquid insulation combined with solid insulation. In *Proc. Nordic Insulation Symposium NORD-IS 1984*, pages 8.1–8.9, Kunglv, Sweden, 1984.

[85] A. Kurita, E. Takahasi, J. Ozawa, M. Watanabe, and K. Okuyana. Dc flashover voltage characeteristics and their calculation method for oil-immersed insulation systems in hvdc transformers. *IEEE Trans. Power Del.*, 1(3):184–190, July 1986.

[86] J. C. Devins and S. J. Rzad. Streamer propagation in liquids and over liquid-solid interfaces. *IEEE Trans. Electr. Insul.*, EI-17(6):512–516, December 1982.

[87] L. Lundgaard and H. Danielsen. The influence of pressboard parallel to the field on ac-breakdown in oil gaps. In *Proc. International Symposium on High Voltage Engineering ISH 1983*, pages 24.01–24.04, September 5-9 1983.

[88] E. F. Kelley and R. E. Hebner. Electrical breakdown in composite insulating systems: liquid-solid interface parallel to the field. *IEEE Trans. Electr. Insul*, EI-16(4):297–303, August 1981.

[89] E. F. Kelley and R. E. Hebner. Measurement of the electric field in the vicinity of an oil-pressboard interface parallel to the field. *IEEE Trans. Electr. Insul.*, EI-19(6):519–523, December 1984.

[90] E. F. Kelley, R. E. Hebner, W. E. Anderson, J. A. Lechner, and J. L. Blue. The effect of an oil-paper interface parallel to an electric field on the breakdown voltage at elevated temperatures. *IEEE Trans. Electr. Insul.*, 23(2):249–259, April 1988.

[91] O. Lesaint and G. Massala. Transition to fast mode streamers in mineral oil in the presence of insulating solids. In *Proc. IEEE International Symposium on Electrical Insulation ISEI 1996*, pages 737–740, 1996.

[92] U. Gafvert, O. Hjortstam, Y. Serdyuk, C. Tornkvist, and L. Walfridsson. Modeling and measurements of electric fields in composite oil/cellulose insulation. In *Proc. IEEE Conference on Electrical Insulation and Dielectric Phenomena CEIDP 2006*, pages 154–157, Kansas City, MO, USA, October 15–18, 2006.

[93] R. J. Taylor. Effect of permittivity matching on the flashover of solid/liquid interfaces. *Proc. IEE*, 124:899–904, 1977.

[94] M. Nozaki, H. Ishizuka, E. Ooe, H. , I. Tani, Y. Kamata, and K. Endo. Low-dielectric constant press board for oil impregnation insulation. European Patent EP 0272497 A3, November 27, 1993.

[95] O. Hjortstam, R. Liu, A. Jaksts, and L. A. Pettersson. An electrical insulation amterial, an electric device comprising the insulation material and a transformer. International Patent WO 2009/083343, July 9 2009.

[96] U. Gafvert, A. Jaksts, C. Tornkvist, and L. Walfridsson. Electrical field distribution in transformer oil. *IEEE Trans. Electr. Insul.*, 27:647–660, 1992.

[97] W. F. Schmidt. Electronic conduction processes in dielectric liquids. *IEEE Trans. Electr. Insul.*, EI-19:389–418, 1984.

[98] A. O. Allen. *Drift Mobilities and Conduction Band Energies of Excess Electrons in Dielectric Liquids.* NSRDS-NBS, 1976.

[99] A. Denat, B. Gosse, and J. P. Gosse. Electrical conduction of solutions of an ionic surfactant in hydrocarbons. In *Proc. IEEE International Conference on Dielectric Liquids ICDL 2008*, pages 130–134, Berlin, Germany, July 1981.

[100] W. F. Schmidt. *Liquid State Electronics of Insulating Liquids.* CRC Press, 1997.

[101] J. Qian, R. P. Joshi, E. Schamiloglu, J. Gaudet, J. R. Woodworth, and J. Lehr. Analysis of polarity effects in the electrical breakdown of liquids. *J. Phys. D: Appl. Phys.*, 39:359–369, 2006.

[102] Se-Hee Lee, Se-Yeon Lee, Young-Ki Chung, and Il-Han Park. Finite-element analysis of corona discharge onset in air with artificial diffusion scheme and under fowler nordheim electron emission. *IEEE Trans. Magn.*, 43(4):1453–1456, April 2007.

[103] G. E. Georghiou, R. Morrow, and A. C. Metaxas. A two-dimensional finite element flux-corrected transport algorithm for the solution of gas discharge problems. *J. Phys. D: Appl. Phys.*, 33(19):2453–2466, 2000.

[104] T. N. Tran, I. O. Golosnoy, P. L. Lewin, and G. E. Georghiou. Two dimensional studies of trichel pulses in air using the finite element methhod. In *Proc. Annual Report Conference on Electrical Insulation and Dielectric Phenomena CEIDP 2009*, pages 592–595, Virginia Beach, VA, USA, October 18–21, 2009.

[105] Y. Nakamura, K. Shinsaka, and Y. Hatano. Electron mobilities and electron-ion recombination rate constants in solid, liquid and gaseous methane. *J. Chem. Phys.*, 78:5820–5824, 1983.

[106] M. Tachiya. Breakdown of the debye theory of bulk ion recombination. *J. Chem. Phys.*, 87:4108–4113, 1987.

[107] T. J. Lewis. Basic electrical processes in dielectric liquids. *IEEE Trans. Dielectr. Electr. Insul.*, 1(4):630–643, August 1994.

[108] M. Sack, Y. Julliard, R. Badent, and A. J. Schwab. Electrical trees in solids and streamers in liquids - structural analogies and differences. In *Proc. Annual Report Conference on Electrical Insulation and Dielectric Phenomena CEIDP 2002*, pages 60–63, Cancun, Mexico, October 20–24, 2002.

[109] Sir J. Townsend. *The Theory of Ionization of Gases by Collision.* Constable & Company, London, 1910.

[110] J. M. Meek and J. D. Craggs, editors. *Electrical Breakdown of Gases.* John Wiley & Sons, Chichester, 1978.

[111] R. Badent. Streamer model based on electronic processes in liquids. In *Proc. Annual Report Conference on Electrical Insulation and Dielectric Phenomena CEIDP 1999*, volume 2, pages 447–450, Austin, TX, USA, October 17–20, 1999.

[112] W. G. Chadband. Electrical breakdown - from liquid to amorphous solids. *J. Phys. D.: Appl. Phys.*, 24:56–64, 1991.

[113] T. J. Lewis. A new model for the primary process of electrical breakdown in liquids. *IEEE Trans. Dielectr. Electr. Insul.*, 5(3):306–315, June 1998.

[114] L. Onsager. Deviations from ohm's law in weak electrolytes. *J. Chem. Phys.*, 2:599–615, 1934.

[115] A. Alj, A. Denat, J. P. Gosse, B. Gosse, and I. Nakamura. Creation of charge carriers in nonpolar liquids. *IEEE Trans. Electr. Insul.*, (2):221–231, April 1985.

[116] F. Pontiga and A. Castellanos. Electrical conduction of electrolyte solutions in non-polar liquids. *IEEE Trans. Ind. Appl.*, 32(4):816–824, July/August 1996.

[117] W. An, K. Baumung, and H. Bluhm. Underwater streamer propagation analyzed measurements from pressure release. *J. Appl. Phys.*, 101(053302):1–10, 2007.

[118] B. Halpern and R. Gomer. Field ionzation in liquids. *J. Chem. Phys.*, 51:1048–1056, 1969.

[119] K. Dotoku, H. Yamada, S. Sakamoto, S. Noda, and H. Yoshida. Field emission into non-polar liquids. *J. Chem. Phys.*, 69:1121–1125, 1978.

[120] W. Schnabel and W. F. Schmidt. Polymerization by high electric fields: field emission and field ionization. *J. Polymer Sci.*, 42:273–280, 1973.

[121] C. Zener. A theory of the electrical breakdown of solid dielectrics. *Proc. Roy. Soc. A*, 145:523–529, 1934.

[122] R. A. Holroyd and W. F. Schmidt. Transport of electrons in nonpolar fluids. *Annu. Rev. Phys. Chem.*, 40:439–468, 1989.

[123] J. K. Baird. Negative ion photodetachment and the electron effective mass in liquids. *J. Chem. Phys.*, 79:316–320, 1983.

[124] ExxonMobil. *Marcol 82: medicinal grade white oil*, 2009.

[125] A. Denat. High field conduction and prebreakdown phenomena in dielectric liquids. *IEEE Trans. Dielectr. Electr. Insul.*, 13(3):518–525, June 2006.

[126] M. Sparks, D. L. Mills, R. Warren, T. Holstein, A. A. Maradudin, L. J. Sham, Jr. E. Loh, and D. F. King. Theory of electron-avalanche in solids. *Phys. Rev. B*, 24(6):3519–3536, September 1981.

[127] S. E. Dorenzo, T. S. Mast, and H. Zaklad. Electron avalanche in liquid xenon. *Phys. Rev. A*, 9(6):2582–2592, June 1974.

[128] M. Haidara and A. Denat. Electron multiplication in liquid cyclohexane and propane. *IEEE Trans. Electr. Insul.*, 26(4):592–597, August 1991.

[129] A. Denat (private communication). 2009.

[130] R. Badent, K. Kist, and A.J. Schwab. Prebreakdown phenomena in insulating oil at large gap distances. In *Proc. International Conference on the Properties and Applications of Dielectric Materials ICPADM 1994*, pages 103–106., Brisbane, Australia, July 1994.

[131] R. S. Sigmond. The residual streamer: return strokes and secondary streamers. *J. Appl. Phys.*, 56(5):1355–1370, September 1984.

[132] A. Hallac, G. E. Georghiou, and A. C. Metaxas. Secondary emission effects on streamer branching in transient non-uniform short-gap discharges. *J. Phys. D: Appl. Phys.*, 36:2498–2509, 2003.

[133] S. K. Dhali and A. K. Pal. Numerical simulation of streamers in sf6. *J. Appl. Phys.*, 63(5):1355–1362, March 1988.

[134] P. A. Vitello, B. M. Penetrante, and J. N. Bardsley. Simulation of negative-streamer in nitrogen. *Phys. Rev. E*, 49(6):5574–5600, June 1994.

[135] A. V. Likhanskii, M. N. Schneider, S. O. Macheret, and R. B. Miles. Modeling of dielectric barrier discharge plasma actuators driven by repetitive nanosecond pulses. *Phys. Plasmas*, 14(073501), July 2007.

[136] Thorsten Schutte. The influence of the molecular packing on electrical breakdown strength of liquids. In *Proc. Nordic Insulation Symposium NORD-IS 1994*, pages 2.4:1–2.4:14, Vaasa, Finland, 1994.

[137] M. Zahn. *Space charge dynamics of liquids.* PhD thesis, Massachusetts Institute of Technology, 1970.

[138] M. Zahn and J. R. Melcher. Erratum: Space-charge dynamics of liquids. *Phys. Fluids*, 15:2082, 1972.

[139] M. Zahn. Space charge coupled interfacial waves. *Phys. Fluids*, 17:343–352, 1974.

[140] R. Morrow. Properties of streamers and streamer channels in sf6. *Phys. Rev. A*, 35(4):1778–1785, February 1987.

[141] A. A. Kulikovksy. The role of photoionization in positive streamer dynamics. *J. Phys. D: Appl. Phys.*, 33:1514–1524, 2000.

[142] Y. V. Serdyuk, A. Larsson, S. M. Gubanski, and M. Akyuz. The propagation of positive streamers in a weak and uniform electric field. *J. Phys. D: Appl. Phys.*, 34:614–623, 2001.

[143] S. V. Pancheshnyi and A. Y. Starikovskii. Two-dimensional numerical modelling of the cathode-directed streamer development in a long gap at high voltage. *J. Phys. D: Appl. Phys.*, 36:2683–2691, 2003.

[144] R. Morrow (private communication). 2008.

[145] J. G. Hwang, M. Zahn, F. O'Sullivan, L. A. A. Pettersson, O. Hjortstam, and R. Liu. Electron scavenging by conductive nanoparticles in oil insulated power transformers. In *2009 Electrostatics Joint Conference*, Boston, MA, USA, June 2009.

[146] J. G. Hwang, F. O'Sullivan, M. Zahn, O. Hjortstam, L. A. A. Pettersson, and R. Liu. Modeling of streamer propagation in transformer oil-based nanofluids. In *Proc. Annual Report Conference on Electrical Insulation and Dielectric Phenomena CEIDP 2008*, pages 361–366, Quebec City, QC, Canada, October 26–29, 2008.

[147] F. J. W. Whipple and J. A. Chalmers. On wilson's theory of the collection of charge by falling drops. *Quart. J. Roy. Met. Soc.*, 70:103–119, 1944.

[148] J. R. Melcher. *Continuum Electromechanics.* The MIT Press, 1981.

[149] J. M. D. Coey, A. E. Berkowitz, L. I. Balcells, F. F. Putris, and F. T. Parker. Magnetoresistance of magnetite. *Appl. Phys. Letts.*, 72(6):734–736, 1998.

[150] A. Dey, A. De, and S. K. De. Electrical transport and dielectric relaxation in fe_3o_4-polypyrrole hybrid nanocomposites. *J. Phys.: Condens. Matter*, 17:5895–5910, 2005.

[151] S. Wolfram. *The Mathematica Book.* Wolfram Media/Cambridge University Press, fourth edition, 1999.

[152] R. E. Rosensweig. *Ferrohydrodynamics.* Dover Publications, 1997.

[153] Y. Lagmich, Th. Callegari, L. C. Pitchford, and J. P. Boeuf. Model description of surface dielectric barrier discharges for flow control. *J. Phys. D: Appl. Phys.*, 41(095205):1–10, April 2008.

[154] L. Papageorghiou, E. Panousis, J. F. Loiseau, N. Spyrou, and B. Held. Two-dimensional modelling of a nitrogen dielectric barrier (dbd) at atmospheric pressure: filament dynamics with the dielectric barrier on the cathode. *J. Phys. D: Appl. Phys.*, 42(105201):1–10, 2009.

[155] S. Bhosle, G. Zissis, J. J. Damelincourt, and A. Capdevila. A new approach for boundary conditions in dielectric barrier discharge modeling. In *Proc. XVI International Conference on Gas Discharges and their Applications*, Xian, China, September 2006.

[156] S. Kumara, Y. V. Serdyuk, and S. M. Gubanski. Charging of polymeric surfaces by positive impulse corona. *IEEE Trans. Dielectr. Electr. Insul.*, 16(3):726–733, June 2009.

[157] COMSOL AB. *COMSOL Multiphysics Modeling Guide*, 2008.

[158] L. Li, N. Bowler, S. H. Yoon, and M. R. Kessler. Dielectric properties of ptfe wiring insulation as a function of thermal exposure. In *Proc. Annual Report Conference on Electrical Insulation and Dielectric Phenomena CEIDP 2008*, pages 95–98, Quebec City, QC, Canada, October 26–29, 2008.

[159] M. Zahn. Optical, electrical and electromechanical measurement methodologies of field, charge and polarization in dielectrics. *IEEE Trans. Dielectr. Electr. Insul.*, 5(5):627–650, October 1998.

[160] R. Coelho and J. Debeau. Properties of the tip plane configuration. *J. Phys. D: Appl. Phys.*, 4:1266–1280, 1971.

[161] T. Maeno and T. Takada. Electric field measurement in liquid dielectrics using a combination of ac voltage modulation and a small retardation angle. *IEEE Trans. Dielectr. Electr. Insul.*, EI-22(4):503–508, August 1987.

[162] A. Helgeson and M. Zahn. Kerr electro-optic measurements of space charge effects in hv pulsed propylene carbonate. *IEEE Trans. Dielectr. Electr. Insul.*, 9(5):838–844, October 2002.

[163] K. Nakamura, K. Kato, H. Koide, Y. Hatta, and H. Okubo. Fundamental property of electric field in rapeseed ester oil based on kerr electro-optic measurement. *IEEE Trans. Dielectr. Electr. Insul.*, 13(3):601–607, June 2006.

[164] S.-H. Lee, I.-H. Park, F. O'Sullivan, M. Zahn, L. Pettersson, R. Liu, O. Hjortstam, A. Jaksts, T. Auletta, and U. Gafvert. Evaluation of discharge current by generalized energy method and integral ohm's law. In *Proc. Conference on the Computation of Electromagnetic Fields Compumag 2009*, page 4, Florianopolis, Brazil, 2009.

[165] J. G. Hwang, M. Zahn, and J. H. Lang. A low ionization potential additive method to increase the electrical breakdown strength of insulation materials. US Provisional Patent Application 61/316524, March 23, 2010.